Development of innovative silicon radiation detectors

Juan Pablo Balbuena Valenzuela

Thesis director: Dr. Giulio Pellegrini
Thesis tutor: Prof. Enrique Fernández Sánchez

Abstract

Silicon radiation detectors fabricated at the IMB-CNM (CSIC) Clean Room facilities using the most innovative techniques in detector technology are presented in this thesis. TCAD simulation comprises an important part in this work as becomes an essential tool to achieve exhaustive performance information of modelled detectors prior their fabrication and subsequent electrical characterization. Radiation tolerance is also investigated in this work using TCAD simulations through the potential and electric field distributions, leakage current and capacitance characteristics and the response of the detectors to the pass of different particles for charge collection efficiencies. Silicon detectors investigated in this thesis were developed for specific projects but also for applications in experiments which can benefit from their improved characteristics, as described in Chapter 1.

Double-sided double type columns 3D (3D-DDTC) detectors have been developed under the NEWATLASPIXEL project in the framework of the CERN RD50 collaboration for the ATLAS Inner Detector upgrades and the introduction of a new pixel layer called Insertable B-Layer. The radiation tolerance of *slim-edge* ("edgeless") detectors, whose current terminating structure reduces the insensitive area of detectors to 50 µm, for close-to-beam experiments like the TOTEM experiment at HL-LHC, have been simulated under the EU TOSTER project. *Ultra-thin 3D* detectors, which combine 3D detector technology and thin membrane fabrication process, are also studied in this work. They provide an alternative to the present Neutral Particle Analyzers at the International Thermonuclear Experimental Reactor (ITER) in the ions detection for plasma diagnosis, and they are also being used in neutron detection experiments after being covered with any layer containing ^{10}B whose high capture cross-section of thermal neutrons allows their detection through the emitted alpha. Finally, *active-edge* detectors have been studied for applications in X-ray beam positioning, X-ray sensors for beamstops and detectors with pad, microstrip and Medipix2 designs for research purposes.

Acknowledgments

NEWATLASPIXELS Referencia: FPA 2009-13896-C02-02
NEWATLASPIXELS2 Referencia: FPA 2010-22060-C02-02
EU TOSTER Referencia: INTAS 2005-103-7533

Index

Index of figures

Index of tables

Chapter 1

Applications of semiconductor radiation detectors

This chapter presents a brief introduction to the projects and experiments in which the technology of radiation detectors developed in this work can be applied.

- The CERN RD50 collaboration [1], that continues the work of RD48 [2] for the future High Luminosity LHC (HL-LHC) [3], has the objective of the research and development of new semiconductor devices able to work correctly under hard radiation environments. In this framework, *3D-DDTC* silicon detectors have been developed at IMB-CNM (CSIC) within the NEWATLASPIXELS projects (References: FPA2009-13896-C02-02 and FPA2010-22060-C02-02) for the upgrades of the ATLAS experiment [4] and the introduction of a new pixel layer in the ATLAS Inner Detector called Insertable B-Layer. The main features of the 3D-DDTC detectors are their intrinsic radiation hardness properties (low depletion voltages and short collection distances) as well as their low charge sharing.

- Close-to-beam experiments require radiation detector with the least dead region surrounding the active sensor. Silicon radiation detectors in p-type substrate with a current terminating structure, called *slim-edge* detectors, were simulated for the TOTEM experiment [5, 6] for this purpose. The dead region of these detectors is reduced to less than 50 μm offering an adequate performance. Based on those results, the EU TOSTER project arises with the objective of studying the radiation tolerance of these detectors and the development of new techniques to improve their radiation hardness. Studies of irradiated slim-edge detectors have been carried out in this context.

- A novel ultra-thin detector called *U3DTHIN* have been designed, simulated and fabricated for applications that range from plasma diagnosis in tokamak fusion reactors to very low energy spectroscopy. The main purpose of this detector is to provide an alternative to the present Neutral Particle Analyzers at the International Thermonuclear Experimental Reactor (ITER) [7] experiment which is being built to demonstrate the scientific and technological feasibility of fusion power for peaceful purposes. U3DTHIN detectors are also presently used in neutron detection experiments after being covered by any layer containing ^{10}B that produces alphas that are suitable for detection.

- *Active-edge* detectors are being fabricated in collaboration with DIAMOND Light Source Ltd [8] for X-Ray beam positioning, X-Ray sensor for beamstops and Medipix2 detectors for imaging. This new termination method does not require the inclusion of any guard ring or trench for confining the space charge region and the surrounding dead area is highly reduced to only a few micrometers.

1.1 High-Luminosity Large Hadron Collider (HL-LHC)

The Large Hadron Collider (LHC) [3] is the largest particle accelerator and hadron collider located at CERN, near Geneva, Switzerland. This accelerator started to work on spring 2009 with the aim of investigate physics beyond the Standard Model. The LHC is being funded and built in collaboration with hundreds of physicists from thirty-four countries, universities and institutes.

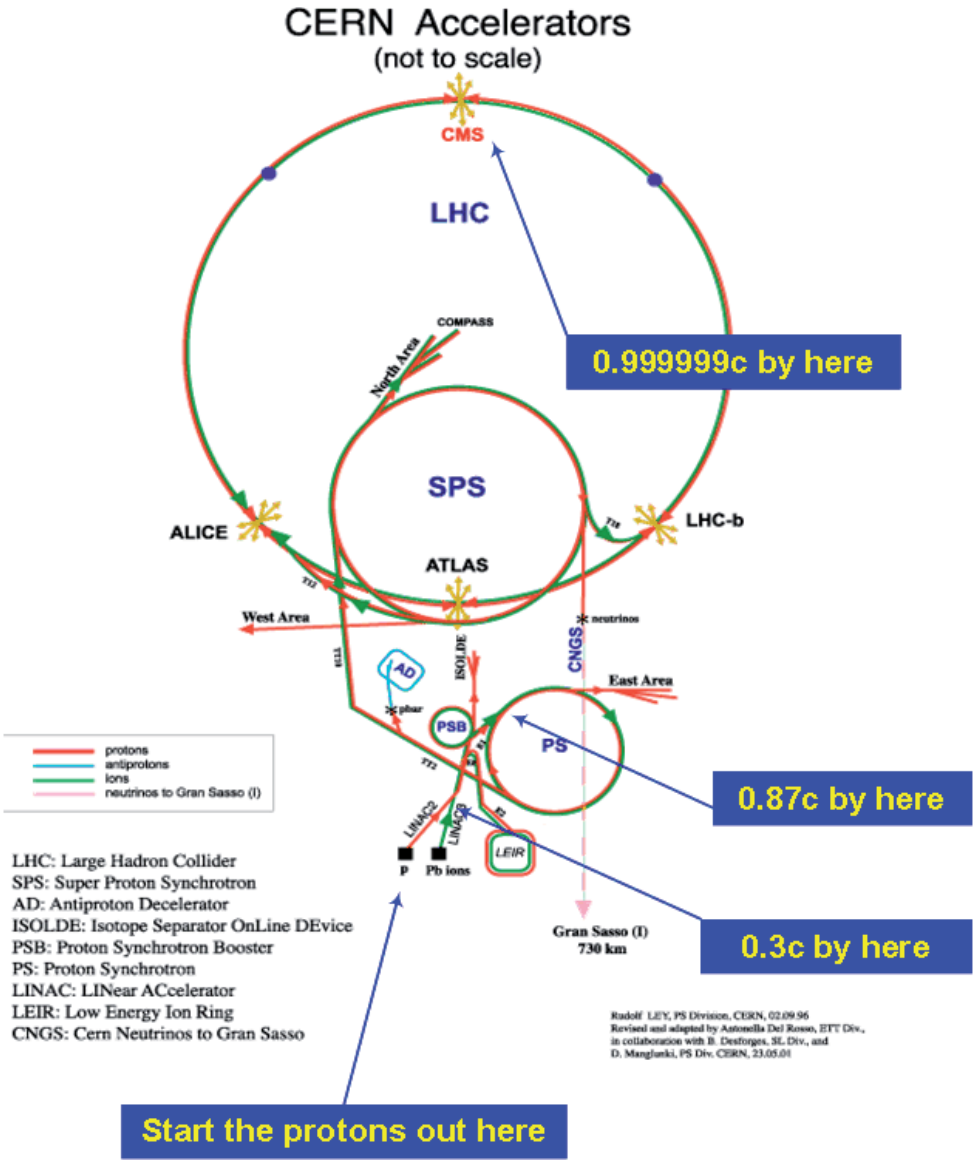

Figure 1.1: *Schema of CERN complex at Geneve.*

The collider is contained in a 27 km circumference tunnel located underground at a depth ranging from 50 to 175 m. The tunnel was formerly used to house the LEP, an electron-positron collider. The collider tunnel contains two pipes enclosed within superconducting magnets cooled by liquid helium, each pipe containing a proton beam. The two beams travel in opposite directions around the ring. Additional magnets are used to direct the beams to four intersection points where the collisions take place.

The nominal energy of protons is 7 TeV, giving a total collision energy of 14 TeV in the centre-of-mass. It takes around 90 microseconds for an individual proton to travel once around the LHC. Protons in the collider are "bunched" together into approximately 2800 bunches, with a proton bunch frequency of 25 ns.

Prior of being injected into the main accelerator, the particles are prepared through a series of systems that successively increase the particle energy levels. The first system is the linear accelerator LINAC2 generating 50 MeV protons which feeds the Proton Synchrotron Booster (PSB). Protons are then injected at 1.4 GeV into the Proton Synchrotron (PS) at 26 GeV. The Low-Energy Injector Ring (LEIR) will be used as an ion storage and cooler unit. The Antiproton Decelerator (AD) will produce a beam of anti-protons at 2 GeV, after cooling them down from 3.57 GeV. Finally the Super Proton Synchrotron (SPS) can be used to increase the energy of protons up to 450 GeV. Six detectors are being constructed at the LHC. They are located underground, in large caverns excavated at the LHC's intersection points. Two of them, ATLAS and CMS are large "general purpose" particle detectors. The other four (LHCb, ALICE, TOTEM, and LHCf) are smaller and more specialized. A scheme of the different experiments in LHC is shown in figure 1.1.

Proton beams

Proton beams are collided using superconductivity to make possible achieve the very strong magnetic fields that are required [9]. Superconductivity is the ability of certain materials to conduct electricity without resistance or energy loss, usually at very low temperatures, so the LHC operates at a temperature of 1.9 K. To keep the machine as compact and economical as possible, the magnets for both proton beams moving in opposite directions are built into a single 2-in-1 housing. The beams move around the LHC ring inside a continuous vacuum guided by magnets. There are many types of magnets used in LHC although the biggest are the main dipoles shown in figure 1.2.

Figure 1.2: *Close look of one of the main dipoles.*

The LHC is built in the same tunnel as CERN's Large Electron Positron collider, LEP, and so will cost much less than a similar machine on a green field site. Proton beams will be prepared by CERN's existing accelerator chain before being injected into the LHC. Each proton beam at full energy will consist of 2808 bunches per beam, and each bunch contains 1.15×10^{11} protons at the start of nominal fill. The particles in the LHC are ultra-relativistic and move at 0.999997828 times the speed of light at injection and 0.999999991 the speed of light at top energy. So the total beam energy at top energy is

$$2808\ bunches \times 1.15 \cdot 10^{11}\ protons\ @\ 7TeV = \mathbf{362\ MJ}$$

Physics at LHC

Studies on the physics potential and the experimental challenges for an upgrade of the LHC to a 10 times higher luminosity of 10^{35} $cm^{-2}s^{-1}$ have been performed for the accelerator and the experiments. A clear gain in physics potential has been identified but also the urgent need for setting up as soon as possible an intensive R&D program for both, in order to match the more stringent and very challenging requirements of HL-LHC. The luminosity[1] of the colliding beams is formulated as follows

$$L = \frac{N_b^2 n_b f_b}{4\pi\varepsilon\beta^*} \qquad \textbf{[1]}$$

for a circular cross-section beam with head-on collisions, where N_b is the number of particles in a bunch, n_b, is the number of bunches, f_b is the bunch frequency, ε is the transverse emittance, and β^* is the amplitude function defining the transverse beam size at the interaction point, IP.

The increase of luminosity by a factor of 10 can be achieved with three factors. By increasing the N_b to an ultimate value of 1.7×10^{11} protons per bunch, limited by beam-beam limit, from the nominal value of 1.1×10^{11}, the luminosity can be increased to 2.3×10^{34} $cm^{-2}s^{-1}$. By reducing the beta function, β^*, to 0.25m from the nominal of 0.5m by modifying the IP-Q magnets and/or IP layouts the luminosity can be increased to 4.6×10^{34} $cm^{-2}s^{-1}$. By doubling the number of bunches, n_b, to 5616 bunches from the nominal 2808, the luminosity can be increased to 9.2×10^{34} $cm^{-2}s^{-1}$. Doubling the number of bunches means reducing the bunch spacing to 12.5ns from the nominal value of 25ns. This requires upgrading cryogenics, collimation, the dumping system, and possibly upgrading the RF system in the Super Proton Synchrotron (SPS) and modifications to the injectors.

For the second stage of the HL-LHC upgrade the beam intensity and brilliance can be increased by a factor of 2 from its nominal ultimate value by upgrading the SPS with superconducting magnets and upgrading the transfer lines, thus injecting protons into the LHC at 1 TeV and reducing the energy swing by a factor of 2. By upgrading the LHC with new dipole magnets with a field of 15 T, the beam energy can be increased to 12.5 TeV. The stage-2 of HL-LHC would be operating by 2022.

[1] Luminosity is the effective rate of collisions between bunches.

1.1.1 RD50 Collaboration

The objective of the CERN RD50 Collaboration is the development of radiation hard semiconductor detectors for very high luminosity colliders. As it was previously described, a luminosity of 10^{35} $cm^{-2}s^{-1}$ is expected at the HL-LHC, corresponding to fast hadron fluences above 10^{16} n_{eq}/cm^2 in the inner detectors with a bunch frequency of 25 ns.

Different materials have been studied in both n and p-type substrates as DOFZ, Cz, MCz, EPI, and exposed to different hadron fluences of pions, protons and neutrons to evaluate their behaviour. Current-voltage and capacitance-voltage characteristics, charge collection, signal to noise, defect analysis, etc have been carried out for this purpose resulting in a huge literature about the understanding of the radiation damage in semiconductors.

Also new structures have been proposed and tested. Thin planar detectors with high radiation tolerance (low depletion voltages, higher collection efficiency due to small depleted volume) and 3D structures (low depletion voltages, short collection distances and low charge sharing) have promising features which are leading to promising results.

1.1.2 The TOTEM experiment

The objective of the TOTEM experiment is to obtain accurate information on the basic properties of proton-proton collisions at the maximum accelerator energy. The experimental program consists of the measurements of the total cross section of proton-proton collisions, elastic scattering with high momentum transferred and diffractive dissociation (closely related to elastic scattering). This experiment is in charge of the detection of particles emitted at low angles in the very forward cone that is not covered by other large detectors present at the LHC.

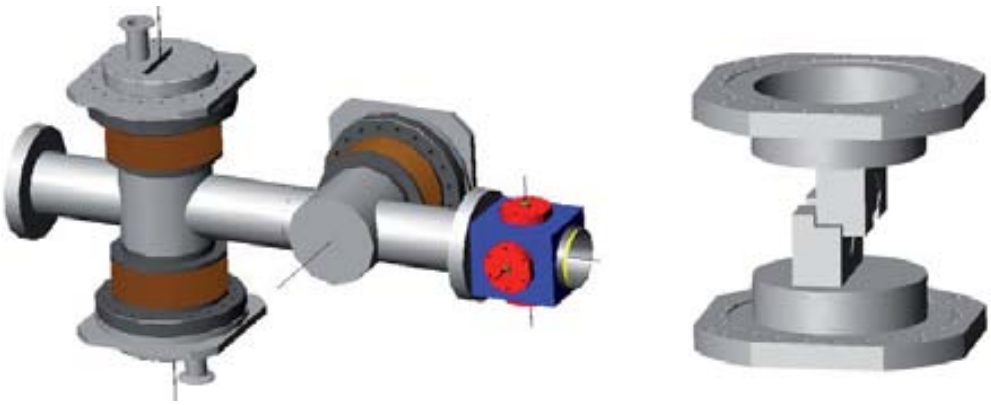

Figure 1.3: *Roman Pot unit (left) and detail of vertical setup (right).*

The measurement of elastic *p-p* scattering is accomplished by silicon detectors installed into special beam pipe insertions called *Roman Pots* [10] placed symmetrically on both sides of the crossing region, as shown in figure 1.3. Two Roman Pot stations are placed at 147 m and 220 m from the interaction point 5 (IP5), separated by a distance of several meters that permits a precise determination of the angle, even on the trigger level, thus reducing the background due to beam-gas and halo interactions, figure 1.4. It

is important to note that the 147 m Roman pots are located before the D2 magnet, while the 220 m tracking station is well behind it. This geometry naturally implements a magnetic spectrometer in the standard insertion, permitting TOTEM to measure particle momenta, with an accuracy of a few parts per thousand, allowing the accurate determination of the momentum loss of quasi-elastically scattered protons in diffractive processes.

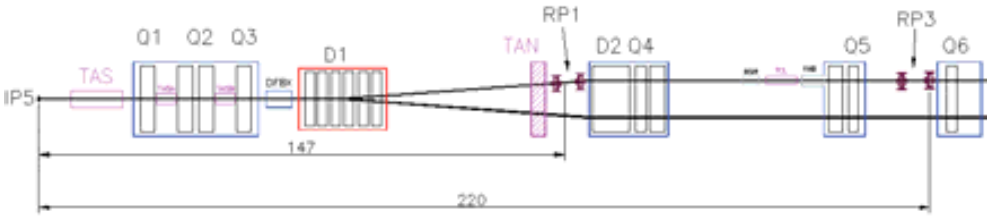

Figure 1. 4: *The LHC line with Roman Pots at 147 m and 220 m.*

During operation the detector edge is positioned at a distance of less than 1 mm from the axis of the high intensity proton beam where a 200 µm window separates the detectors from the primary beam vacuum. The beam of the LHC is rather thin, as it is shown in figure 1.5, with a 10 σ envelope of about 1 mm. For optimal performance, the detector has to approach the envelope of the beam as closely as possible. Consequently, the detectors must be active up to their physical edge. This is the case of the *slim-edge* detectors where a current terminating structure allows the reduction of the dead region surrounding the sensitive volume to less than 50µm.

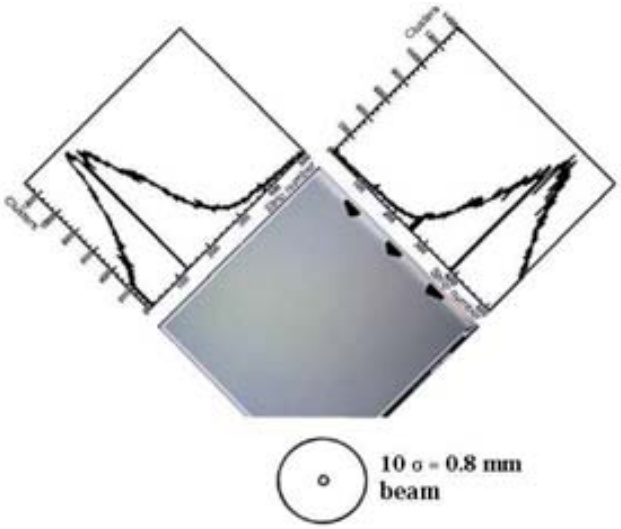

Figure 1.5: *Tracks response of slim-edge detector.*

IMB-CNM has worked in collaboration with CERN and other institutions in the development of new radiation hard slim-edge detectors in the framework of the EU TOSTER project [11]. The TOtem STrip Egeless Radiation detector project, TOSTER, has the aim of extending the potential of semiconductor *slim-edge* (initially called edgeless) detectors. Such detectors are provided with a current terminating structure that allows the reduction of the surrounding dead region of the active area of the sensor to less than 50 µm. The main task of this project consists in studying the radiation

tolerance of these detectors and the development of techniques to improve their radiation hardness suitable for close-to-beam experiments in the future HL-LHC upgrade.

1.1.3 ATLAS Upgrades

ATLAS (A Toroidal LHC ApparatuS [4]), figure 1.6, is one of the two general purpose particle physics experiments present at the LHC. The ATLAS detector is used to measure sets of path, energy and identity of the created particles in the head-on collisions of protons of extraordinarily high energy. ATLAS is one of the largest collaborative efforts ever attempted in the physical sciences. There are more than 2900 scientists participating from than 172 universities and laboratories in 37 countries.

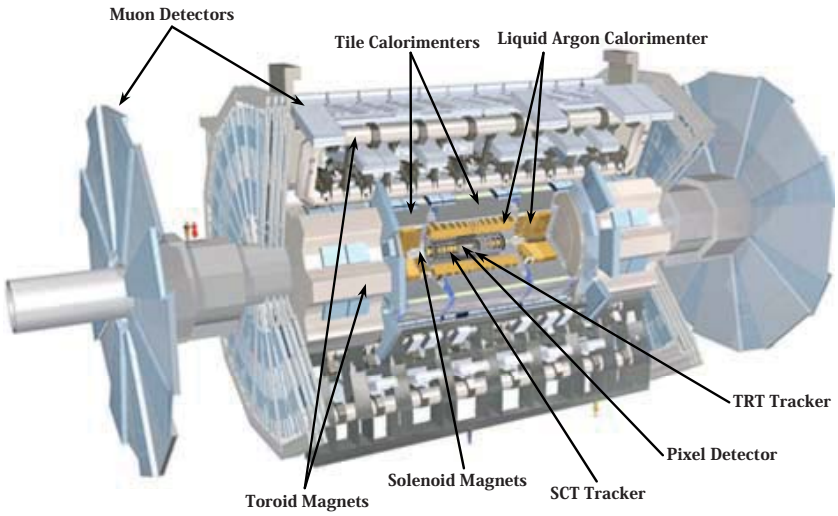

Figure 1.6: *Design of the ATLAS detector at CERN.*

This is the largest detector ever made, whose dimensions are: 46 m long, 25 m high and 25 m wide, with a total weight of 7000 tons. It is formed by six different detection subsystems plus a huge magnet system (Toroid and Solenoid magnets) for bending charge particles tracks for their identification, tracking, momentum and energy measurements.

The Inner Detector (ID) consists of three tracking systems contained in the Central Solenoid that provides a nominal magnetic field of 2 T. The size of the ID is 7 m long and an outer diameter of 1.15 m. In the barrel region the high-precision detectors are arranged in concentric cylinders around the beam axis, while the end-cap detectors are mounted on disks perpendicular to the beam axis.

The Pixel Detector [12] is the innermost detector which is composed by three barrels at three radii: 50.5 mm, 88.5 mm and 122.5 mm (1456 modules) from the interaction point, and three end-cap disks on each side (288 modules) between radii of 9 and 15 cm perpendicular to the beam. Each module is 62.4 mm long and 21.4 mm wide, with 46080 pixel elements readout by 16 chips, each serving an array of 18 by 160 pixels. The 80 million pixels cover an area of 1.7 m^2. The pixel detectors are *n-on-n*

fabricated in DOFZ[2] silicon and, for being located in the closest region to the interaction point, their exposition to the radiation is the highest where the expected accumulated fluence in the innermost layer (called B-layer and located at 50.5 mm) is expected to be 10^{15} n_{eq}/cm^2 after 10 years of operation. The radiation in this region is mostly due to pions and neutrons, and besides it is able to find short lived particles.

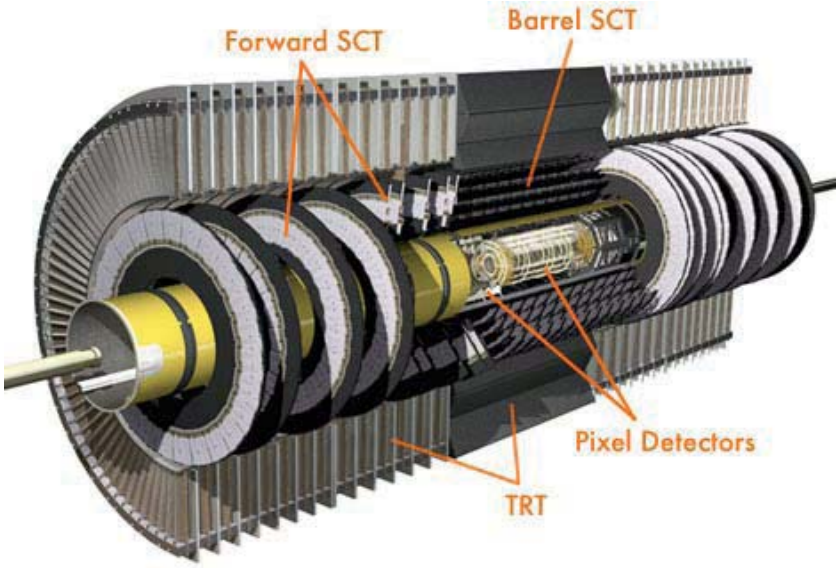

Figure 1.7: *Schematic of the ATLAS Inner Detector.*

The next detector consists of the Semiconductor Tracker (SCT) which is designed to provide eight precision measurements per track in the intermediate radial range, contributing to the measurement of momentum, impact parameter and vertex position. In the barrel SCT eight layers of DOFZ n-type silicon microstrip detectors provide precision point in (r, φ, z) coordinates, using small angle stereo to obtain the z-measurement. Each silicon detector is 6.36 × 6.40 cm^2 with 780 readout strips of 80 μm pitch. The barrel modules are mounted on carbon-fibre cylinders at radii of 299 mm, 371 mm, 443 mm and 514 mm. The end-cap modules are very similar in construction but use tapered strips with one set aligned radially. The radiation damage which suffers this detector is mostly due to neutrons.

In the outer region within the ID is the Transition Radiation Tracker (TRT), based on the use of straw detectors. The TRT, as well as the rest of the detection subsystems are beyond the study of this work, as they are not using semiconductor radiation detectors.

[2] These n-on-n DOFZ detectors have n^+ readout electrodes isolated by moderated p-spray implantations on n-type substrates that will undergo bulk type inversion after high fluences turning into “p-type”.

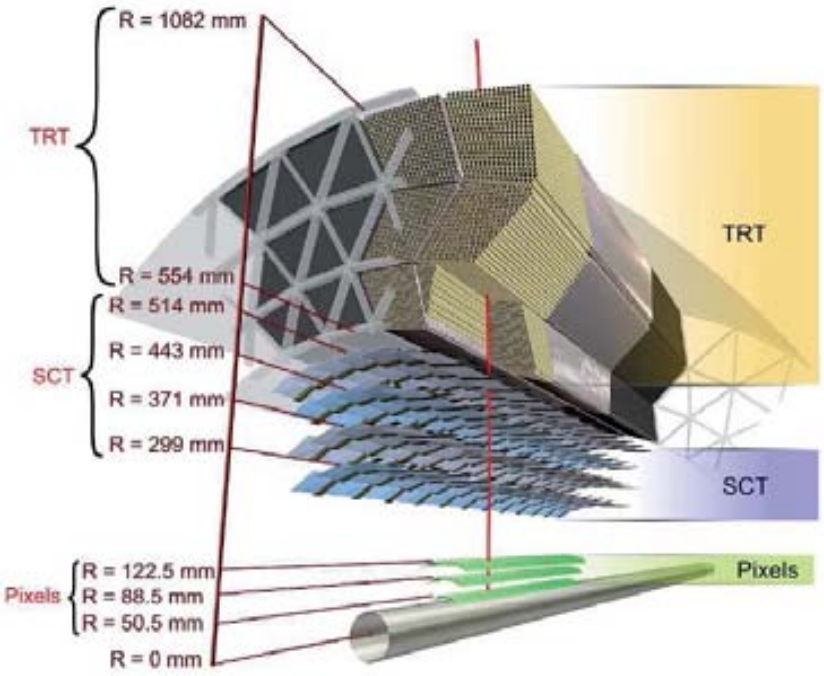

Figure 1.8: *Layout of the ATLAS ID showing the different layers of each detection system.*

As it was mentioned earlier, the Large Hadron Collider LHC started to work in 2009 and will continue recording collisions at even higher energies until 2013. At this time the first long shutdown will take place to prepare the LHC to run at design energy 14 TeV, and also the first upgrade of the ATLAS ID will take place with the introduction of an additional layer of pixel detectors, called Insertable B-Layer, closer to the beam-pipe. In 2014 the LHC will be operating again until 2017, when the second expected shutdown will take place. The instant luminosity at this stage will be increased up to 2.2 $\times 10^{34}$ $cm^{-2}s^{-1}$ with ~ 85 collisions per bunch crossing are expected. During the second shutdown the entire Pixel Detector will be replaced and upgraded to cope with the expected higher luminosity, 5×10^{34} $cm^{-2}s^{-1}$, and rate events ~ 200 collisions per bunch crossing. The next shutdown is scheduled by 2020 and the entire Inner Detector will be replaced.

The introduction of the IBL will be the first upgrade of the ATLAS ID and will be very useful to provide technological information for the following upgrades.

Insertable B-Layer

The layer closest to the beam-pipe in the Pixel Detector is called B-Layer. Silicon pixel detectors contained in this layer are the first one degrading in terms of efficiency with the increasing radiation damage and thus a replacement of this layer was initially proposed for the first long shutdown of LHC by 2013. As the materials of the Pixel Detector will be activated due to the radiation and a longer time than the first scheduled shutdown would be needed for cooling down, an alternative was decided: the introduction of a fourth pixel layer closer to the beam-pipe called *Insertable B-Layer* [13]. A new beam-pipe with smaller radius is needed for this task and thus the final layer will be located at an average radius of 33 mm.

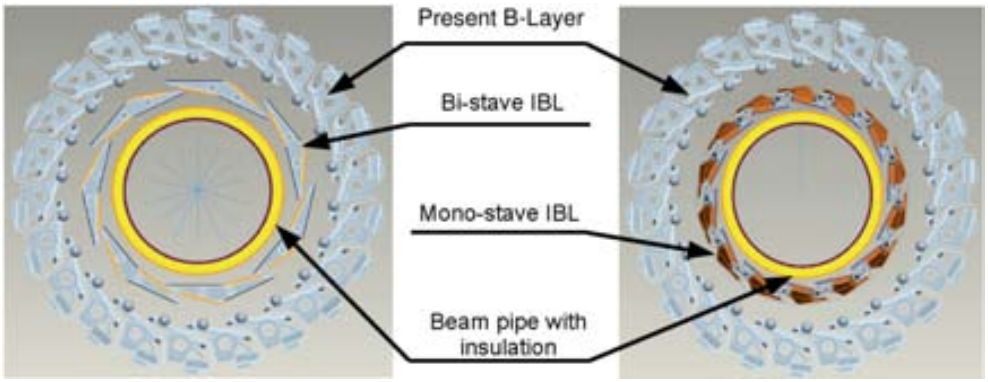

Figure 1.9: *Two possible configurations for the IBL stave [14].*

The higher instant luminosity and rate events that must withstand the additional pixel layer IBL involve the development of new technologies in silicon detectors to cope with the increasing radiation levels. In order to keep or even improve the performance of the current Pixel Detector, a new ATLAS pixel sensor has been designed. The sensor is thinner and the pixel size is smaller than the ones present in the B-Layer and currently are being fabricated in two technologies [15]: planar pixel sensors as in the current Pixel Detector, and 3D-DDTC pixel sensors which offer better performance although their fabrication is more complicated.

1.2 The ITER project

The International Thermonuclear Experimental Reactor, ITER, is a project whose aim is to demonstrate the scientific and technological feasibility of fusion power for peaceful purposes [16]. ITER is an experimental plant with a tokamak reactor at its core, in which strong magnetic fields confine a toroidal 10^3 m^3 fusion plasma. The ITER plasma will be heated with a mixture of the following heating system mechanisms: *1)* a changing current in the primary winding induces and sustains the plasma current that is heated by Joule effect, *2)* highly energetic neutral beams (^2H, 1 MeV) that will transfer their momentum to the ions, and *3)* radiofrequency waves are launched and coupled to the electrons transfering their energy to the ions by collisions.

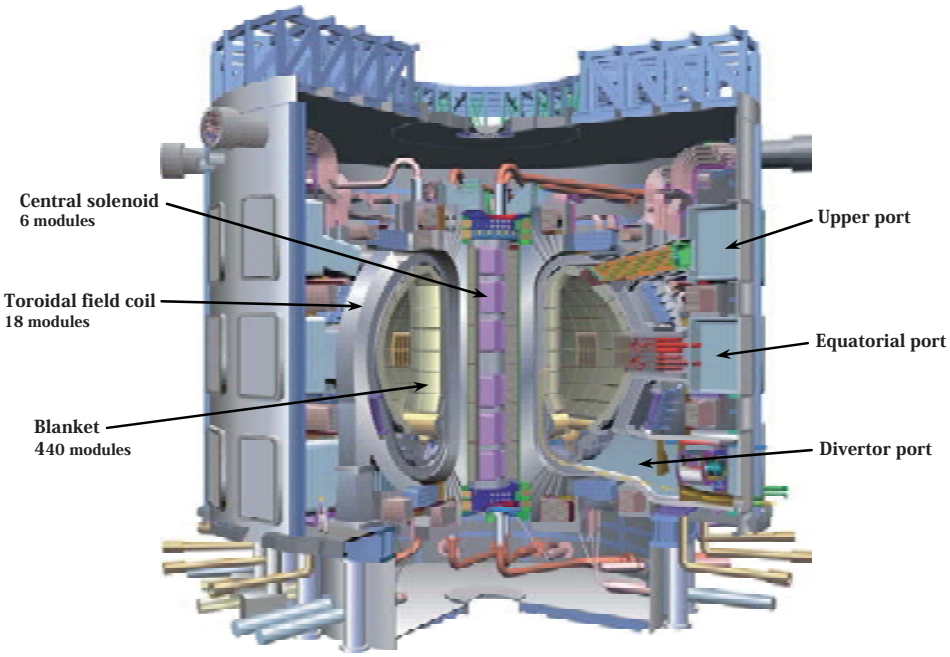

Figure 1.10: *Layout of the ITER machine that is being built in Cadarache, France.*

Energy is released in light nuclei fusion reactions and is suitable to be extracted in power plants. The fusible fuels of the reactor are deuterium and tritium, as their fusion cross-section is the largest at accessible temperatures, ~ 10^8 K. The reaction that takes place in the plasma is

$$^2H + {}^3H \rightarrow {}^4He\,(3.5\ MeV) + n\,(14.1\ MeV)$$

where the deuterium ^2H is found in water that is abundant, however tritium ^3H is not found in significant amounts in nature and therefore must be created artificially in neutrons reactors. For this purpose, a tritium breeding module of lithium will be mounted in ITER based on the reactions

$$^7Li + n\,(fast) \rightarrow {}^4He + {}^3H + n\,(E - 2.8\ MeV)$$
$$^6Li + n\,(thermal) \rightarrow {}^4He\,(2.1\ MeV) + {}^3H\,(2.7\ MeV)$$

Neutrons escape isotropically from the fusion plasma carrying the 80% of the energy released in the fusion reaction. They are absorbed in the blanket volume for the tritium breeder and transferring power to the heat exchangers and turbines. The rest of the energy, 20%, is inverted by the resulting alphas in heating the plasma and thus maintaining the ignition.

The challenges that are to be achieved with this experiment are [17]:

- Extended fusion in inductively-driven deuterium tritium plasma operation with $^3Q \geq 10$, not precluding ignition, with an inductive burn duration of 300 – 500 s.

[3] Q is the ratio of fusion power to auxiliary power injected to the plasma.

- Non-inductive fusion operating in steady state with $Q \geq 5$.

From the point of view of engineering performance, the objectives are to demonstrate the availability and integration of the essential technologies for a future fusion reactor, including superconducting magnets, components able to withstand high heat loads, and remote handling. In addition, it will be used to test and develop concepts for the tritium breeding module from lithium-containing materials inside thermally efficient high temperature blankets surrounding the plasma.

Neutral Particle Analyzers

The Neutral Particle Analyzers are used to perform corpuscular diagnostics of plasma [18]. They are designed to measure the hydrogen isotope composition: tritium-to-deuterium and hydrogen-to-deuterium ion density ratios in the plasma, n_T / n_D and n_H / n_D respectively, and to provide information on the distribution function of fast alphas generated as a result of the additional heating and nuclear fusion reactions in the MeV range.

The NPA system is allocated in the equatorial port 11 (of 18) sharing the same vaccum chamber with the X-ray and VUV systems[4]. It is directly coupled with a 200 mm tapering to 70 mm conical tube, approximately 6 m long. The incoming neutral particles are ionized in a thin carbon diamond-like foil (thickness ~ 100Å, diameter 20 mm) and then pass the magnetic and electric fields of the analyzing magnet and electrostatic condenser before detection.

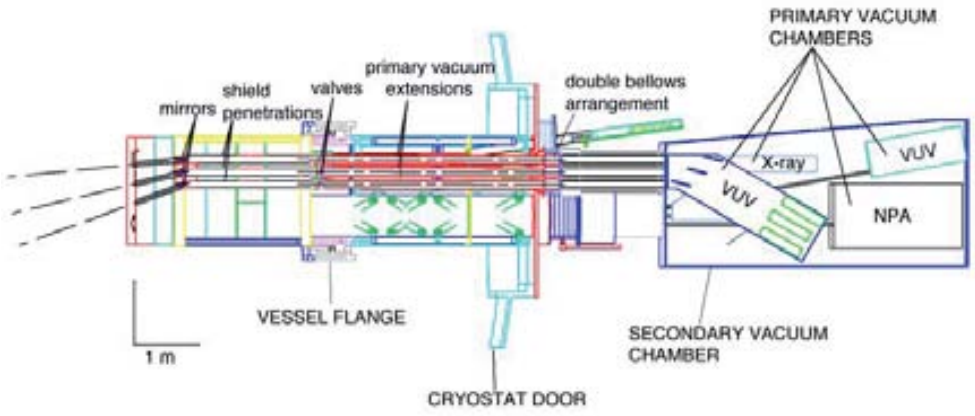

Figure 1.11: *Diagnostic port 11 of the equatorial port level.*

The NPA currently under development [19] has found difficulties to cover the full energy range 10 keV – 4 MeV of the incident particles. As a solution two analyzers are proposed: the low energy neutral particle analyzer (LENPA), which cover the thermal energy range 10 – 200 keV, and the high energy neutral particle analyzer (HENPA), for supra-thermal energies 0.1 – 4 MeV. Both analyzers are based in the using of photomultipliers with very thin CsI(Tl) scintillation layers of the micron range to reduce the neutron-gamma radiation sensitivity of the detectors.

[4] X-ray and vacuum ultraviolet spectroscopy systems.

An accelerator is needed for these detectors to increase the energy of the incident ions as the gamma-neutron sensitivities of the scintillation layers decreases significantly as the energy of the ions increases, thus increasing the signal to neutron-gamma noise ratio. For the case of thermal deuterium and tritium this value is ~ 100, meanwhile for supra-thermal the ratio is ~ 10. However, the neutron-gamma background is too much high for the fusion alphas detection.

Semiconductor sensors, using the newer technology of radiation hard sensors developed by the CERN RD50 collaboration, are proposed as an alternative for the NPA. The high quantity neutrons and gammas background in this environment that could eventually saturate the photomultiplier detectors is not supposing a problem in the proposed 3D Ultra-thin detector. The main features of this new detector are their sensitive thickness of only tens of microns, which makes them *transparent* to gammas and neutrons and offers near 100% of detection efficiency for ions, and their 3D electrodes structure that is intrinsically radiation hard [20] which presents low depletion voltages, short collection distances and low charge sharing. Besides, no additional ion accelerator is required.

1.3 Synchrotron facilities

Charged particles describing circular orbits emit a small fraction of their energy through electromagnetic radiation in a tangential direction during each cycle. This radiation, that receives the name of *synchrotron radiation*, has a broad energy spectrum and whose radiated power depends on the charge and mass of the particle, its velocity and the radius of the circular orbit. This source of synchrotron radiation has become an important source of X-rays accelerating electrons up to ultra-relativistic velocities.

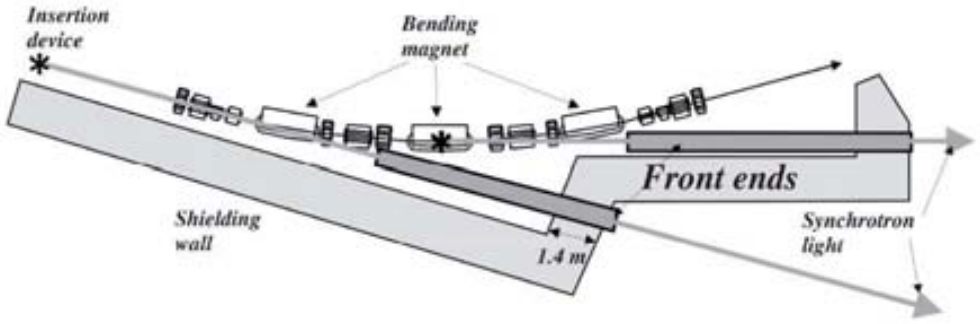

Figure 1.12: *Front ends and beamline of a synchrotron facility.*

Source of synchrotron radiation

From the basic electromagnetism theory we know that the positive (negative) charges are sources (drains) of electric field lines. The radiation fields of the charged particles in ultra-relativistic motion can be determined, obtaining the 4-vector potentials known as *Lienard-Wiechert potentials* [21]:

$$\varphi(x,t) = \left[\frac{e}{(1-\vec{\beta}\cdot\hat{n})R} \right]_{ret} \quad [2]$$

$$\vec{A}(x,t) = \left[\frac{e\vec{\beta}}{(1-\vec{\beta}\cdot\hat{n})R} \right]_{ret} \quad [3]$$

where $\vec{\beta} = \vec{v}_s / c$, r_s and v_s are the position and velocity of the particle, $\hat{n}$ is an unitary vector in the direction of $\vec{R}$, and $R = |\vec{x} - \vec{r}_s|$. The E and B fields are obtained from the equations 5, 6 using the following expressions

$$\vec{E} = -\nabla\varphi - \frac{\partial\vec{A}}{\partial t} \quad [4]$$

$$\vec{B} = \vec{\nabla}\times\vec{A} \quad [5]$$

The total instantaneous power radiated by an ultra-relativistic particle undergoing centripetal acceleration is calculated by integrating the time-averaged Poynting vector[5] over all solid angle, resulting

$$P = \frac{2}{3}\frac{e^2 c}{r^2}\beta^4\gamma^4 = \frac{2}{3}\frac{e^2 c}{r^2}\beta^4\left(\frac{E}{mc^2}\right)^4 \quad [6]$$

where r is the orbit radius, m is the mass of the charged particle and $\gamma = \left(\sqrt{1-\beta^2}\right)^{-1}$ is the *Lorentz factor*. As an example, the comparison between the synchrotron power radiated of an electron and a proton with the same energy is

$$\frac{P_{electron}}{P_{proton}} = \frac{\left(m_p c^2\right)^4}{\left(m_e c^2\right)^4} = \left(\frac{938\ MeV}{0.511\ MeV}\right)^4 = 1.1\times10^{13}$$

revealing that in practice the synchrotron radiation is much more important for electrons than for protons. The exception is found at LHC, where the super proton synchrotron SPS can increase the kinetic energy of protons up to 450 GeV.

Radiation characteristics

The emitted radiation by deflected ultra-relativistic electrons due to the bending magnets is beamed in a narrow cone in the direction of the velocity vector, largely confined to the plane of motion with an angular width of the beam $\Delta\theta \sim 1/\gamma$. The overall spectrum consists of the sum of a large number of harmonics of the fundamental frequency of the electron's motion, $\omega_0 = c/r$. The radiation is strong at high harmonics of ω_0 and can be considered continuous, reaching the maximum photon flux per

[5] The instantaneous energy flux is given by the Poynting vector **S** = c/4π **E**×**B**

horizontal angle at 0.3 ω_c, with $\omega_c = \frac{3}{2}\gamma^3\omega_0$ as the critical frequency beyond which there is negligible radiation at any angle θ.

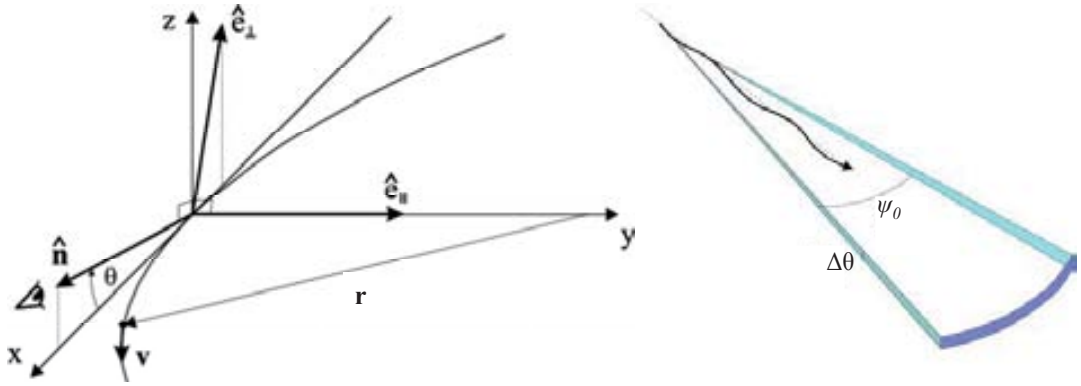

Figure 1.13: *Coordinate system for the electron deflection by magnets (left), wiggler radiation beam profile (right).*

Crystal monochromators can be used to select specific frequencies thus producing nearly monoenergetic photon beams with very high intensity. In order to obtain X-ray beams ever more concentrated in frequency and higher brilliance, insertion devices (undulators and wigglers) are used.

Insertion devices

Undulators and *wigglers* are introduced in the storage ring for inducing ultra-relativistic electrons to move in the transversal direction of their forward motion. This task is achieved by periodically alternated magnetic fields which cause small transverse oscillations of the electrons thus producing repeatedly synchrotron radiation about the forward direction.

For a periodicity λ_0 of the magnetic field structure and a maximum amplitude of oscillation a, the maximum angular deviation ψ_0 is given by

$$\Psi_0 = \frac{2\pi a}{\lambda_0} \qquad [7]$$

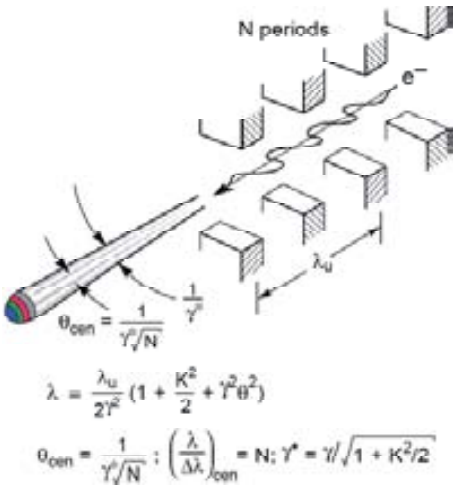

Figure 1.14: *Undulator radiation photon beam profile [22].*

Depending on the ratio between ψ_0 and $\Delta\theta$ different radiation spectra are obtained. In the case of the wigglers the ratio is $\psi_0 >> \Delta\theta$, where the frequency spectrum extends to γ^3 times the basic frequency $\Omega = c / R$ where R is the effective radius of the circular orbit induced by the magnets. For a magnetic structure with N periods, the intensity of the photon beam will be N times the one that for a single particle in an equivalent circular machine. Another useful parameter is $K = \gamma\psi_0$, that in the case of the wigglers is $K >> 1$.

In the case of undulators, $\psi_0 << \Delta\theta$ ($K<<1$), the decrease of the bending radius is making the radiation harder and the sum of the emitted radiation is almost the coherent superposition of all the oscillations of the trajectory. For a number N of magnet periods, the spread in frequency $\Delta\omega/\omega$ is in the order of $1/N$. Higher values of the parameter K lead to higher harmonics decreasing in intensity at shorter wavelengths.

Active-edges detectors have been proposed as diagnostics sensors for monitoring the position, beam profile and intensity of synchrotron X-ray beams [23]. As the dead area surrounding the sensors has been suppressed using this termination technique, they are suitable for been placed near the edges of the beam and for these purposes several designs of planar active-edge detectors are being fabricated at IMB-CNM (CSIC) in collaboration with DIAMOND Light Source Ltd.

Chapter 2

Silicon radiation detectors

Semiconductor radiation detectors are used in many science fields, such as nuclear physics, medical imaging for radiodiagnosis, astrophysics, material properties, anti-bomb security systems, etc. The fundamental of their behaviour is based on the interaction of radiation with matter which produces the ionization of the atoms along their track through the material, thus a large amount of relatively low energy electrons are freed and collected by an electronic equipment.

Since last decades, many kinds of nuclear charged particles and radiation detectors where developed by using several ionizing sensor materials, such as gases, organic and inorganic scintillators and semiconductors, but semiconductors provides extremely precise position measurement with high readout speed, direct availability of signals in electric form, simultaneously precise measurements of energy and position, and finally the possibility of integrating detector and readout electronics on a common substrate.

Depending on the type of radiation and on the information to be obtained, there are different semiconductor materials that can be used for the detection system. For heavy ions and low energy charged particles it is enough with very thin detectors, as the range of such particles in most solid is typically lower than 100 microns. In the case of beta particles, the thickness of the material must be increased. Thicknesses of several cm or more can be needed for gamma rays as their penetration in matter is “theoretically” infinite. In the case of neutrons, their detection is given by secondary particles (alphas, betas, gamma-rays, X-rays) as they produce indirect ionization, so converter layers including atoms with high interaction cross sections with neutrons are required.

2.1 Silicon as semiconductor sensor material for particle detection

Compared with other materials such us scintillators materials, gases, etc, semiconductors present properties that make them more suitable for radiation detection. Silicon is the most investigated and used semiconductor in microelectronic technology. Properties of silicon are well known and it is present in computers, photovoltaic cells and telecommunication systems.

The advantages of silicon can be described as:

The small band gap (1.12 eV at room temperature) leads to a large number of electron/hole pairs generated by incident particles. The average transferred kinetic energy for the creation of electron-hole pairs is 3.6 eV, three times larger than the bangdap. Compared to 30 eV required for gas detectors it is almost ten times lower. For a MIP particle 24000 e/h pairs are obtained for a 300 μm thick silicon sensor, or 80 e/h pairs per micrometer.

Electron and hole mobilities at room temperature are μ_e = 1400 cm^2/Vs and μ_h = 450 cm^2/Vs respectively, thus both charge carriers can be collected in a short time (~ 10 ns). Are also remarkable the existence in abundance of silicon and the existence of a natural oxide which is formed at high temperatures.

2.2 Diode: the pn junction

Given the fact that for intrinsic silicon the total amount of electron/hole pairs generated by an incident particle is several orders of magnitude lower than the amount of free charge carriers, one of these two solutions is needed in order to measure them: cooling the detector to cryogenic temperatures (unpractical for the new generation of huge detectors that requires large amounts of sensors) or by depleting the silicon volume forming a reverse biased highly doped *pn* junction structure.

2.2.1 Semiconductor physics

This section will introduce aspects of semiconductor physics important for the understanding of the silicon detector behaviour [24].

2.2.1.1 Crystalline structure

Silicon is an element of the IV group of the periodic table of elements and has four valence electrons which create bonds with other four neighbouring atoms located in the four edges of a tetrahedron. This type of structure is known as Diamond lattice, see figure 2.1.

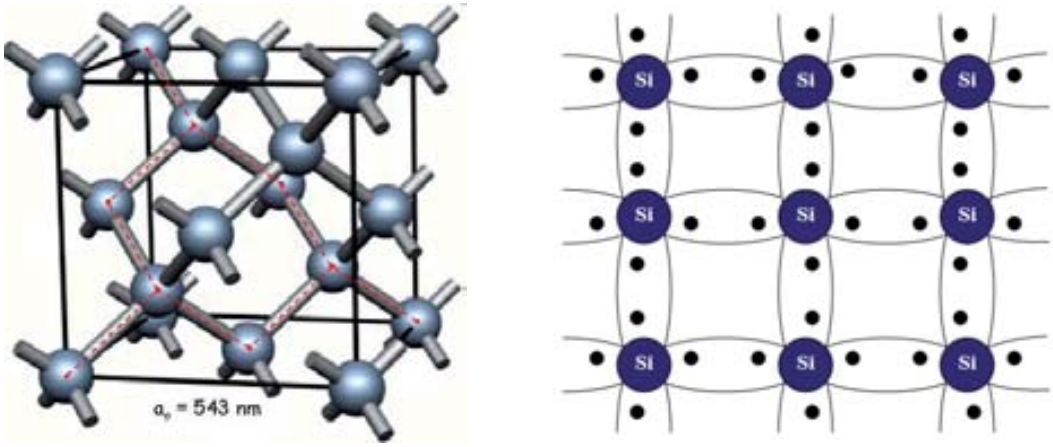

Figure 2.1: *Diamond lattice, typical of Diamond, Si and Ge (left), and schematic covalent bond representation of the Silicon crystal (right).*

It is important to notice that the plane <1 1 1> (red dot line in figure 2.1) has the highest packing density of atoms and may be considered in order to proceed to the cut direction of silicon, nevertheless for standard detectors fabrication the silicon wafer used are <1 0 0> because they present less dangling bonds in the cut and therefore less surface charge density at the Si/SiO_2 interfaces.

2.2.1.2 Energy levels

As every semiconductor, silicon has a forbidden region in the energy band structure: the bandgap. At low temperatures and in absence of impurities the valence band is full and the conduction band is empty. For higher temperatures thermal vibrations may break the covalent bonds and a valence electron can reach the conduction band, leaving behind a free place or hole. Both electron and hole are available for conduction.

The energy of the forbidden band in silicon is E_g = 1.12 eV at 300 K, and its temperature dependence follows the equation:

$$E_g(T) = 1.17 - \frac{(4.73\times10^{-4})\cdot T^2}{T+636} \qquad \textbf{[8]}$$

Direct and indirect semiconductors

The energy bands of a semiconductor are not flat as they depend on the *crystal momentum* $\vec{p} = \hbar\vec{k}$.

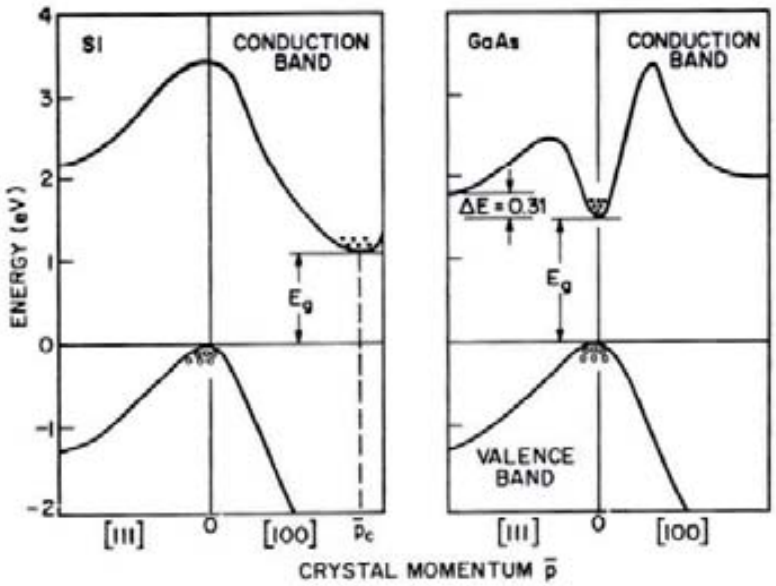

Figure 2.2: *Energy band structures of silicon (left) and GaAs (right).*

The width of the energy bandgap of a semiconductor is measured from the bottom of the conduction band to the top of the valence band. For semiconductors in which these band edges are aligned an electron can transit from the conduction band to the valence band emitting one photon without changing considerably its momentum. This is the case of *direct semiconductors*, such us GaAs.

On the other hand, for those semiconductors in which the edge bands are not aligned the electron does not transit directly between band but involving in the process a photon and a momentum transfer to the crystal lattice: a phonon. These types of semiconductors are called *indirect semiconductors*, eg. Si and Ge. In silicon, the maximum of the valence band is located at $\vec{p} = 0$, and the minimum of the conduction band is in the direction <100> at $\vec{p} = \vec{p}_c$, as shown in figure 2.2. The average energy to promote an electron from the valence band to the conduction band in Silicon is 3.6 eV.

2.2.1.3 Carriers concentration

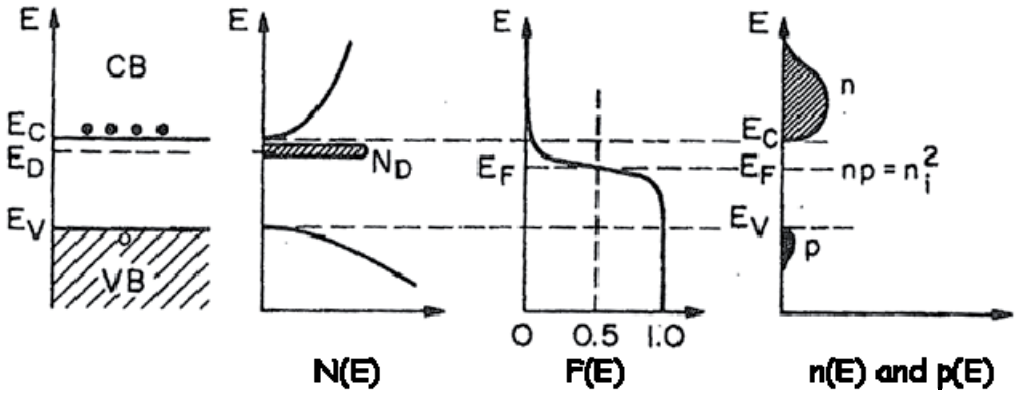

Figure 2.3: *Band diagrams, density of states, Fermi-Dirac distribution and doping concentrations for an n-type semiconductor in thermal equilibrium.*

The density of electrons in thermal equilibrium in a intrinsic semiconductor, n_0, is obtained by integrating the electron density *n(E)* in a interval of energy *dE*, for all the range of energies in the conduction band:

$$n_0 = \int_{E_C}^{E_{\max}} n(E)dE = \int_0^{\infty} N(E)F(E)dE \qquad \textbf{[9]}$$

where *N(E)* is the density of states in the conduction band and *F(E)* is their occupation probability according to the Fermi-Dirac statistics. E_C is the energy of the lower bound of the conduction band, arbitrary set to zero. The density of states in the conduction band is defined as

$$N(E)dE = 4\pi\left(\frac{2m_n}{h^2}\right)^{3/2} E^{1/2}dE \qquad \textbf{[10]}$$

and the occupation probability

$$F(E) = \frac{1}{1 + e^{\frac{E-E_F}{k_B T}}} \qquad \textbf{[11]}$$

where m_n is the effective mass of electrons, k_B is the Boltzmann constant and h is the Planck constant. E_F is the Fermi level which is the energy level in which the probability of finding an electron is exactly ½. The distribution of $F(E)$ is symmetrical around E_F and is temperature dependant. This expression $F(E)$ can be approximated separately for electrons and holes if the E_F is within the bandgap at a distance of more than roughly $3k_BT$ from either band, in other words, if the semiconductor is non-degenerated, as is certainly the case of intrinsic semiconductors, obtaining

$$F_n(E) \approx e^{-\frac{E-E_F}{k_BT}} \quad \textbf{[12]}$$

$$F_p(E) = 1 - F(E) \approx e^{-\frac{E_F-E}{k_BT}} \quad \textbf{[13]}$$

Thus, replacing these expressions in equation **9** the density of electrons in the conduction band is

$$n_0 = N_C e^{-\frac{E_C-E_F}{k_BT}} \quad \textbf{[14]}$$

where E_C is the minimum energy of the conduction band, and N_C is the effective density of states in the conduction band, defined as

$$N_C \equiv 2\left(\frac{2\pi m_n k_B T}{h^2}\right)^{3/2} \quad \textbf{[15]}$$

In the same way, E_V is the maximum energy of the valence band so the density of holes in the valence band is

$$p_0 = N_V e^{-\frac{E_F-E_V}{k_BT}} \quad \textbf{[16]}$$

where N_V is the effective density of states in the valence band

$$N_V \equiv 2\left(\frac{2\pi m_p k_B T}{h^2}\right)^{3/2} \quad \textbf{[17]}$$

In an intrinsic semiconductor the free carriers are produced by the rupture of a valence bond, so for every electron will be a hole for the conduction, being electrons and holes concentrations in the same quantity

$$n_i = n_0 = p_0 = \sqrt{n_0 p_0} = \sqrt{N_C N_V} e^{-\frac{E_g}{2k_BT}} \quad \textbf{[18]}$$

where n_i is known as the *intrinsic carriers density*, and $E_g = E_C - E_V$ is the energy bandgap. There is no E_F dependence in this parameter.

2.2.1.4 Extrinsic semiconductors

A mechanism to alter the conductivity behaviour of a semiconductor is by inserting impurities (doping) to introduce energy states in the bandgap to increase the probability to excite electrons or holes to those energy levels. The resulting material is called *extrinsic semiconductor*.

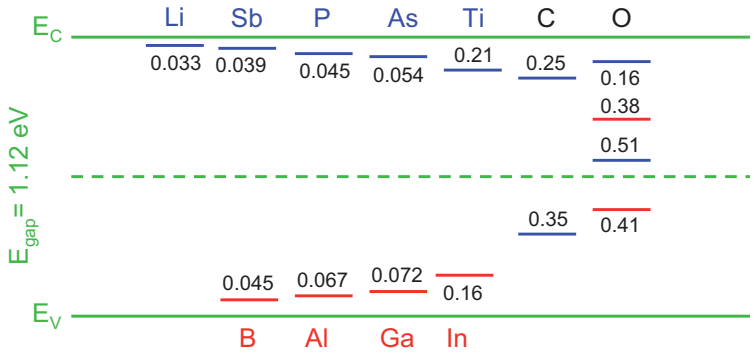

Figure 2.4: *Different energy levels for acceptor (red) and donor (blue) impurities within the bandgap in silicon.*

When silicon is doped with an element of the group V (phosphorous, arsenic) the dopant atoms replace the location of silicon atoms in the lattice. Each impurity has five valence electrons, four of them will form covalent bonds with four neighbouring atoms, while the fifth electron is not bound to a specific atom but is free for conduction. The crystal as a whole remains uncharged.

If a silicon atom is replaced by an atom of the group III, like boron, with only three valence electrons, there is a missing electron to make bounds with the four neighbouring atoms, it is, there is an extra hole easily to excite to the valence band.

The concentrations of electrons and holes in a doped semiconductor follow the same equation **9** that the one for the intrinsic semiconductors: an increment of a type or carriers implies a decrease in the concentration of the other type by recombination processes, remaining constant the multiplication of both concentrations:

$$n \cdot p = n_i^2 = N_C N_V e^{-\frac{E_g}{k_B T}} \qquad [19]$$

On the other side, the material must remain neutral, so

$$N_A + n = N_D + p \qquad [20]$$

where N_A and N_D are the donor (group V) and acceptor (group III) concentrations respectively. For an n-type material, $N_A = 0$ and p << n, thus the majorities and minorities densities are, respectively:

$$n_n = N_D = n_i e^{\frac{E_F - E_i^n}{k_B T}} \qquad [21]$$

$$p_n = \frac{n_i^2}{N_D}$$

where E_i is the intrinsic Fermi level. In the same way, the majorities and minorities densities in a p-type material are given by

$$p_p = N_A = n_i e^{\frac{E_p^i - E_F}{k_B T}} \qquad [22]$$

$$n_p = \frac{n_i^2}{N_A}$$

2.2.1.5 Transport of charge carriers

In the previous sections, only semiconductors in equilibrium were considered. However, carriers are mobile and under the effect of an electric field or a gradient of concentration they are induced to move producing an electrical current. The driving mechanisms to produce this transport of charge carriers are *drift* and *diffusion*.

Mobile carriers are essentially free particles, since they are not associated to a particular lattice site. In a semiconductor at uniform temperature, electrons have a kinetic energy due to their thermal vibrations whose mean value is *3/2* $k_B T$, so their mean thermal velocity at room temperature is of the order of 10^7 cm/s. The movement of each electron is a random path in which they scatter on imperfections within the lattice, which are due to thermal vibrations, impurity atoms, and defects. A typical mean free path is 10^{-5} cm meanwhile the mean free time between collisions is $\tau_c = 10^{-12} s$.

Drift

The average movement of charge carriers in a semiconductor is zero, however under the presence of an electric field they will be accelerated between random collisions in a direction determined by the electric field. The average velocity of the charge carrier is given by

$$v_n = -\left(\frac{q \cdot \tau_c}{m_n}\right) E = -\mu_n E \qquad [23]$$

$$v_p = \left(\frac{q \cdot \tau_c}{m_p}\right) E = \mu_p E \qquad [24]$$

As it will be mentioned later in section 2.2.2.4, this linearity between the electric field and the charge carrier velocity holds for low enough electric fields which produce small changes in the velocity with respect to the thermal velocity, and the mean collision time is independent of the electric field. For higher fields the kinetic of the charge carriers can reach values appreciably higher than the thermal energies and strong

deviations from linearity appear in their drift velocities reaching saturation values of ~ 10^7 cm/s in silicon.

This flux of charges leads to a drift current that for electrons and holes is described as

$$J_n = -qnv_n = qn\mu_n E \quad \textbf{[25]}$$

$$J_p = qpv_p = qp\mu_p E \quad \textbf{[26]}$$

Electrons and holes are drifted through the semiconductor by the electric field in opposing directions, so the total current at some point is the sum of the contribution of both carriers,

$$J = \left(qn\mu_n + qp\mu_p\right)E \quad \textbf{[27]}$$

Diffusion

Let us consider a semiconductor with a gradient of carrier concentration neglecting all effects related to electric fields, like the one generated by the inhomogeneous charge-carrier distribution or doping concentration. Thus electrons and holes are treated as if they were electrically neutral. In this situation, charge carriers will flow from the higher density regions to the lower concentration regions. This movement of charges leads to a diffusion current, described by the diffusion equation

$$F_n = -D_n \nabla n \quad \textbf{[28]}$$

$$F_p = -D_p \nabla p \quad \textbf{[29]}$$

F_n and F_p are the flux of electrons and holes respectively, $D_{n,p}$ are the diffusion constants and $\nabla n, p$ are the gradients of carrier concentrations.

Combining the effects of drift (equations **25**, **26**) and diffusion (equations **28**, **29**) one obtains the current densities equations:

$$J_n = q\mu_n nE + qD_n \nabla n \quad \textbf{[30]}$$

$$J_p = q\mu_p pE - qD_p \nabla p \quad \textbf{[31]}$$

Mobility and diffusion are related to each other by the Einstein equation, thus deriving the equations (equations **30**, **31**) considering a system in thermal equilibrium:

$$D_n = \frac{k_B T}{q}\mu_n \quad \textbf{[32]}$$

$$D_p = \frac{k_B T}{q} \mu_p \qquad \textbf{[33]}$$

2.2.1.6 Resistivity

The doping of silicon, in addition to a tiny fraction of the foreign atoms (ie. C, O), can be performed during the growing process of the crystalline silicon ingot or later during the processing of wafers in Clean Rooms. The introduction of impurities of III-V groups leads us to get extrinsic silicon of acceptor or donor type, respectively, and alter the properties of silicon.

Conduction depends on the number of free carriers present in the material, so the resulting conduction/resistivity for extrinsic silicon, using the equation **27** in the expression $\sigma = J/E$, is given by

$$\sigma = q\left(\mu_n n + \mu_p p\right) \qquad \textbf{[34]}$$

and therefore

$$\rho = \frac{1}{q\left(\mu_n n + \mu_p p\right)} \qquad \textbf{[35]}$$

$$\mu_{n,p} = \frac{q\tau_s}{m^*_{n,p}} \qquad \textbf{[36]}$$

where q is the electron charge, μ_n and μ_p are the mobilities of electrons and holes respectively, τ_s is the average scattering time and m^* is the charge carriers effective mass. Impurities are not only acting as trapping centers in the band gap but also as sources of free charge carriers.

2.2.1.7 Charge generation and recombination in silicon

The generation of free electrons and holes in silicon is produced by the lifting of electrons from the valence band to the conduction band, leaving the corresponding hole in the valence band. This process creates equal amount of free electrons and holes, and can be achieved by different mechanisms such us thermal agitation, optical excitation or ionization by radiation.

Thermal generation of charge carriers

The thermal agitation of electrons at room temperature may produce their excitation from the valence band to the conduction band in semiconductors where the bandgap is low. This effect results in an undesired source of noise and these materials (eg. Germanium) have to be operated at low temperatures.

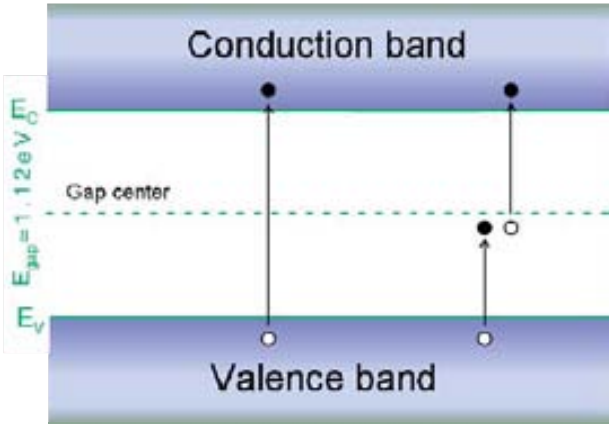

Figure 2.5: *Direct and indirect excitation of electrons from the valence band in silicon.*

In the case of silicon, this excitation is not very probable at room temperature but may take place in two steps: one excitation from the valence band to an intermediate state (due to impurities or defects in the lattice), and from that state to the conduction band.

Although thermal generation and recombination are continuously occurring in the semiconductors, in thermal equilibrium the concentration of charge carrier is constant in time obeying the *mass-action law* (equation **19**), thus the generation rate equals the recombination rate

$$R_{th} = G_{th} = \beta n_0 p_0 = \beta n_i^2 \qquad \textbf{[37]}$$

where β is the generation coefficient.

Generation of charge carriers by electromagnetic radiation

This process consists of the interaction of photons with the matter. In this process the photon transfers some energy (or is completely absorbed) used to lift an electron from the valence band to the conduction band, leaving a hole in the valence band. If the energy transferred is greater that the bandgap the electron will be in one of the empty states of the conduction band. Both electron and hole will move to the edge of each band (valence band for holes and conduction band for electrons) thereby emitting energy in the form of phonons (lattice vibrations) or lower energy photons. For photons with lower energy than E_{gap} the shifting of electrons is possible through states in the bandgap created by crystal defects or impurities.

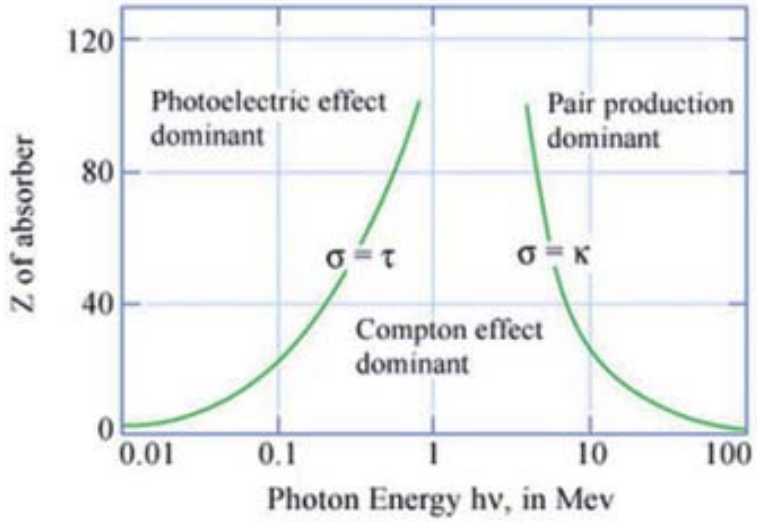

Figure 2.6: *Importance of the atomic number Z and the photon energy in the cross-section of the photon-matter interaction.*

The interaction of photons with matter is achieved by one of these processes: *photoelectric effect*, *Compton scattering, Rayleigh scattering*, *pair production* and *photonuclear reactions.* Although the photonuclear reactions occur for photons with energies above 1 MeV their relative amount remains less that 5% of those due to pair production for higher energies. Rayleigh scattering is neither taken into account because the photon interacts with the atom as a whole, being scattered a small angle and losing an unappreciable amount of energy dissipated by a small vibration of the atom, just to verify the linear momentum conservation.

The attenuation of a monochromatic photon beam can be characterized by a fixed probability of occurrence per unit path in the absorber material. The sum probability of all the interaction process is the probability pre unit path length that the photon is removed from the beam, known as *linear attenuation coefficient*:

$$\mu = \tau + \sigma + \kappa \qquad \textbf{[38]}$$

where μ, σ and κ are the attenuation coefficients for photoelectric, Compton and pair creation processes. These processes involve X-ray/Auger electron emission when the target electron belongs to an inner atomic orbital, due to atomic de-excitation.

Photoelectric effect

In the photoelectric effect a photon is absorbed completely by an electron of the atomic shell, transferring all its energy to the electron. This energy is inverted in breaking the binding energy (work function) of the electron in its original shell, and the rest is converted in kinetic energy.

$$T_e = h\nu - h\nu_0 - T_a \qquad \textbf{[39]}$$

where T_e is the kinetic energy of the electron, $h\nu$ is the photon energy, $h\nu_0$ is the work function and T_a is the kinetic energy transferred to the atom. The kinetic energy of the electron is independent of the outgoing angle because the energy transferred to the atom is negligible, $T_a \sim 0$.

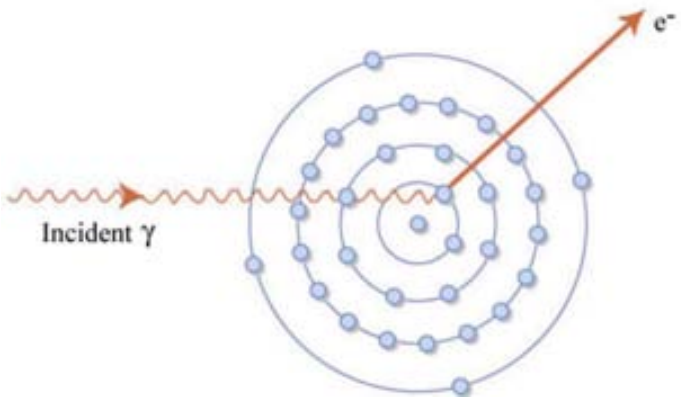

Figure 2.7: *Schematic representation of the Photoelectric effect.*

The interaction is with the atom as a whole and can not take place with free electrons due to the conservation of the linear momentum. This is the dominant process of interaction photon-matter for low energies (< 0.1 MeV). This process is also enhanced for absorber materials of high atomic number *Z*, being the

$$\tau \propto \frac{Z^n}{(h\nu)^{3.5}} \qquad \textbf{[40]}$$

where *n* lays between 4 and 5 over the photon energy region of interest (see figure 2.7).

Compton scattering

In this process a photon of energy $h\nu$ collides against an electron of the outer atomic shell and both particles (electron and photon) are scattered in different directions. The electron is initially considered stationary and unbounded in this process. Energy and linear momentum are conserved.

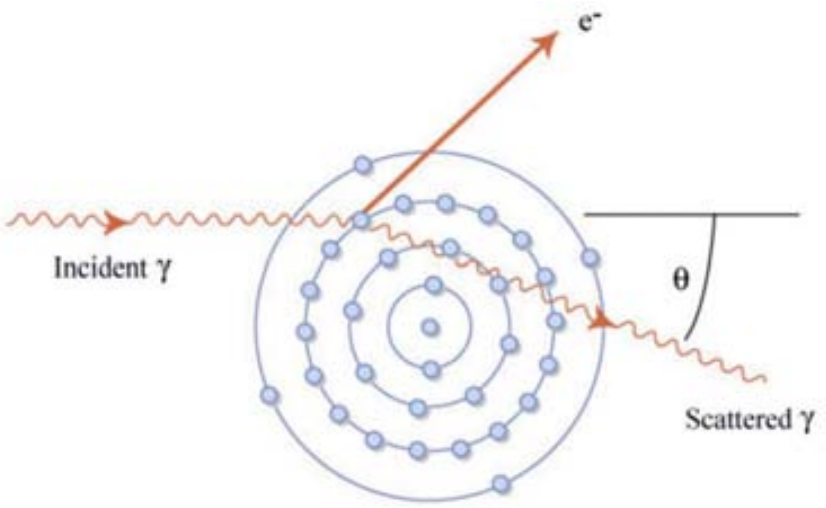

Figure 2.8: *Schematic representation of the Compton effect.*

In Compton scattering, the photon is deflected a relative angle θ with respect to the initial direction of incidence, and its remaining energy is hv'. The difference between initial and final energy of the photon is transferred to the electron as kinetic energy

$$T_e = hv - hv' \qquad \textbf{[41]}$$

The relation between the energy of the scattered photon hv' and the scattered angle θ is:

$$hv' = \frac{hv}{1 + \frac{hv}{m_0 c^2}(1 - \cos\theta)} \qquad \textbf{[42]}$$

where m_0c^2 is the rest-mass energy of the electron (511 keV). The photon always keeps some energy after being scattered, transferring a small part for small scattering angles, while the maximum transference is for $\theta = \pi$.

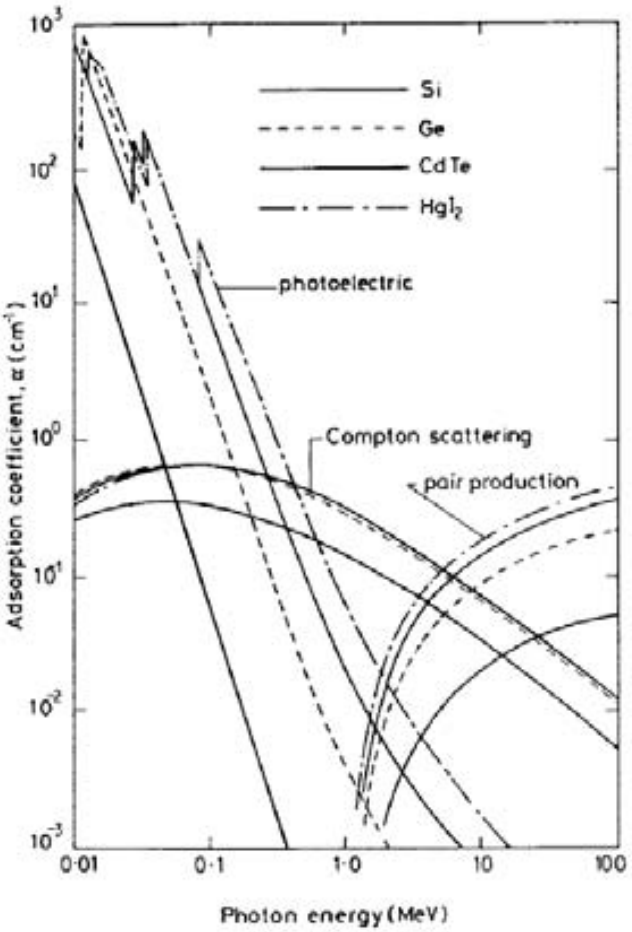

Figure 2.9: *Absorption coefficients as a function of the photon energy for different materials at 300 K. The Compton effect starts to be dominant in Silicon for energies above 60 keV.*

According to the theory of Klein-Nishina for the Compton effect, the differential scattering cross section for this process is

$$\frac{d\sigma}{d\Omega} = Zr_0^2\left(\frac{1}{1+\alpha(1-\cos\theta)}\right)^2\left(\frac{1+\cos^2\theta}{2}\right)\left(1+\frac{\alpha^2(1-\cos\theta)^2}{(1+\cos^2\theta)[1+\alpha(1-\cos\theta)]}\right) \quad \textbf{[43]}$$

where $\alpha = h\nu/m_0c^2$ is the energy of the incident photon in units of the electron mass, and r_0 is the classical electron radius. The cross section increases linearly with the atomic number Z, thus depending on the amount of electrons for the interaction, and decreases with the incident photon energy.

Pair production

Pair production is an absorption process in which an incident photon disappears and creates an electron and a positron using the photon energy. This process can only take place in an electromagnetic field, usually close to a nucleus. It may also occur, but much less probably, in the electromagnetic field of an electron. This case is commonly called

triple production, because the local electron also earns kinetic energy due to the linear momentum conservation, therefore obtaining two electrons and one positron.

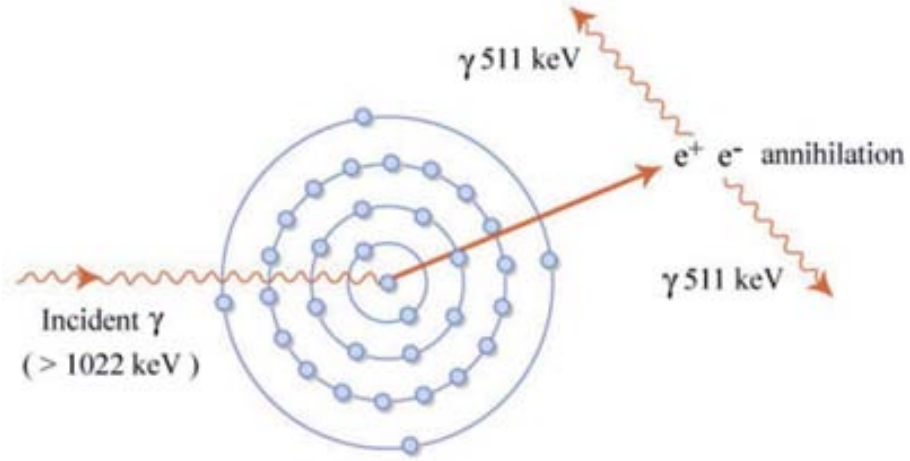

Figure 2.10: *Schematic representation of the pair production process in the Coulomb field of a nucleus.*

The energy needed for the pair production process must exceed twice the rest-mass energy of an electron (1.02 MeV) for being energetically possible. The rest of the energy is used as kinetic energy for both electron and positron.

$$h\nu = 2m_0c^2 + T_{e^-} + T_{e^+} \qquad \textbf{[44]}$$

According to the Bethe and Heitier theory, the pair production cross section is:

$$\kappa = \int_{T_{e^+}} d\kappa = \sigma_0 Z^2 \int_0^{h\nu - 2m_0c^2} \frac{PdT^+}{h\nu - 2m_0c^2} = \int_0^1 Pd\left(\frac{T_{e^+}}{h\nu - 2m_0c^2}\right) = \sigma_0 Z^2 \overline{P} \qquad \textbf{[45]}$$

where P is a function of the photon energy $h\nu$ and the atomic number Z. The parameter σ_0 is defined as

$$\sigma_0 = \alpha r_0^2 \approx \frac{r_0^2}{137} \approx 5.80 \times 10^{-28}\ cm^2/electron \qquad \textbf{[46]}$$

The probability of pair production κ depends on Z^2, but there is also a small dependence with Z in the P function. The dependence with the photon energy is logarithmic through P, having a constant which is independent on the energy $h\nu$ for high energy photons due to the shielding of electrons by the nuclear Coulomb field. Thus

$$\textbf{Low energetic photons} \rightarrow \kappa \propto \ln E$$

$$\textbf{High energetic photons} \rightarrow \kappa \propto cte$$

Generation of charge carriers by charged particles

Charged particles interact with the electrons, or even with the nucleus, of the atoms they meet along their track in the material. In each interaction, the incident particle transfers a part of its energy to the electrons of the material by ionization or by excitation of these electrons that will be promoted to higher atomic orbitals. Most of the collisions transfer a small fraction of the kinetic energy of the incident particle, therefore it is possible to consider the particle loosing its kinetic energy gradually, process known as Continuous Slowing-Down Approximation (CSDA). The probability for a particle of crossing a material without interactions is zero. A charged particle of 1 MeV typically will suffer in the order of 10^5 interactions before losing all of its kinetic energy.

Interactions of charge particles with matter can be parameterized depending on the relative size of the classical impact parameter *b* and the atomic radius *a*. According to this there are three possible cases:

- $b >> a$ Soft collisions
- $b \approx a$ Hard collisions (or knock-on collisions)
- $b << a$ Coulomb interactions with external nuclear field

Soft collisions are the most probable case for the energy loss of charged particles. They consist of charged particle interacting with the atom as a whole. This is, exciting the atom to a higher energetic level and eventually ionizing it by the removal of an atomic electron. The mean effect is a small transfer of energy.

In the case of hard collisions, the particle will interact mainly with an atomic electron which will be expelled with a substantial amount of energy. These secondary electrons that are also capable to excite/ionize other electrons are called *delta rays*, dissipating their energy in a different direction from the initial particle. Note that for expelled electrons from the inner atomic orbitals there will be emissions of characteristic X-rays and/or *Auger electrons*, contributing to spread the energy of primary particle in other directions.

When the particle track verifies $b << a$ the interaction is mainly with the nucleus. In almost all of the cases the particle is deflected elastically transferring a negligible amount of energy just to satisfy the linear momentum conservation. In the case of light charged particles, there is another process known as *Bremmsstrahlung*, which consists of the emission of X-rays of an important fraction (even 100%) of the energy of the particle in an inelastic collision. The cross section of this process depends on the nuclear charge, *Z*, and the mass of the interacting particle as $\sigma \propto \frac{Z^2}{m^2}$. Because of this, deceleration radiation is insignificant for heavy charged particles.

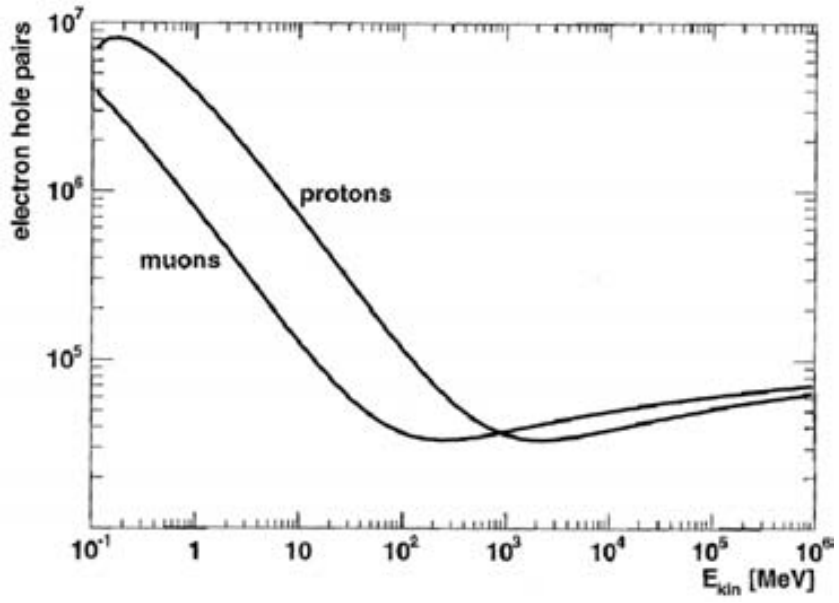

Figure 2.11: *Number of electron-hole pairs generated by protons and muons in silicon as a function of their kinetic energy (Si thickness: 300 μm).*

The Bethe-Bloch formula gives the rate of ionization loss of a charged particle in matter for moderate velocities is

$$\left(-\frac{dE}{dx}\right) = 2\pi N_0 r_e^2 m_e c^2 \rho \frac{Z}{A}\frac{z^2}{\beta^2}\left[\ln\left(\frac{2m_e\gamma^2 v^2 T_{\max}}{I^2}\right) - 2\beta^2 - \delta - 2\frac{C}{Z}\right] \qquad \textbf{[47]}$$

where $\beta = v/c$ and T_{max} is the maximum energy transfer in a single collision with an electron, whose expression is:

$$T_{\max} = \frac{2m_e c^2 \beta^2 \gamma^2}{1 + 2\gamma\frac{m_e}{M} + \left(\frac{m_e}{M}\right)^2} \qquad \textbf{[48]}$$

For low energies (non-relativistic), the term $1/\beta^2$ is dominant and the energy loss rate is inversely proportional to the energy, reaching a minimum value about $\beta = 0.96$. Particles at this velocity are called *minimum ionizing particles* (MIP). The value of the minimum depends on the square of the particle charge but very weak on the particle mass. Due to the flatness of the energy loss rate curve, this expression is often also used for all particles with $\beta > 0.96$.

The number of electron/hole pairs generated by an incident charged particle in silicon is calculated by dividing the deposited energy by the ionization mean energy, I = 3.6 eV. The difference between the silicon bandgap, E_{gap} = 1.12 eV, and the ionization energy is inverted in the generation of phonons that will dissipate as thermal energy.

Avalanche generation

This generation process consists of the production of electron-hole pairs through the transference of kinetic energy from a highly energetic electron (hole) from the conduction (valence) band to an electron of the valence band, which is subsequently promoted to the conduction band generating an electron hole pair. This process needs a certain threshold electric field and enough space in the space charge region for the carriers to be accelerated; also avalanche breakdown may be produced.

The generation rate of this *impact ionization* process is proportional to the drift current densities (equations **25**, **26**)

$$G_{ii} = \alpha_n n v_n + \alpha_p p v_p \qquad \textbf{[49]}$$

where α is the reciprocal of the mean free path and is called *ionization coefficient*.

Shape of ionization path

The space charge region in silicon radiation detectors acts as an ionization chamber. The ionizing radiations that penetrate this region create electron-hole pairs which are immediately separated and collected in the electrodes, driven by the present linear electric field.

There is no recombination in this mechanism due to the absence of free carriers[1]. The time needed to collect the charge carriers depends on the drift length and the strength of the electric field. Electron-holes generated in undepleted regions are recombined and do not contribute to the charge collected.

The average energy to produce an electron-hole pair in silicon is 3.6 eV, and the total amount of charge generated by an ionizing particle depends on the energy lost along the track in the material. For MIP particles, the average value of energy loss is ~39 keV/100 μm, so the total charge generated is proportional to the length of its track. As the probability function of the energy loss follows a Landau distribution [24], the average value given by the Bethe-Bloch equation is not the same that the most probable value, less that the 70% of that value, 81 keV in a 300μm silicon detector. Thus the total charge generated by a MIP in 300 μm is about 24000 electron/hole pairs.

For X-rays is expected an interaction point through one of the previously studies mechanisms, and the production of many electron-hole pairs in the nearly region.

β radiation generates uniform electron-hole pairs along its path as long as their velocity remains relativistic and producing increased density at the end of its path. This local energy deposition near the end of the track is especially interesting for medical applications when protons (or other charged hadrons) are used to deliver energy to a well-specified location.

Carriers recombination

Recombination is the process in which one electron and one hole annihilate each other, this is, when an electron occupies an empty state (hole). The difference of energy

[1] For non irradiated bulk, otherwise there will be trapping centers generated by the radiation.

between the initial and final states can be emitted as a photon (radiative recombination), dissipated as phonons (non-radiative recombination) or transferred to another electron (Auger recombination).

The charge carrier recombination process is significantly different for direct and indirect semiconductors, as it was told in section 2.2.1.2. For direct semiconductors, in the plot of the energy band structure as a function of the crystalline momentum of the carriers the minimum of the conduction band is aligned with the maximum of the valence band (as can be seen in figure 2.2), allowing direct band-to band electron transitions. However, for indirect semiconductors there is not such alignment and therefore in this case is needed an intergap generation/recombination center, such as impurities or lattice defects, to assist the electron transition, requiring momentum transfer to the crystal lattice (phonons).

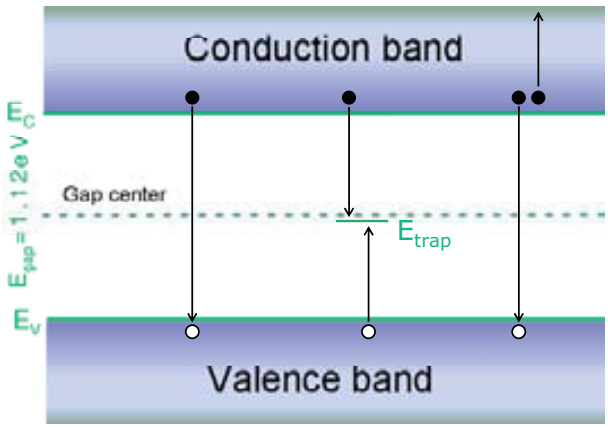

Figure 2.12: *Different carrier recombination mechanisms in silicon: band-to-band recombination (left), Shockley-Read-Hall (or trap-assisted) recombination (centre), and Auger recombination (right).*

According to the energy levels and particles involved in the recombination it is possible to establish a classification of these processes:

Band-to-band recombination

This is the dominant recombination process in direct semiconductors. This a radiative process which consists of the direct recombination of an electron of the conduction band with a hole of the valence band, emitting a photon of energy equal to the band gap.

Band-to-band transitions depend on the concentration of both type of charge carriers available for being recombined and thus the recombination rate depends on the product of n and p in the form:

$$R = \beta np \qquad \textbf{[50]}$$

where β is the recombination coefficient. As in thermal equilibrium the generation rate equals the recombination rate, the net recombination rate U can be defined as

$$U = R - R_{th} = \beta(np - n_i^2) \qquad \textbf{[51]}$$

Shockley-Read-Hall (or trap-assisted) recombination

SHR recombination occurs in two steps: firstly the electron is trapped in an energy level within the bandgap caused by the presence of impurities or lattice defects. Then the trapped electron can fall down to the valence band to recombine with a hole or get recombined in the lattice defect by a trapped hole. This mechanism involves momentum transfer to the lattice as phonons.

The net recombination rate for this process depends on the energy level in the bandgap, because for shallow levels the reemission of the trapped carrier (from the nearest band) will be most probable than trapping a carrier from the further band to obtain the recombination. For this reason, energy levels near mid-gap are very effective for recombination.

The net recombination rate for this process is given by

$$U_{SRH} = \frac{pn - n_i^2}{p + n + 2n_i \cosh\left(E_i - E_t / k_B T\right)} N_t v_{th} \sigma \qquad \textbf{[52]}$$

where n_i is the impurities density, E_i is the intrinsic energy level, E_t is the trap energy level, v_{th} the thermal velocity, N_t the defects/traps concentration, σ the cross section of the generation process for carriers. This expression can be simplified for n and p-type semiconductors as follows

$$U_{SRH,n} = \frac{n_p - n_{p0}}{\tau_n} \qquad \textbf{[53]}$$

$$U_{SRH,p} = \frac{p_n - p_{n0}}{\tau_p} \qquad \textbf{[54]}$$

where $\tau_{n,p}$ is the generation lifetime of the minority carriers whose expression is given by

$$\tau = \frac{1}{N_t v_{th} \sigma} \qquad \textbf{[55]}$$

Auger recombination

Auger recombination is a process in which an electron and a hole recombine in a band-to-band transition, but rather that emitting the energy as a photon or phonons the energy is transferred to an electron or hole. This process is most important in heavily doped semiconductors.

The introduction of a third particle alters the net recombination rate from the expression for band-to-band transitions, resulting:

$$U_{Auger} = C_n n(np - n_i^2) + C_p p(np - n_i^2) \qquad \textbf{[56]}$$

where C_n and C_p are the Auger coefficients corresponding to the two possible mechanisms.

Trap-assisted Auger recombination is also possible as a modification of the SRH recombination.

Surface SRH recombination

Recombination at the surface and interfaces of the semiconductor can become important due to the large amount of defects that can be found in those regions, due to the dangling bonds and the end of the semiconductor, impurities in the transition in the interface to the other material and impurities that may be introduced in the fabrication processes. This high recombination rate in the vicinity of a surface depletes this region of minority carriers and therefore the surface recombination rate depends on the rate of velocity of minority carriers that move to the surface. In this case, the net recombination rate is expressed as

$$U_{surface,SRH} = \frac{pn - n_i^2}{p + n + 2n_i \cosh\left(E_i - E_{st}/k_B T\right)} v_s \quad \textbf{[57]}$$

This expression is the same that the SRH net recombination rate in which the defects/traps concentration N_t has been substituted by the surface density of defects/traps N_{st} and v_s is the surface recombination velocity

$$v_s = N_{st} v_{th} \sigma_s \quad \textbf{[58]}$$

2.2.1.8 Metal-semiconductor contacts

Metallic contacts are required for every semiconductor device in order to establish communication with input/output devices. Depending on the characteristics of the metals and semiconductors involved in the junction it is possible to obtain rectifying Schottky junctions or ohmic contacts. In the following lines these two types of junctions will be analyzed.

Metal and semiconductor

The conduction and valence bands of a metal are overlapped such that the Fermi level is located inside the conduction band. This represents that the density of free charge carriers at the Fermi level is very high and therefore they present high conductivity. Besides it is also high enough to prevent the built-up of a static electric field in the metal side of the junction.

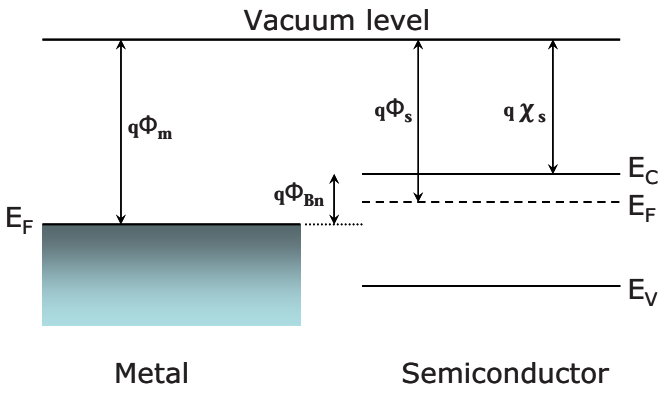

Figure 2.13: *Band diagrams for a metal (left) and an n-type semiconductor with $\Phi_m > \Phi_s$ (right) before being in contact.*

Electrons bounded to atoms own the energy corresponding to the energy level in which they are located (negative energy) while unbounded electrons are said to be at the vacuum level (energy zero). So, the energy to extract an electron from the most probable energy level equals the Fermi level and it is denoted *metal work function* $e\Phi_m$ in the case of metals, and *semiconductor work function* $e\Phi_s$ for semiconductors. In the case of releasing an electron from the conduction band, the necessary energy is defined by the *electron affinity* $e\chi_s$.

When a metal and a semiconductor whose work functions satisfy $\phi_m > \phi_s$ (as in figure 2.13) are set in contact, there is a current of electrons flowing from the semiconductor to the metal due to the higher energy of electrons in the semiconductor which try to reach lower energy states, leaving behind positively charged ions. This diffusion current of electrons creates a thin layer in the metal side of the interface which produces an electric field in the semiconductor opposing to the flow of electrons. The equilibrium is reached when both drift and diffusion currents are equal and the Fermi levels of both materials are in the same level, leading to a bend upward of the semiconductor bands given by the *built-up voltage* V_{bi}.

According to the sign of the potential barrier Φ_B, defined as the difference of the Fermi level of the metal and the semiconductor band of the majority carriers, these charge carriers may be free to move from the metal to the semiconductor and vice versa (ohmic contact) or find a barrier potential from the metal to the semiconductor (rectifying barrier).

Rectifying Schottky barrier

As occurs in Schottky diodes, a potential barrier is formed in the metal-semiconductor interface with rectifying properties very similar to those found in p-n junctions. This barrier avoids the free pass of majority charge carriers from the semiconductor to the metal since the band of majorities has been moved away from the Fermi level of the metal a quantity qV_{bi}. The barrier height is therefore different for n and p-type semiconductors.

n-type semiconductors

The barrier height for n-type substrates is obtained as the difference between the Fermi level of the metal and the conduction band of the semiconductor

$$\phi_{Bn} = \phi_m - \chi_s \qquad \textbf{[59]}$$

As the work function of the metal is higher than the electron affinity of the semiconductor this results in a barrier potential $\Phi_{Bn} > 0$ that avoids the free pass of electrons in the junction.

The bend up of the semiconductor energy bands is measured as the built-in potential, given by

$$V_{bi} = \phi_m - \phi_s = \phi_m - \chi_s - \frac{E_C - E_F}{q} \qquad \textbf{[60]}$$

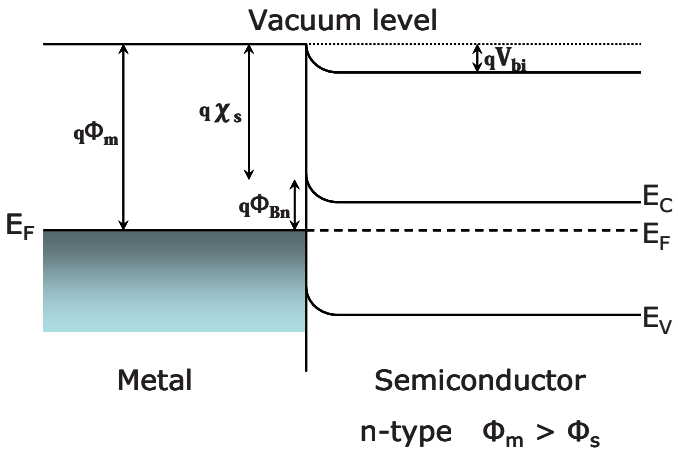

Figure 2.14: *Band structure of a metal n-type semiconductor rectifying junction.*

p-type semiconductors

In the case of p-type semiconductors, the barrier height is obtained as the difference the Fermi level of the metal and the valence band of the semiconductor

$$\phi_{Bp} = \frac{E_C - E_V}{q} + \chi_s - \phi_m \qquad \textbf{[61]}$$

As well as for the n-type, this value also satisfies $\Phi_{Bp} > 0$ avoiding the free pass of holes from the valence band of the semiconductor to the metal.

The built-in potential in this case is given by

$$V_{bi} = \phi_s - \phi_m = \chi_s + \frac{E_C - E_F}{q} - \phi_m \qquad \textbf{[62]}$$

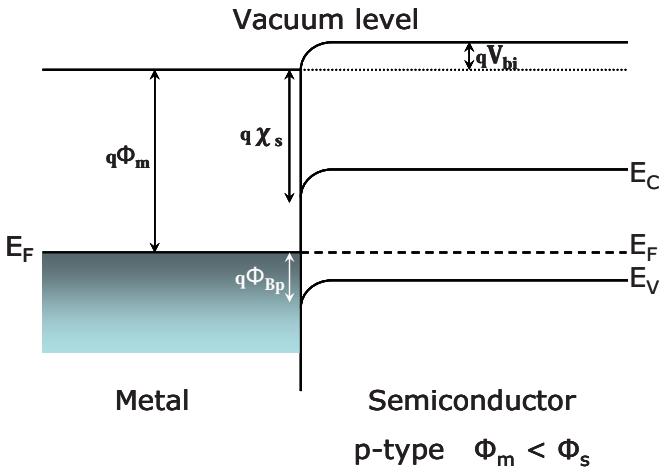

Figure 2.15: *Band structure of a metal p-type semiconductor rectifying junction.*

Forward and reverse bias

The current-voltage characteristic of rectifying metal-semiconductor junctions is similar to the equation for p-n junctions, but with the difference of having different potential barriers for majorities, V_{bi}, and for minority carriers, Φ_B.

$$I = I_s\left(e^{\frac{qV}{k_BT}} - 1\right) \qquad \textbf{[63]}$$

where I_s is the saturation current

$$I_s \propto e^{-\frac{q\phi_B}{k_BT}} \qquad \textbf{[64]}$$

The application of a forward bias, V_F, to the metal side of the metal-semiconductor n-type (p-type) junction will lower (shift) the Fermi level of the metal reducing the built-up potential. Therefore more electrons (holes) will diffuse from the conduction (valence) band of the semiconductor to the metal than the ones that are driven by drift in the opposing direction, resulting in a net current to the metal.

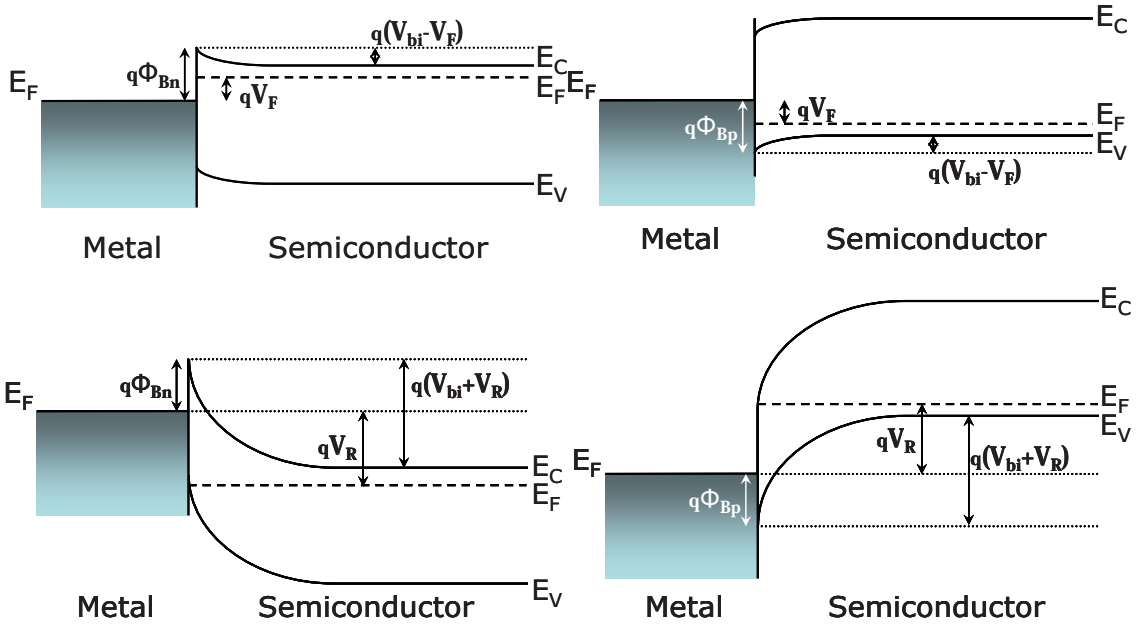

Figure 2.16: *Band diagram of metal on n-type (left) and on p-type (right) semiconductors under forward (top) and reverse (bottom) bias voltages.*

However, applying a reverse bias, V_R, will shift (lower) the Fermi level of the metal with respect of the Fermi level of the semiconductor, increasing the built-up potential. In both cases, forward and reverse biasing, the barrier potential remains unchanged.

Ohmic contact

In ohmic junctions the barrier height of the junction is also obtained by using the equations **60**, **62**, resulting in negative values. This means that the charge carriers are allowed to move freely from the metal to the semiconductor, and vice versa, for any applied voltage following the Ohm's law. The expressions for the built-in potential are also the same than the ones exposed for the rectifying contact.

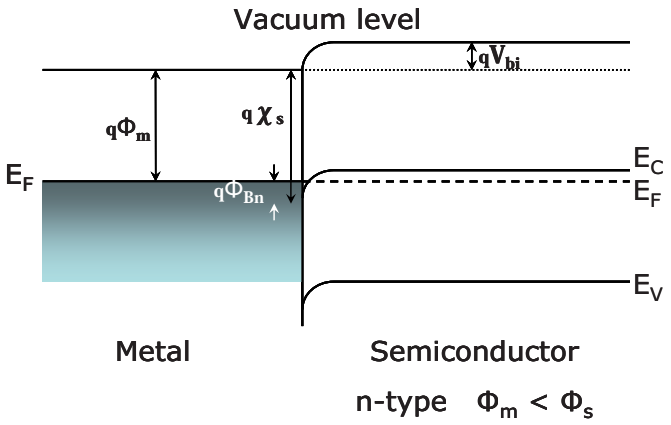

Figure 2.17: *Band structure of a metal n-type semiconductor ohmic junction.*

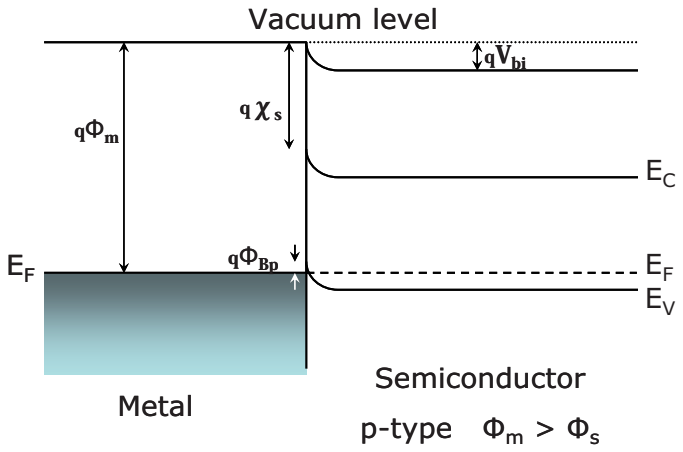

Figure 2.18: *Band structure of a metal p-type semiconductor ohmic junction.*

Specific contact resistance

It is also possible use rectifying contacts and make them work as ohmic contacts. The method of achieving this behaviour is as follows:

A characteristic parameter of the contacts is the *specific contact resistance* defined as

$$R_c = \left(\frac{dJ}{dV} \right)^{-1}_{V=0} \qquad \textbf{[65]}$$

calculated at $V = 0$ because no voltage should ideally drop across the junction. In ohmic junctions this resistance is negligible compared with the bulk resistance but for rectifying contacts is high. A highly doped layer of the same type of the semiconductor doping is introduced at the interface in order to reduce the contact resistance by reducing the thickness of the potential barrier and enhances the transmission coefficient of tunnelling [25]. In addition, this highly doped layer prevents the formation of high leakage currents that would be originated by the injection of minority carriers[2] from the backside metal contact [26].

2.2.2 Polarization of the pn junction

When two semiconductors of different type (p and n-type) are joined, two diffusion fluxes of majority carriers (holes and electrons respectively) are produced to the other side of the junction due to their difference of concentration. These fluxes leave non compensated atoms near the junction (space charge region w) and an electric field is produced, which generates a barrier potential, inducing drift currents to oppose to the diffusion currents.

[2] According to the mass action law, equation **19**.

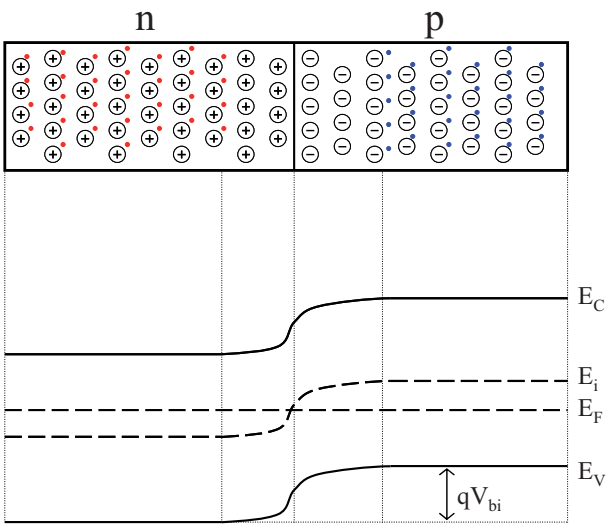

Figure 2.19: *Bands diagram of a pn junction in thermal equilibrium.*

The equilibrium is reached when the drift current is able to equal the diffusion current, and the equilibrium build-in potential V_{bi} is established. Intrinsically the generation and recombination of charge are in equilibrium. The build-in potential can be obtained from equations **21**, **22** as the difference of the intrinsic Fermi levels of both semiconductors

$$V_{bi} = \frac{E_i^p - E_i^n}{q} = \frac{k_B T}{q} \ln\left(\frac{N_A N_D}{n_i^2}\right) \qquad \textbf{[66]}$$

An external voltage will disturb this equilibrium. Silicon sensors are operated in reverse bias so this is the case that will be analyzed in this section.

p^+p and n^+n structures

As it was earlier commented, highly doping layers of the same type than the substrates are used to create ohmic metal-semiconductor junctions and also prevent from high leakage currents. Due to the gradient of doping concentration between the layer and the substrate, majority carriers from the highly doped region flow to the less doped region, thus creating an electric field opposing to the diffusion current. In this state, there is a built-in potential whose expressions for n- and p-type materials are also obtained from equations **21**, **22** and they are

$$V_{bi} = E_i^n - E_i^{n^+} = \frac{k_B T}{q} \ln \frac{N_D^+}{N_D} \qquad \textbf{[67]}$$

$$V_{bi} = E_i^{p^+} - E_i^p = \frac{k_B T}{q} \ln \frac{N_A^+}{N_A} \qquad \textbf{[68]}$$

2.2.2.1 Depletion region

For the detector case, we are interested in large depleted space charge regions because the charge generated by incident radiation in non-depleted regions is recombined and therefore is lost. In this way, *pn* junctions in detectors are formed by a highly doped region and another one less doped, which allow the creation of a large space charge region by diffusion inside the less doped silicon, as it can be seen in figure 2.20, $w = \left|-x_p\right| + x_n$.

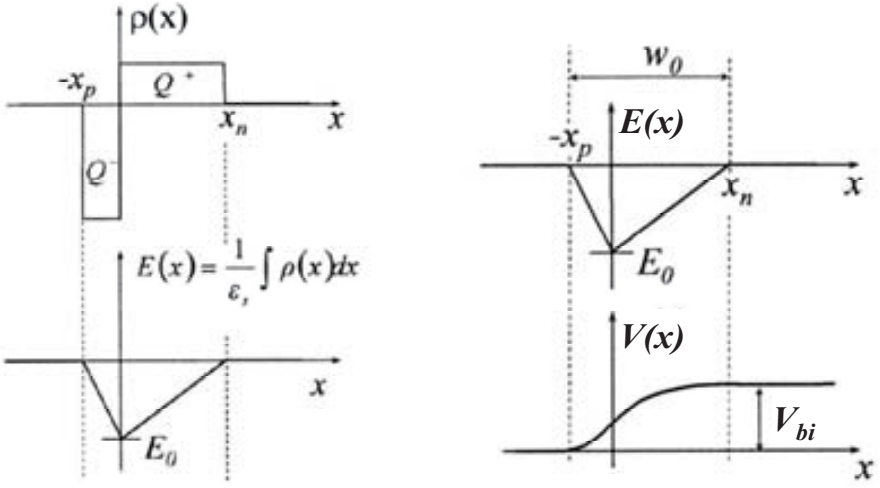

Figure 2.20: *Charge density and electric field distribution in a p^+n junction with planar geometry (left). The plots on the right represent the space charge regions at both sides of the junction and the electrostatic potential.*

Planar detectors

Considering a p^+n junction of a planar detector, where $N_A >> N_D$, as shown in the figure 2.20, the charge density is given by

$$\rho(x) = \begin{cases} -qN_A & -x_p < x < 0 \\ qN_D & 0 < x < x_n \end{cases} \quad \textbf{[69]}$$

For this geometry, the Poisson's equation that it is required to obtain the electric field and the potential distribution along the detector is

$$\frac{d^2V(x)}{dx^2} = -\frac{\rho(x)}{\varepsilon_{Si}} = \begin{cases} \dfrac{qN_A}{\varepsilon_{Si}} & -x_p < x < 0 \\ -\dfrac{qN_D}{\varepsilon_{Si}} & 0 < x < x_n \end{cases} \quad \textbf{[70]}$$

Integrating of this equation and using the boundary condition $E(-x_p) = E(x_n) = 0$, null electric field outside the depletion region, it results

$$E(x) = -\frac{dV(x)}{dx} = \begin{cases} -\frac{qN_A}{\varepsilon_{Si}}(x + x_p) & -x_p < x < 0 \\ \frac{qN_D}{\varepsilon_{Si}}(x - x_n) & 0 < x < x_n \end{cases} \quad \textbf{[71]}$$

The electric potential is obtained integrating again and using the boundary condition $V(0) = 0$,

$$V(x) = \begin{cases} \frac{qN_A}{\varepsilon_{Si}}(\frac{x^2}{2} + xx_p) & -x_p < x < 0 \\ -\frac{qN_D}{\varepsilon_{Si}}(\frac{x^2}{2} - xx_n) & 0 < x < x_n \end{cases} \quad \textbf{[72]}$$

The electric field must have the same values at $x = 0$. As a consequence, $x_p N_A = x_n N_D$ that combined with $w = x_p + x_n$ is used to calculate the size of the space charge region. In addition, the build-in potential can be calculated as $V(x_n) - V(-x_p) = V_{bi}$, obtaining

$$w = x_p + x_n = \sqrt{\frac{2\varepsilon_{Si}(N_A + N_D)}{qN_D N_A}(V_R + V_{bi})} \approx \sqrt{\frac{2\varepsilon_{Si}}{qN_D}(V_R + V_{bi})} \quad \textbf{[73]}$$

where V_R is the applied reverse bias, V_{bi} is the build-in potential, ε_{Si} is the electrical permittivity of Silicon, N_D is the effective doping concentration of the n-type side of the junction. From this equation is easy to deduce the required value to set the full depletion condition, with D as the full sensor thickness:

$$V_{full\ depletion} = V_{FD} = \frac{qD^2 N_D N_A}{2\varepsilon_{Si}(N_D + N_A)} - V_{bi} \approx \frac{qD^2 N_D}{2\varepsilon_{Si}} - V_{bi} \quad \textbf{[74]}$$

Another expression [27] of the resulting electric field substituting boundary condition values is given by

$$|E(x)| = \frac{V_R}{w} + \frac{qN_{eff}}{\varepsilon_{Si}}\left(\frac{w}{2} - x\right) \quad \textbf{[75]}$$

Applying a bias voltage higher than V_{FD}, with all of the silicon bulk operating as space charge region, the equilibrium of spontaneous generation and recombination of electrons is disturbed, and all that charge is taken out from the depleted region.

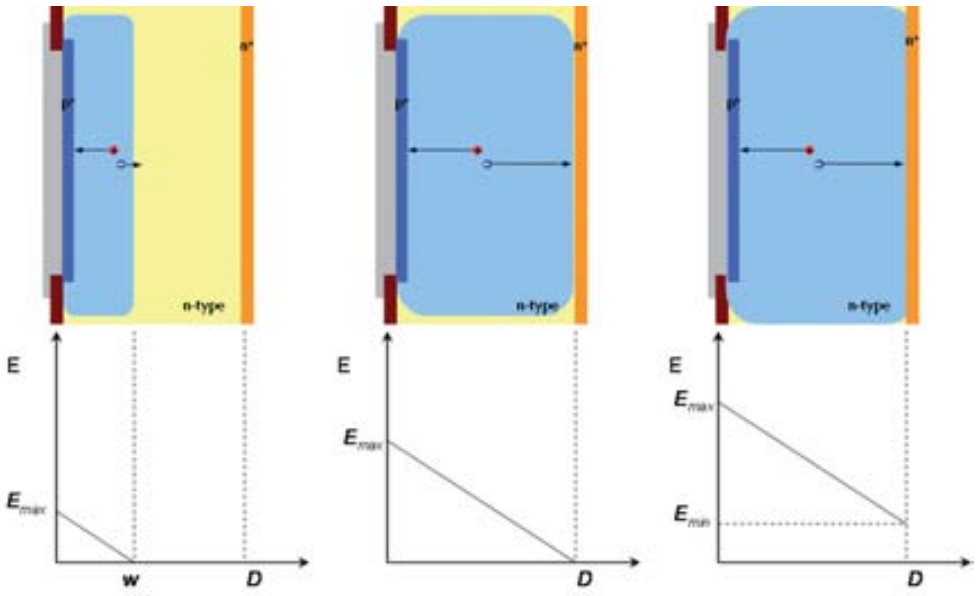

Figure 2.21: *Absolute values of the electric field for a p^+n junction under-depleted (left), depleted (middle) and over-depleted (right).*

Modelling the full sensor as a planar capacitor with a dielectric inside can be used in order to obtain the full capacitance of the detector. This capacitance depends on the area of the detector, thickness and charge density, as it will be shown later in section 2.2.2.3.

Coaxial geometry

The geometry of the 3D detectors (see Chapter 5) can be approximated to a coaxial geometry to resolve the Poisson's equation in order to obtain the electric field and the electric potential distributions in a p^+n junction [27, 28]. The radial part of Poisson equation in cylindrical coordinates is

$$\frac{1}{r}\frac{\partial}{\partial r}\left(r\frac{\partial V}{\partial r}\right)=-\frac{\rho(r)}{\varepsilon_{Si}} \qquad \textbf{[76]}$$

Integrating once, considering $\rho(r)=cte$ at both sides of the junction (abrupt junction) and using the boundary condition $V(r_{ext})-V(r_{\text{int}})=V_R$, where r_{ext} and r_{int} are the external and internal radii of the coaxial geometry respectively and V_R is the reverse bias applied, it is obtained

$$E(r)=\frac{N_{eff}}{2\varepsilon_{Si}}r+\frac{V_R+\frac{N_{eff}}{4\varepsilon}\left(r_{ext}^2-r_{\text{int}}^2\right)}{r\ln\left(\frac{r_{ext}}{r_{\text{int}}}\right)} \qquad \textbf{[77]}$$

The required voltage to fully deplete the detector is obtained by setting the condition $E(r_{ext})=0$, null field outside the depletion region, when the applied voltage is $V_R=V_{FD}$, resulting

$$V_{FD} = \frac{N_{eff}}{2\varepsilon_{Si}} \left\{ r_{ext}^2 \left[\ln\left(\frac{r_{ext}}{r_{\text{int}}} \right) - \frac{1}{2} \right] + \frac{1}{2} r_{\text{int}}^2 \right\} \quad \textbf{[78]}$$

2.2.2.2 Leakage current

The application of a bias voltage on a *pn* junction will break the equilibrium between drift and diffusion currents. Under a reverse bias the depletion region and the barrier potential are increased. This effect diminishes the diffusion current and propitiates the appearance of a small reverse current. The current-voltage characteristic for an ideal diode is given by

$$I = I_{sat} \left(e^{\frac{qV}{k_B T}} - 1 \right) \quad \textbf{[79]}$$

where

$$I_{sat} = q \left(\frac{D_p p_{n0}}{L_p} + \frac{D_n n_{p0}}{L_n} \right) \quad \textbf{[80]}$$

where I_{sat} is the saturation reverse current, k_B is the Boltzman constant, $D_{n,p}$ is the diffusion coefficient for carriers, $L_{n,p} = \sqrt{D_{n,p} \tau_{n,p}}$ is the diffusion length, and n_{p0}, p_{n0} are the minority carriers density in each side of the function at thermal equilibrium. As it can de deduced from equation **79**, the reverse currents saturates at $-I_{sat}$. This expression assumes that no charge is being generated in the space-charge region. Later it will be explained that this saturation value can reach an electrical breakdown as the reverse voltage is increased. This breakdown can be either explained by avalanche mechanisms, due to charge multiplication collisions with the lattice, by Zener breakdown, based on the quantum mechanical tunnel effect, or by thermal instability.

In reversal polarization the free carriers density is low and thus the recombination is improbable, so the main effect is generation. The reversal current equation can be reduced to

$$I_{bulk} = q \cdot w \cdot A \cdot G_{th} = q \cdot w \cdot A \frac{n_i}{\tau_g} = q \cdot w \cdot A \cdot n_i \cdot \sigma \cdot v_{th} \cdot N_t \quad \textbf{[81]}$$

where w is the space charge region, G_{th} is the carriers generation, A is the surface of the junction, n_i is the intrinsic density of impurities, τ_g the generation lifetime of the minority carriers, v_{th} the thermal velocity, N_t the defects/traps concentration, σ the cross section of the generation process for carriers, according to the Shockley-Read-Hall theory about the function of the impurities, acting not only as traps but also as sources of free carriers.

Current measurements in full depletion condition are a good method to evaluate the radiation damage in detectors, because their value will be proportional to the density of defects induced by radiation.

It is important to note that the bulk generation current depends strongly on the temperature and can be described as

$$I_g(T) \propto T^2 e^{-\frac{E_{eff,gap}}{2k_B T}} \quad \textbf{[82]}$$

where $E_{ff,gap}$ is the effective gap value, 1.21 eV [29]. This dependence suggests that is possible scaling the current measurements to a reference temperature, commonly 20ºC. To rescale the measured leakage current at a given temperature T to another temperature of reference T_{ref} it is used the following expression

$$I(T_{ref}) = I(T) \cdot R(T, T_{ref}) = I(T) \cdot \left(\frac{T_{ref}}{T} \right)^2 \exp\left[-\frac{E_{eff,gap}}{2k_B} \left(\frac{1}{T_{ref}} - \frac{1}{T} \right) \right] \quad \textbf{[83]}$$

2.2.2.3 Bulk capacitance

The capacitance of a *pn* junction in planar detectors[3] operating in reverse bias can be modelled like the one of a parallel plate capacitor, where the space between the plates is the space charge region. Therefore the bulk capacitance per unit area is determined by the depth of the depletion layer w

$$C_{bulk} = \frac{\varepsilon_{Si}}{w} = \sqrt{\frac{\varepsilon_{Si} N_{eff}}{2(V_R + V_{bi})}} \quad \textbf{[84]}$$

If the voltage applied is V_{FD}, this is when w has grown from the *pn* junction reaching the full thickness of the sensor D, the value of the bulk capacitance per unit area is

$$C_{bulk} = \frac{\varepsilon_{Si}}{D} \quad \textbf{[85]}$$

and will remain constant with an increasing bias. This capacitance is also known as *geometric capacitance* given the fact that only depends on the size of the sensor.

In the case of 3D detectors[4], the capacitance between the junction column and the surrounding ohmic columns can be calculated approximating that capacitance to the one of a cylinder capacitor

[3] See section 2.3.1.
[4] See section 2.3.2.

$$C_{cylinder} = 2\pi\varepsilon_{Si}\frac{L}{\ln\left(\frac{r_{ext}}{r_{\text{int}}}\right)} \quad \textbf{[86]}$$

where L and r_{ext} are the overlapping depth and gap distance between the junction and the ohmic columns respectively, and r_{int} is the radius of the columnar electrodes.

2.2.2.4 Electrical breakdown

At low electric fields, the drift velocity of the carriers inside a semiconductor is proportional to the electric field through the mobility, which is independent of the electric field, as can be seen in equations **23**, **24**. This condition is not true when there are applied voltages high enough to produce medium and high electric fields, achieving nonlinearity and saturation of drift velocity. For medium electric fields, carriers start to interact with acoustic phonons and the linear relation between carriers drift velocity and electric field becomes:

$$v_D = \mu E\sqrt{\frac{T}{T_e}} \quad \textbf{[87]}$$

where

$$\frac{T_e}{T} = \frac{1}{2}\left[1+\sqrt{1+\frac{3\pi}{8}\left(\frac{\mu E}{c}\right)^2}\right] \quad \textbf{[88]}$$

T_e is the effective temperature of carriers at medium voltages while T is the lattice temperature and μ is the charge carrier mobility (μ_n for electrons and μ_p for holes). Finally for high values of electric field the carriers start to interact with optical phonons and the above equation is no longer accurate. In this case the carriers drift velocities are not dependant on the electric field and reach a saturation value given by

$$v_{D\ saturation} = \sqrt{\frac{8E_p}{3\pi m^*}} \approx 10^7\, cm/s \quad \textbf{[89]}$$

where E_p is the optical phonon energy and m^* is the effective mass of the charge carrier (m_n for electrons and m_p for holes). This saturation value is independent of impurity dopings.

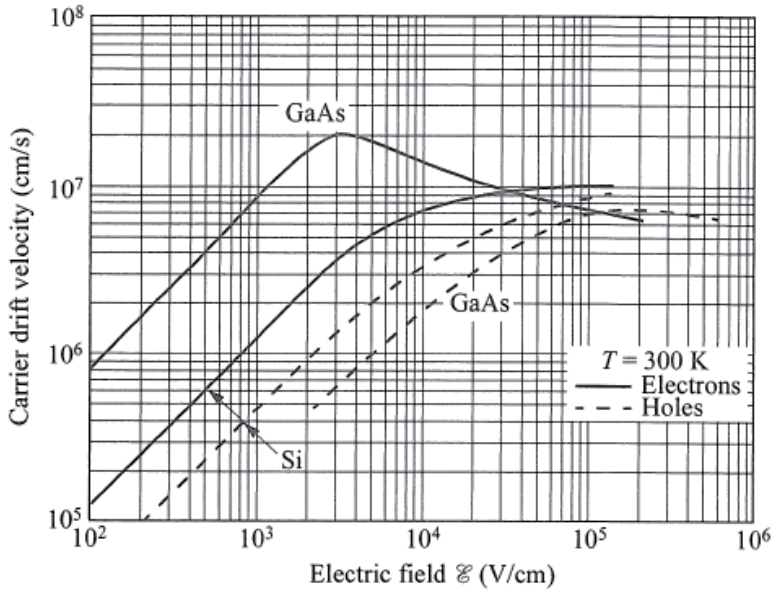

Figure 2.22: *Carriers drift velocity dependence with electric field. In semiconductors like GaAs, GaP, the relationship between drift velocity and electric field is more complicated because the band gap must be taken into account.*

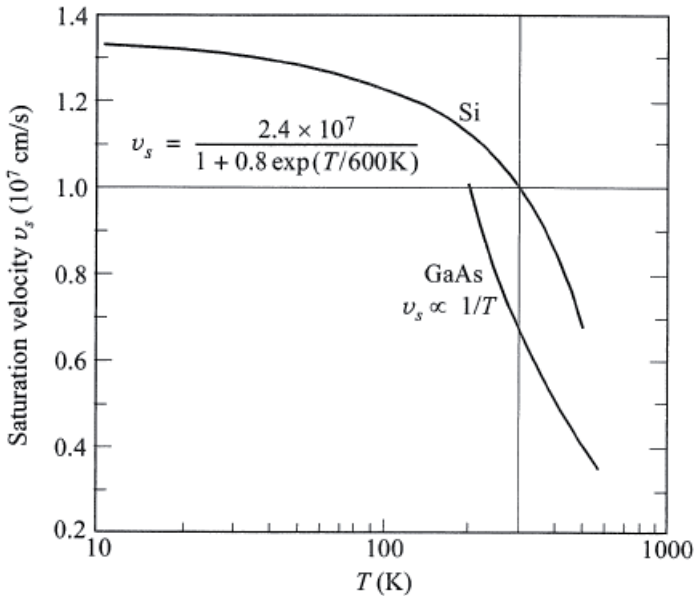

Figure 2.23: *Saturation drift velocity as a function of the temperature. Here it can be appreciated that the saturation velocity is inversely proportional to the temperature.*

For *pn* junctions, operating in such high reverse bias voltages which generate high electric fields, it can take place the phenomenon of *break down* and large leakage currents conduct through the junction. There are mainly three breakdown mechanisms, described below.

Thermal instability

We have seen that high electric fields lead to the saturation of drift velocities. The carriers are doted with more kinetic energy and this is translated into thermal instability, caused by the increase of temperature in the junction by heat dissipation by the collisions of the carriers moving in the leakage current, this increasing of temperature also increases the reverse current, turning in a positive feedback and therefore causing the breakdown of the junction.

Tunneling

A second process related to high bias operation is the band-to-band tunnelling, in which carriers can tunnel through the potential barrier induced by a large electric field. When an electric field reaches values of 10^6 V/cm, significant current flows by this tunnelling process increasing the leakage current. In order to obtain this value of electric field, the junction should have high concentration of doping impurities. This mechanism can also produce the electrical breakdown of the *pn* junction.

Impact ionization

The third mechanism is the impact ionization, in which charge carriers have enough kinetic energy to excite electron-hole pairs, and the parameter that quantifies this effect is the *ionization rate α*

$$\alpha(E) = \frac{qE}{I}\exp\left\{-\frac{E_I}{E\left[1+\left(E/E_p\right)\right]+E_T}\right\} \qquad \textbf{[90]}$$

where I is the high-field effective ionization threshold energy (in silicon, 3.6V for electrons and 5.0V for holes), and E_T, E_p and E_I are threshold fields for carriers to overcome the deceleration effects of thermal, optical and ionization scattering, respectively. Equation **90** can be reduced for silicon resulting in

$$\alpha(E) = \frac{qE}{I}\exp\left(-\frac{E_I}{E}\right) \qquad \textbf{[91]}$$

as in the case of silicon $E_p > E > E_T$. As occurred to the saturation drift velocity, the ionization rate decreases as the temperature increases.

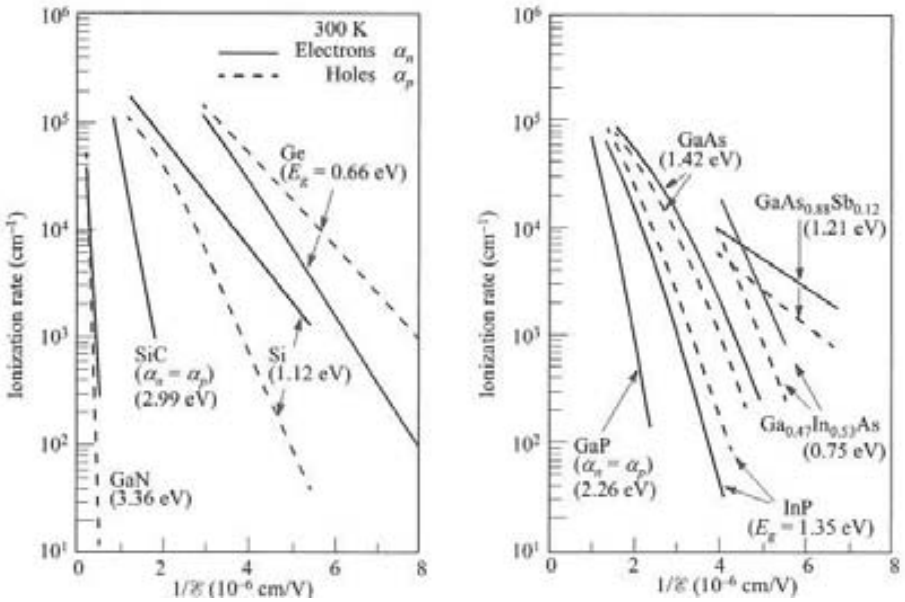

Figure 2.24: *Ionization rate versus reciprocal electric field for several semiconductor compounds. Note that there is a general trend which makes the ionization rate decreases as the bandgap increases. Plots obtained measuring photomultiplication in pn junctions.*

2.2.3 Physical models in TCAD simulations

This section contains the physical models implemented in Synopsys TCAD Sentaurus simulation toolkit [30] used to simulate the electrical behavior of devices studied in this thesis. Most of them have been explained in this chapter.

2.2.3.1 Semiconductor band structure

Due to the introduction of high doping levels in the active region (above 10^{19} cm^{-3}), the bandgap narrowing is important. Therefore an effective bandgap is defined

$$E_{g,eff}(T) = E_g(T) - \Delta E_g \qquad \textbf{[92]}$$

The temperature evolution of the bandgap $E_g\ (T)$ is described in equation **8**, and the bandgap narrowing, using the Old Slotboom model, has de form

$$\Delta E_g = \Delta E_g^0 + \Delta E_g^{Fermi} \qquad \textbf{[93]}$$

$$\Delta E_g^0 = E_{bgn}\left[\ln\left(\frac{N_i}{N_{ref}}\right) + \sqrt{\left(\ln\left(\frac{N_i}{N_{ref}}\right)\right)^2 + \frac{1}{2}}\right] \qquad \textbf{[94]}$$

where ΔE_g^{Fermi} is a compensation term when using the wrong statistics for high doping levels (Maxwell-Boltzmann) instead of using the more realistic Fermi-Dirac statistics.

The values or the other parameters are $E_{bgn} = 9\times10^{-3}$ eV and $N_{ref} = 10^{17}$ cm^{-3}. $N_i = N_A + N_D$ is the total doping concentration.

2.2.3.2 Mobility

There are many modules available in the simulator to describe the carrier mobilities in a semiconductor. They affect the mobility inside the bulk as well as in the surface, and their contributions are combined following the Mathiessen's rule

$$\frac{1}{\mu} = \frac{1}{\mu_{bulk1}} + \frac{1}{\mu_{bulk2}} + \ldots + \frac{1}{\mu_{surf1}} + \frac{1}{\mu_{surf2}} + \ldots \quad \textbf{[95]}$$

For the high field saturation model this expression will result in the mobility μ_{low}, used later in the computation of the final mobility by using any of models using a formula as a function of the high field.

Doping dependence

Impurities introduced in doped semiconductors leads to a degradation of the mobility as carrier will scatter with them. The model to describe this behavior in silicon used by default in the simulation is the Masetti Model:

$$\mu_{dop} = \mu_{\min 1} e^{-\frac{P_c}{N_i}} + \frac{\mu_{const} - \mu_{\min 2}}{1 + \left(\frac{N_i}{C_r}\right)^{\alpha}} - \frac{\mu_1}{1 + \left(\frac{C_s}{N_i}\right)^{\beta}} \quad \textbf{[96]}$$

where $N_i = N_A + N_D$ is the total ionized impurities, μ_{const} is the mobility of carriers as a function of the lattice temperature, given by

$$\mu_{const} = \mu_L \left(\frac{T}{T_0}\right)^{-\zeta} \quad \textbf{[97]}$$

T is the lattice temperature and T_0 is a reference temperature whose value is 300K. The rest of the parameters are listed in table 2.1

Table 2.1: Parameters of the Masetti model for the doping dependence mobility.

	Electrons	Holes	Unit
μ_L	1417	470.5	cm^2/(Vs)
ζ	2.5	2.2	1
μ_{min1}	52.2	44.9	cm^2/(Vs)
μ_{min2}	52.2	0	cm^2/(Vs)
μ_1	43.4	29.0	cm^2/(Vs)
P_c	0	9.23×10^{16}	cm^{-3}
C_r	6.68×10^{16}	2.23×10^{17}	cm^{-3}
C_s	3.34×10^{20}	6.10×10^{20}	cm^{-3}
α	0.680	0.719	1
β	2.0	2.0	1

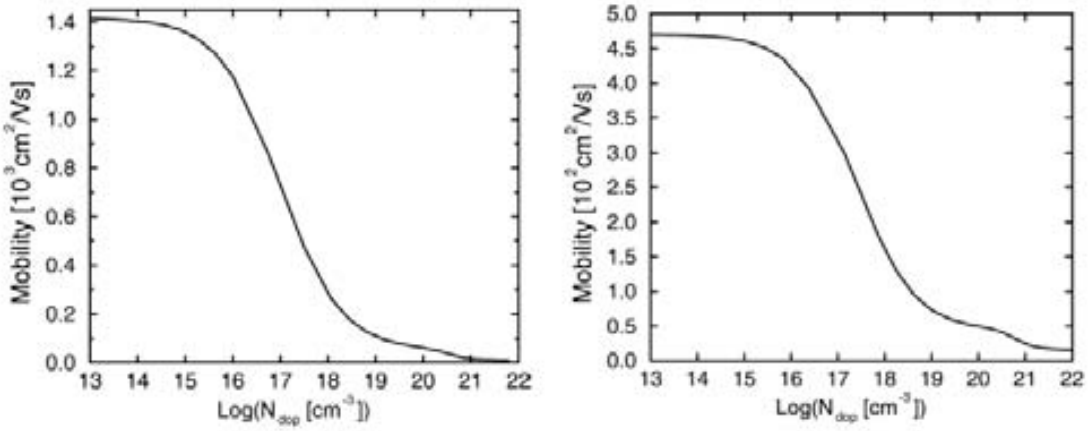

Figure 2.25: *Computed doping dependence mobilities for electrons (left) and holes (right).*

Degradation at interfaces

High transverse electric fields present at the interfaces force the carriers to interact with acoustic surface phonons and surface roughness. The degradation by these effects is described in the Lombardi model. The contribution due to the scattering by the acoustic phonons is given by

$$\mu_{ac} = \frac{B}{E_\perp} + \frac{C\left(\frac{N_i}{N_0}\right)^\lambda}{E_\perp^{1/3}\frac{T}{T_0}} \qquad \textbf{[98]}$$

and the contribution of the scattering with the surface roughness, by

$$\mu_{sr} = \left[\frac{\left(E_\perp / E_{ref}\right)^2}{\delta} + \frac{E_\perp^3}{\eta}\right]^{-1} \qquad \textbf{[99]}$$

The resulting mobility (bulk and surface contributions) by using the Mathiessen's rule is

$$\frac{1}{\mu} = \frac{1}{\mu_{bulk}} + \frac{D}{\mu_{ac}} + \frac{D}{\mu_{sr}} \qquad \textbf{[100]}$$

where $E_\perp$ is the transverse electric field in the interface, E_{ref} and N_0 are reference values to ensure unitless numerators whose values are 1 V/cm and cm^{-3} respectively, and the parameter $D = e^{-\frac{x}{l_{crit}}}$ is referred to the distance x from the silicon/oxide interface. The rest of the parameters are listed in table 2.2

Table 2.2: Parameters of the Lombardi model for the mobility degradation at interfaces.

	Electrons	Holes	Unit
B	4.75×10^{7}	9.925×10^{6}	cm/s
C	5.80×10^{2}	2.947×10^{3}	$cm^{5/3}/(V^{2/3}s)$
λ	0.1250	0.0317	1
δ	5.82×10^{14}	2.0546×10^{14}	$cm^{2}/(Vs)$
η	5.82×10^{30}	2.0546×10^{30}	$V^{2}/(cms)$
l_{crit}	10^{-6}	10^{-6}	cm

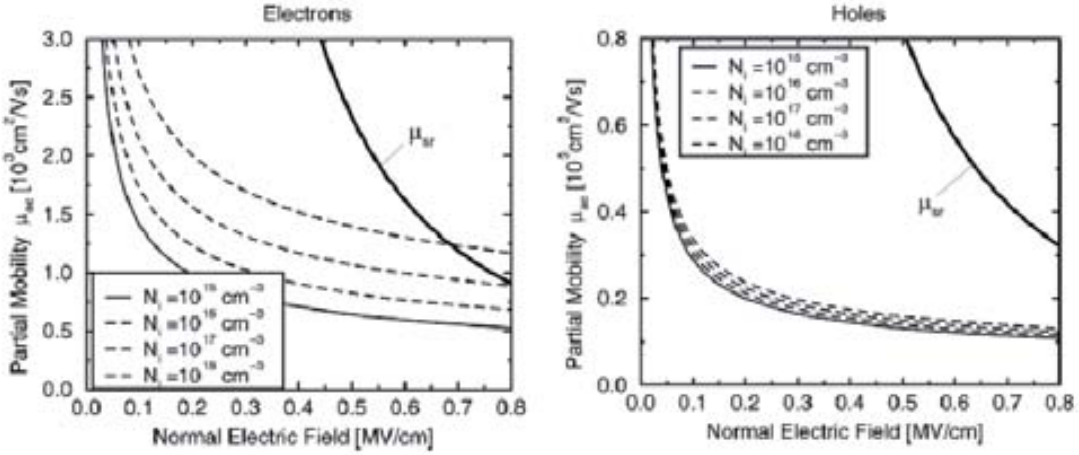

Figure 2.26: *Computed partial mobilities μ_{ac} and μ_{sr} for electrons (left) and holes (right) for different concentrations.*

Carrier-carrier scattering

The degradation in the mobility due to the carrier-carrier scattering is described by the Conwell-Weisskopf screening theory,

$$\mu_{eh} = \frac{D\left(\frac{T}{T_0}\right)^{3/2}}{\sqrt{np}}\left[\ln\left(1+F\left(\frac{T}{T_0}\right)^{2}(pn)^{-1/3}\right)\right]^{-1} \qquad \textbf{[101]}$$

where n and p are the electron and hole densities respectively, D and F are parameters whose values are 1.02×10^{21} $(cmVs)^{-1}$ and 7.452×10^{13} cm^{-2} respectively.

This contribution to the total mobility is included according to the equation **95**.

High field saturation

In the case of high electric fields, the carrier drift velocity is no longer dependant of the electric field reaching a saturation value, v_{sat}, as it was told in section 2.2.2.4. This effect is implemented in the simulator by using the Canali model,

$$\mu = \frac{\mu_{low}}{\left[1+\left(\frac{\mu_{low}E}{v_{sat}}\right)^{\beta}\right]^{1/\beta}} \quad [102]$$

The saturation drift velocity, v_{sat}, and the exponent β, are given by

$$v_{sat} = v_{sat,0}\left(\frac{T_0}{T}\right)^{v_{sat,\exp}} \quad [103]$$

$$\beta = \beta_0\left(\frac{T}{T_0}\right)^{\beta_{\exp}} \quad [104]$$

μ_{low} is the low field mobility obtained by the Mathiessen's rule, as it was said previously, and E is the electric field. The rest of the parameters of these expressions are listed in table 2.3

Table 2.3: Parameters of the Canali model for mobility saturation for high electric fields.

	Electrons	**Holes**	**Unit**
$v_{sat,0}$	1.07×10^7	8.37×10^6	cm/s
$v_{sat,exp}$	0.87	0.52	1
β_0	1.109	1.213	1
B_{exp}	0.66	0.17	1

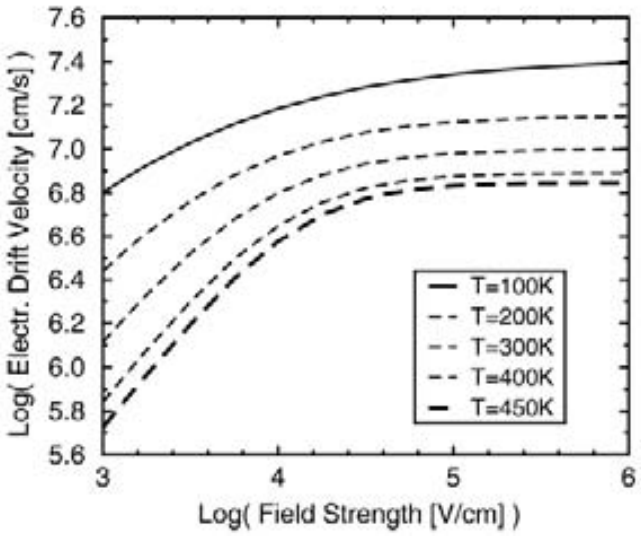

Figure 2.27: *Temperature drift velocity of electrons according to the Canali model.*

2.2.3.3 Generation and Recombination

Theory of the generation and recombination was introduced in section 2.2.1.7. Basic semiconductor physics on this mechanisms are included by default in the simulator so in

this section are only presented the different models implemented for the doped materials. Any avalanche generation model was included because the values of the electric field reached in these simulations were not high enough.

Shockley-Read-Hall (or trap -assisted) recombination

The net recombination of the SRH process is given by the expression

$$U_{SRH} = \frac{pn - n_i^2}{\tau_p (n + n_1) + \tau_p (p + p_1)} \quad \textbf{[105]}$$

where the carriers concentrations n_1 and p_1 related to the traps are

$$n_1 = n_i e^{\frac{E_{trap} - E_i}{k_B T}} \quad \textbf{[106]}$$

$$p_1 = p_i e^{\frac{E_i - E_{trap}}{k_B T}} \quad \textbf{[107]}$$

and the doping dependence of the minority carriers lifetimes are modeled with the Scharfetter relation

$$\tau_{dop}(N_i) = \tau_{\min} + \frac{\tau_{\max} - \tau_{\min}}{1 + \frac{N_i}{N_{ref}}} \quad \textbf{[108]}$$

Table 2.4 shows the parameters τ_{min}, τ_{max}, and N_{ref} for electron and holes

Table 2.4: Parameters of the Scharfetter relation for the doping dependence of the minority carriers lifetimes.

	Electrons	**Holes**	**Unit**
τ_{min}	0	0	s
τ_{max}	10^{-5}	3×10^{-6}	s
N_{ref}	10^{16}	10^{16}	cm^{-3}

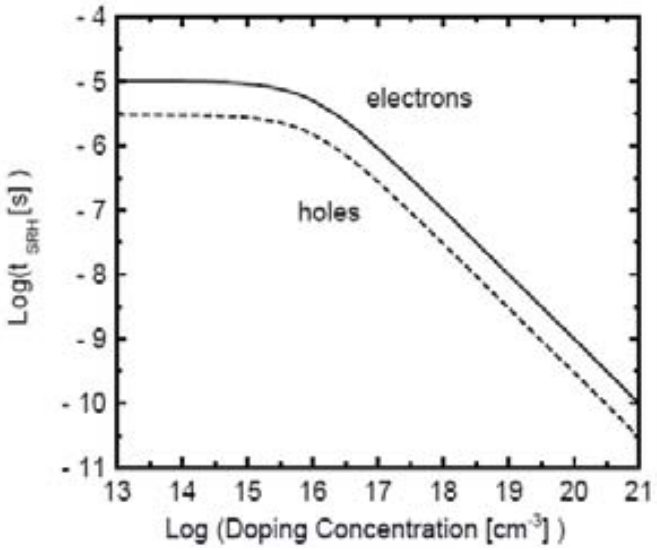

Figure 2.28: *Doping dependence of the SRH lifetimes according to the Schafertter relation.*

Auger recombination

This recombination process is important at high carrier densities and involves the presence of a third particle (electron or hole) that receives the difference of energy of this band-to-band transition. The net recombination through this mechanism is given by

$$U_{Auger} = C_n n(np - n_i^2) + C_p p(np - n_i^2) \qquad \textbf{[109]}$$

where the Auger coefficients C_n and C_p, corresponding to the two possible transitions, are

$$C_n(T) = \left(A_{A,n} + B_{A,n}\frac{T}{T_0} + C_{A,n}\left(\frac{T}{T_0}\right)^2 \right)\left(1 + H_n e^{-\frac{n}{N_{0,n}}} \right) \qquad \textbf{[110]}$$

$$C_p(T) = \left(A_{A,p} + B_{A,p}\frac{T}{T_0} + C_{A,p}\left(\frac{T}{T_0}\right)^2 \right)\left(1 + H_p e^{-\frac{p}{N_{0,p}}} \right) \qquad \textbf{[111]}$$

The parameters A_A, B_A, C_A, H and N_0 are listed in table 2.5

Table 2.5: Parameters of the Auger recombination coefficients.

	Electrons	**Holes**	**Unit**
A_A	0.67×10^{-31}	0.72×10^{-31}	cm^6/s
B_A	2.45×10^{-31}	4.50×10^{-33}	cm^6/s
C_A	-2.2×10^{-32}	2.63×10^{-32}	cm^6/s
H	3.46667	8.25688	1
N_0	10^{18}	10^{18}	cm^{-3}

The keyword *withGeneration* is added to allow the net recombination U_{Auger} for obtaining negative values which mean generation of electron/hole pairs instead of their recombination.

Surface SRH recombination

This keyword enables the surface SRH recombination between two different regions or materials, whose expression is

$$U_{surf,net}^{SRH} = \frac{pn - n_i^2}{(n + n_1)/s_p + (p + p_1)/s_n} \quad \textbf{[112]}$$

where the carriers concentrations n_1 and p_1 related to the traps are given by the equations **106**, **17**. The recombination velocities s_n and s_p depends on the concentration of dopants at the surface

$$s = s_0 \left[1 + s_{ref} \left(\frac{N_i}{N_{ref}} \right)^{\gamma} \right] \quad \textbf{[113]}$$

The parameters s_0, s_{ref}, N_{ref} and γ are listed in the table 2.6.

Table 2.6: Parameters of the recombination velocities.

	Electrons	**Holes**	**Unit**
s_0	1×10^3	1×10^3	cm/s
s_{ref}	1×10^3	1×10^3	1
N_{ref}	1×10^{16}	1×10^{16}	cm^{-3}
γ	1	1	1

Shockley-Read-Hall (or trap-assisted) tunnelling.

Trap-assisted tunnelling results in a reduction of the recombination lifetimes for regions where strong electric fields are present. It is an important factor to take into account in highly reverse biased *pn* junctions, where the leakage current is sensitive to trap-assisted tunnelling that causes electron/hole pairs generation, before the electrical breakdown of the junction.

In the Hurkx trap-assisted tunnelling model the lifetime and capture cross-sections are now dependent of the trap-assisted tunnelling factor Γ_{tat},

$$\tau = \frac{\tau_0}{1 + \Gamma_{tat}} \quad \textbf{[114]}$$

$$\sigma = \sigma_0 \left(1 + \Gamma_{tat}\right) \quad \textbf{[115]}$$

Impact ionization (University of Bologna model)

This model covers a wide range of temperatures (up to 700 K) and electric fields (50 – 600 kV/cm). The impact ionization coefficient for this model is given by

$$\alpha_{n,p}(E,T) = \frac{E}{a(T) + b(T)e^{\frac{d(T)}{E+c(T)}}} \qquad \textbf{[116]}$$

where the coefficients a,b,c and d were determined by fitting experimental data, and their expressions for electrons are

$$a(T) = a_0 + a_1 T^{a_2} \qquad b(T) = b_0 \qquad c(T) = c_0 + c_1 T + c_2 T^2 \qquad d(T) = d_0 + d_1 T + d_2 T^2$$

and for holes

$$a(T) = a_0 + a_1 T \qquad b(T) = b_0 e^{b_1 T} \qquad c(T) = c_0 T^{c_1} \qquad d(T) = d_0 + d_1 T + d_2 T^2$$

The values of the above parameters are listed in the table 2.7.

Table 2.7: Parameters of the University of Bologna model for the impact ionization.

Silicon	Electrons	Holes	Unit
a_0	4.338	2.736	V
a_1	-2.42×10^{-12}	1.033×10^{-2}	V/K
a_2	4.123	0	1
b_0	0.235	0.177	V
b_1	0	-2.178×10^{-3}	1/K
c_0	1.68×10^{4}	9.47×10^{-3}	V/cm
c_1	4.379	2.492	V/(cm K), 1
c_2	0.13	0	V/(cm K^2), 1
d_0	1.234×10^{6}	1.404×10^{6}	V/cm
d_1	1.204×10^{3}	2.974×10^{3}	V/(cm K)
d_2	0.567	1.483	V/(cm K^2)

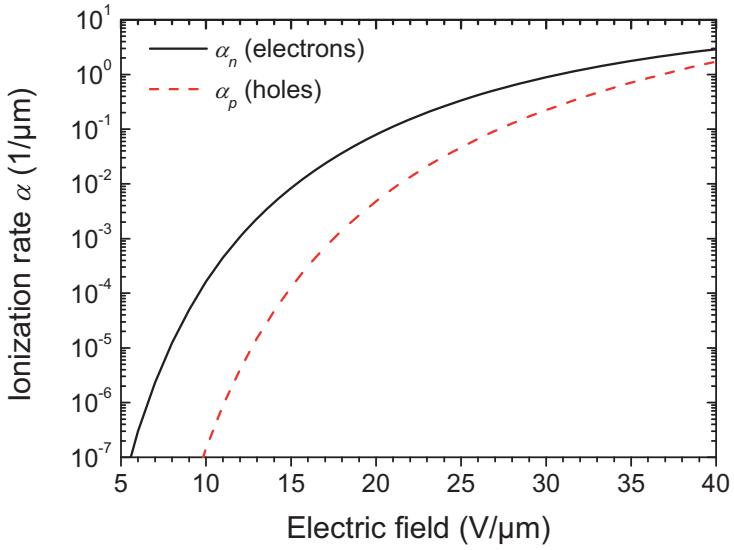

Figure 2.29: *Ionization rate for electrons and holes in silicon at -20ºC, according to the University of Bologna impact ionization model.*

Band-to-band tunneling

The Hurkx band-to-band tunnelling model takes into account the carriers tunnelling by introducing an additional generation-recombination contribution

$$G^{bb} = -A \cdot D \cdot \left(\frac{E}{E_0} \right)^{P} e^{-\frac{B \cdot E_g(T)}{\left[E_g(300K)\right]^{\beta * 2} E)}} \qquad \textbf{[117]}$$

where E is the electric field, E_0 = 1 V/m, the parameter D is expressed as

$$D = \frac{np - n_i^2}{(n + n_i)(p + n_i)} \qquad \textbf{[118]}$$

The values of the rest of the parameters A, B and P for generation and recombination can be introduced in the parameter section of the simulator, however the default values were not found in the TCAD manual.

2.3 Detector designs

This section describes the most common designs of planar detectors that have been widely used in high energy physics experiments and medical imaging. Additionally, the new design of the so-called *3D detectors* using columnar electrodes is introduced.

2.3.1 Planar detectors

The technology employed in modern semiconductor radiation detectors is based in the so-called *planar technology* in microelectronics. Planar technology consists on the execution of a series of processing steps on crystalline silicon wafers, but recently has been derived to detectors which have been implanted and processed in the nearest region of the top and bottom sides of the detector. Alternatively there is a newer technology that exploits the capability of these processing steps resulting in electrode passing through the whole thickness of the detectors that is called *3D technology*, commented later.

2.3.1.1 PAD Detectors

Pixel Array Detectors (PAD) are structures relatively simple in planar technology and their study as radiation detector has been very helpful for understanding the behaviour of different substrates in which detectors are fabricated.

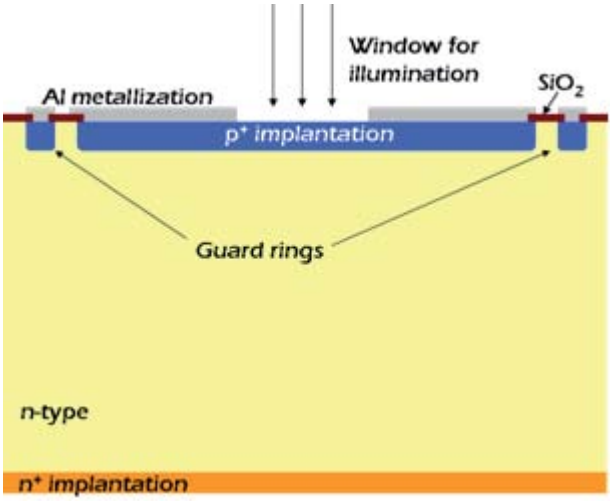

Figure 2.30: *Schematic of a p-on-n PAD detector.*

As it can be seen in figure 2.30, they consist on a highly doped layer at the top of the detector on a moderated doped bulk (opposite doping type than the top) promoting the growth of the space charge region of the *pn* junction within the bulk. Finally, there is a high doping layer at the bottom with the same doping type of the bulk. This highly doped layer has the function of forming an ohmic contact with the backplane metallization, as explained in section 2.2.1.8.

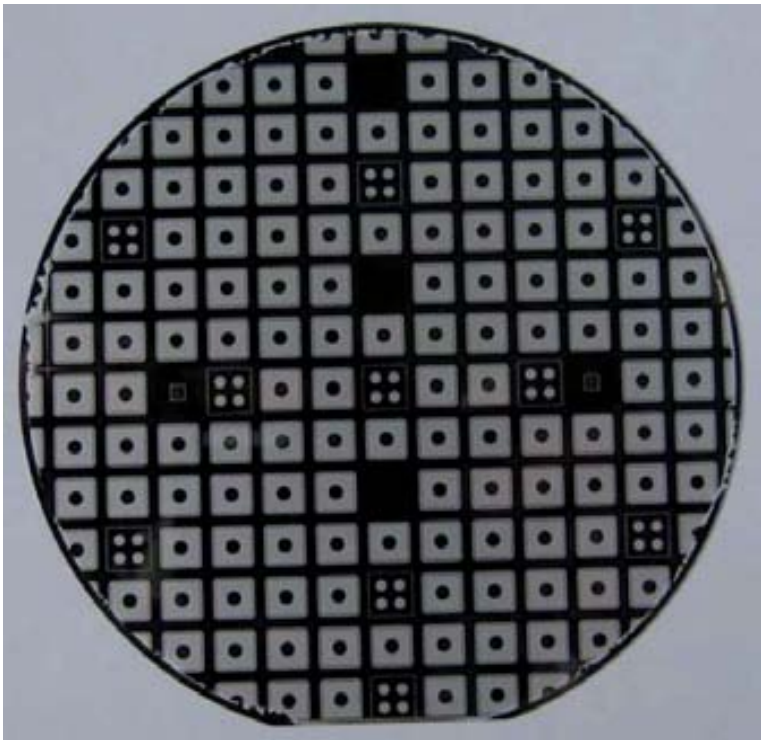

Figure 2.31: *Picture of a wafer containing p-on-n PAD detectors fabricated at the IMB-CNM (CSIC) Clean Room facilities for the CERN RD48 (ROSE) collaboration.*

In figure 2.31 is shown a wafer which contains PAD detectors fabricated at the IMB-CNM (CSIC) Clean Room facilities for the CERN RD48 (ROSE) collaboration. In the middle of each detector there is a circular window in the metal to allow the pass of laser light for the measurements of charge collection efficiency. The following plots (figures 2.32 and 2.33) correspond to typical IV and CV curves, respectively, for these detectors.

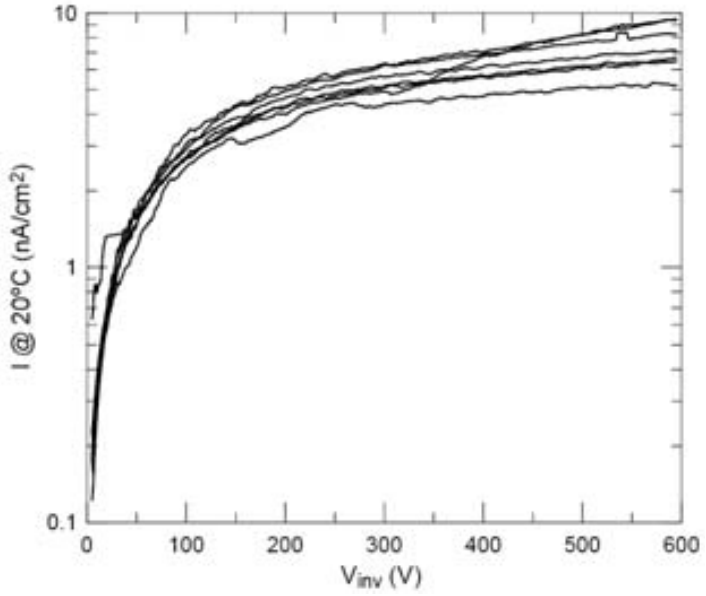

Figure 2.32: *Reverse current-voltage characteristics for 8 p-on-n PAD detectors fabricated at the IMB-CNM (CSIC) Clean Room facilities for the CERN RD48 (ROSE) collaboration [31].*

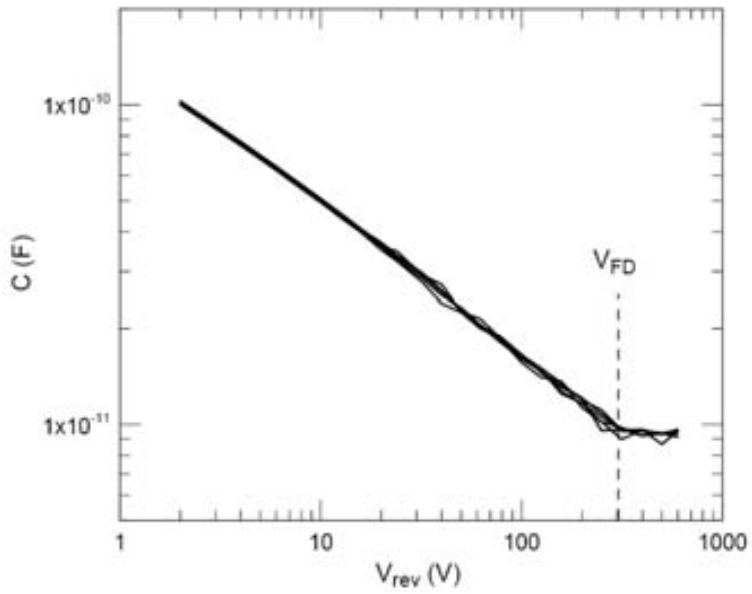

Figure 2.33: *Capacitance-voltage characteristics for 8 p-on-n PAD detectors fabricated at the IMB-CNM (CSIC) Clean Room facilities for the CERN RD48 (ROSE) collaboration [31].*

2.3.1.2 Strip detectors

Planar technology allows the segmentation of the implants in order to get signal collected in each segment for particle positioning and tracking. In the case of strip detectors [32, 33], these segments are narrowed implants covering most of the sensor surface.

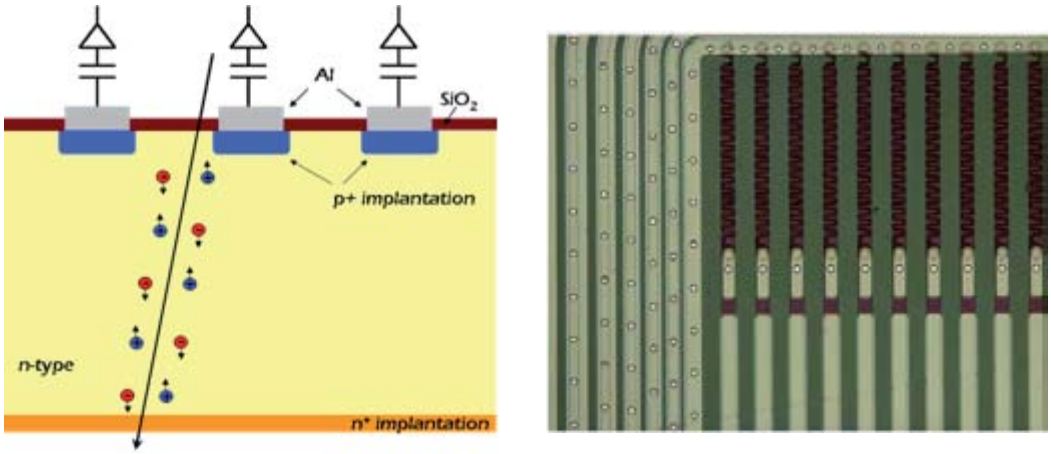

Figure 2.34: *Schematic of a p-on-n strip detector(left) and picture of a microstrip detector fabricated at IMB-CNM (CSIC) for the CERN RD50 collaboration (right).*

Ionizing particles through the detector create electron-hole pairs in the depletion zone that are collected in the electrodes producing a signal that will be amplified by an amplifier connected to each strip, see figure 2.34. From the signals on the individual strips is possible to deduce one coordinate of the position of the through going particle.

Coupling capacitance

A problem appeared in this segmented detectors when they were trying to be coupled to the read-out chip. The very large scale integration technique allows the integration of large amounts of preamplifiers channels on a single chip, but there is no enough space in small chip surfaces to integrate the coupling capacitors. One easy solution was the integration of the coupling capacitors in the detector itself in standard planar process. Looking at the cross section of a strip detector it is easy to deduce that creating a coupling capacitor for each strip could be done just by introducing an insulator layer between the strip implantation and the metallization, as shown in figure 2.35.

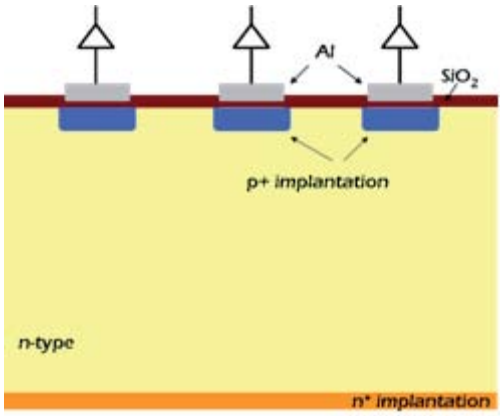

Figure 2.35: *Schematic of a p-on-n strip detector with integrated coupling capacitors.*

In high speed data transmission circuits, too much load capacitance causes significant signal attenuation. Load capacitance is also a noise contribution element which is mostly comprised by the inter-strip capacitance and the strip to backplane capacitance therefore both of them should remain as low as possible. In an AC-Coupled sensor, the coupling capacitance must be larger than the inter-strip capacitance and other parasitic capacitances. A 100 – 200 nm SiO_2 layer can be grown/deposited on the silicon, whose electrical permittivity is 0.34 pF/cm, obtaining coupling capacitances in the range of 32 pF/cm, high enough compared to the inter-strip capacitance, in the order of 1.1 pF/cm, ensuring a good charge collection [34, 35].

Biasing voltage

In order to bias these AC-coupled or DC-coupled strip detectors several methods are possible.

Polysilicon resistor

One way to providing the biasing voltage to the strips is through resistors integrated on the detector. This method consists on the deposition of polycrystalline silicon between the final edge of each strip implant and a common bias line, as shown in figure 2.36.

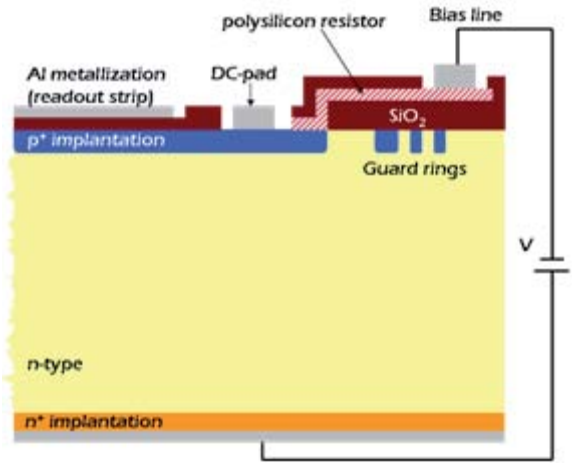

Figure 2.36: *Cut through an AC coupled p-on-n strip detector with integrated polysilicon resistor.*

Depending on the doping level a sheet resistance up to 250 kΩ/sq can be reached. The final resistance depends on the width and length of the resistor, $R = R_{sheet} \frac{Lengh}{Width}$ achieving values over 20 MΩ. For higher resistor values winding polysilicon structures are deposited.

Punch-through biasing

In this method the unbiased strips are polarized by the increasing width of the depletion region under the bias line. The process is show in figure 2.37, in which we can se that under the absence of bias there is a thin space charge region under the strip implantations, but when the voltage is increased in the bias line, its depletion region reaches the space charge around the junctions of the strips at a certain threshold potential, V_{pt}. A hole current flows between the strip and the bias ring until a state of equilibrium is attained. Therefore, the potential of the floating strips is $V_{bias} - V_{pt}$. Above that threshold potential the depleted region of the strips is increased.

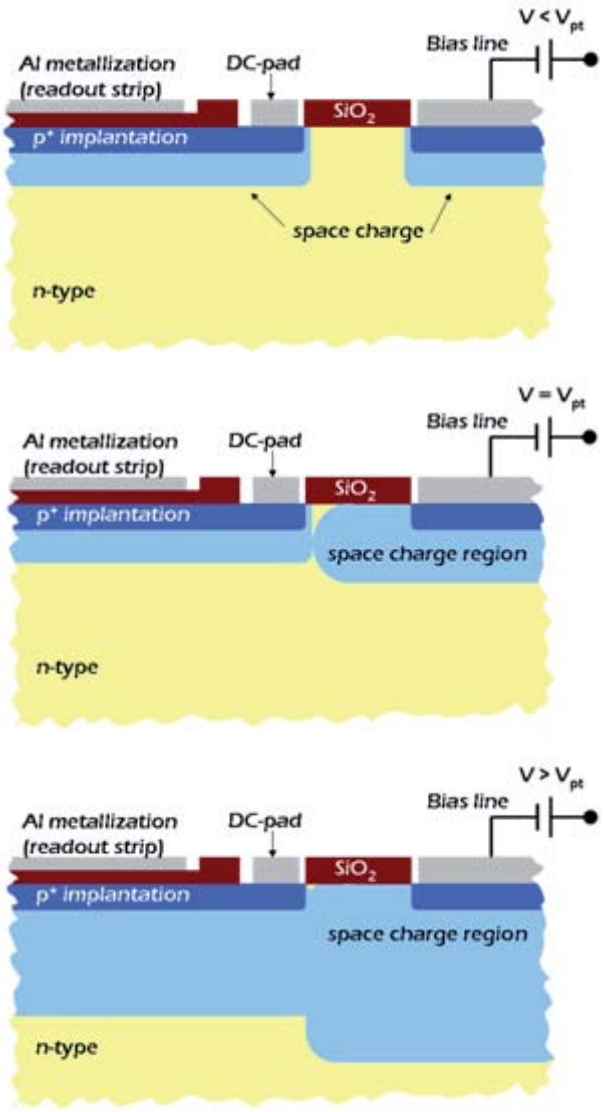

Figure 2.37: *Schematic sequence of punch through biasing method.*

The punch-through biasing method is simpler to fabricate, however it could give significant strip to strip voltage variation with strip current and it would affect the charge division and thus, the resolution.

2.3.1.3 Pixel detectors

A pixel detector consists of an array of detection elements, and in the case of semiconductor detectors, these elements are small diode structures. The fabrication of pixel sensors is very similar that the one for fabricating strip detectors, but in this case the strips are segmented down to a pixel structure. The read-out is adapted to small capacitances and is designed to handle DC coupling to the pixel implants. Each pixel of the detector is individually connected to its own electronics. This is the so-called *hybrid pixel detector*, hybrid because both sensor and electronics chips are fabricated separately and then joined [36].

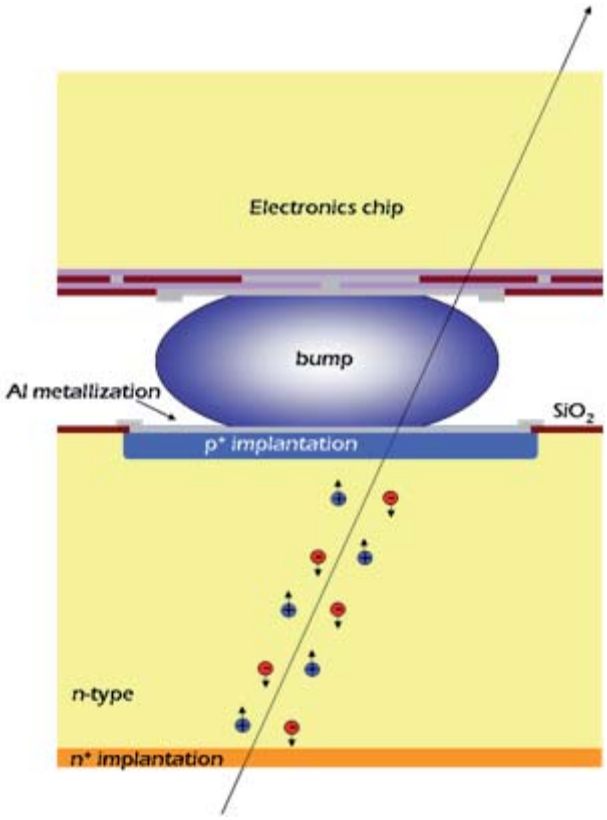

Figure 2.38: *Schematic view of one single pixel connected to the electronics chip by bump-bonding. The charge generated by the ionizing particle is collected by each pixel and amplified by its own read-out electronics.*

In this new design the wire bonding is no longer possible for joining the sensor to the electronics and therefore it requires a new technique for bonding, called bump-bonding. Such structure of a pixel, the bonding bump and its electronics is shown in figure 2.38.

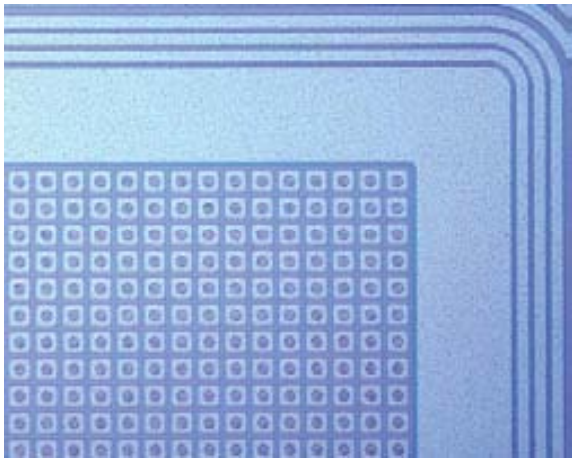

Figure 2.39: *Picture of one Medipix2 sensor fabricated at the IMB-CNM (CSIC) Clean Room facilities.*

According to the way of operation, these detectors are separated in two broad categories: charge coupled devices (CCD), and active pixel sensors (APS). CCDs are a

matrix of diodes sequentially clocked out, by varying the potential applied to each element of the array, to a single pre-amplifier. Their energy range of applications for incident photons lays in the visible. In APS each detection element has a dedicated electronic read-out channel which leads to a high read-out rate, and therefore more suitable for high energy physics experiments [37].

2.3.2 3D detectors

Irradiated planar detectors present the drawback of requiring high bias voltages to deplete the whole thickness of the detectors. This causes an increment of the leakage current as a consequence of an even higher voltage needed to increase the charge collection efficiency to avoid the trapping of radiation induced defects. To overcome the limitations of current silicon planar detectors in high energy experiments, a new detector architecture has been proposed by Kenny and Parker [38, 39]. Electrodes of planar structures discussed before are fabricated by ion implantation on the material surface. This new design proposes columnar electrodes of several microns of diameter which penetrate from the surface most or the whole thickness in the bulk, see figure 2.40.

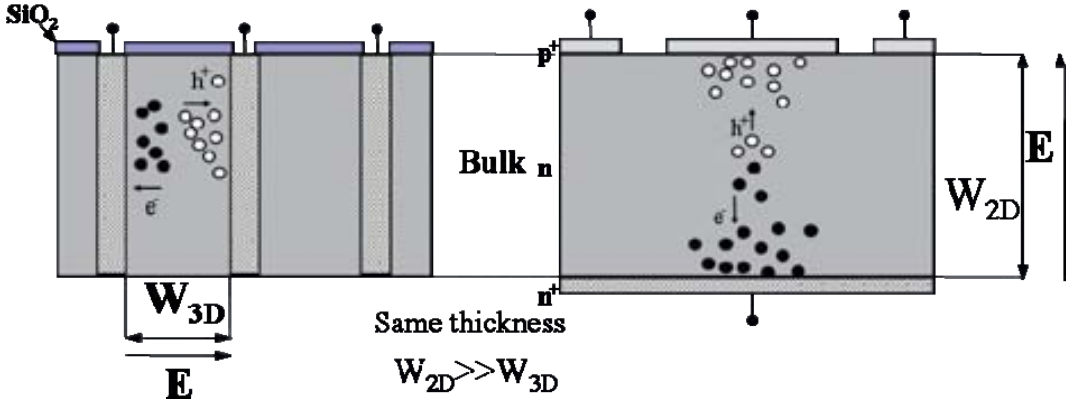

Figure 2.40: *Comparison of the cross sections of 3D and planar geometrics.*

The distance between two columnar electrodes of different polarity is determined by the desired spatial resolution of the detector. Using pitch distances of several tens of microns provide full depletion voltages about one order of magnitude lower than for planar structures. Also the collection time is reduced to less than nanoseconds due to the shorter drift distances that reduces the charge trapping of radiation induced defects. Due to the geometry of 3D detectors, charge sharing between neighbouring electrodes is negligible, therefore in applications such as single photon counting X-ray imaging, the imaging and differential spectroscopy could be achieved at the same time with proper read-out electronics.

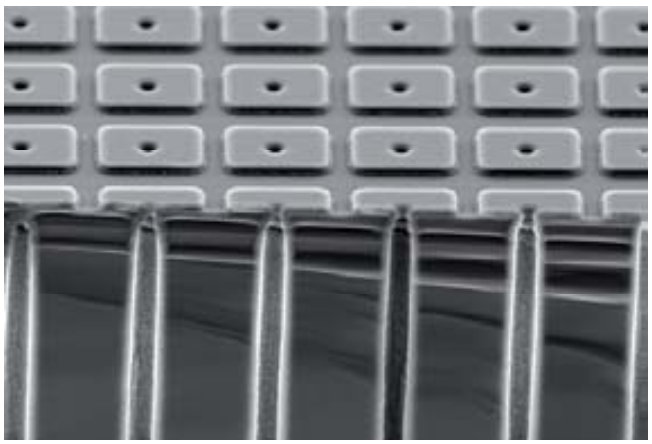

Figure 2.41: *Detail of 3D columnar electrodes of a test structure with 55 µm of pitch between electrodes fabricated at the IMB-CNM (CSIC) Clean Room facilities.*

The fabrication of such columnar electrodes, as shown in figure 2.41, requires the using of plasma etching process to make the holes, that in last instance is what limits their aspect ratio. Pixel and strip detectors fabricated at the IMB-CNM (CSIC) Clean Room facilities using 3D technology [40] are part of this study and they will be presented in Chapter 5. They consist of detectors that have been fabricated using the conventional 3D technology but also there are detectors that have been fabricated using a proposed alternative: double-sided 3D detectors, whose fabrication is simpler as they do not need support wafer.

Chapter 3

Radiation effects in silicon detectors

Silicon radiation detectors are used in many high energy physics experiments at LHC [41]. These sensors are present in the inner tracking layers of huge particle detectors receiving very large doses of radiation. The main effects of radiation damage are located within the bulk, causing the displacement of atoms from their original position in the lattice, and at the silicon/oxide interfaces, producing interface defects and transient/long-term positive ionization in the oxide layer. These effects alter the electric properties of the sensors resulting in:

- Change of the effective doping concentration N_{eff} with severe consequences for the operating voltage needed for total depletion.
- Increase in the reverse current, caused by the creation of generation-recombination centers.
- Deterioration of the charge collection efficiency (CCE) due to the trapping of charge carriers which causes to a reduction of the effective drift length for both electrons and holes.

The objective of this section is to shed light on the origin and time evolution of radiation induced defects to find the best choice of material/design to minimize the degradation effects on the electrical response of the sensor, as well as the implementation of adequate traps models in TCAD simulations to match experimental results.

3.1 Bulk (crystal) damage due to Non Ionizing Energy Loss (NIEL)

Displacement damage is the consequence of a non ionizing particle interaction of an impinging particle ($\beta^{+/-}$, p, n, ions, γ-rays) with the lattice atoms. The collision between the particle and the nucleus displaces the nucleus from its position in the lattice, producing point defects known as *Frenkel pairs*, which consist of one interstitial atom and a vacancy. Most of these defects are not stable. Interstitials and vacancies are mobile at room temperature and will therefore partially anneal if by chance an interstitial fills the place of a vacancy. However, it is also possible the formation of other (room temperature) stable defects.

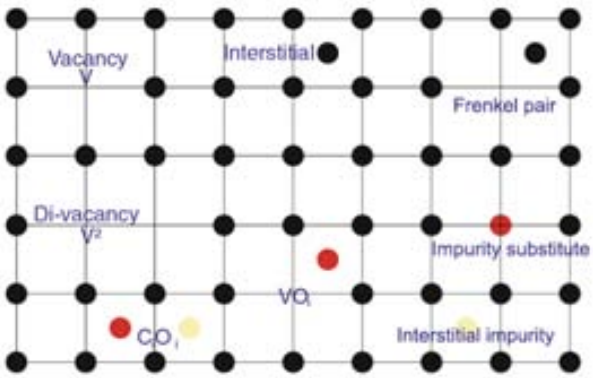

Figure 3.1: *Impurities and displacement defects in the lattice [34].*

The minimum ionizing energy needed to displace one silicon atom is around 15 eV, although it depends on the backscattering direction. From the point of view of probabilities, if the impinging particle transfers an energy greater than 25 eV to the silicon atom one Frenkel pair will be created, while for lower energies occurs the dissipation of the energy via lattice vibrations [24].

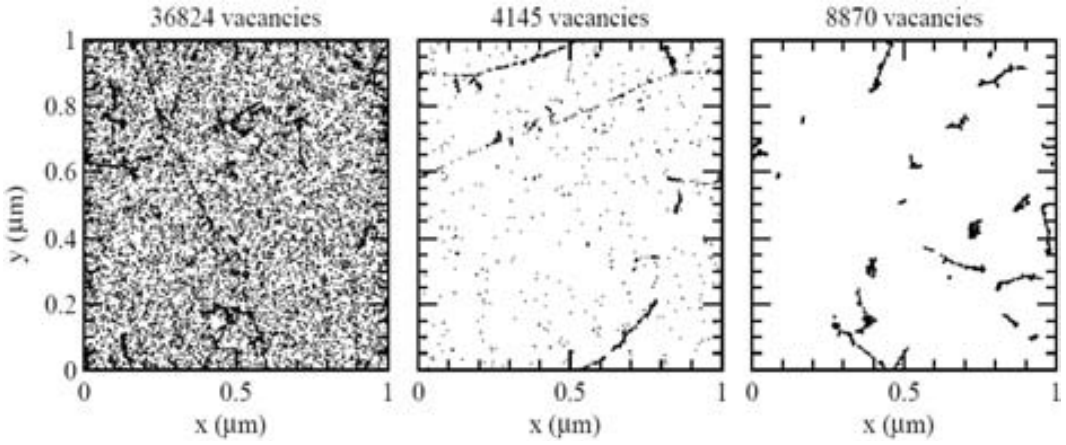

Figure 3.2: *Initial distribution of vacancies produced by 10 MeV protons (left), 24 GeV protons (middle) and 1 MeV neutrons (right). The plots are projections over 1 µm of depth (z) and correspond to a fluence of* 10^{14} n_{eq}/cm^2 *[48].*

The Primary Knock-on Atom (PKA) in its movement is able to generate another point defects or high density groups, known as *clusters*, depending on the energy transferred in the collision. An atom of silicon with backscattering energy of 1-2 keV only produces point defects; with 2-12 keV it is able to produce a cluster and several point defects, and with higher energies than 12 keV it will create some clusters [24]. Clusters appears at the end of the silicon atom track, where it losses its last keVs of energy and the cross section for the elastic collision is increased several orders of magnitude.

3.1.1 Displacement damage function, D(E)

It is proven that the damage in silicon created by the impinging particle is generally proportional to the non ionizing energy loss (NIEL), which is the energy that the

particle leaves per unit length in its interaction with the nuclei of the lattice [46]. This behavior can be expressed by the so-called *displacement damage function D(E)*. This quantity is equivalent to the NIEL [42] and hence the proportionality between the NIEL[1] value and the resulting damage, *D(E)* is normally quantified in MeV·mb, while NIEL is given in keV·cm^2/g. For silicon with atomic mass A = 28.086 g/mol the relation between *D* and NIEL is 100 MeV·mb = 2.144 keV·cm^2/g. According to an ASTM[2] standard, the displacement damage cross section for 1 MeV neutrons is set as a normalizing value: D_n(1 MeV) = 95 MeV·mb [43]. NIEL value depends on the particle type and energy and can be scaled to the reference value for 1 MeV neutrons using the *hardness factor k* [44]. This way, respecting to displacement damage, the fluence of impinging particles Φ can be replaced by an equivalent fluence of neutrons of 1MeV, $\Phi_{eq} = k\Phi$ [45, 46].

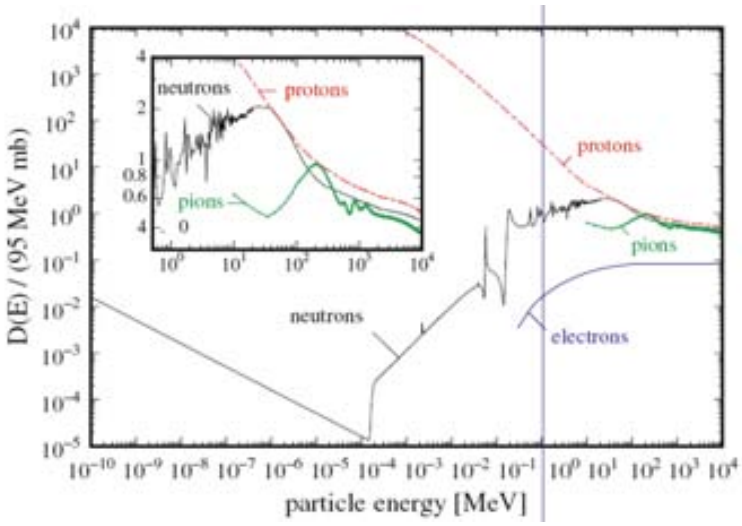

Figure 3.3: *Energy dependence of non-ionizing energy loss (NIEL) displacement damage function D(E) in silicon for various types of radiation, normalized to 95 MeV·mb [46].*

However, there are differences depending on the type and energy of the radiation. Gamma irradiations will result in point defects by Compton electrons, neutron irradiation creates mainly clusters as silicon displacements by neutron are dominated by head-on collisions, meanwhile charged hadrons (protons, pions) interacts via Coulomb thus generating both isolated point defects (low energy transfers) and clusters (PKA with enough energy).

3.1.2 Impurities in silicon

The primary defects within the bulk due to radiation damage are interstitials *I*, vacancies *V* and di-vacancies V_2. These defects are not fixed, *I* and *V* are mobile at room temperature, while di-vacancies are static until 600K [47], and those which escape from recombination (*I* + *V*) diffuse through the crystal until they are trapped at impurity atoms or other lattice defects. Table 3.1 shows the main possible quasi-chemical reactions that can take place inside an n-type silicon substrate. The reaction rates depend on the concentration of impurities and defects and their relative capture radii.

[1] NIEL is the rate at which energy is lost to non-ionizing events (energy per unit length).
[2] The American Society for Testing and Materials (ASTM) is an organization that develops and publishes international voluntary consensus standards.

Table 3.1: Some interstitials and vacancies reactions with silicon, impurities and radiation induced defects taken from references [48-51], where $C_s + C_i \rightarrow CC$.

V reactions	I reactions
$V + I \rightarrow Si$	$I + I \rightarrow I_2$
$V + V \rightarrow V_2$	$I + V_2 \rightarrow V$
$V + V_2 \rightarrow V_3$	$I + V_3 \rightarrow V_2$
$V + O \rightarrow VO$	$I + VO \rightarrow O$
$V + VO \rightarrow V_2O$	$I + V_2O \rightarrow VO$
$V + V_2O \rightarrow V_3O$	$I + V_3O \rightarrow V_2O$
$V + P_s \rightarrow VP$	$I + VP \rightarrow P_s$
$V + I_2 \rightarrow I$	$I + C_s \rightarrow C_i$
$V + ICC \rightarrow CC$	$I + CC \rightarrow ICC$
$V + ICO \rightarrow CO$	$I + CO \rightarrow ICO$

P, *O* and *C* are phosphorous, oxygen and carbon respectively. *P* is the donor impurity used in radiation detectors for n-type silicon meanwhile *O* and *C* are undesired impurities of monocrystalline silicon introduced during the growth of the wafer ingots. The impurity *C* is divided in C_i and C_s, since both *C* and silicon belong to the group IV and in addition to C_i interstitial it is possible to find substitutional carbon C_s, more important because of the low migration velocity of interstitial carbon at room temperature [52].

The donor removal is mainly represented by the reaction $V + P_s \rightarrow VP$, as the experimental evidence of $C_i + P_s \rightarrow C_iP_s$ and $I + P_s \rightarrow P_i$ in detector grade silicon is still missing [44]. However, *V* also reacts with *O* producing the *VO* defect that for high oxygen concentrations acts suppressing the donor removal reaction.

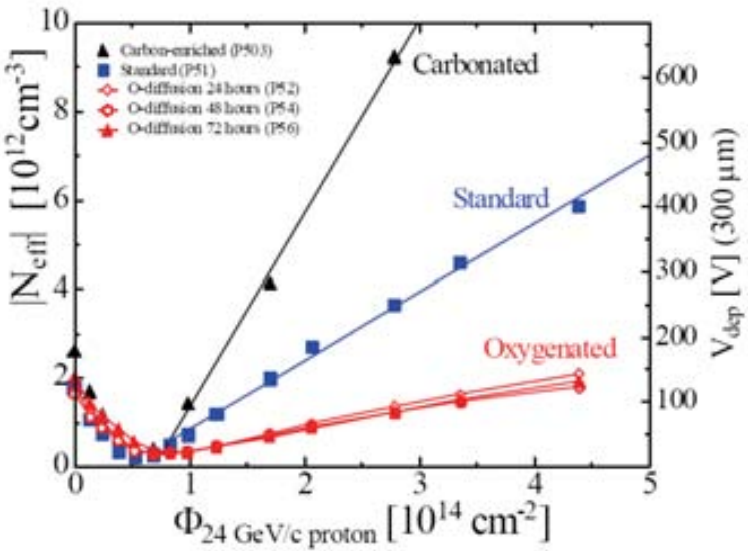

Figure 3.4: *Influence of carbon and oxygen enrichment to changes of the effective doping concentration after proton irradiation [53].*

The *VO* defect itself has no significant influence on the electrical properties of the silicon. However, evolution of *VO* formation as a function of fluence has an important role in the formation of V_2O defect, which has been proposed as a possible candidate of deep acceptor state to explain the main changes of N_{eff}. Oxygen enrichment of silicon (see figure 3.4) is used to prevent from V_2O formation [54], this is because the oxygen

getters the vacancies produced during irradiation and suppresses the channel $V + VO \rightarrow V_2O$. But it seems to be not true at all. NIEL and formation defects simulations reveal that a high concentration O is suppressing V_2O production only at fluences well beyond 10^{13} n_{eq}/cm^2. At low fluences an increase of oxygen leads to a higher V_2O production. The exception is neutron irradiation, where V_2O production within the cluster appears to dominate at all fluences, independent of oxygen concentration [55].

Oxygen dimmers, O_{2i}, have also an important role in the change of the effective doping concentration of irradiated silicon substrates as they are assumed to form part of the shallow bi-stable donor, BD[3], and therefore in the generation of positive space charge after charged hadron irradiation. The relative concentration of O_{2i} in different substrate wafers can be determined by DLTS[4] through the measurements of the introduction rates of the O_{2i} related defect IO_{2i} [56, 57].

3.1.3 Different substrate wafers

The CERN RD48 (ROSE) collaboration [2] had the objective of studying and developing new silicon materials in order to obtain radiation detectors that could operate under high radiation fluences. One of the conclusions of this collaboration led to the beneficial role of oxygen enrichment of silicon to improve the radiation tolerance of detectors. Different types of silicon wafers have been investigated for the fabrication of silicon detectors in the framework of CERN RD50 collaboration [58]. Standard Float Zone (STFZ) silicon shows best results due to its uniformity and higher resistivities for both n and p-type, but FZ n-type silicon wafers present space charge sign inversion (SCSI), whose oxygen concentration is lower than 10^{16} cm^{-3}, so the use of oxygenated materials is better. Diffusion Oxygenated Float Zone (DOFZ) wafers are obtained by a diffusion of oxygen from the Si/SiO_2 interface at high temperature (72h at 1150ºC), obtaining oxygen concentrations in the order of 10^{17} cm^{-3}.

Czochralski (Cz) and Magnetic Czochralski (MCz) silicon are materials which contain a variable amount of oxygen concentration as they are produced in quartz (SiO_2) crucibles into the silicon melt, achieving homogeneous oxygen concentrations ranging from 4 to 10×10^{17} cm^{-3} depending on the specific Cz or MCz growth technique.

Thin epitaxial silicon wafers (EPI) are grown on Cz silicon and therefore they own a high concentration of oxygen by out-diffusion. EPI-DO are also fabricated by an additional diffusion step (24h at 1100ºC) obtaining a high and homogeneous oxygen concentration, similar to Cz and MCz. The drawbacks are their higher capacitances and their smaller initial signal which involves additional requirements on the electronics.

[3] BD: Bi-stable donor BD is a linear dose dependent defect, related to the concentration of oxygen dimmers in silicon that is found in two configurations: BD_A $^{(0/++)}$ and $BD_B$$^{(+/++)}$. The concentration of BD_B (50K) increases as the BD_A (98K) decreases while the diodes are stored in the dark at room temperature, however as the fluence is increased this storage is less necessary. In figure 3.13 are shown the peaks at 50K and 98K that correspond to BD_B and BD_A respectively.

[4] DLTS: Capacitance-Deep Level Transient Spectroscopy.

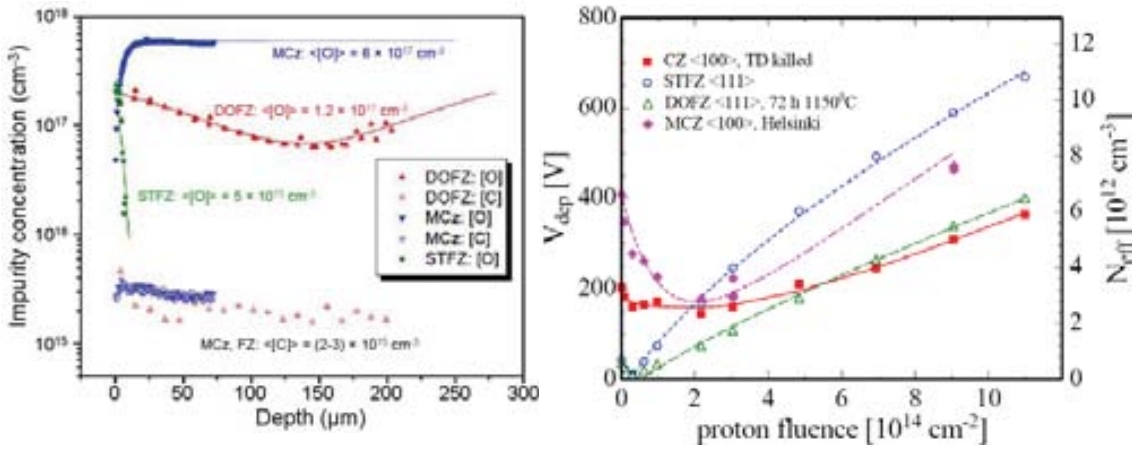

Figure 3.5: *Depth profiles of oxygen and carbon concentrations in MCz, DOFZ and FZ diodes [59] (left), and a comparison of their N_{eff} and depletion voltage evolution after irradiation with 23 GeV protons at CERN [60] (right).*

The concentration of oxygen dimmers, denoted $[O_{2i}]$, in silicon differs for each material, and although it is related to the concentration of oxygen [O] it does not imply necessary that a higher [O] involves a higher $[O_{2i}]$. In fact, although MCz and EPI-DO own the highest oxygen concentrations, the introduction rate of stable shallow donors is higher for both EPI-ST and EPI-DO substrates, probably by an out-diffusion of O_{2i} from the Cz substrate to the epitaxial silicon during the EPI layer formation.

Table 3.2: Typical values of oxygen concentration in different n-type silicon substrates [59].

	STFZ	**DOFZ**	**EPI-ST**	**EPI-DO**	**Cz**	**MCz**
Resistivity ρ (Ω·cm)	$1\text{-}7\times10^{3}$	$1\text{-}7\times10^{3}$	50-500	50-500	$\sim10^{3}$	$\sim10^{3}$
O concentration [O] (cm^{-3})	$< 10^{16}$	$1\text{-}3\times10^{17}$	$\sim10^{17}$	$4\text{-}10\times10^{17}$	$8\text{-}9\times10^{17}$	$4\text{-}9\times10^{17}$

3.1.4 P-type substrates

The combination of the donor removal process and the formation of defects that contribute with negative charge to the effective doping concentration N_{eff} of irradiated n-type silicon substrates may lead to the effective type inversion of the substrate turning into p-type. This is posing a problem since the *pn* junction is switching from the structured readout side to the back side of the detector accompanied by a loss in spatial resolution and, if not operated with voltages well above the depletion voltage, by a reduction of the charge collection efficiency (CCE) as holes have to move crossing an undepleted region with low electric field (see figure 3.6). This is the reason why the more expensive *n-on-n* technology is used for pixel detectors in harsh radiation environments. Hence, the development of *n-on-p* detectors which do not type invert as they are already p-type is a reasonable approach.

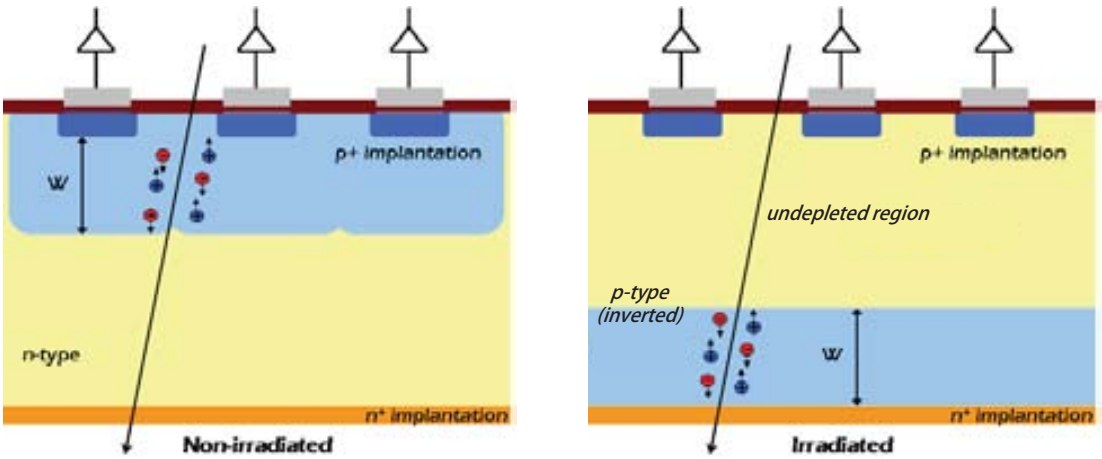

Figure 3.6: *Cross section of a reverse-biased p-in-n detector before (left) and after (right) irradiation.*

Microstrip detectors on p-type silicon present the advantage of collecting electrons in the amplifiers, which are faster than holes thanks to their higher mobility in silicon (see table 3.7), reducing the chance of being trapped. However they have the challenge of achieving a proper interstrip insulation, given that positive charges are always present at the silicon/oxide interface, an inversion layer of electrons attracted from the bulk is formed below the oxide leading to a decrease of the interstrip resistance and the short-circuit of the n^+ electrodes. This effect is more severe after irradiation as the positive charge is increased. Different solutions for the insulation of n^+ electrodes have been developed [31][61].

p-stop insulation

P-stop insulation consists on a p-type implantation surrounding n^+ electrodes. These p-stop implantations interrupt the electron inversion layer and provide a complete insulation, but has the inconvenient of an extra photolithographic step compared to standard *p-on-n* detectors, increasing costs. Besides, microdischarges appear in the leakage current and in the electronic noise, which are produced by the intense electric fields that take place at the edges of p-stops when a sufficiently high bias voltage is applied.

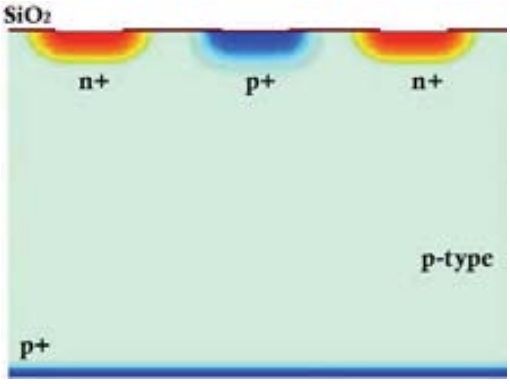

Figure 3.7: *P-stop method for the insulation for n^+ implantations.*

p-spray insulation

This method is simpler to fabricate than p-stop and consists of a uniform p-type implantation on the whole wafer before the fabrication steps for balancing the electronic inversion layer. Various studies have demonstrated that irradiated detectors treated with p-spray present better behavior than p-stop detectors [31][62-64], which can suffer from early breakdowns or microdischarges. However, for having a correct insulation and prevent from a low breakdown voltage the implantation profile needs to be calibrated carefully.

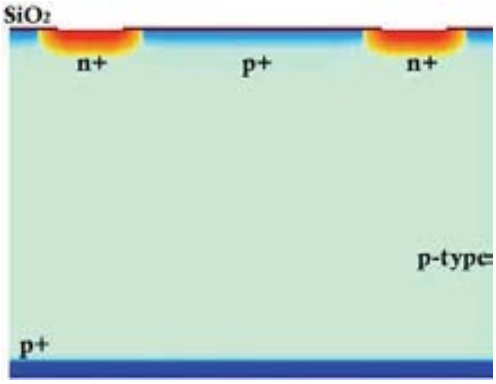

Figure 3.8: *P-spray method for the insulation for n^+ implantations.*

Moderated p-spray

Both p-stop and p-spray insulation methods present the challenge of balancing the implant doping concentration for being high enough for ensuring a proper insulation without reaching low breakdown voltages because of the high electric fields. Moderated p-spray is a combination of both p-stop and p-spray insulations. Here the p-stop insulation guarantees the insulation of strips while p-spray, which prevents from microdischarges, consists of a thin p^+ diffusion layer that favors a low breakdown voltage [31].

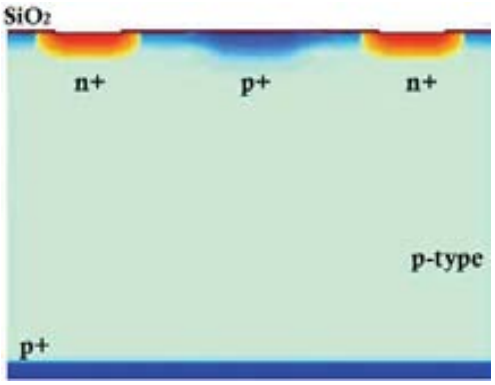

Figure 3.9: *Moderated p-spray method for the insulation for n^+ implantations.*

Compared to n-type detectors, studies on irradiated detectors fabricated in p-type silicon [65-67] gave evidence of a sensitive improvement in the charge collection efficiency performances.

3.1.5 Changes in the operation of silicon detectors

Radiation induced defects alter the electric properties of the sensors which have an influence on leakage current, depletion voltage and charge collection efficiency. The trapping/detrapping of charge carriers by the defects within the bandgap is described by the emission rates of carriers to the conduction and valence bands. According to the statistics of Shockley-Read-Hall, the emission of trapped charge carriers is given by:

$$e_n(T) = c_n(T) N_C e^{\frac{E_t - E_C}{k_B T}} \quad \textbf{[119]}$$

$$e_p(T) = c_p(T) N_V e^{-\frac{E_t - E_V}{k_B T}} \quad \textbf{[120]}$$

where $c_{n,p}(T) = \sigma_{n,p}(T) v_{n,p}^{th}$ is the capture coefficient for electrons/holes, $\sigma_{n,p}$ is the electron/hole capture cross-section, $v_{n,p}^{th}$ is the average thermal velocity of electrons/holes, $N_{C,V}$ is the effective density of states in the conduction/valence band, $E_{C,V}$ is the band level energy, and E_t is the energy level of the trap.

The contribution of traps in the space charge region to the effective doping concentration N_{eff} is given by the summing of all of the donors traps occupied by holes and all of the acceptor traps occupied by electrons:

$$N_{eff} = \sum n_t^{donor} + \sum n_t^{acceptor} \quad \textbf{[121]}$$

where the steady-state occupancies of defects n_t are given by

$$n_t^{donor}(T) = Nt \frac{c_p(T) p + e_n(T)}{e_n(T) + e_p(T) + c_n(T) n + c_p(T) p} \quad \textbf{[122]}$$

$$n_t^{acceptor}(T) = Nt \frac{c_n(T) n + e_p(T)}{e_n(T) + e_p(T) + c_n(T) n + c_p(T) p} \quad \textbf{[123]}$$

where N_t is the defect concentration. The concentrations of free charge carriers n and p are very small in the space charge region and therefore can be neglected in diodes with low reverse currents.

According to the characteristics of the traps such as energy level, concentration and emission/capture cross-sections, it results in the fact that not all of the defects contribute to the macroscopic electrical behavior of the silicon detectors.

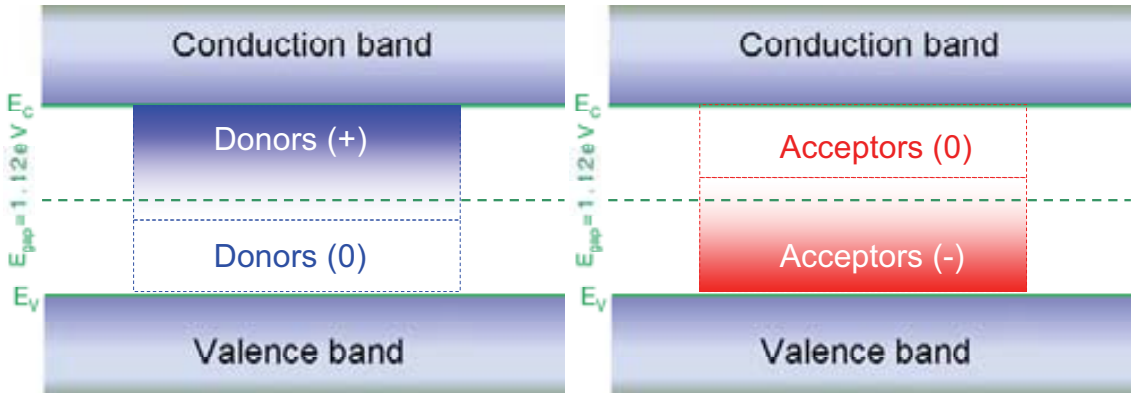

Figure 3.10: *Contributions to N_{eff} at room temperature of donors (left) and acceptors (right) traps according to their energy level within the bandgap. Donors occupied by a hole (electron) are positive (neutral) whereas acceptors occupied by an electron (hole) are negative (neutral).*

Donors (+/**0**) in the upper part of the bandgap are occupied by a hole, contributing with positive charge to N_{eff} at room temperature. They are traps for electrons and show the Poole-Frenkel effect[5] [68]. However, donor traps in the lower part are occupied by an electron (neutral) acting as traps for holes and they only contribute to N_{eff} at room temperature if they are close to the midgap. In the other hand, acceptors (**–/0**) in the lower part of the bandgap are occupied by an electron contributing with negative charge to N_{eff}. They are traps for holes and show the Poole-Frenkel effect, whereas those in the upper part are occupied by a hole (neutral) and act as traps for electrons and do not contribute to N_{eff} unless they are close to the midgap. A schematic summary is shown on figure 3.11.

The contribution of the radiation induced defects after severe radiation damage to the leakage current is given by equation **81'**, where the electron/hole pairs generation G_t is determined by the electron and hole emission coefficients, e_n and e_p respectively:

$$I_{dep}(T) = q \cdot w \cdot A \cdot G_t = q \cdot w \cdot A\left(\sum e_n(T) n_t^{donor}(T) + \sum e_p(T) n_t^{acceptor}(T)\right) \qquad \textbf{[81']}$$

The introduction of energy levels in the silicon band-gap due to the creation of trapping centers by the radiation favors the reduction of the electrons and holes trapping times. The trapping rate depends on the number of trapping centers N_i (impurities, lattice defects) and therefore depends on the radiation fluence. The trapping probability for charge carriers can be expressed as

$$\frac{1}{\tau_{eff}} = \sum_i N_i (1 - P_i) \sigma_i v_{th} \qquad \textbf{[124]}$$

where P_i is the trap occupation probability (0 or 1) and σ_i is the charge carrier trapping cross section.

[5] *Poole-Frenkel effect*: It consists of the thermal ionization -or detrapping- of electrons (holes) from their trap potential well into the conduction (valence) band by the lowering of the coulombian potential barrier assisted by high electric fields. This effect enhances a certain electric field dependence of the emission rates of charge carriers.

In table 3.3 is presented a list of impurities and radiation induced defects in silicon, including their type, their energy level within the silicon bandgap and their contribution to the effective doping concentration at room temperature.

Table 3.3: Impurities and radiation induced defects in silicon [24][57, 59, 69-73].

Defect	Form	Type	Energy level (eV)	Contribution to N_{eff} at RT[6]	Comments
Boron	$B_s^{(-/0)}$	Acceptor	$E_V + 0.045$	–	Impurity substitute
	$B_i^{(-/0)}$	Acceptor	$E_C – 0.45$	–	Impurity interstitial
	$B_i^{(0/+)}$	Donor	$E_C – 0.12$	+	Impurity interstitial
Phosphorus	$P_s^{(0/+)}$	Donor	$E_C – 0.045$	+	Impurity substitute
Interstitial	$I^{(-/0)}$	Acceptor	$E_V + 0.39$	–	Silicon interstitial
	$I^{(0/+)}$	Donor	$E_C – 0.40$	+	Silicon interstitial
Vacancy	$V^{(--/-)}$	Acceptor	$E_C – 0.09$	0	
	$V^{(-/0)}$	Acceptor	$E_C – 0.40$	–	
	$V^{(0/+)}$	Donor	$E_V + 0.05$	0	
	$V^{(+/++)}$	Donor	$E_V + 0.13$	0	
Di-vacancy	$V_2^{(--/-)}$	Acceptor	$E_C - 0.23$	0	
	$V_2^{(-/0)}$	Acceptor	$E_C – 0.42$	–	
	$V_2^{(0/+)}$	Donor	$E_V + 0.21$	0	
VB	$VB^{(0/+)}$	Donor	$E_V + 0.45$	+	
VP	$VP^{(-/0)}$	Acceptor	$E_C – 0.44$	–	P donors removal
VO	$VO^{(-/0)}$	Acceptor	$E_C – 0.18$	0	
Carbon	$C_i^{(-/0)}$	Acceptor	$E_C – 0.12$	0	Impurity interstitial
	$C_i^{(0/+)}$	Donor	$E_V + 0.28$	0	Impurity interstitial
C_iC_s	$C_iC_s^{(-/0)}$	Acceptor	$E_C – 0.17$	0	
	$C_iC_s^{(0/+)}$	Donor	$E_V + 0.084$	0	
C_iO_i	$C_iO_i^{(0/+)}$	Donor	$E_V + 0.36$	0	
E(30K)	$E(30K)^{(0/+)}$	Donor	$E_C – 0.1$	+	I_3 ?
TDD2	$TDD^{(0/+)}$	Donor	$E_C – 0.07$	+	Thermal double donor state
	$TDD^{(+/++)}$	Donor	$E_C – 0.15$	+	Thermal double donor state
	$TDD^{(0/++)}$	Donor	$E_C – 0.22$	+	Thermal double donor state
BD	$BD(98K)^{(+/++)}$	Donor	$E_C – 0.15$	+	Bi-stable donor, related to $[O_{2i}]$
	$BD(50K)^{(0/++)}$	Donor	$E_C – 0.225$	+	Bi-stable donor, related to $[O_{2i}]$
Ip	$Ip^{(-/0)}$	Acceptor	$E_C – 0.545$	–	V_2O ?
	$Ip^{(0/+)}$	Donor	$E_V + 0.23$	0	
X	$X^{(-/0)}$	Acceptor	$E_C – 0.46$	–	Vacancy-related defect
	$X^{(--/-)}$	Acceptor	$E_C – 0.20$	0	
H(116K)	$H(116K)^{(-/0)}$	Acceptor	$E_V + 0.33$	–	Cluster
H(140K)	$H(140K)^{(-/0)}$	Acceptor	$E_V + 0.36$	–	Cluster
H(152K)	$H(152K)^{(-/0)}$	Acceptor	$E_V + 0.42$	–	Cluster
E4	E4	Acceptor	Ec – 0.36	0	Vacancy-related defect, $V_3^{(--/-)}$ $V_2^{(-/0)}$?
E5	E5	Acceptor	Ec – 0.46	–	Vacancy-related defect, $V_3^{(-/0)}$?
E205a	E205a	Acceptor	-		Vacancy-related defect
IO_{2i}	$IO_{2i}^{(-/0)}$	Acceptor	$E_C – 0.11$	0	
Tri-vacancy	$V_3^{(--/-)}$	Acceptor	Ec – 0.359	0	
	$V_3^{(-/0)}$	Acceptor	Ec – 0.458	–	
	$V_3^{(0/+)}$	Donor	$E_V + 0.19$	0	
	$V_3^{(+/++)}$	Donor	$E_V + 0.105$	0	
V_3O	$V_3O^{(--/-)}$	Acceptor	Ec – 0.337	0	
	$V_3O^{(-/0)}$	Acceptor	Ec – 0.455	–	
	$V_3O^{(0/+)}$	Donor	$E_V + 0.235$	0	
	$V_3O^{(+/++)}$	Donor	$E_V + 0.12$	0	

[6] RT: Room temperature, 293K.

Effective doping concentration

It is found that FZ n-type silicon detectors become progressively less n-type with increasing hadron fluence. This is due to a constant removal of donors ($V + P_s \rightarrow VP$) and the introduction of acceptor traps until they invert to effectively p-type and then continue becoming more p-type. The fluence at which this space charge sign inversion (SCSI) occurs is referred to as the *inversion fluence*. In the case of oxygen-rich materials there is no such inversion after charged hadron irradiation due to the introduction of positive charge (traps acting like donors), however neutron irradiations induce SCSI on n-type silicon materials introduction of negative charge (traps acting like acceptors). The exception is thin n-type EPI layers of low resistivity [74], as the acceptor introduction rate revealed being low for low resistivity materials [75].

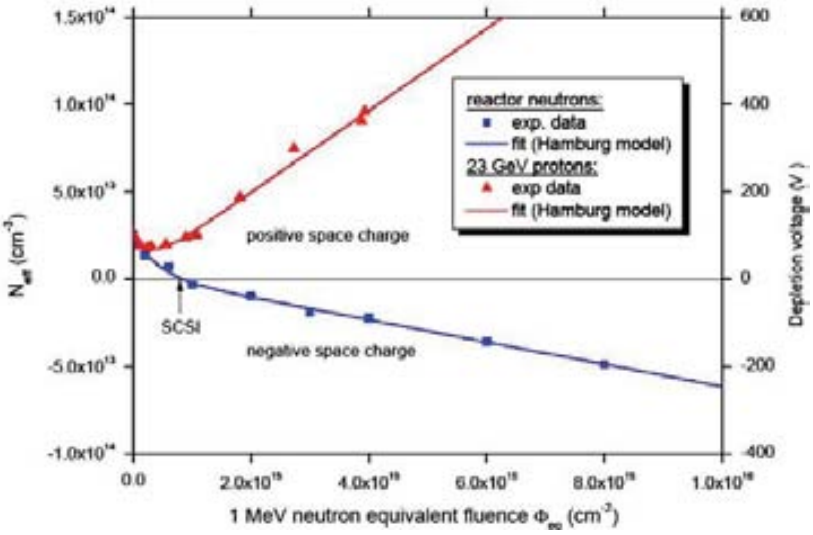

Figure 3.11: *Effective doping concentration of charge obtained from CV measurements of EPI-DO p-in-n diodes as a function of the fluence of reactor neutron and 23 GeV proton irradiations [52].*

In practice, the detectors still work beyond the inversion fluence because the junction moves from the p^+ side to the n^+ back plane contact, leading to high electric fields being located on the non-segmented side of the device. The depletion voltage required to operate a silicon detector is directly proportional to N_{eff} (see equation **74**, where the contribution of V_{bi} has been neglected), hence at high fluences N_{eff} can be such that the required voltage exceeds the breakdown voltage on the device and efficient operation is no longer possible.

Another process that can change the effective doping concentration is the annealing of the substrates. Annealing consists of the exposition to middle and high temperatures to induce the removal of radiation defects by recombination of vacancies and interstitials ($I + V \rightarrow Si$), but also take place the formation of other defects such us I_2, V_2O, V_3, C_iO_i, etc. Studies on time evolution of irradiated silicon detectors proceed using this *accelerated annealing* for later scaling to annealing times at room temperature (20ºC). This method is an approximation that may not always work successfully, as reported in [76] where more accurate results are obtained halving the annealing factors. Some annealing factors are listed in table 3.4.

Table 3.4: Conversion factors used in accelerated annealing.

Temperature	Factor
40ºC	30
60ºC	550
80ºC	7400

The evolution of the effective doping concentration after irradiation can be described by three terms according to *Hamburg model* [44]: the decay of effective acceptors immediately after irradiation N_a (*short-term* or *beneficial annealing*), the stable part N_c (*plateau*) and the creation of effective acceptors at late annealing stages N_y (*long-term* or *reverse annealing*). A graph of this behavior is shown in figure 3.12

According to the *Hamburg model* the evolution of the N_{eff} after irradiation is described by

$$\Delta N_{eff} = N_{eff,0} - N_{eff} = N_a(\Phi,t) + N_c(\Phi) + N_y(\Phi,t) \qquad \textbf{[125]}$$

where $N_{eff,0}$ is the initial effective doping concentration. This model works very well for FZ detectors but only a qualitative evolution of V_{FD} can be obtained for oxygen-rich materials.

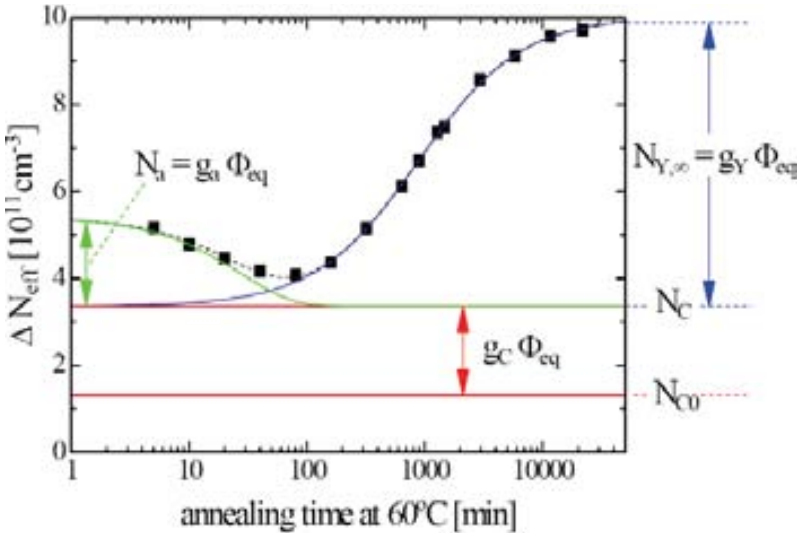

Figure 3.12: *Time evolution of the N_{eff} under annealing at 60ºC [44, 77].*

Short- term annealing

The evolution of the full depletion voltage V_{FD} with the annealing time reveals a decrement of its value for type inverted substrates, meanwhile for non-inverted substrates it is increasing. The explanation of this behavior is given by the introduction of thermal donors *BD* and *E(30K)* which contribute with positive charge to N_{eff}. *E(30K)* defect is produced during the first 20 minutes at 80ºC and its introduction rate is much higher after proton irradiation than neutron [59]. The introduction rate of the bi-stable shallow donor *BD* depends strongly on the material type, as their production is related

to the concentration of oxygen dimmers O_{2i}. Its introduction rate is also higher after proton irradiation than for neutrons.

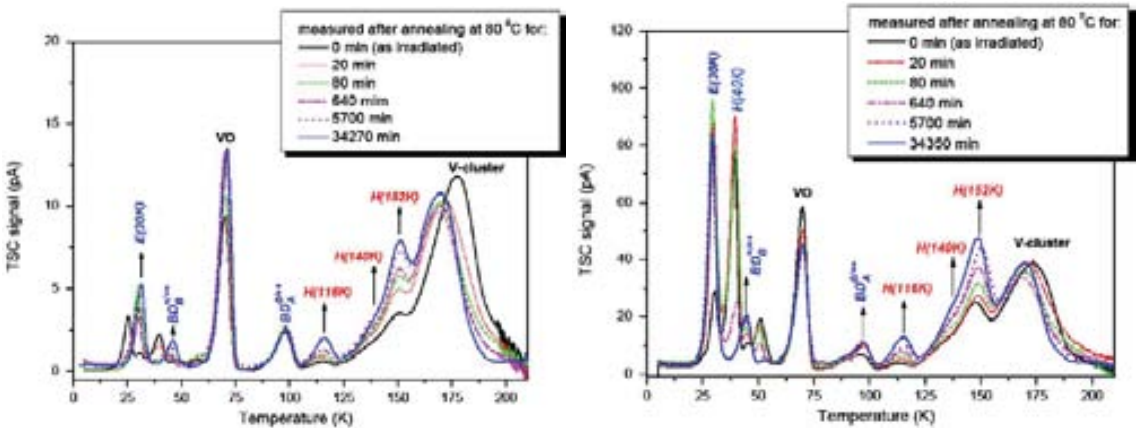

Figure 3.13: *TSC spectra measured on p-in-n EPI-DO silicon diodes after neutron (left) and proton irradiations (right) for different annealing times at 80ºC [51].*

Approaching this behavior by a sum of exponential, and considering only the longest decay time constant, it is obtained:

$$N_a(\phi_{eq},t) = g_a \phi_{eq} e^{-\frac{t}{\tau_a}} \qquad \textbf{[126]}$$

where the value of the introduction rate of defects for the short term annealing is

$$g_a = (1.81 \pm 0.14) \times 10^{-2}\, cm^{-1}$$

Stable damage

The radiation damage induces defects in the detector which changes its effective doping concentration. Those defects that are not affected by annealing are named *stable damage*, which are responsible of the stable part in figure 3.12. This stable part consists of an incomplete donor/acceptor[7] removal in addition to a fluence proportional introduction of stable acceptors

$$N_C(\phi_{eq}) = N_{C,O}(1 - e^{-c\phi_{eq}}) + g_c \phi_{eq} \qquad \textbf{[127]}$$

where c is the donor removal constant, $N_{C,O}$ is the initial concentration of donor removal [VP] that depends strongly on the oxygen concentration, given that a high oxygen concentration will suppress the donor removal rate since most of the vacancies and carbon interstitials will recombine with oxygen instead of Phosphorous. Finally g_c is the introduction rate of stable acceptors whose average value is

$$g_c = (1.49 \pm 0.04) \times 10^{-2}\, cm^{-1}$$

[7] For p-type silicon, the acceptor removal reaction is: $I + B_s \rightarrow B_i$

Long-term annealing

After a long time annealing, the space charge is becoming more negative, as deep acceptors *Ip*, *H(116K)*, *H(140K)*, *H(152K),…* are being introduced increasing the space charge concentration. This introduction of negative charge is not dependent on the silicon type neither the substrate material.

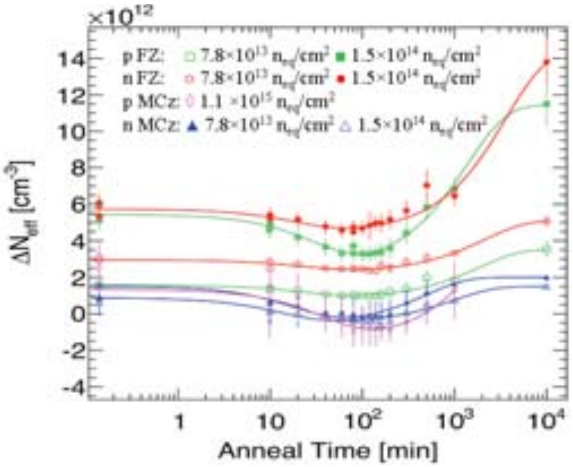

Figure 3.14: *Evolution of effective doping concentration with the accelerated annealing at 60ºC of different silicon substrates after 800 MeV proton irradiations [78].*

A second order expression is used to parameterize the evolution of the defect concentration $N_Y(t)$

$$N_Y(\phi_{eq},t) = N_{Y,1}\left(1-e^{-t/\tau_Y}\right)+N_{Y,2}(\phi_{eq},t) \qquad \textbf{[128]}$$

where $N_{Y,\infty}$ is the reverse annealing amplitude assuming 1st order dynamics, expressed as $N_{Y,1} = g_y \cdot \Phi_{eq}$, and τ_Y is the reverse annealing time constant. $N_{Y,2}$ is a second order kinetics component recently found in annealing studies of EPI and MCz detectors [79, 80]. The average value of the introduction rate of long term acceptor is

$$g_Y = (5.16 \pm 0.09) \times 10^{-2}\, cm^{-1}$$

Leakage current

The defects produced by the radiation that create mid-gap energy levels, such us *E4*, *E5*, *E205a*, *Ip*, act like generation/recombination centers which increase the dark currents. *Leakage current damage rate* α(t), defined as seen in equation **129**, which is confirmed to be independent on material and irradiation particles [81], presents a linear dependence with the fluence.

$$\alpha = \frac{\Delta I}{V \cdot \phi_{eq}} \qquad \textbf{[129]}$$

and its evolution with annealing is

$$\alpha(t) = \alpha_0 + \alpha_I e^{-\frac{t}{\tau_I}} - \beta \ln \frac{t}{t_0} \qquad [130]$$

where ΔI is the change in leakage current after irradiation, V the detector volume, Φ_{eq} is the neutron equivalent fluence, $\alpha_I \sim 1.25\times10^{-17}$ A/cm, $\beta \sim 3\times10^{-18}$ A/cm and $t_0 = 1$ min. τ_I depends on the annealing temperature and some common values can be found in table 3.5.

Table 3.5: *Some values of α parameter and time constant τ_I for the current annealing for different temperatures [44].*

Annealing temperature (ºC)	21	40	60	80
α_0 in 10^{-17} A/cm	7	6	5	4
τ_I in min	140000	260	94	9

The average value of the leakage current rate α(t) after an annealing of 80 minutes at 60ºC is 3.99×10^{-17} A/cm. Unlike the effect of the annealing depends on the depletion voltage, which raises after some time - *reverse annealing* - , the effect of the annealing on the current always makes decrease the leakage current [78, 82].

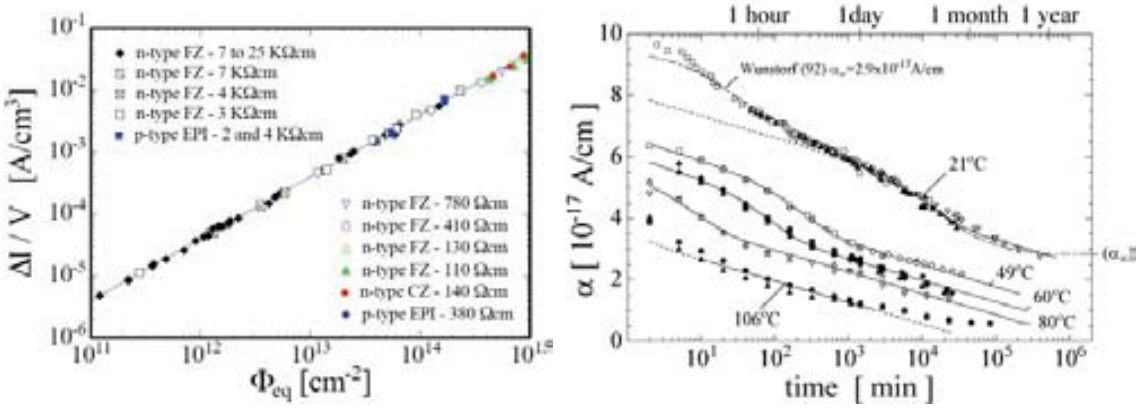

Figure 3.15: *Material independence of current related damage α (top) and also as a function of accumulated annealing time at different temperatures (bottom) [45].*

Charge collection efficiency

Since the trapping times have been experimentally demonstrated to have a linear behavior with the fluence [77], we can write

$$\frac{1}{\tau_{eff,e,h}} = \beta_{e,h}\Phi_{eq} \qquad [131]$$

$$\beta_{e,h} = \sum_{traps} \eta\sigma_{e,h}v_{e,h}^{th} \qquad [132]$$

where β_e and β_h are the electron and hole trapping constants respectively, η is the traps introduction rate. Given the fact that electrons mobility in silicon is several orders of magnitude greater than for holes, electron collection will be less affected by trapping

and therefore n^+ readout electrodes will produce a greater contribution to the total current.

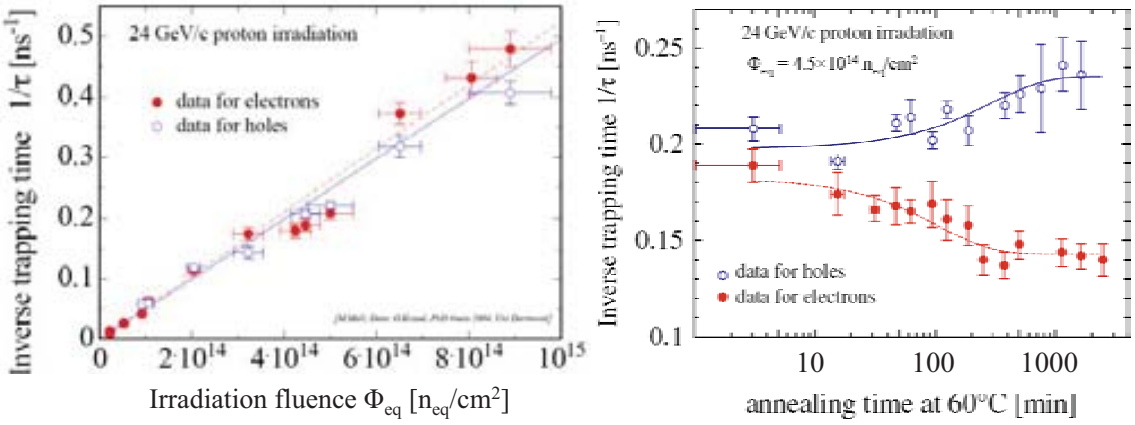

Figure 3.16: *Trapping time dependence with fluence (left) and annealing time (right) [83].*

For 10^{15} n/cm^2 neutron equivalent fluences and higher the trapping becomes the most limiting factor of the use of silicon as sensor material for detectors, which leads to an important degradation of the charge collection efficiency CCE, expressed by

$$Q(t) = Q_0 e^{-\frac{t}{\tau_{eff}}} \qquad \textbf{[133]}$$

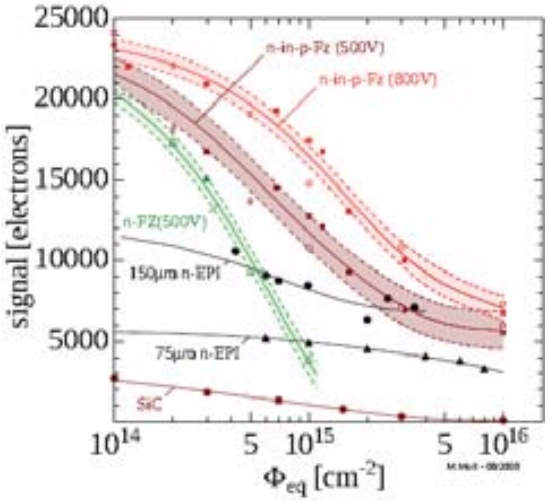

Figure 3.17: *Comparative graph showing the signal collected for different silicon detectors as a function of the radiation fluence [84-86].*

Trapping times, and therefore CCE, are also affected by annealing but showing different behaviors for electrons and holes. Experimental measurements reveal a decreasing trapping probability for electrons meanwhile for holes is increased [83], as shown in figure 3.16. Consequently, the use of p-type materials is more adequate as they have electrons readout and therefore they present higher charge collection [67]. Besides, an interesting behaviour is found in FZ p-type detectors which show charge multiplication effect after either proton or neutron high radiation fluences (> 10^{15} n_{eq}/cm^2) in long-term annealing stages [67, 82, 87]. This occurs due to the increasing of negative space charge concentration previously described for the long-term annealing

which hence increases the electric field in the n^+p junction allowing the charge multiplication. Otherwise, silicon substrates with higher oxygen concentration such as MCz present small influence of annealing in the charge collection [67, 82].

Studies of $\beta_{e,h}$ as a function of irradiation particle type, silicon material, temperature and its time dependence after irradiation can be found in [58, 88, 89]. The results evidenced that the effective trapping time constants do not depend on resistivity, oxygen and carbon concentrations, n- or p-type silicon or silicon material.

Table 3.6: Effective trapping time constants for electrons and holes in silicon after neutrons and fast charged hadrons irradiations, T = -10ºC.

	β_e [10^{-16} cm^2/ns]	β_h [10^{-16} cm^2/ns]
Reactor neutrons	3.5 ± 0.6	4.7 ± 1
Fast charged hadrons	5.3 ± 0.5	6.6 ± 1

The effective trapping probability depends on the temperature and is expressed through the temperature dependence of the trapping constants

$$\beta_{e,h}(T) = \beta_{e,h}(T_0)\left(\frac{T}{T_0}\right)^{\kappa_{e,h}} \qquad \textbf{[134]}$$

where T_0 is a reference temperature, and the values of the exponents are $\kappa_e = -0.86 \pm 0.06$ for electrons and $\kappa_h = -1.52 \pm 0.07$ for holes. The effective drift length of the charge carriers can be calculated from the effective trapping times by using the expression

$$L_{drift} = \tau_{eff} v_{drift} \qquad \textbf{[135]}$$

The values of the constants $\beta_{e,h}$ are lower for electrons than for holes and therefore the drift distances of electrons are longer than for holes. Examples of drift distances using the equation **135** for charge carriers moving at saturation velocity, 10^7 cm/s, for two representative fluences are:

$$\tau_{eff}(10^{15} n_{eq}/cm^2) = 2ns \qquad L_{drift} = v_{sat}\tau_{eff} = 10^7 cm/s \times 2ns = 200\mu m$$

$$\tau_{eff}(10^{16} n_{eq}/cm^2) = 0.2ns \qquad L_{drift} = v_{sat}\tau_{eff} = 10^7 cm/s \times 0.2ns = 20\mu m$$

3.2 Surface damage due to Ionizing Energy Loss (IEL)

Radiation damage on the surface of the detectors differs from bulk given the fact that bulk has a crystal structure and the surface region is composed by oxide (SiO_2) and the interface silicon/oxide, which are highly irregular, so the additional damage to the material structure caused by the interaction of radiation with the nuclei can therefore be safely ignored. However, the number of electron/hole pairs generated by ionizing radiation is indeed important and they increase the surface charge at the interface.

Table 3.7: *Values of some parameters for silicon and SiO_2 at 300K.*

Parameter	Si	SiO_2
E_g (eV)	1.124	8 – 9
μ_e (cm^2/Vs)	1417	20
μ_h (cm^2/Vs)	471	$\sim 10^{-8}$

Oxides can be modeled as high density volumes of charge states that can be changed by capturing electrons or holes. Because of the high value of the energy gap of the oxide, see table 3.67, it is almost impossible that electrons (holes) generated in deep levels by irradiation could reach the conduction (valence) band and, as result, trapped charges in the oxides are obtained.

Most of trapped charge in the oxide is positive. This is because of the difference between electron and hole mobilities, which makes holes stay longer times in the oxide and consequently the charge states will usually capture holes turning positive. These semi-permanent trapped holes are located mainly in the Si/SiO_2 interface, in which the density of defects (dangling bonds) is higher, and increase the positive fixed charge in oxide, producing a shift in the flat-band voltage expressed by

$$\Delta V_{flat} = -\frac{1}{\varepsilon_{ox}}\left(\sigma_{\text{int}} d_{ox} + \int_0^{d_{ox}} \rho(x) x dx\right) \qquad \textbf{[136]}$$

where d_{ox} is the oxide thickness, σ_{int} is the surface charge in the Si/SiO_2 interface and $\rho(x)$ is the additional charge density inside the oxide volume.

The positive charge in the oxide reaches a saturation value, it is explained by the number of semi-permanent traps in the oxide which is limited, and if all of them are filled, no further increase of the charge is possible. The value of $Q_{ox,sat}$ depends on the type or particle, energy, total absorbed dose, electric field during irradiation and the oxide properties, and usually its value is 1-3 × 10^{12} cm^{-2} [90], that can be calculated from the following expression

$$Q_{ox,sat} = Q_{ox,0} + C_{ox}\frac{\Delta V_{flat}}{q} \qquad \textbf{[137]}$$

where $C_{ox} = \varepsilon_{ox} / t_{ox}$ is the oxide capacitance per unit area, q is the electron charge and t_{ox} is the oxide thickness.

This charge accumulation in the oxide and the Si/SiO_2 interface affects the interstrip capacitance, introducing a noise factor, and in *n-on-p* and *n-on-n* strips detectors this positive charge produces an accumulation of electron from bulk forming an inversion layer, which leads to a decrease of the interstrip resistance and may short-circuit the strips.

Another factor to take into account is the annealing. Time evolution measurements of irradiated silicon samples reveal that degradation in oxide is not stable and it is possible to get back to the initial state. That means that charge distribution in the oxide depends on time through the time dependence of the electric field, which is in last

instance who rules the charge movement. This process also depends strongly on temperature, allowing the recovering process be carried out from milliseconds to years [91].

The passivation of p-type silicon substrates using aluminium oxide (alumina) instead of silicon oxide is presently under study, as well as the radiation effects, since the Si/Al_2O_3 interface has negative surface charge, thus forming a hole channel instead of an electron channel.

3.3 Radiation damage models

A modified version of the Perugia traps model [92] carried out in collaboration with the University of Glasgow [93] has been implemented in the simulations of this work to model the radiation damage in silicon detectors.

Perugia traps model

Perugia traps model adopted a simplified approach in which only a reduced set of dominant defects had been considered. For n-type silicon, this reduced set consisted of three levels composed by two acceptor levels, corresponding to di-vacancies $V_2^{(-/0)}$ and the $V_2O^{(-/0)}$ complex, which is supposed to be the main responsible of the space charge sign inversion. Both defects contribute with negative charge to the effective doping concentration at room temperature. The third defect is one donor level, corresponding to $C_iO_i^{(+/0)}$ which does not contribute to N_{eff} at room temperature, as shown in table 3.3, and its contribution to the leakage current is negligible, however its introduction in the traps model allowed to fit the experimental data of charge collection efficiency [92].

Table 3.8: *Traps parameters in the physics section for n-type silicon of the Perugia traps model [92].*

Type	Energy (eV)	Trap	σ_e (cm^2)	σ_h (cm^2)	η (cm^{-1})
Acceptor	$E_C - 0.42$	$V_2^{(-/0)}$	2.2×10^{-15}	1.2×10^{-14}	13
Acceptor	$E_C - 0.50$[8]	$V_2O^{(-/0)}$	5.0×10^{-15}	3.5×10^{-14}	0.08
Donor	$E_V + 0.36$	$C_iO_i^{(0/+)}$	2.0×10^{-18}	2.5×10^{-15}	1.1

In the other hand, for p-type silicon the model adopts the same levels than in n-type silicon but without considering the di-vacancy related defect V_2O, just the tri-vacancy V_3.

Table 3.9: *Traps parameters in the physics section for p-type silicon of the Perugia traps model [92].*

Type	Energy (eV)	Trap	σ_e (cm^2)	σ_h (cm^2)	η (cm^{-1})
Acceptor	$E_C - 0.42$	$V_2^{(-/0)}$	2.0×10^{-15}	2.0×10^{-14}	1.613
Acceptor	$E_C - 0.46$	$V_3^{(-/0)}$	5.0×10^{-15}	5.0×10^{-14}	0.9
Donor	$E_V + 0.36$	$C_iO_i^{(0/+)}$	2.5×10^{-14}	2.5×10^{-15}	0.9

[8] The energy level of the V_2O defect of the model is slightly different from the experimental values as it is an average value of 2 acceptor defects that were suggested to be related with it. V_2O at $E_C - 0.545$ eV and $\Gamma - (V_2O - V_3)$ at $E_C - 0.46$ eV. For more information see Ref [83].

The election of these energy levels in the Perugia traps model for n-type silicon, see table 3.8, is owing to the reported energy levels commonly related to di-vacancies defects. The energy range of the traps measured experimentally is *Ec*-0.42 eV to *Ec*-0.55 eV [94] and the best results in simulations were obtained using the energy levels of table 3.8.

Modified traps model

The simulated leakage current curves using the Perugia trap model agree with the experimental measurements, also the estimated radiation damage constant α is in agreement with the experimental values, whose average value is 3.99×10^{-17} A/cm [45]; the depletion voltages match to experimental results [95], CCE curves are also well reproduced. However, trapping times do not match experimental results of table 3.6. This is the reason of a modified version of the traps model [93] carried out in collaboration with the University of Glasgow. These modifications were performed altering the cross-sections to reach accurate values for carrier trapping while keeping σ_h/σ_e constant for not to alter the space charge of equation **138**,

$$\frac{1}{\tau_{e,h}} = \beta_{e,h}\Phi_{eq} = \nu_{th}^{e,h}\sigma_{e,h}\Phi_{eq}\eta$$

$$n_{e,trap} = N_{trap} f_n \approx N_{trap} e^{-\frac{E}{kT}}\left(\frac{n}{n_i} + \frac{\sigma_h \nu_{th}^h}{\sigma_e \nu_{th}^e} e^{-\frac{E_t}{kT}}\right) \qquad \textbf{[138]}$$

where the effective trapping probability ($1/\tau_{e,h}$) increases linearly with the fluence (Φ_{eq}), the slope is denoted β, which is given by the thermal velocity of drifting carriers, v_{th}, the carrier capture cross section, $\sigma_{e,h}$, and the introduction rate of defects, η. The simulated results match experimental data up to 10^{14} n_{eq}/cm^2 for n-type substrates and up to 2×10^{16} n_{eq}/cm^2 in the case of p-type substrates, and trapping times have intermediate values compared to measured trapping times after neutron and charged hadron irradiations of table 3.6. The parameters of this modified trap model are listed in tables 3.11 and 3.12.

Table 3.10: *Comparison of calculated β values using model and measured values for the β parameter [88].*

Calculated values from n-type old model	Calculated values from n-type new model
$\beta_e = 5.3\times10^{-16}$ cm^2/ns	$\beta_e = 4.0\times10^{-16}$ cm^2/ns
$\beta_h = 0.45\times10^{-16}$ cm^2/ns	$\beta_h = 5.3\times10^{-16}$ cm^2/ns

Table 3.11: *Modified traps model for n-type silicon [93].*

Type	Energy (eV)	Trap	σ_e (cm^2)	σ_h (cm^2)	η (cm^{-1})
Acceptor	$E_C - 0.42$	$V_2^{(-/0)}$	1.5×10^{-15}	0.9×10^{-14}	13
Acceptor	$E_C - 0.50$	$V_2O^{(-/0)}$	5.0×10^{-15}	3.5×10^{-14}	0.08
Donor	$E_V + 0.36$	$C_iO_i^{(0/+)}$	2.5×10^{-17}	3.1×10^{-15}	1.1

Table 3.12: *Modified traps model for p-type silicon [93].*

Type	Energy (eV)	Trap	σ_e (cm^2)	σ_h (cm^2)	η (cm^{-1})
Acceptor	$E_C - 0.42$	$V_2^{(-/0)}$	9.5×10^{-15}	9.5×10^{-14}	1.613
Acceptor	$E_C - 0.46$	$V_3^{(-/0)}$	5.0×10^{-15}	5.0×10^{-14}	0.9
Donor	$E_V + 0.36$	$C_iO_i^{(0/+)}$	3.23×10^{-13}	3.23×10^{-14}	0.9

Oxide surface charge

The effect of charge build up at the Si/SiO_2 interfaces after irradiation is implemented in the TCAD simulations by increasing the constant value of the oxide charge concentration. The surface charge concentration before irradiation is approximately in the range $10^{10} - 10^{12}$ cm^{-2}, depending on the silicon properties and the oxide growth method [24]. According to Ref [90], trapped charge in the oxide after irradiation reaches similar saturation values for < 1 0 0 > p-type wafers (FZ and MCz), resulting ~1.5×10^{12} cm^{-2}, and ~2×10^{12} cm^{-2} in the case of < 1 1 1 > FZ n-type as this orientation has more dangling bonds.

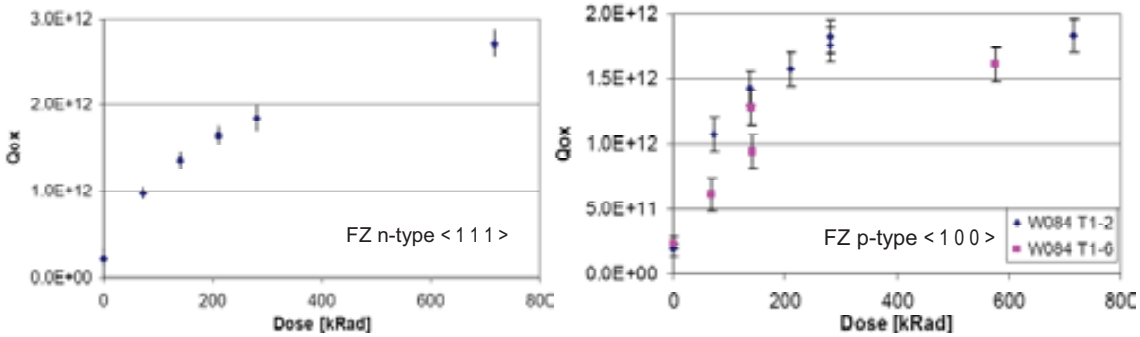

Figure 3.18: *Oxide charge Q_{ox} as a function of the total dose [90].*

Chapter 4

Slim and active edge detectors: simulation and fabrication

The standard termination of radiation detectors consists of guard rings structures which can extend more than 1 mm for high voltage applications. The purposes of those structures is to confine the space charge region within the active volume away from the detector rims where are found lattice defects produced by the saw cut during the dicing of the sensors. Lattice defects act as generation-combination centers leading to undesired high surface currents at the edge of the sensors. The width of the guard rings structure is therefore a dead region that surrounds the sensitive volume. In close-to-beam experiments such as the TOTEM experiment [5] that dead region is required to be highly reduced to allow the active area of detectors being placed as close as possible to the beam. Silicon radiation detectors with a current terminating structure that reduces the dead region to less than 50 μm, called *slim-edge* detectors, have been developed at CERN [11] for the TOTEM experiment offering an adequate performance. In this framework, the EU TOSTER project arose with the aim of studying the radiation tolerance of these detectors and the development of new techniques to improve their radiation hardness suitable for close-to-beam experiments in the future HL-LHC.

Additionally, silicon detectors with active edges [96] are being developed in collaboration with DIAMOND Synchrotron Light Source for X-ray beam positioning, X-ray sensors for beamstops and Medipix2 detectors for imaging. This new termination method does not require the inclusion of any guard ring or trench for confining the space charge region and the surrounding dead area is highly reduced to only a few micrometers.

4.1 Guard rings

Guard rings are metalized implants surrounding the detector to shape the electric field inside the sensitive area to minimize edge effects which lead to breakdown and guarantee a defined homogeneous potential in the sensor.

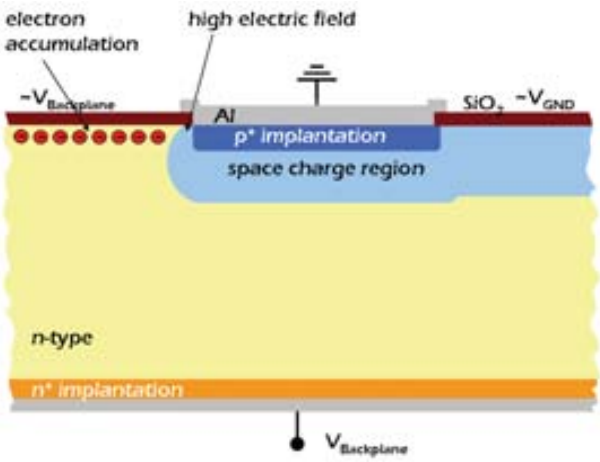

Figure 4.1: *Layout of a reverse biased p-in-n silicon diode presenting two extreme cases in the growth of the space charge region: severe potential drop at the end of the p^+ implantation, which leads to high electric fields and avalanche breakdown may occur (left-side), and an space charge region with extends to the cut rim, leading to large leakage currents coming from defects originated by the saw cut (right-side).*

As it was previously explained in Chapter 2, electrical breakdown takes place when the electrical field is high enough to initiate avalanche multiplication accelerating mobile charge carriers (electrons and holes) and producing electron/hole pairs in collisions with lattice atoms. In the case of silicon, the electric field at room temperature to start the charge multiplication is in the order of 10^5 V/cm. The mean free path of electrons in the range of 0.1 μm in silicon, although it is shorter in Si/SiO_2 interfaces due to a higher density of crystal defects. The breakdown avalanche is therefore achieved in those regions where there is a severe potential drop as occurs in the *pn* junctions formed at the edges of readout implantations. The maximum value of the electric field in the detector depends strongly on the geometric design, the operation voltage, and the defects in the crystal due to doping impurities or radiation induced defects.

In order to have a more detailed outlook, let's consider two extreme cases on the detector of figure 4.1. The layout corresponds to a simple diode, in which the reverse bias voltage is applied between the diode electrode and the backplane contact. In the first case there is a severe potential drop at the edge of the diode. In this configuration there is an electron accumulation layer present in the Si/SiO_2 interface while the bulk below the oxide remains undepleted. The voltage drop in the short region near the edge of the diode leads to a high electric field which could cause the avalanche breakdown of the detector.

In the second case, the interface Si/SiO_2 is charged up to the diode potential almost all the way to the cutting edge, then an inversion layer (positive, acting as the p^+ electrode) is formed under the oxide surface that will enlarge the space charge region up to the cutting edge. As the crystal is heavily damaged in the cutting edge due to the diamond saw dicing, a very large reverse-bias current is generated.

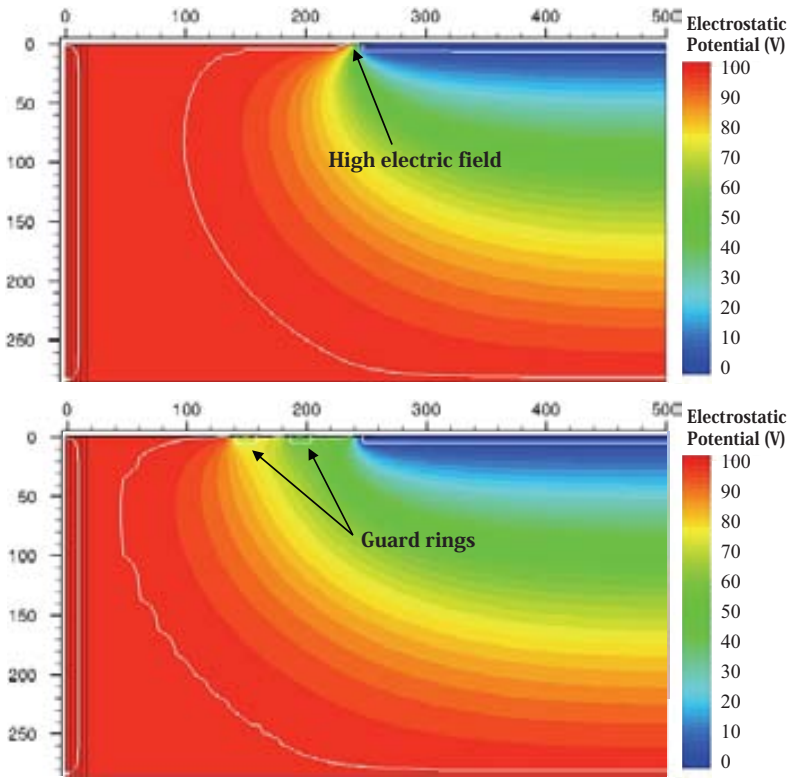

Figure 4.2: *(Top) Termination edges without guard rings lead to high electric fields in the region where the p^+ implantation meets the electron channel below the oxide; (down) however, a guard ring structure favours a gradual potential drop towards the edge. The white line corresponds to the space charge region contour.*

As a consequence, from the first case it has become clear that it is important a gentle voltage drop from the edge of the diode towards the cutting edge of the detector, and there are many ways to achieve this. The simplest case is by adding individual rings consisting of implantation and aluminum metallization, as shown in figure 4.2b. The biasing of the individual rings is achieved by punch-through[1]. An important aspect of the structure is the connection of the implant with the aluminum to define the oxide surface potential in the vicinity of the rings. Extending the aluminum contact to partially overlapping the gap between implants creates a field plate effect which extends the charge space region, thus reducing the electric field on the oxide surface. Adjusting the number of rings and the gap between them makes possible to achieve a gradual voltage drop from ring to ring, and thereby no early breakdown will occur [24].

4.2 Dicing methods

After processing the wafers in the Clean Room facilities it is necessary to separate the sensors with the less damage as possible in order to avoid altering their electrical behaviour. The common mechanism for dicing the devices is by using a diamond saw. Other methods are also possible such as laser scribing or using plasma etching process in the final steps during the fabrication which provides a less damaged cut profile, as shown in figure 4.3.

[1] See biasing voltage subdivision in Section 2.3.1.2.

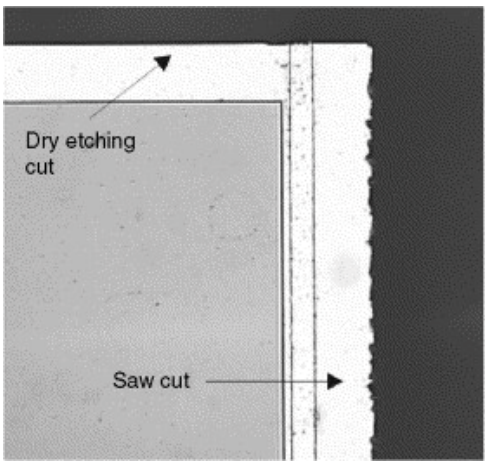

Figure 4.3: *Comparison of the edge profile due to dry etching cut (RIE) and standard diamond sawcut.*

4.2.1 Diamond saw

Dicing processed wafers using a diamond saw is the common method to separate the individual chips. This method does not require special conditions of environment temperature or pressure. Due to the mechanical friction of this method a pressure adjustable flow of deionized water is used to cool the spinning diamond disc. The velocity of the cut depends on the wafer material, thickness, etc. For a 300 μm thick silicon wafer the velocity of the cut is 10 mm/s at 32.000 rpm.

Figure 4.4: *Diamond saw used at the IMB-CNM (CSIC) facilities.*

This mechanical cut produces high density of lattice defects, dangling bonds and disordered regions in the cut surface of the material which act like generation/recombination centers. This leads to an undesired increment of the surface current.

4.2.2 Plasma etch

Plasma etch is a physical and chemical reaction between the material undergoing etching and a plasma of the appropriate gases. In plasmas used for RIE (reactive ion etching) process, free electrons are accelerated to collide with the neutral molecules of the reactive gases and remove an additional electron which can be used to ionize another molecule. The final desired plasma is a partially ionized gas ($n_{charged} << n_{neutral}$), non-equilibrium ($T_{electron} >> T_{gas}, T_{ion}$) and chemically reactive [97-99].

The gases are chosen for generating either volatile or easily dislodge products when the ions are being bombarded on the material desired to be etched. The technique to get High Aspect Ratio (HAR) silicon etch involves two alternating time-multiplexed process: etching and passivating steps. The patent was assigned to Robert Bosch GmbH in 1996, so it is known as the Bosch method. The main steps of this process are:

- Ionization of the reactive gas
- Energetic ion bombardment on the surface of material to be etch
- Adsorption[2] and chemisorption[3] of the ion on the surface
- Formation of the product molecule
- Desorption[4] of the product molecule
- Removal of that molecule from the reactor

The gas chosen for etching silicon is SF_6 for its rapidly etching of silicon and its relatively non-reaction with the underlying material. The dissociation of the reactive gas and the later reactions that take place between the reactive ions and the silicon are listed below:

Gas dissociation	**Products**
$SF_6 + e^- \rightarrow SF_5 + F + e^-$	$Si + F \rightarrow SiF$ (not volatile)
$SF_5 + e^- \rightarrow SF_4 + F + e^-$	$SiF + F \rightarrow SiF_2$
$SF_4 + e^- \rightarrow SF_3 + F + e^-$	$SiF_2 + F \rightarrow SiF_3$
$SF_3 + e^- \rightarrow SF_2 + F + e^-$	$SiF_3 + F \rightarrow SiF_4$ (volatile)
$SF_2 + e^- \rightarrow SF + F + e^-$	
$SF + e^- \rightarrow S + F + e^-$	$SiF_2 + SiF_2 \rightarrow SiF_4$ (volatile)

C_4F_8 gas is used for the passivation step. The polymer is deposited in the sidewall and the bottom after the etching step. A fast Ar etching removes the polymer layer on the bottom after each polymerization step for allowing the next etch by SF_6. This way the sidewall of the trenches is protected for preventing the lateral etching of the isotropic etching made by SF_6. A schematic of this process is illustrated in figure 4.5.

[2] Adsorption: adhesion of atoms/molecules to a surface.
[3] Chemisorption: adsorption driven by a chemical reaction at the exposed surface.
[4] Desorption: process in which a substance is released from a surface.

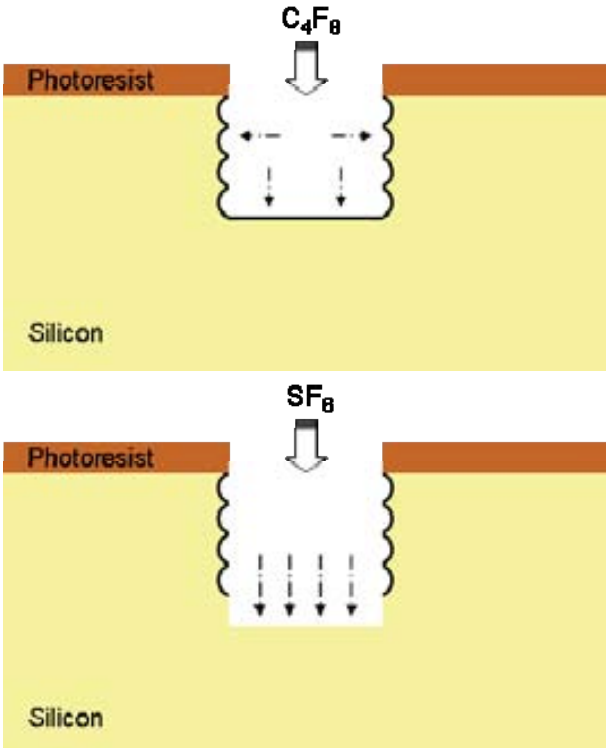

Figure 4.5: *Steps of the time-multiplexed alternating process of the Bosch method where sidewall passivation uses C_4F_8 (top) and silicon isotropic etching uses SF_6 (bottom).*

The result is a surface profile of low surface damage compared to diamond saw cut or laser scribing which offers the possibility of being part of the standard microelectronics fabrication process. Furthermore, the pattern of the cut lines can be determined by the photolithography step what allows almost no limitations on the shape of the final detector.

4.3 Slim-edge detectors

Standard silicon detectors have a large insensitive region around their active area due to the introduction of multiple guard rings in order to homogenize the potential drop up to the edge of the sensor. The purpose is to insulate the active area of the sensor from the lattice defects of the detector rim. The dead area for the guard ring structure can extend more than 1 mm so the aim of this work is studying another terminating structure to reduce that width to less than 50 μm thus maximizing the effective area of the detectors.

The main difficulty to get a workable slim-edge detector is to decouple the surface current of the detector from the current due to the active volume, since a significant fraction of the high concentration of lattice defects produced during the dicing of the chips are electrically active and they are responsible of the high conductivity of the cut surface that produces an effective screening of the electric field in the layers adjacent to the cut edge. In addition to this effect, the oxidation of the outer layer of silicon is produced under an oxidizing atmosphere, which reduces the conductivity of the cut surface. From the combination of both effects it is not easy to have well determined the

electrical properties of the edge. To solve this problem a *current terminating structures* (CTS) [100, 101] is modeled.

4.3.1 Edge design (CTS)

The concept of the current terminating structure consists of two grounded rings located between the end of the sensitive region and the edge of the detector, see figure 4.6. The outer ring, called *current terminating ring* (CTR), collects the leakage current generated at the detector cut and grants a homogeneous distribution of the electrostatic potential. Typical current in this electrode under high overdepletion is in the order of hundreds of µA. The second ring, called *clean-up ring* (CUR), collects a fraction of the current originated by the charge carriers that drift towards the sensitive volume [102]. This current is typically three orders of magnitude lower that the I_{CTR}. These two rings collect together almost all of the current generated by the lattice defects of the cut surface.

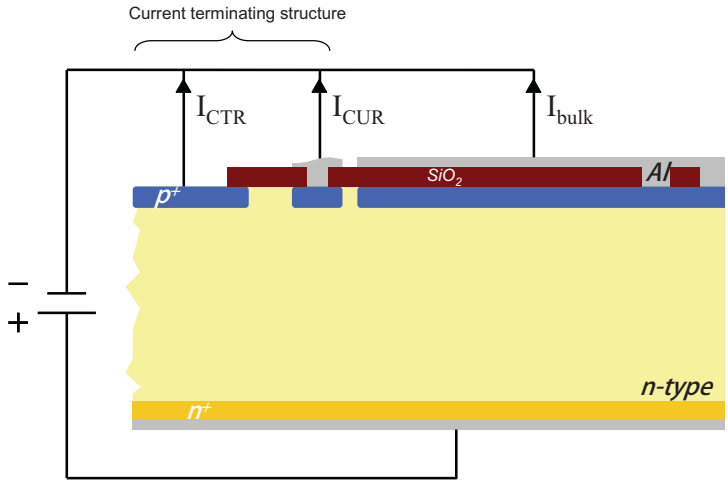

Figure 4.6: *Schematic cross-section of a slim edge n-type silicon detector with the CTS.*

4.3.2 TCAD simulations

Simulation results of irradiated slim-edge detectors are presented in this section [103]. For this purpose, the detector response for particle tracking was simulated, modeling the lattice defects generated by the diamond saw cut as a gradient of charge traps from the edge, and the radiation induced defects as acceptor/donor traps within the bandgap and an increase of the Si/SiO_2 interface charge concentration.

The geometry simulated for the CTS is a two dimensional slice of 520 µm × 300 µm, while the third dimension for the electrical simulations is set by the software to 1 µm. The first stage on the design of this cell consisted of using the DIOS[5] program for the simulation of the fabrication processes of standard planar technology employed during the manufacturing of the real device. These fabrication steps are oxidations and etching of silicon surfaces, photolithography for opening oxides for later ion

[5] DIOS (or Sentaurus process in the newest version) is part of the Synopsys TCAD software package dedicated to the simulation of the fabrication steps of semiconductor devices.

implantations, annealing stages for dopants diffusion and contacts metallization in order to obtain the structured side as realistic as possible.

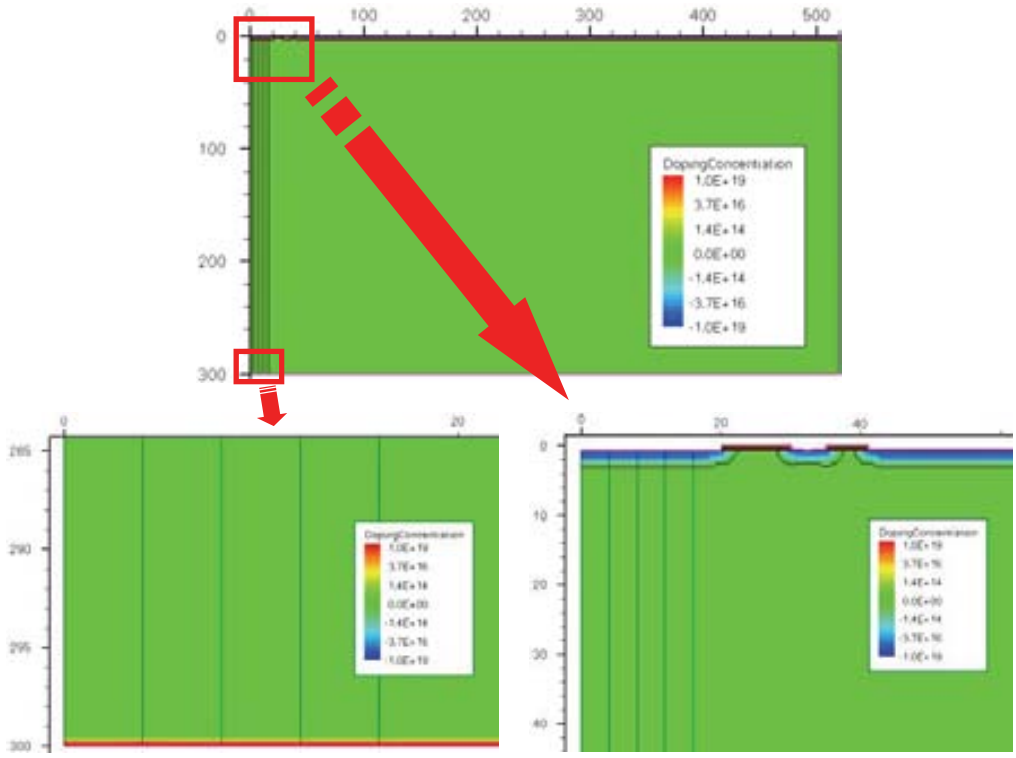

Figure 4.7: *View of the doping concentration of the n-type silicon detector (top) and details of the doping concentration at top and bottom surfaces (bottom). The brown line below the p^+ implantations corresponds to the pn junction contour.*

The p^+ doping of the CTR, CUR and strip electrodes were made simulating the boron implantation with a dose of 10^{15} cm^{-2} and an energy of 50 keV, resulting in a peak concentration of 4×10^{18} cm^{-3} after the annealing process for diffusion, while for the n-type bulk and the n^+ backplane electrode the concentrations were set to 5×10^{11} cm^{-3} and 10^{18} cm^{-3} respectively. The correspondent resistivity to the n-type bulk is 8.1 kΩ·cm, according to the Thurber's equation, and the nominal value of the full depletion voltage using the equation **74** is around 35 V.

Simulations of this structure on p-type silicon have been also carried out. The substrate resistivity is 19 kΩ·cm, corresponding to a depletion voltage of 49 V. The insulation method for the n^+ implantations consisted on a p-spray implantation covering the whole top surface whose peak doping concentration is 8×10^{16} cm^{-3}.

Saw cut damage model

In order to model the roughness and cracks produced in the surface and the lattice defects in the outer region by the cut of the wafer using a diamond saw, neutral charge traps are introduced at the edge. These traps are modeled in those regions as amorphous silicon by using a traps gradient from the surface to the bulk. This gradient is divided in four zones, due to the fact that Sentaurus TCAD software does not allow the implementation of a gradually decreasing concentration profile from the edge. It was

necessary to create four different profiles taking into account the decreasing concentration of traps [104].

Traps for each region consist of two neutral electrons traps (1, 2) and two neutral holes traps (3, 4) with exponential distributions, given by the following function [30]

$$f_t(E) = N_1 e^{-\left|\frac{E-E_C}{E_{S1}}\right|} + N_2 e^{-\left|\frac{E-E_C}{E_{S2}}\right|} + N_3 e^{-\left|\frac{E-E_V}{E_{S3}}\right|} + N_4 e^{-\left|\frac{E-E_V}{E_{S4}}\right|} \quad \textbf{[139]}$$

where N_1 and N_2 are the electron traps concentrations, N_3 and N_4 are the hole traps concentrations, E_{S1} and E_{S2} are the standard deviations for electron traps while E_{S3} and E_{S4} are standard deviation for hole traps. Figure 4.9 shows a graph of the distribution function of neutral electron and hole traps.

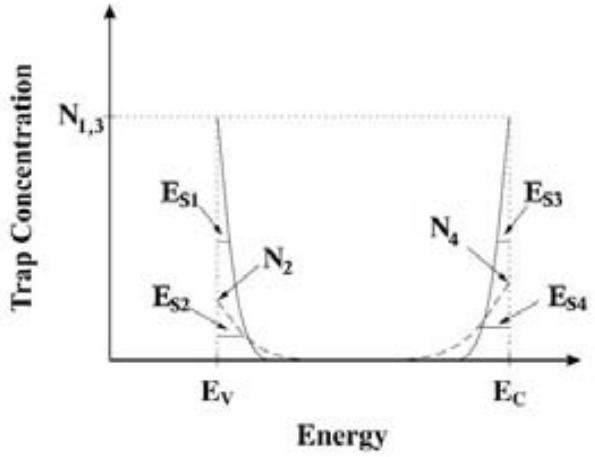

Figure 4.9: *Energy levels distribution in the forbidden gap for polysilicon with four exponential distributions [30].*

The values for the concentration of traps for each region follow the next equation

$$\left(N_{1,2,3,4}\right)_m = \left(N_{1,2,3,4}\right)_0 \times 10^{-m}, m = 0,1,2,3 \quad \textbf{[140]}$$

The width of each region is 4 μm, reaching a total length of 16 μm from the edge. The trap concentration values, standard deviations and carriers capture cross sections for the first region ($m=0$) are listed in table 4.1. The carriers capturing cross-sections remain invariant in the four regions.

Table 4.1: Parameters for Traps section in the command file of Dessis [29][104, 105].

Type	Energy (eV)	E_S (eV)	σ_e (cm^2)	σ_h (cm^2)	N (cm^{-3})
e neutral	Ec	0.035	10^{-10}	10^{-12}	10^{21}
e neutral	Ec	0.1	10^{-10}	10^{-12}	4.0×10^{16}
h neutral	Ev	0.035	10^{-12}	10^{-10}	10^{21}
h neutral	Ev	0.08	10^{-12}	10^{-10}	2.5×10^{15}

Before Irradiation

Electrostatic potential

In figure 4.10a it can be appreciated that the potential is uniformly distributed across the detector. A comparison of the electrostatic potential profile obtained for cuts along the edge of the detector (x = 0) and along an inner position sufficiently separated from the edge (x = 400 μm) is shown in figure 4.10b according to the Poisson's equation

$$\nabla^2 \varphi = -\frac{qN_{eff}}{\varepsilon_{Si}}$$

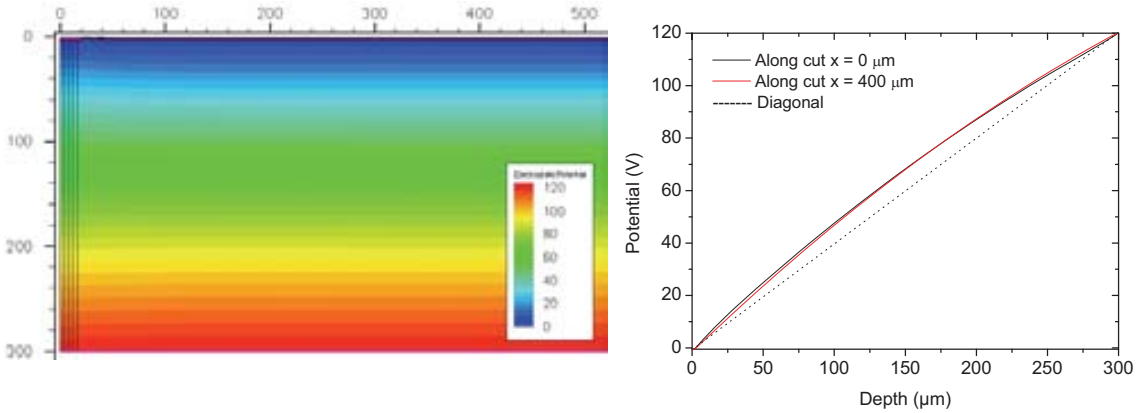

Figure 4.10: *Electrostatic potential distribution within the p-in-n detector (left), and potential profiles for slices at x = 0 and x = 400 μm (right).*

Electric field

The electric field is obtained from the gradient of the electrostatic potential, resulting the distribution of figure 4.11a, whose profile is a decreasing linear slope from the *pn* junction to the backplane, as it was described in Section 2.2.2. High values of electric field are also appreciated at the edges of the electrodes (CTR, CUR and strip electrode) due to a more severe potential drop at the edges of the implantations. At the top and bottom of the CTR there is also an increasing of the electric field that is caused by the junction of the trapped charge in the diamond sawcut induced defects and the implantations n^+ and p^+ at both surfaces [106].

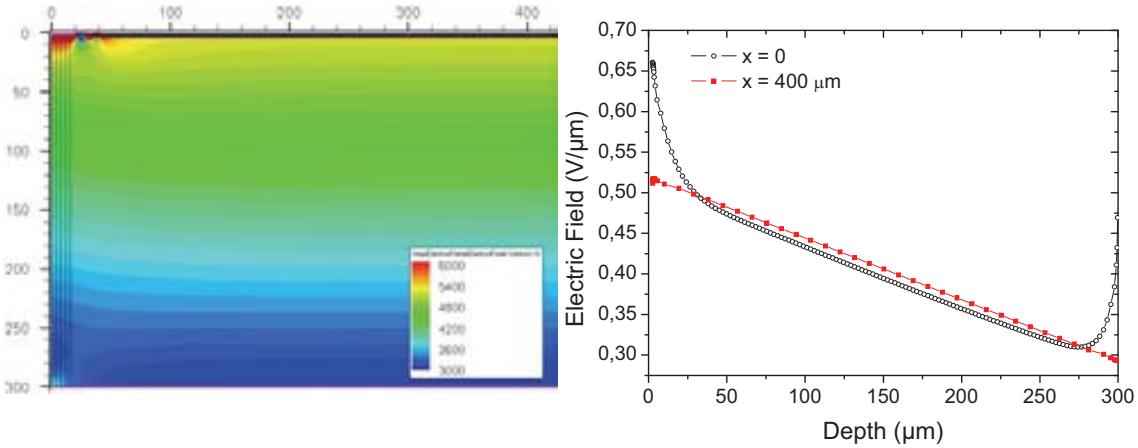

Figure 4.11: *Electric field distribution of the unirradiated p-in-n detector biased at 120 V (left), and field profiles for slices at x = 0 and x = 400 μm (right).*

Figure 4.11b shows the plots corresponding to the profile of the electric field of cuts along $x = 0$ and $x = 400$ μm. The values of the higher electric field located at top and bottom locations in the edge ($x = 0$) correspond to the double peak distribution attributed to a small double-junction effect. In this case, the space charge near the contacts is generated by the diamond sawcut defects instead of high radiation fluences [107].

Current density

The electron and hole current densities at the cut edge of both n-in-p (left) and p-in-n (right) detectors biased at 120 V are shown in figure 4.12. The result reveals that most of the generated current due to the high concentration of traps flows to the *CTR*, and only a small fraction flows to the *CUR* as expected.

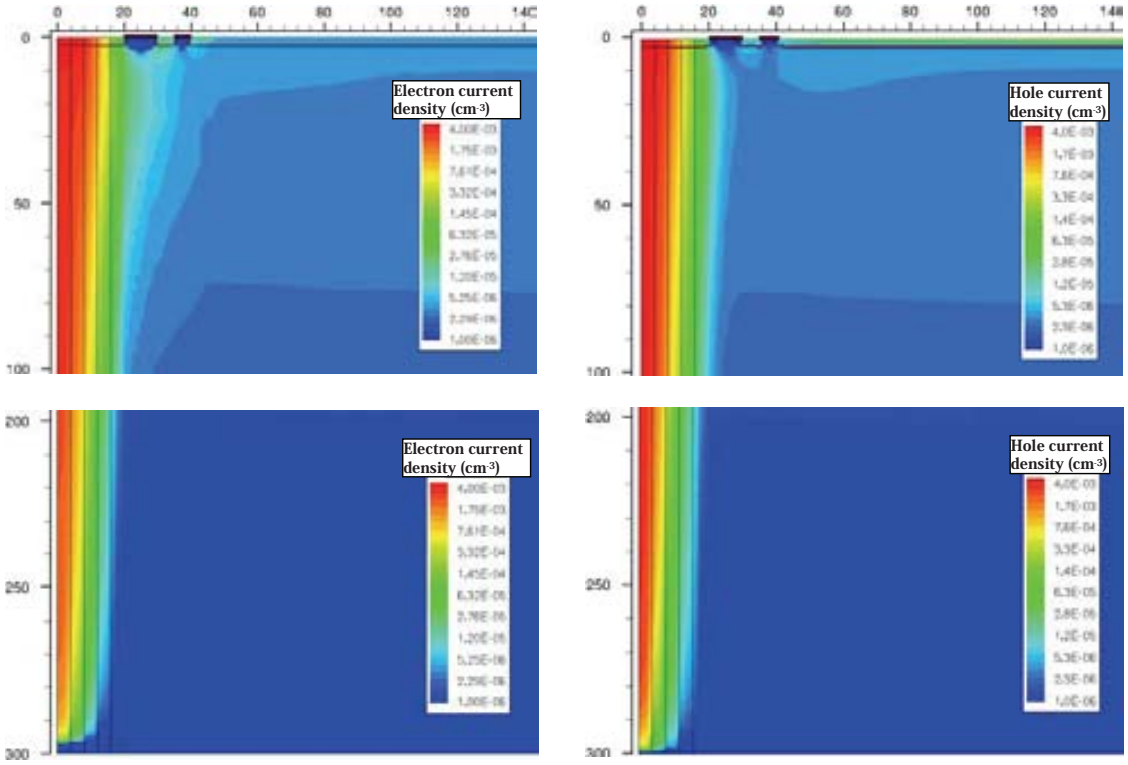

Figure 4.12: *Electron current density (left) and hole current density (right) at the edge of the n-in-p and p-in-n detectors respectively, before irradiation. Both detectors are biased at 120 V.*

After irradiation

Bulk type inversion

The traps model for n-type silicon of table 3.11 was introduced in the physics section of the simulator in order to reproduce the radiation damage. Different neutron equivalent radiation fluences were implemented in this study: 5×10^{13}, 10^{14}, 2×10^{14}, 4×10^{14}, 7×10^{14} and 10^{15} n_{eq}/cm^2. The way in which the fluence changes the traps concentration is through the introduction rate parameter η:

$$N_{traps} = \eta\phi_{eq} \qquad [141]$$

Figure 4.13 shows the variation of the full depletion voltage of the detector as a function of the fluence. The full depletion voltage for each fluence was obtained from the CV characteristic applying the LogC-LogV method. This plot also shows that the p-in-n detector is type inverted for fluences above 10^{14} n_{eq}/cm^2.

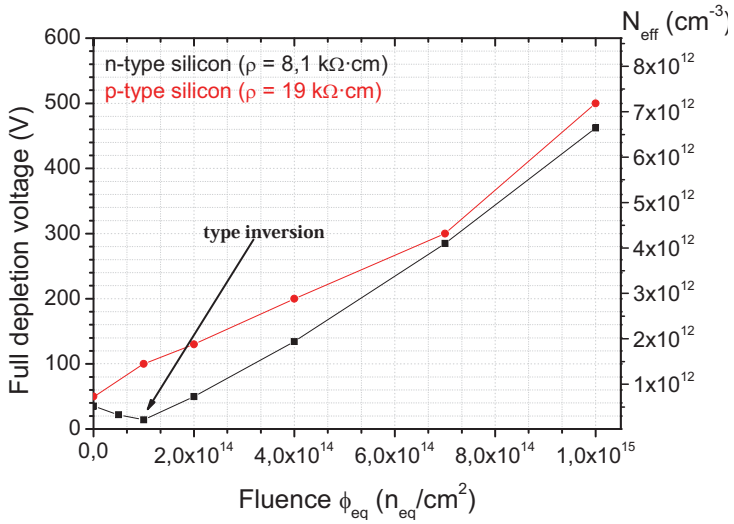

Figure 4.13: *Full depletion voltage as a function of the radiation fluence from simulated CV curves.*

Electric field

Figures 4.11 and 4.14 show the electric field distributions before irradiation and after bulk type inversion respectively for the case of the p-in-n detector. As it was mentioned in section 3.1.4, before irradiation the *pn* junction is given between the p^+ implantations and the n-type substrate. However, as the radiation fluence is increased, the radiation induced defects make the substrate to become progressively less n-type, and therefore the electric field in the junction is reduced consequently. This trend continues until the effective bulk concentration reaches the *type inversion*, what implies that the *pn* junction is not located anymore at the top surface but it is displaced to the n^+ implantation at the backplane, as the n-type bulk is turned into "p-type".

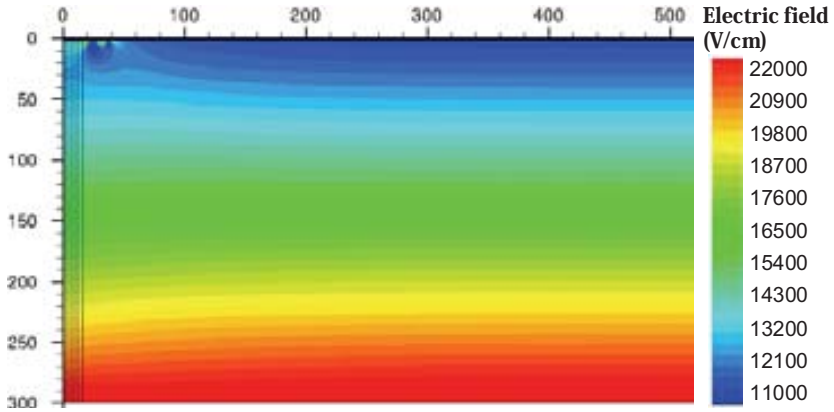

Figure 4.14: *Electric field distribution of a p-in-n silicon detector irradiated at 4×10^{14} n_{eq}/cm^2 biased at 500 V.*

The profiles of the electric field across the bulk at the edge and inside the detector for different radiation fluences are shown in figure 4.15 for an applied voltage of 500 V. It can be appreciated in both plots that the electric field in the *pn* junction decreases as the radiation fluence increases due to the progressive increasing of acceptor defects. This behavior changes after the *type inversion fluence*, with an increasing electric field for higher fluences at the new location of the junction. This change in the *pn* junction has a drawback: the growth of the depletion region is also inverted, making the collecting p^+ electrodes be placed in an undepleted region if the applied voltage is not enough to reach the V_{FD} value for the correspondent fluence which are shown in figure 4.13.

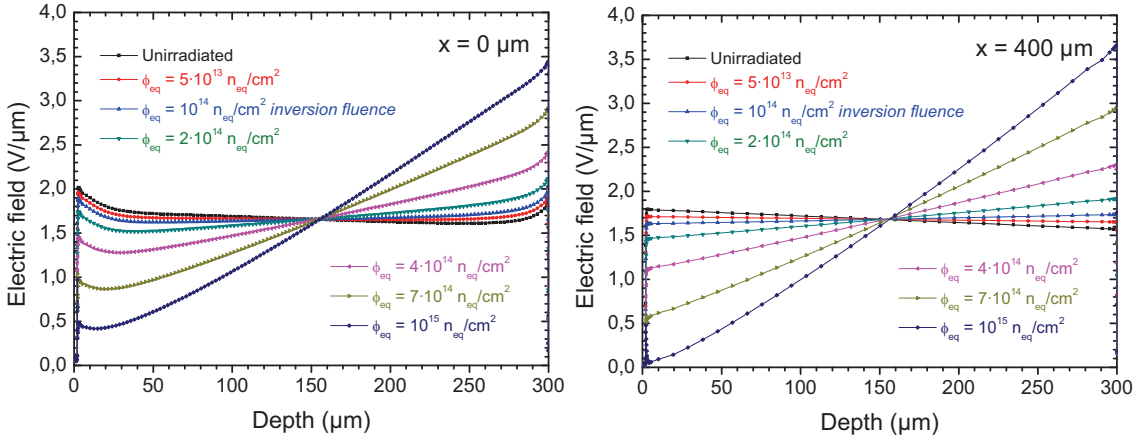

Figure 4.15: *Electric field profiles along the edge (left) and within an inner region (right) of a p-in-n silicon detector for an applied bias voltage of 500 V.*

There is another effect can be appreciated in these figures: the double peak in the electric field profile for the detector irradiated at the highest fluence, 10^{15} n_{eq}/cm^2, [108] due to the existence of two depleted regions, in the same way than for the lattice defects of the edge due to the diamond sawcut. Simulations reveal that this effect is more important in inner regions than in the edge for such fluence, probably because the gradient of the neutral traps reduces the amount of free charge carriers near the ohmic contact p^+p formed after the type inversion and hence also the possibility of reaching very high electric fields.

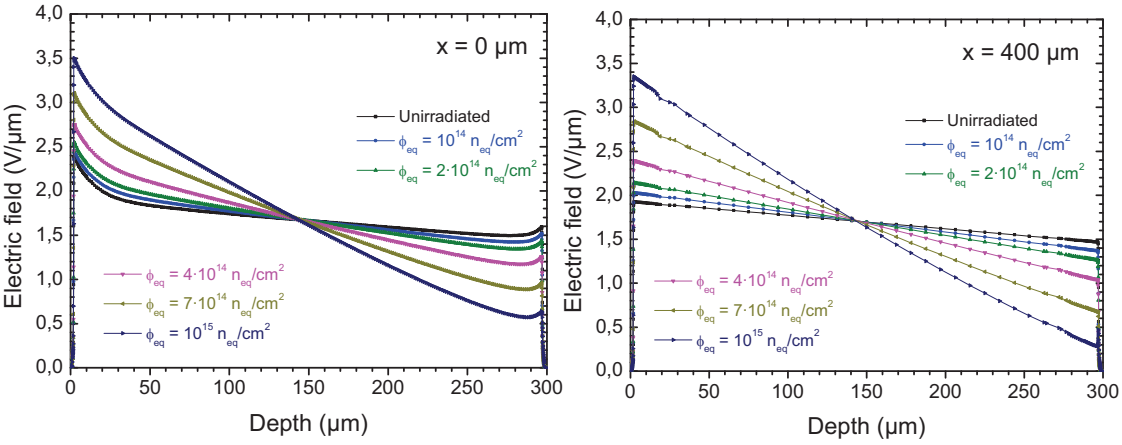

Figure 4.16: *Electric field profiles along the edge (left) and within an inner region (right) of an n-in-p silicon detector for an applied bias voltage of 500 V.*

Current density

Figure 4.17 shows the minority carrier current densities[6] in both p- and n-type silicon substrates. According to figures 4.15b and 4.16b which show the electric field distribution along the detectors, it can be appreciated a higher current density near the electrodes in figure 4.17a, as the *pn* junction in the detector of in figure 4.17b is displaced to the backside after the type inversion.

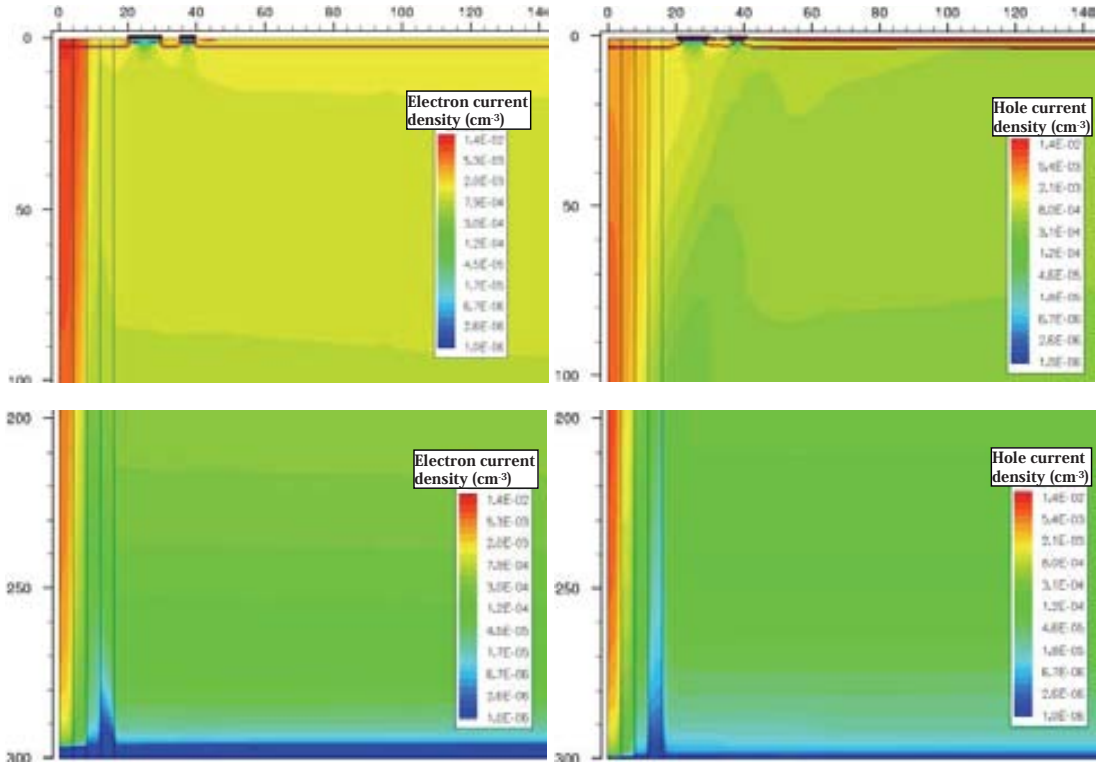

Figure 4.17: *Electron current density (left) and hole current density (right) at the edge of the n-in-p and p-in-n detectors respectively, after a radiation fluence of* 10^{15} n_{eq}/cm^2. *Both detectors are biased at 500 V.*

CTR, CUR and bulk leakage currents

Simulated currents corresponding to each electrode for different fluences are shown in the following figures. Figure 4.18a shows how the effect of the type inversion affects the current at the CTR electrode, since the electrodes are placed in an undepleted region until the bias voltage is enough to deplete the whole bulk from the backplane, increasing the current. In the n-in-p detector (figure 4.18b), the CTR collects entirely the current from the cut edge at all fluences.

[6] Note that the minority carriers in *type inverted* substrates are electrons, however in figure 4.17b it is represented the density of holes as they are collected on the p^+ implantations of the electrodes of interest.

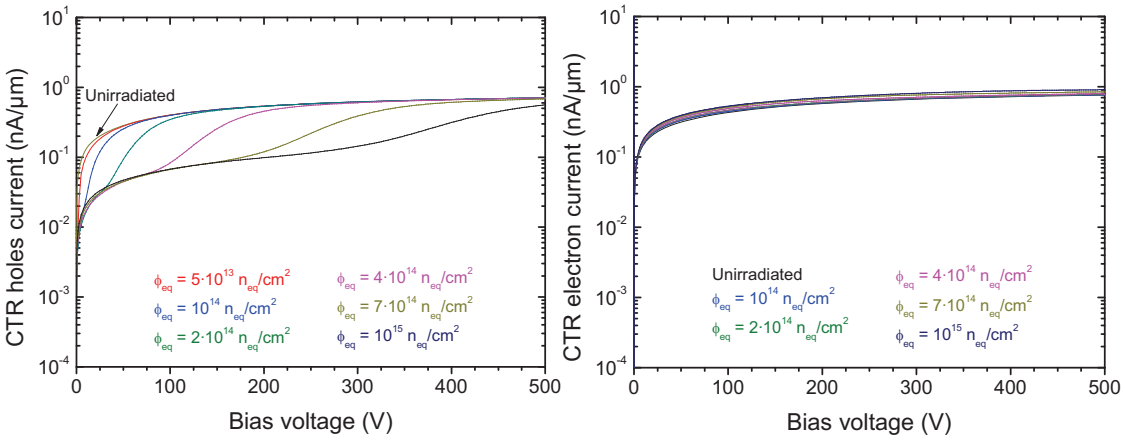

Figure 4.18: *Collected currents at the CTR for p-in-n (left), and n-in-p (right) detectors up to 500 V.*

The opposite effect is observed in the clean-up ring in figure 4.19a. Biasing the detector to voltages greater than V_{FD} is observed a reduction of the current, whose origin is the decreasing number of holes that diffuse from the edge to the bulk which are now collected on the CTR. The current collected in the CUR electrode experiences an increasing of the current due to the increasing concentration of radiation induced defect of the silicon below this electrode, in both n and p-type substrates.

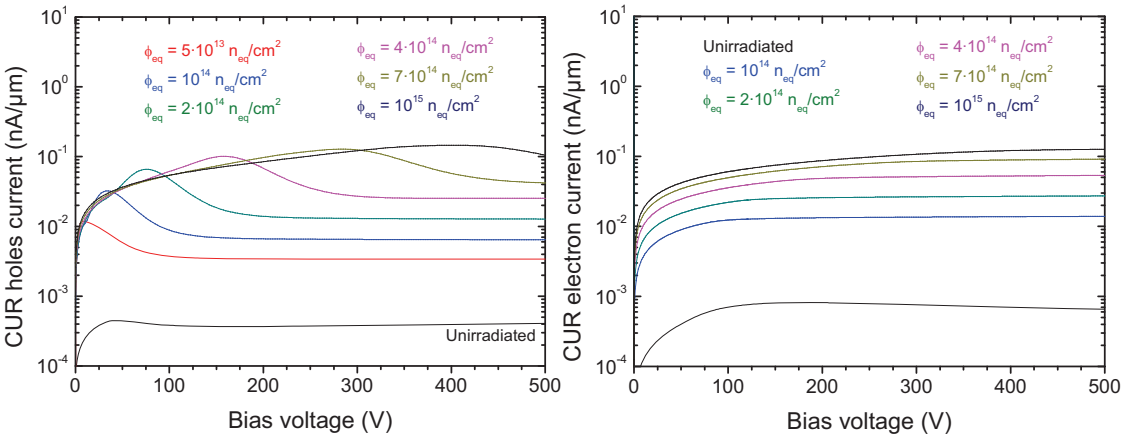

Figure 4.19: *Collected currents at the CUR (Clean-Up ring) for p-in-n (left), and n-in-p (right) detectors up to 500 V.*

Figures 4.20a and 4.20b show the increment of the leakage current with the fluence of the bulk electrode caused by the increasing traps concentration of the three midgap levels introduced from the radiation damage models of tables 3.11 (n-type) and 3.12 (p-type), as they act like generation-recombination centers in equation **81**.

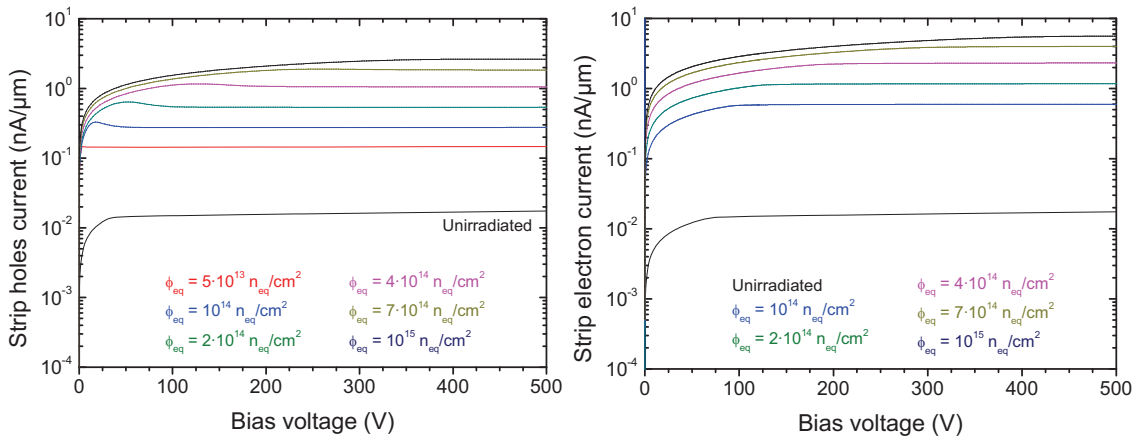

Figure 4.20: *Leakage currents collected at the bulk electrode for p-in-n (left), and n-in-p (right) detectors up to 500 V.*

The increasing of the leakage current ΔI is given by the difference of the current after and before irradiation at full depletion voltage. This increase in the current is proportional to the fluence, as seen in equation **129**, and the resulting simulated value of the *leakage current damage rate* $\alpha = (1.668 \pm 0.035) \times 10^{-17}$ A/cm for n-type silicon is nearly in agreement with the reported experimental values obtained after an accelerated annealing treatment at 60ºC for 80 minutes as shown in figure 3.15a, $\alpha = 3.99 \times 10^{-17}$ A/cm. The leakage current damage rate corresponding to the traps model for p-type silicon results in $\alpha = (3.581 \pm 0.003) \times 10^{-17}$ A/cm that is much closer to the experimental values.

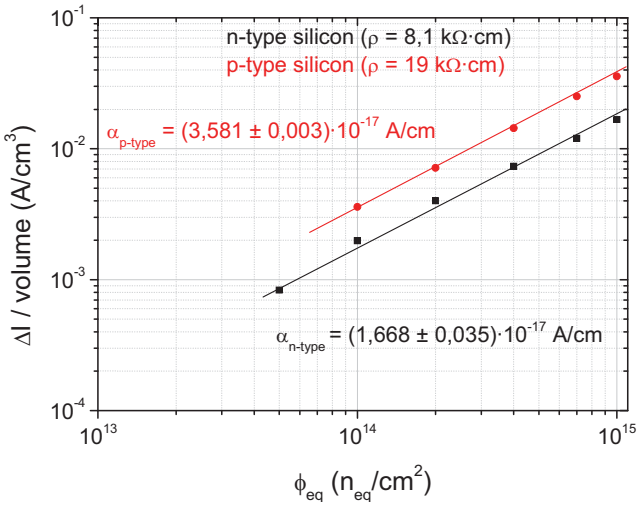

Figure 4.21: *Simulated leakage current damage rates for both n- and p-type substrates as a function of the radiation fluence.*

Charge collection efficiency

The response of slim-edge detectors to tracking particles is carried out using minimum ionizing particles, MIP, at different location from the cut edge to the inner active area for different irradiation fluences. The simulation of such particles crossing

the sensor in Sentaurus Device software consisted on creating a Gaussian distribution of electron/hole pairs 1 µm width and a depth equal to the detector thickness. The charge generated along the MIP track is 80 electron/hole pairs per µm, covering the whole thickness of the detector. Figure 4.23 shows the electron and hole current densities for a n-in-p detector irradiated at 10^{15} n_{eq}/cm^2 for a MIP crossing at 100 µm from the edge side and biased at 500 V. Some frames of the transient simulation have been taken at 0.05 ns, 1 ns, 3 ns and 25 ns.

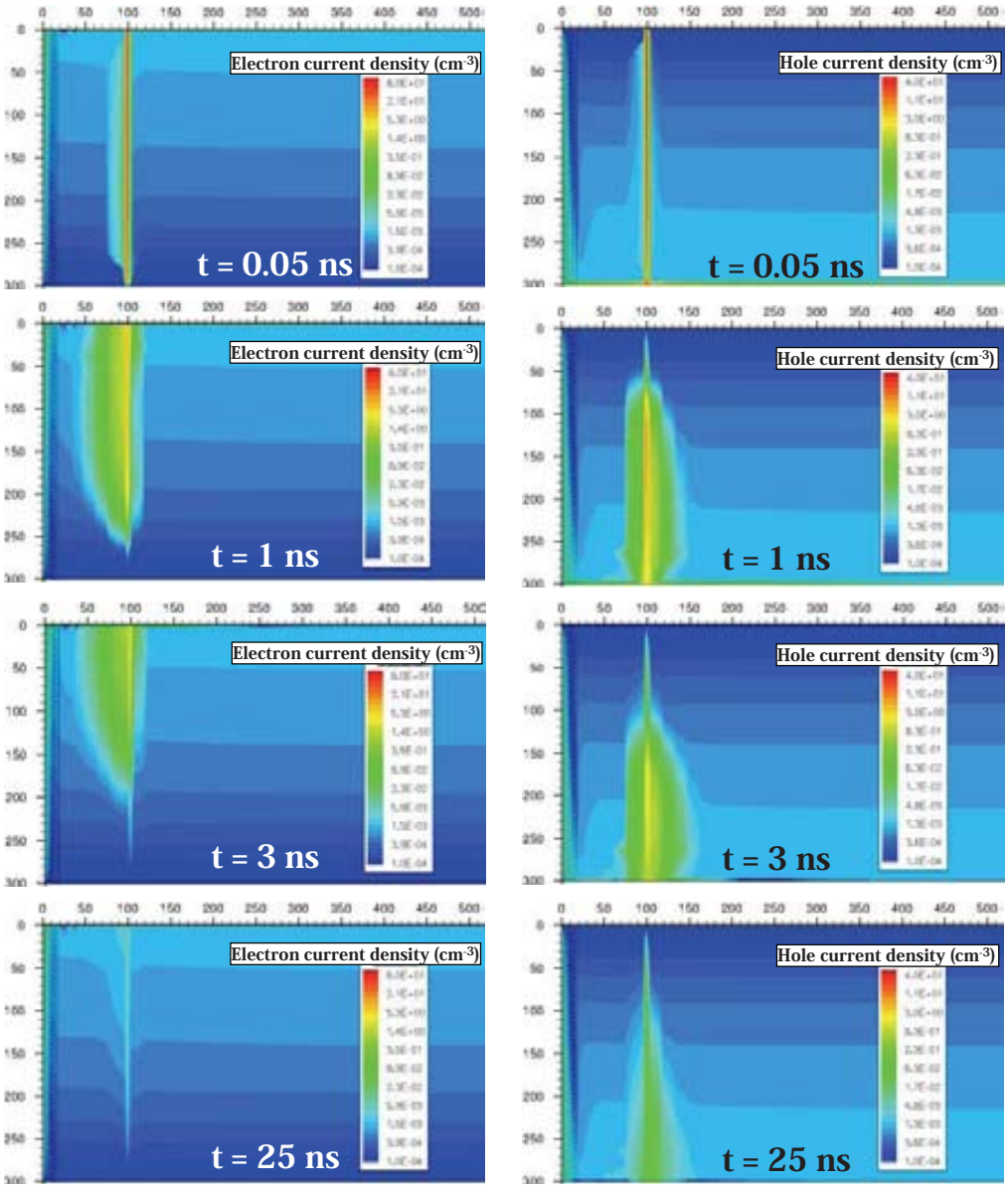

Figure 4.22: *Electron and hole current densities in an n-in-p detector for a MIP track at 100 µm from the cut edge. The detector is irradiated at 10^{15} n_{eq}/cm^2 and the biasing voltage 500 V.*

Figures 4.23a and 4.23b contain the charge collection efficiency (CCE) curves for the simulated detectors using MIPs crossing at different positions and for different radiation fluences. These CCEs, which corresponds to the bulk electrode, have been obtained for a collection time of 25 ns biasing the detector at 500 V. As expected, the efficiency decreases as the fluence increases due to the increasing of charge traps within the bulk. However, simulations of CCE in the p-in-n detector only agree experimental

results for fluences lower than 10^{14} n_{eq}/cm^2 [85-86] and therefore curves above this value are not plotted in the graph.

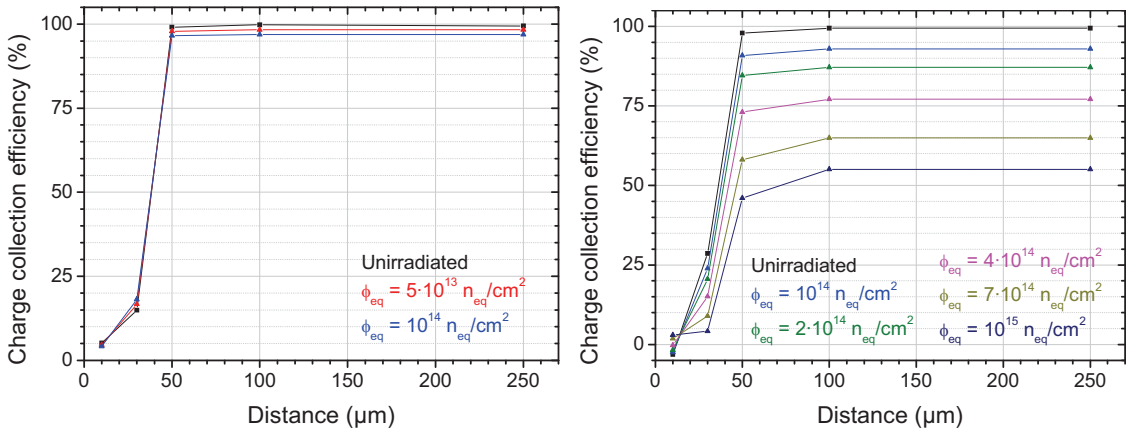

Figure 4.23: *Charge collection efficiencies of the p-in-n (left) and n-in-p (right) detectors biased at 500 V for different radiation fluences. Curves corresponding to higher fluences than 10^{14} n_{eq}/cm^2 are not plotted for the p-in-n detector as the collected signals using the traps model for n-type substrates (table 3.11) are overestimated in more than 5 ke^- from experimental results [85-86] and the difference increases from that fluence.*

The CTS revealed to work successfully for the two detectors as presented in figure 4.23, hardly increasing the current that flows to the bulk detector for particles crossing within the first 50 μm from the cut edge. Comparative curves of particles crossing at two different locations (10 μm and 100 μm), evidencing such behaviour, are shown in figure 4.24. The figure also includes experimental measurements of charge collection carried out on FZ n-in-p strip detectors for several radiation fluences and different radiation damaging particles for comparison. The negative efficiency reported in figure 4.24 for 10 μm is due to the displacement current at the n^+ strip electrode caused by the induction current at the CTR and CUR electrodes, and it would be null for an *infinite* collection time.

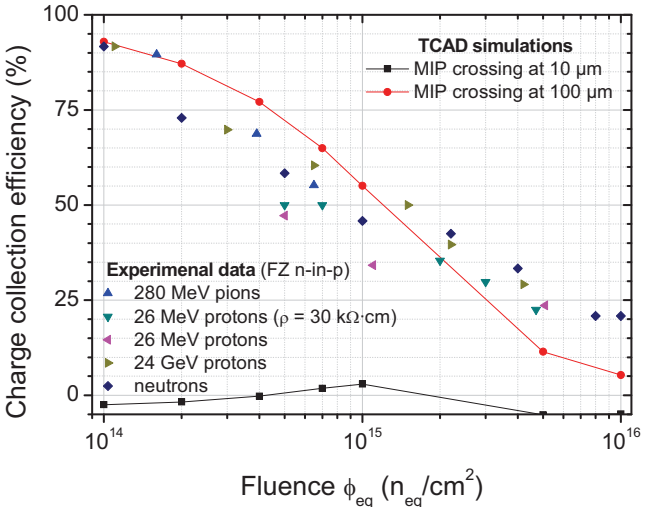

Figure 4.24: *Charge collection efficiencies versus fluence for 2 crossing MIP locations at 10 and 100 μm biased at 500 V bias using the traps model for p-type substrates. Experimental results on n-in-p FZ detectors (ρ = 14 kΩ·cm) were added for comparison [85-86].*

4.4 Active-edge detectors

The need of radiation sensors with minimum dead area has led to a new termination structure design applying the fabrication technology used in 3D detectors [38][96]. Technological issues of the fabrication of columnar electrodes are detailed later in Chapter 5, however some fabrication steps are also described in this section in order to understand the fabrication process.

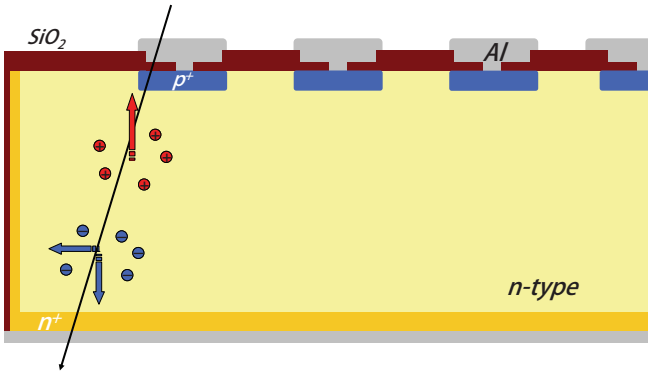

Figure 4.25: *Layout of the active-edge structure for an n-type silicon strip detector.*

The main features of the active-edge termination are shown in the schematic design of figure 4.25, where it can be seen that the edge of the sensor is doped, what makes edge and backplane to share the same electrode. This termination does not suffer from surface currents that are found after diamond sawcut, and therefore the dead area of this sensor is limited only to the thickness of the TEOS (silicon oxide) for passivation, the doped polysilicon and the diffusion length of the sidewall dopants [96], and the high electric field at the edge which may limit the breakdown of the sensor.

4.4.1 Detectors layouts

A small set of active-edge detectors have been modeled and are presently under fabrication at IMB-CNM (CSIC). Simulation of different edge configurations have been modelled for studying the potential and electric field distributions. The detectors consisted in PAD and microstrip geometrics for testing, but also Medipix2, circular and beam stop detectors, according to the specifications from DIAMOND Light Source Ltd.

Circular detectors for X-ray beam positioning

This detector is based on the designs presented in Ref[23] for synchrotron X-ray beam positioning. The design of these detectors allows the beam passing through its central hole. This way, for the non-segmented device there is an increasing current as the beam moves towards the sensor from the central hole position, meanwhile in the detector with either two or four segmented electrodes it is possible to obtain directional information from the sections measurements due to the displacement of the beam. The detectors under fabrication correspond to the electrode segmented in four sections with two sizes of hole diameter.

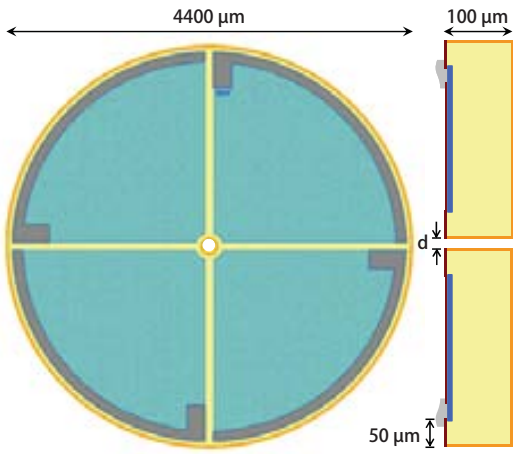

Figure 4.26: *Circular detector design for X-ray beam positioning which is being fabricated in two configurations: diameter of the central hole 100 µm and 200 µm. The distance from the edge to the p^+ implantation is 50 µm. The left-side picture corresponds to an actual view from the mask layout for d = 200 µm.*

Beamstop detector

In macromolecular spectroscopy, a collimated X-ray beam is headed towards a rotating crystal sample to obtain an image of its crystallographic structure due to the diffraction pattern collected in the detector. As the sample only absorbs a small fraction of the incident beam, most of the synchrotron radiation will hit the sensor producing serious detector damage. In order to avoid this circumstance, beamstops with high Z materials are placed in an intermediate location between the sample and the detector to block the direct beam and to reduce the main beam background air scatter. For this reason beamstops must be aligned properly and the active-edge detectors proposed in Ref[23] suppose a great tool for this task.

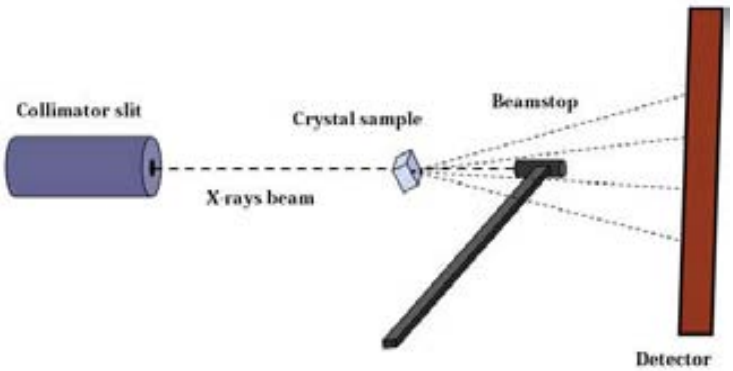

Figure 4.27: *Schematic of the X-ray scattering/diffraction setup.*

The idea is to integrate active-edge X-ray sensors into the beamstop located downstream of the crystal sample to obtain an accurate measurement of the beam flux transmitted through the crystal that could also contribute to the sample alignment [113]. The front side of these p-on-n diodes is 230 µm × 100 µm, with a total length of 3 mm. They would be mounted on a 1.85 mm × 0.5 mm × 4.6 mm circuit board that provides the bias voltage and collect the signals produced by the X-rays. The detectors are being

fabricated in two configurations: the first design has one electrode that collects the photocurrent of the whole sensor that is used to calculate the X-ray photon flux [114]; and a second design with the strip segmented in three electrodes, for measuring the content of higher energetic photons that could contain the synchrotron X-ray beam due to higher harmonics as in the spectrum of undulator radiation [23].

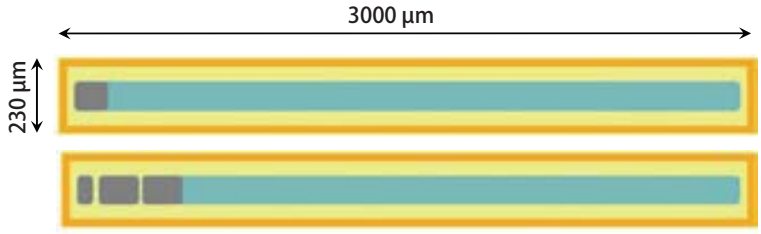

Figure 4.28: *X-ray beamstop detectors in two configurations: (top) with one strip electrode along the surface, and (bottom) one strip segmented in three electrodes.*

PAD, microstrip and Medipix2 detectors

In addition to the use of active-edge detectors in X-ray beam monitoring, the main benefit of this termination structure is the possibility of tiling large number sensors with almost negligible dead area around the edge of the devices. This is fundamental in small angle X-ray scattering (SAXS) and X-ray diffraction (XRD) to avoid missing any detail of the structural information obtained through the diffraction pattern that the detector provides.

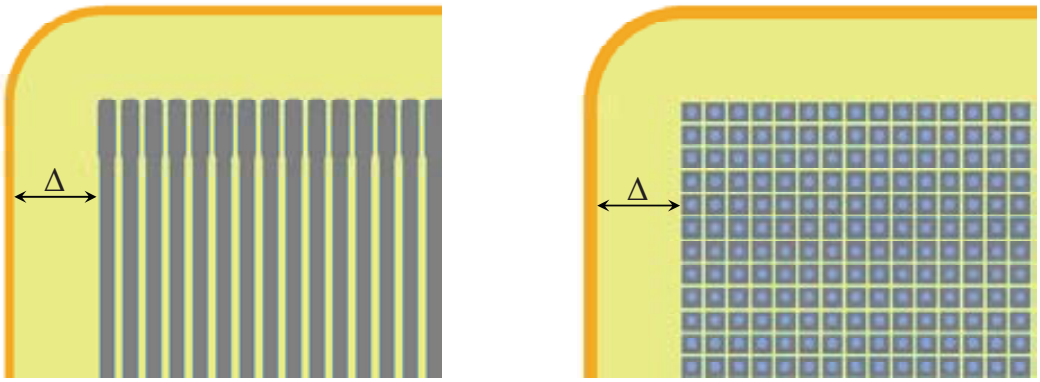

Figure 4.29: *Upper-left details from the mask layouts that correspond to one microstrip detector (left) and one Medipix2 detector (right).*

Several test devices using widely studied geometrics are also under fabrication to evaluate their electrical behaviour. These designs correspond to the PAD, strip and pixel planar detectors described in Section 2.3. Different edge-p^+ implantation distances Δ have been set in these devices, ranging from 50 µm to 500 µm, as it can be seen in table 4.3. TCAD simulations of such configurations have been carried out to study the electrostatic potential and electric field distribution at the edge region and are presented in the next section.

Table 4.3: *Geometrical specifications of the three designs of active-edge planar detectors under fabrication.*

PAD detector	
PAD size:	8 mm × 8 mm
Separation Δ:	50, 100, 200, 300, 400, 500 µm

Microstrip detector	
Strip size	40 µm × 8 mm
No. of strips	128
Pitch	80 µm
Separation Δ:	50, 100, 200, 300, 400, 500 µm

MediPix2 detector	
Pixel size	45 µm × 45 µm
Pixel array	256 × 256
Pitch	55 µm
Separation Δ:	20, 50, 200 µm

4.4.2 TCAD simulations

A 2D layout has been used to study the potential and electric field distributions in this termination structure, as it is shown in figure 4.30. The dimensions of this design are 500 µm × w, where w is the wafer thickness. Despite the thickness of the wafers under fabrication is 100 µm, the simulations also cover 200 µm as it is envisaged another fabrication batch using the same masks. The substrate consists of n-type silicon whose effective doping concentration is 10^{12} cm^{-3}, the Boron concentration of the p^+ implantation of the readout electrode is 10^{19} cm^{-3} with a diffusion length of 3 µm. In the case of n^+ electrodes, the Phosphorous concentration of the backplane and the 0.5 µm of deposited doped polysilicon is 10^{19} cm^{-3}, with a diffusion length of 2 µm through the substrate. The thickness of the silicon oxide layers used for passivation is 200 nm on the edge sidewall and 800 nm on the top surface. Both the backplane and the p^+ electrodes are covered by 1 µm of Aluminium for contacts. The fixed positive charge in the Si/SiO_2 interface is taken into account by a surface charge density of 5×10^{11} cm^{-2}. The distance Δ between the edge and the p^+ implantation is the simulation parameter that is changed to study how it affects the electrical properties of this termination design.

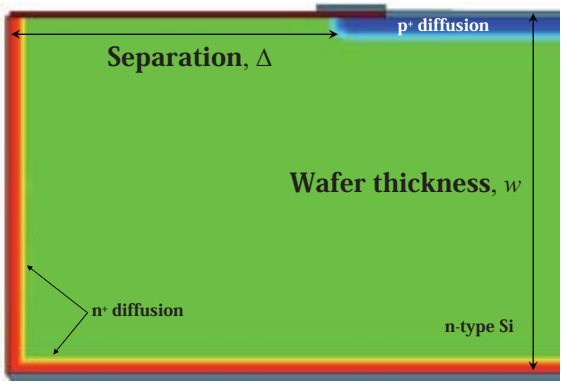

Figure 4.30: *Schematic of the 2D layout used in the simulations. The choice of the separation parameter Δ is obtained from the mask layouts: 20, 50, 100, 200, 300, 400 and 500 µm, while the thicknesses of the wafer w are 100 and 200 µm.*

Electrostatic potential

The nominal values of the full depletion voltages are obtained from the equation **74** corresponding to 7.7 V and 30.9 V for 100 µm and 200 µm respectively. The ramping voltage in the simulations was realized up to 100 V, saving relevant information every 10 V such as electrostatic potential, electric field, carriers density, etc, and no sign of breakdown was found in any of the possible (Δ, w) configurations. In figure 4.30 are shown the different potential distributions at the edge for the 100 µm thick detectors. The upper part of the figure shows the potential distributions for the separation distances Δ equal to 20, 50 and 100 µm for a bias of 10 V, when the detector is already fully depleted, while at the bottom are shown the ones that correspond to 100 V for comparison. As it can be appreciated, the main difference is the growth of the space charge region towards the active-edge electrode, and once is reached the growth is headed to its lower corner with the backplane. This region is not easy to deplete and that is why an alternative design, appeared in Ref[23], is made placing the diode junction along the back and edge sides, what would have required an p-type substrate to keep the same doping diffusion configuration without the requirement of insulation techniques for n^+ electrodes. Electric field lines are superposed to the potential plots to illustrate the electric force applied to the charge carriers generated at the edge.

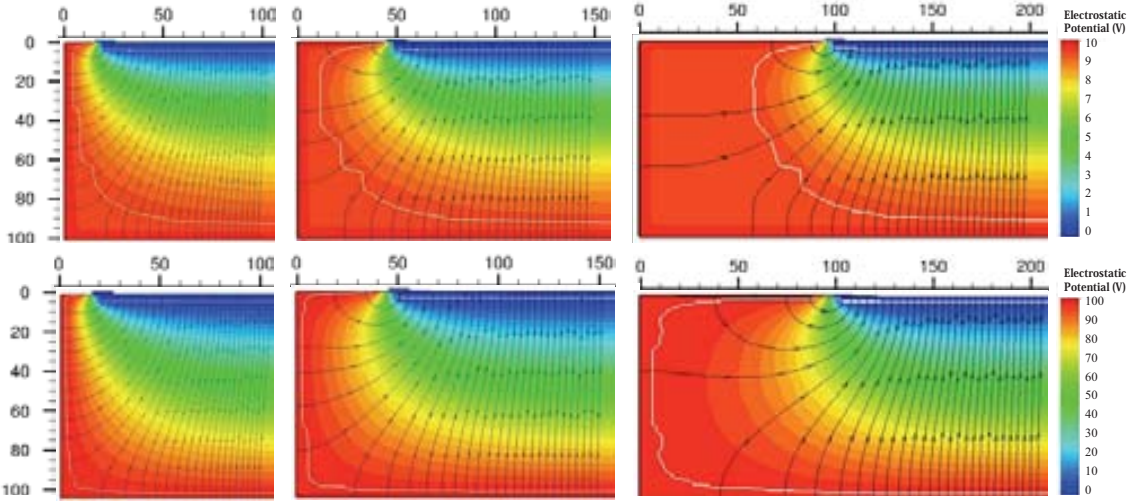

Figure 4.31: *Potential distributions for 10V, 100 V (w = 100 µm) d = 20, 50, 100 µm. Electric field lines are superposed in the plots. The white line corresponds to the space charge region contour.*

The are not significant differences between the potential distribution at the edge for the two wafer thicknesses, 100 and 200 µm, when the detector is fully depleted (10 V) and overdepleted (100 V), so only the plots for 100 µm case are shown in figure 4.31. Separation distances Δ longer than the wafer thickness w lead to large undepleted regions towards the edge side even for high voltages, as it can be appreciated in figure 4.32. For this reason, figure 4.31 only shows the cases which satisfy the condition $\Delta \leq w$ as the rest would not shed additional information because the potential distribution remains unchanged.

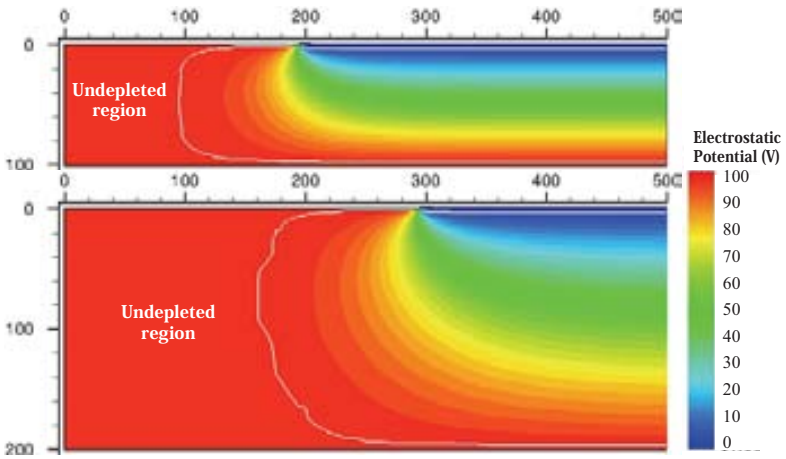

Figure 4.32: *Edge regions for separation distances Δ = 300 μm (thickness w = 200μm) and Δ = 200 μm (thickness w = 100 μm) biasing the detectors at 100 V.*

Electric field

The electric field distribution in planar detectors within the region between electrodes is homogeneous, following a decreasing linear slope from the *pn* junction to the ohmic electrode (backplane), as figures 2.21 and 4.11b show. So the interest in this study relies on the electric field distribution at the edge of detectors which have this termination. Previously it was told that it is not easy to deplete the lower corner of this structure and so the electric field in that region is negligible. On the other hand, in the upper part there is a variable separation distance Δ where the potential drop takes place between the edge of the p^+ implantation and the n^+ side electrode. In figure 4.33 are plotted the electric field profiles that correspond to that region for different bias voltages in all the possible configurations which satisfy $\Delta \leq w$.

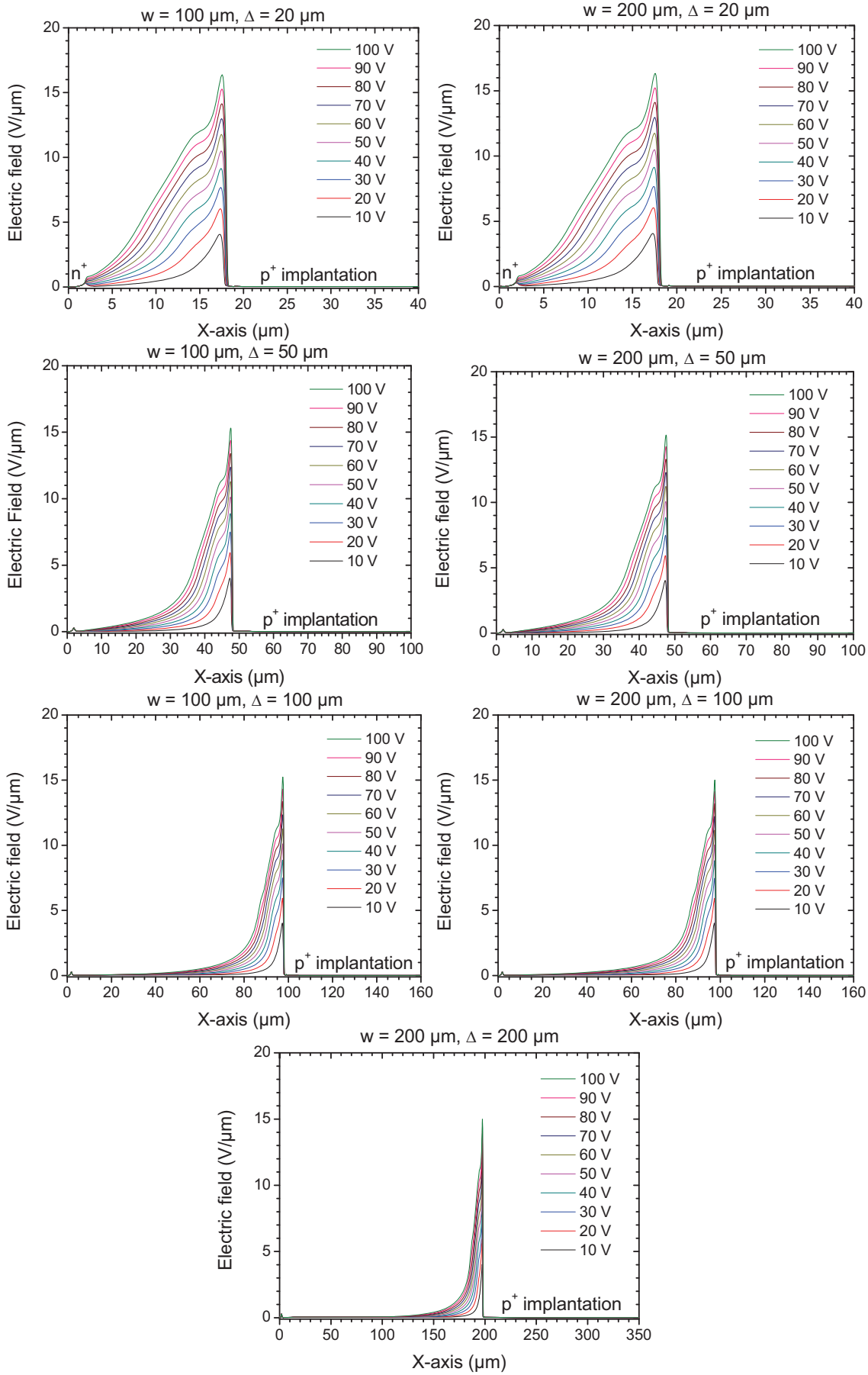

Figure 4.33: *Electric field distributions across the surface (1.5 µm depth) from the active-edge to the p^+ implantation for several separation distances, Δ, and 100 µm and 200 µm of wafer thickness w.*

At first sight it can be appreciated a first high field peak which takes place at the edge of the p^+ diffusion as a consequence of the p^+n junction. A second region of medium field is also observed after the first peak whose origin is due to the potential drop between the end of the field plate effect, provided by the metallization which extends beyond the p^+ diffusion, and the beginning of the electron layer below the Si/SiO_2 interface, which is bias-dependent as it will be discussed later separately. The increment of the separation distance Δ is translated into a longer and less pronounced drop of the electric field after the second field drop. In the case of Δ = 20 μm, the distance between the end of both n^+ and p^+ diffusions is only 16 μm what compresses the potential drop distance rising the field values.

From the comparison between the field profiles of the two different wafer thicknesses is deduced that the thickness of the wafer has no influence on the field distribution near the upper region of the edge termination.

Role of the electron channel

The accumulated positive charge at the Si/SiO_2 interfaces attract electrons from the bulk creating an electron channel, which in the separation Δ acts as an extension of the backplane biasing assisted by the n^+ diffusion at the edge. Metalized surfaces exceeding the implantations help in the reduction of the electrons channel acting as field plates and therefore reducing the peak fields that are formed in those regions.

As the applied voltage is increased, the space charge region grows depleting the bulk thus avoiding the formation of electron channels below the oxides. However, the depletion in planar detectors grows from the junction towards the opposite electrode through the bulk, so regions below the passivation oxides remain as an undepleted thin layer keeping the electron channel. A reduction of the electron channel length is observed nevertheless in the active-edge detectors because of the top part of the implanted edge, slightly reducing the increment of the peak field and enlarging the potential drop distance from the p^+ diffusion to the beginning of the electron channel for increasing voltages.

4.4.3 Fabrication process

Several planar detectors have been designed and are currently being fabricated at the IMB-CNM (CSIC) Clean Room facilities for testing and for X-ray beams monitoring in collaboration with DIAMOND Light Source Ltd.

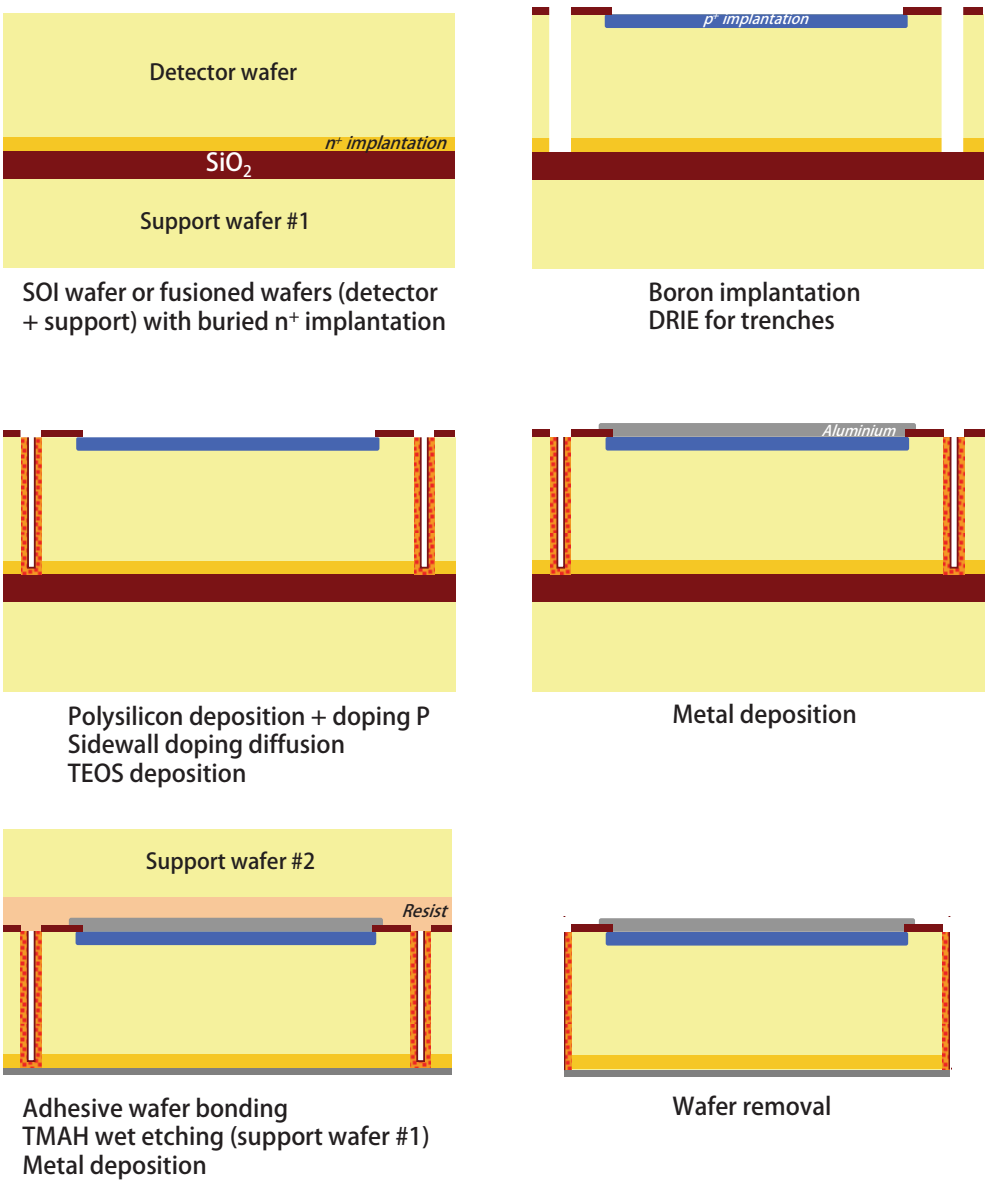

Figure 4.34: *Schematic of the fabrication process of active-edge detectors.*

The fabrication started with 5 n-type SOI wafers with a buried n^+ implantation at the bottom of the detector wafer, as it can be seen in figure 4.34. These wafers consist of a 100 µm high resistivity silicon substrate with Phosphorous implantation at the bottom, then 1 µm layer of SiO_2, and finally 200 µm of low resistivity silicon as support wafer. At first place Boron is implantated using standard planar technology, followed by the creation of the 10 µm width trenches which define the size of the active area of the sensors. Trenches are filled with 500 nm of polysilicon, subsequently doped with phosphorous using $POCl_3$ at 1050ºC for 60 minutes. A 200 nm layer of SiO_2 is grown for the passivation of polysilicon in a thermal process that also diffuses the phosphorous dopants of the sidewall polysilicon towards the silicon substrate. In order to provide mechanical support for the photoresist in the following steps (risk of opened trenches) an additional 2 µm layer of TEOS is deposited inside the trench to reduce their width before being covered by the photoresist. The next steps consist of the metallization of the p^+ electrodes with 1 µm of aluminium/cooper and the passivation of the top surface

of the detector with 0.4 μm of silicon oxide plus 0.2 μm of silicon nitride before the adhesive wafer bonding. When the support wafer is etched the detectors would not have any mechanical support because of the trenches completely surrounds them, so an additional support wafer is required. Both the detector wafer and support wafer #2 are bonded using resist, which is subsequently removed after the backside metallization by using an acetone bath.

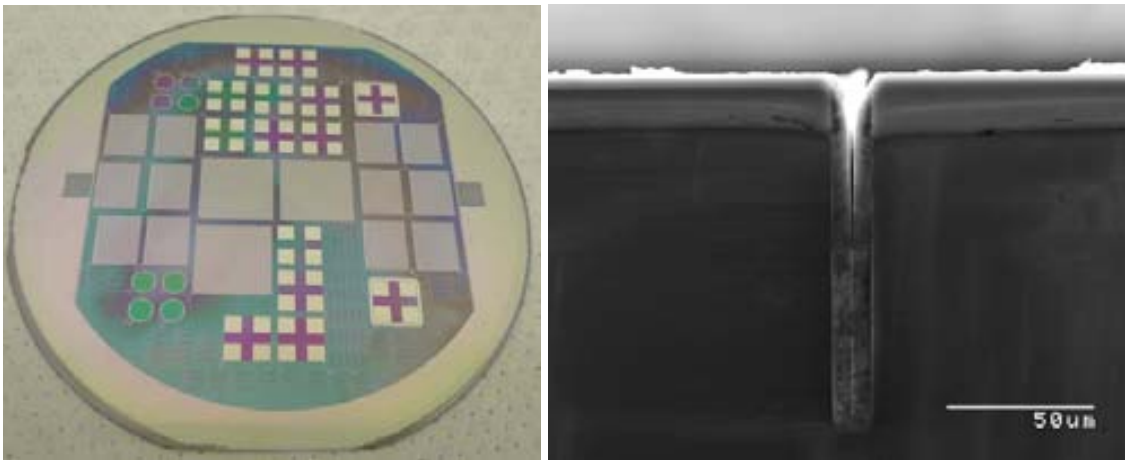

Figure 4.35: *One wafer containing active-edges detectors fabricated at the IMB-CNM (CSIC) Clean Room facilities (left) and detail of a trench filled with polysilicon (right).*

4.5 Conclusions

In this work, irradiated slim-edge detectors developed by the TOTEM collaboration has been described and simulated. Two different sets of defects, one for the diamond saw cut and one for the radiation damage, were implemented and combined to simulate the behavior of slim edge-detectors irradiated at different fluences.

Simulated charge collected before irradiation at the CTS using the sawcut damage model are in agreement with the values reported in experimental measurements [109, 110]. The traps model for n-type substrates of table 3.11 qualitatively reproduces the bulk type inversion that takes place in irradiated n-type detectors. The condition of full depletion became essential in n-type substrates because after the inversion the *pn* junction is displaced from the top side of the detector to the bottom (backplane) and the application of voltages $V < V_{FD}$ makes the p^+ electrodes to be found within an undepleted region. The increasing of leakage currents through the *leakage current damage rate* is also reproduced, nevertheless the results of the charge collection efficiency evidence that the model must be improved for fluences higher than 10^{14} n_{eq}/cm^2. It must be also commented that the model of table 3.12 for p-type substrates successfully works reproducing the charge collection for all fluences involved in this study. Such substrates are shown to be suitable for the TOTEM experiment that will take place at the HL-LHC.

Slim-edge p-in-n detectors have been used recently in the TOTEM experiment at CERN where they were placed at 25σ from the beam centre, see figure 1.5, obtaining the first candidates for *p-p* elastic scattering at a collision energy of 7 TeV [112]. The aim is to approach the detector to a distance as small as 1 mm (~10σ at RP220), as slim-

edge detectors have high sensitivity within 50 μm from the cut edge and can operate at high voltage [110].

Other applications that could benefit from the slim-edge detectors are X-ray synchrotron imaging experiments. For instance, in detection system for clinical breast tomography with synchrotron radiation [111] the detector is oriented with the strips parallel to the incoming beam, so that the absorption thickness is equal to the length of the strips. By using slim-edge detectors the dead area due to guard ring structure would be significantly reduced, thus increasing the intrinsic efficiency.

Active-edges suppose the highest reduction of the surrounding dead area of detectors to only a few micrometers given by the side passivation oxide (0.2 μm), the doped posylisilicon deposition (0.5 μm) and the diffusion length of those dopants within the substrate (2-3 μm). The main advantage of this termination is the possibility of tiling many sensors with negligible non-sensitive area, as it is required in small angle X-ray scattering (SAXS) and X-ray diffraction (XRD). Another potential application is the use of this termination in detectors oriented to close-to-beam measurements such us TOTEM experiment or X-ray beam position monitoring.

A batch of active-edge detectors for synchrotron X-ray applications has been design in collaboration with DIAMOND Light Source Ltd and is presently under fabrication, as shown in figure 4.35a, thus experimental measurements of such detectors couldn't be included in this work. The fabrication masks are valid for different wafer thicknesses since there are designs for separation distances from 20 μm to 500 μm. The simulations of this study are centered in the thicknesses 100 and 200 μm since the detectors currently under fabrication are 100 μm thick and it is foreseen to run a second batch with wafers 200 μm thick.

The separation distance Δ has demonstrated to be an important parameter in order to have an accurate value low enough for avoiding large undepleted regions near the edges and high enough for preventing high electric fields from the last p^+ diffusion to the n^+ active edge in full depletion. From the simulations carried out in this study, an accurate choice would be $\Delta = w / 2$ which grants lateral depletion at the correspondent V_{FD} bias for detector, and for moderated higher voltages also depletes the lower corner of the edge.

Wafers thicker wafers than 300 μm would require depletion voltages greater than 70 V that could lead to the electrical breakdown at the edge of the p^+ diffusion closer to the active-edge.

Chapter 5

3D silicon detectors

Since the appearance of the 3D architecture proposed by Kenny and Parker [38], there have been many research studies concerning their fabrication feasibility, different layouts and potential applications. The advantages of the 3D architecture are clearly remarkable: lateral depletion equal to the half of the pitch between electrodes, negligible dead areas for tiled detectors as the cut edge can be very close to the active area, and negligible charge sharing between neighbouring electrodes. The short distance between electrodes allows low depletion voltages as well as fast collection of charge generated by incident particles which make them intrinsically radiation hard suitable for high energy physics experiments where harsh radiation environments produce severe damage in silicon substrates that largely increases the depletion voltages and also reduces the charge collection efficiency due to the trapping that takes place in the radiation induced defects.

An innovative architecture based on columnar electrodes is also proposed in this work for ions detection. Radiation sensors with very thin sensitive substrates, on the order of tens of micrometers, are *transparent* for neutron and gamma backgrounds and would involve large electrodes-to-backplane capacitances that would increase the load capacitance causing significant signal attenuation if they were fabricated using standard planar technology.

5.1 Technological features of columnar electrodes

In order to minimize the non-sensitive area due to the columnar electrodes, they must be fabricated as narrow as possible as they are within the sensor substrate. The limitation of creating columnar electrodes in silicon detectors is the aspect ratio of the plasma etching process. For this task, Deep Reactive Ion Etching – Inductively Coupled Plasma (DRIE-ICP) is used as it is a highly anisotropic process to create holes which offers high aspect ratios (HAR), as shown in figure 5.1 [40].

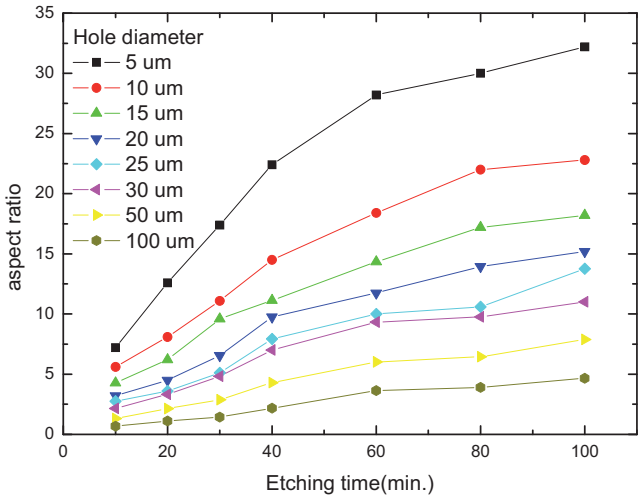

Figure 5.1: *Aspect ratio for different hole diameters as a function of the etching time using an Alcatel-601-E machine at IMB-CNM (CSIC) [40].*

The HAR is defined as the rate between the diameter and depth of holes. Figure 5.1 shows the results of different diameters and their aspect ratio at various etching times obtained with the ICP etching process with an Alcatel-601-E machine at IMB-CNM (CSIC). By simply enlarging the holes diameter or using thinner wafers is possible to obtain columnar electrodes passing through the whole wafer thickness [39][115, 116].

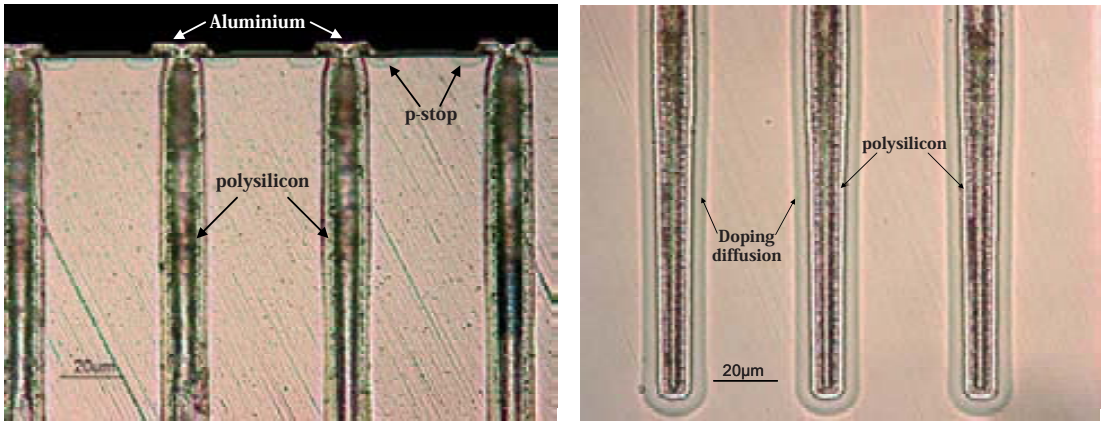

Figure 5.2: *Pictures of n^+ columnar electrodes in p-type silicon. The left-handed figure shows the top part of the columns where the diffusion of the p-stops can be appreciated. In the right-handed figure it can be seen the shape of the phosphorous diffusion in the substrate. The diameter of the holes is 10 µm and 250 µm depth.*

The DRIE-ICP process consists of a sequence of two alternating time-multiplexed steps: etching and passivation cycles, as it was mentioned previously in Section 4.2.2. For small diameters, the deeper the hole is, the more difficult is for the fluorine of the etching gas (CF_6) to reach and etch the passivation coating (C_4F_8) on the bottom of the hole, and therefore the depth of the holes starts to saturate, etching the sidewalls and enlarging the diameter. A good compromise between diameter and depth for 285 µm wafers can be obtained by choosing a 10 µm diameter since a 250 µm depth is achieved after 100 min of etching. This is the case of double-sided 3D detectors [40][117] where the overlapping depth between electrodes would be 215 µm.

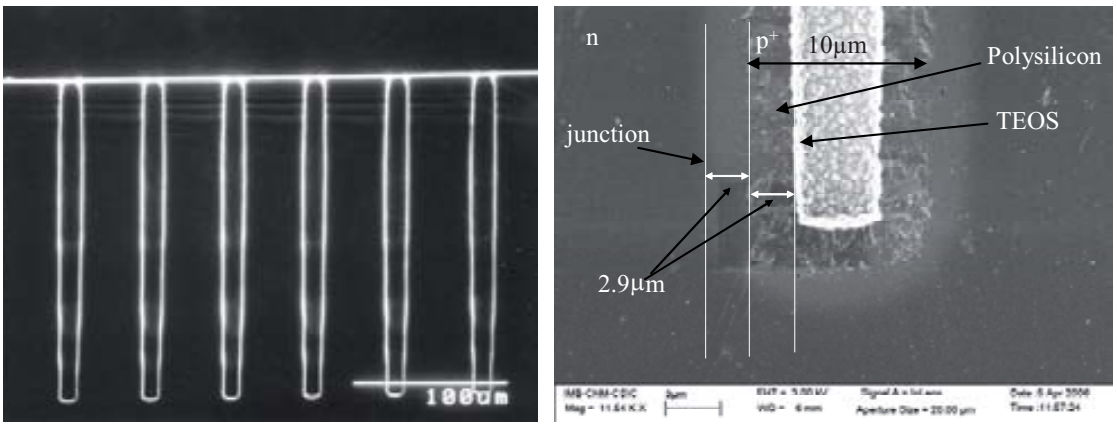

Figure 5.3: *SEM image of high-aspect ratio holes etched in silicon using DRIE-ICP process (left) and close look of doped polysilicon deposited in a 10 μm hole (right). The white material deposited on the polysilicon is a 200 nm layer of TEOS (tetraethyl orthosilicate) used for passivation.*

The electrodes within the dry etched holes are created by the diffusion of acceptor/donor impurities through a doped polysilicon layer deposited onto the wafer surface. The thickness of this polysilicon layer is 3 μm and is diffused into the silicon by annealing forming the junction at about 2.9 μm from the polysilicon/silicon interface. The diffusion smoothes the doping profiles at the column tips what prevents from high electric fields that could lead to early breakdown. Finally, the polysilicon within the columns is passivated by depositing an oxide (TEOS) layer. Figure 5.3b shows the final configuration of the bottom part of a p^+ columnar electrode in n-type silicon.

5.2 Ultra-thin 3D detectors

The huge plasma burning power of modern fusion reactors such us JET tokamak [118] or the upcoming International Thermonuclear Experimental Reactor (ITER) [7] leads to levels of gamma and neutron backgrounds that make the present detectors [19] designed to perform the corpuscular diagnostic of plasma unable to cope with the incident particle rate. The U3DTHIN detector is proposed as a proficient candidate to carry out that task. As the range of the incident ions coming from the burning plasma for the corpuscular diagnostics (deuterons, tritons, alphas) is in the order of microns/few tens of microns for the expected energies, this detector is based on a very thin sensitive substrate to be able to collect the electron/hole pairs they generate along their tracks and also be *transparent* to gamma-neutron backgrounds. This solution has an important drawback: very thin substrates imply large electrode-to-backplane capacitances that attenuate the collection of signals if they are built in standard planar technology, as it can be seen in figure 5.4. To achieve very fast collection of charge carriers generated by the incident ions, a 3D electrode structure [119] has been implemented in the sensitive volume of a thin detector. One of the most innovative features of these detectors is the optimal combination of the thin entrance window and the sensitive substrate thickness. This will make possible to accommodate very large dynamic range of the detected ions.

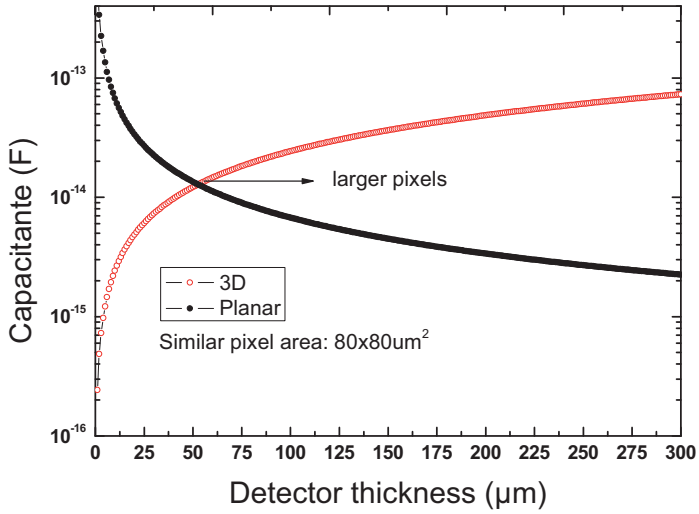

Figure 5.4: *Geometrical capacitance as a function of the thickness of 3D detectors compared to planar detectors with similar surface areas.*

The coaxial detector approximation, which regards the column as being a coaxial cable with radius equal to the distance between n^+ and p^+ electrodes, is used to compare 3D-thin detector capacitance to a planar thin device with the same surface area using the standard parallel plate capacitance. It can be seen in figure 5.4 that the 3D-thin capacitance is two orders of magnitude smaller than the capacitance of planar detectors. However, increasing the thickness (electrodes distance) this difference is reduced reaching the unity at a value depending on the surface area. For thick substrates, the capacitance of 3D sensors is higher than in the case planar sensors as already predicted [120].

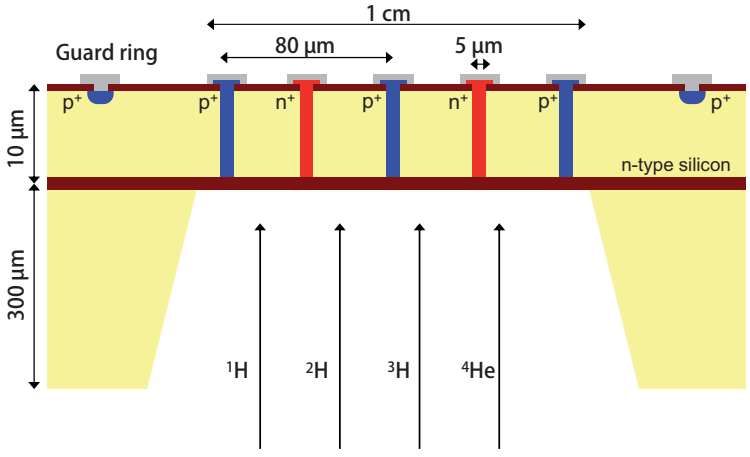

Figure 5.5: *Cross-section of the microstrip detector design. The drawing is not to scale.*

GEANT4 simulations were performed at the Helsinki Institute of Physics (HIP) to find the losses of energy in the oxide entrance and the energy deposition in the silicon substrate for different type of ions and background radiation (neutrons and gammas) to find the optimal thicknesses of both layers; results are found in Ref [20]. An entrance window with a thickness of tens of nanometers together with a sensitive substrate thickness varying from less than 5 µm, to detect the lowest energetic ions, to 20 µm for the higher energetic ones, are the optimal choice.

5.2.1 Detectors layouts

A schematic of the U3DTHIN microstrip detector is shown in figure 5.5. This configuration was obtained combining 3D detector technology and thin membrane fabrication process. Since the detector is illuminated from the back side surface, there will be no dead layer where the ions loose energy. To increase the signal-to-background ratio the detector has spectroscopy capability which allows performing pulse-height analysis [121]. Both the p^+ and n^+ columnar electrodes are connected respectively using aluminium strips in order to bias and collect the charge of every 3D cell in the 128 channels (figure 5.6) or shorted in a common electrode (figure 5.7) if they are not used for particle tracking systems as is the case of fusion reactors or surveillance neutron detection[1].

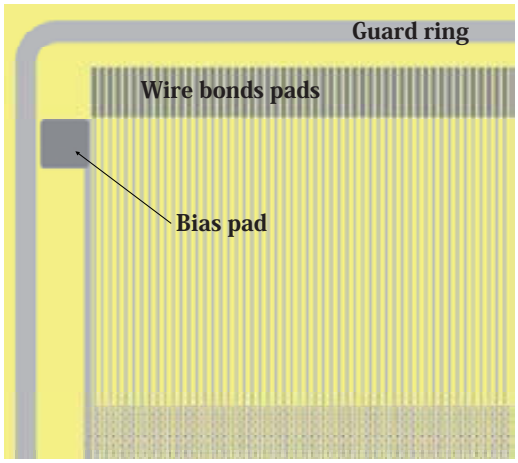

Features

- 128 strips
- 125 electrodes/strip
- 10 mm long strips
- 80 µm pitch distance
- DC coupled
- Both polarization bias pad and readout strips on top surface
- 5 µm holes diameter
- 1 cm^2 sensitive area
- Variable oxide thickness

Figure 5.6: *Layout of the U3DTHIN microstrip detector (left), and design characteristics (right).*

The first batch of U3DTHIN detectors have been fabricated on n-type wafers. Additional fabrication masks for p-stop insulation of the n^+ strips are also at our disposal to fabricate detectors on p-type silicon for electrons readout.

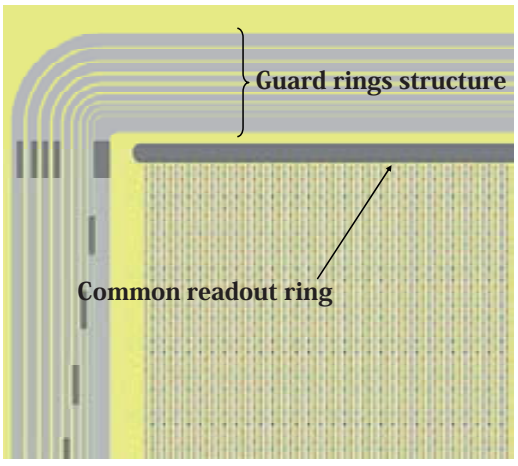

Features

- 59 strips
- 59 electrodes/strip
- All strips of the same type shorted to one electrode
- 80 µm pitch distance
- DC coupled
- Both polarization bias pad and readout strips on top surface
- 5 µm holes diameter
- 0.5 × 0.5 cm^2 sensitive area
- Variable oxide thickness

Figure 5.7: *Layout of the U3DTHIN PAD detector (left), and design characteristics (right).*

[1] U3DTHIN detectors are insensitive to gamma and neutron backgrounds but by using a converter layer containing ^{10}B it is possible to measure neutrons from alphas from the reaction $n + {}^{10}B \rightarrow {}^{7}Li + {}^{4}He$.

5.2.2 TCAD simulations

TCAD simulations are used to study the electrical characteristics and the technological properties of the U3DTHIN detectors in order to find the optimum parameters for the detector geometry and the fabrication process. The simulated geometries are two three-dimensional cells whose surface are 80 µm × 80 µm and two thicknesses 10 and 20 µm. Four n^+ columnar electrodes are located in the four corners plus the central p^+ electrode for holes readout, as it is shown in figure 5.8a. The diameter of the columnar electrodes is 5 µm and their doping concentration is 10^{19} cm^{-3} for both boron (p-type) and phosphorous (n-type).

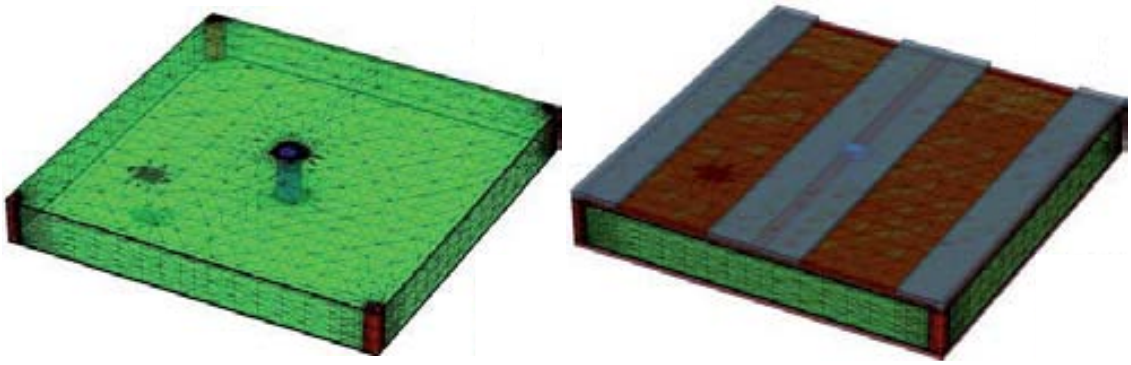

Figure 5.8: *3D cell used in the simulations. The picture on the left shows the silicon sensor volume with the mesh, and the one on the right includes also the oxide layers and the aluminium strips. The thickness of this design is 10 µm.*

The substrate consists of n-type silicon whose doping concentration is 10^{12} cm^{-3}, corresponding to a resistivity of 4 kΩ·cm. The thickness of the buried oxide inside the SOI wafer is 1 µm, while the oxide grown at the top surface is 0.8 µm. The contacts are made using 1 µm thick aluminium strips with a width of 20 µm, as it can be seen in figure 5.8b. The accumulated positive charge in the Si/SiO_2 interface plays an important role in such a thin detector as is detailed later. For this reason, several values of this parameter have been implemented in the simulations in order to study how it affects the sensor behaviour.

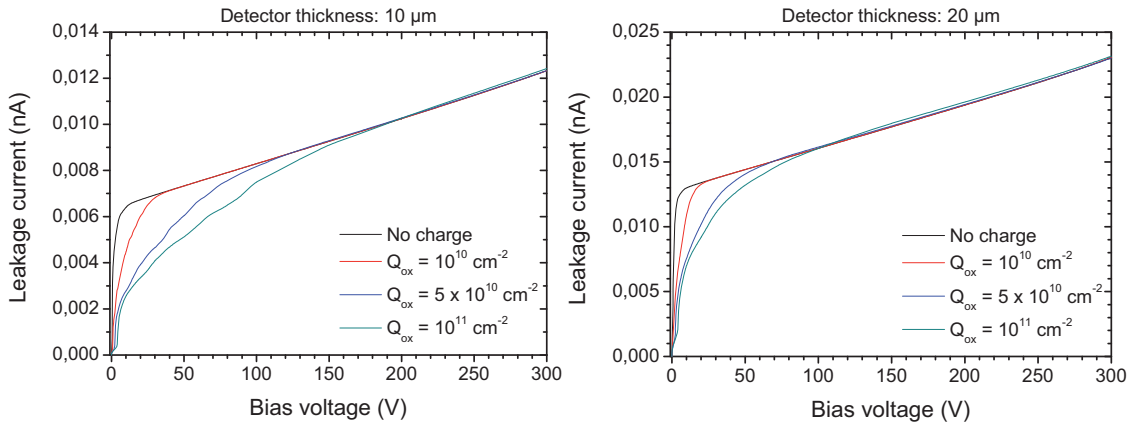

Figure 5.9: *Current-voltage characteristics of the simulated cells for substrates of 10 µm (left) and 20 µm (right) thicknesses. The temperature was set to 20ºC.*

The leakage current obtained from the simulations for the two 3D cells are shown in figure 5.9. As expected, the currents rise rapidly up to the full depletion voltage and after that their increase is slower. The current for the detector of 20 µm doubles the one from 10 µm as corresponds to the linear dependence of the reverse current with the size of the sensor volume. Neither of the simulated currents reaches electrical breakdown up to 300 V what means that the field plate effect provided by the wide metal strips is preventing from high fields up to that voltage. It is remarkable to note the quantitative influence of the accumulated charge on the two detector thicknesses under study. In the case of 10 µm the increasing interface charge involves higher voltages to reach the saturation reverse current than in the case of 20 µm. This behaviour is given by the need of higher voltages to deplete the inversion layer of electrons to effectively fully deplete the sensor. From the simulations results of figures 5.10 and 5.11 it can be deduced that the required voltage to fully deplete ultra-thin 3D detectors with the same pitch is higher if the sensor is thinner due to the proximity of both top and bottom electron layers.

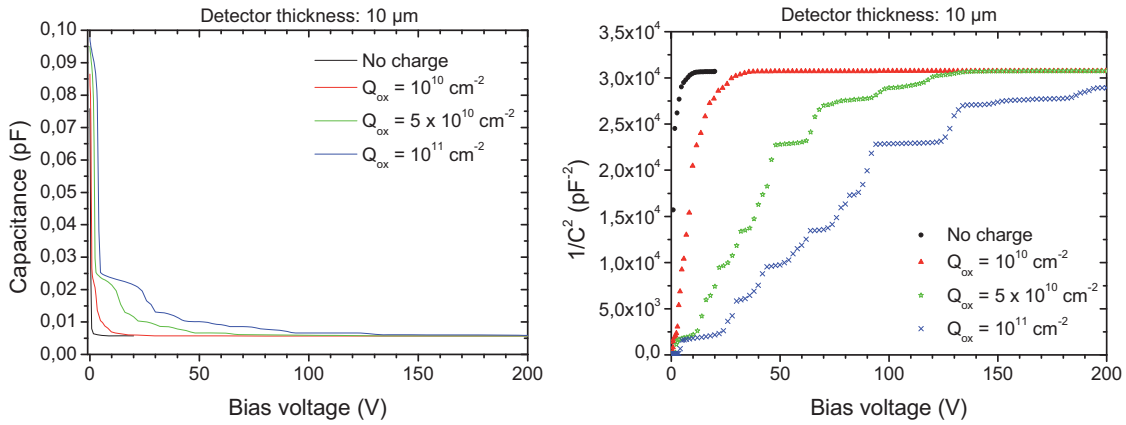

Figure 5.10: *Capacitance-voltage characteristics of the 3D cell for the detector whose thickness is 10 µm. The terraced shape of the right-handed figure is due to the mesh size at the surfaces during the depletion of the electron channel. The temperature was set to 20ºC.*

The capacitance-voltage characteristic of the 10 µm detector and the $1/C^2$ versus voltage are plotted in figure 5.10. As it was previously commented, the voltage required to fully deplete the detector depends strongly on the accumulated charge in the Si/SiO_2 interface. The simulations were performed at room temperature, 20ºC, using an AC signal at 10 kHz. From equation **86**, which gives the capacitance of a cylindrical capacitor, it is possible to calculate a nominal value for the capacitance of 0.0021 pF, different from the capacitance resulting from the simulations 0.0057 pF. As it will be discussed later, the metal strips play an important role in the electrical behaviour of very thin sensors because of the field plate effect that makes the depletion region to grow parallel to the strips. Approximating the simulated 3D cell as a planar detector with a central p^+ strip surrounded by two n^+ strips, as in figure 5.13b, the resulting capacitance is closer to the simulated value, resulting 0.0041 pF from equation **85**.

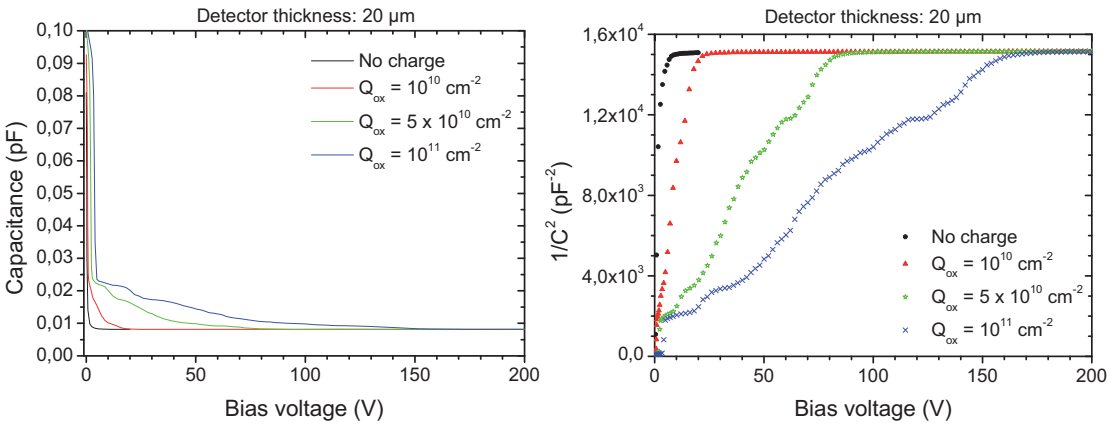

Figure 5.11: *Capacitance-voltage characteristics of the 3D cell for the detector whith thickness of 20 µm. Temperature 20ºC.*

In the case of 20 µm, the capacitance-voltage characteristics are shown in figure 5.11a obtaining a value of 0.0081 pF, again different from the theoretical value obtained for a coaxial detector which is estimated in 0.0042 pF. Using once again the approximation of this 3D cell as two planar capacitors in parallel the resulting value is 0.0083 pF. This approximation trend is only useful for very thin detectors because of the influence of the field plate on the potential distribution within the sensor, but for larger thicknesses it is expected that it is not working anymore as this influence is negligible after several microns of depth from the top surface and the rest of the sensor volume is dominated by the 3D geometry, as shown in figure 5.13a.

Electrostatic potential

Despite of the use of columnar 3D electrodes in the design of the detectors, the potential distribution, and thus the space charge region, presents a growth parallel to the metal strips as if the electrodes were implantations using standard planar technology, as shown in figure 5.13b. This behaviour can be seen in figure 5.12a where it is shown the potential distribution within the 10 µm detector in full depletion and in absence of oxide interface charge.

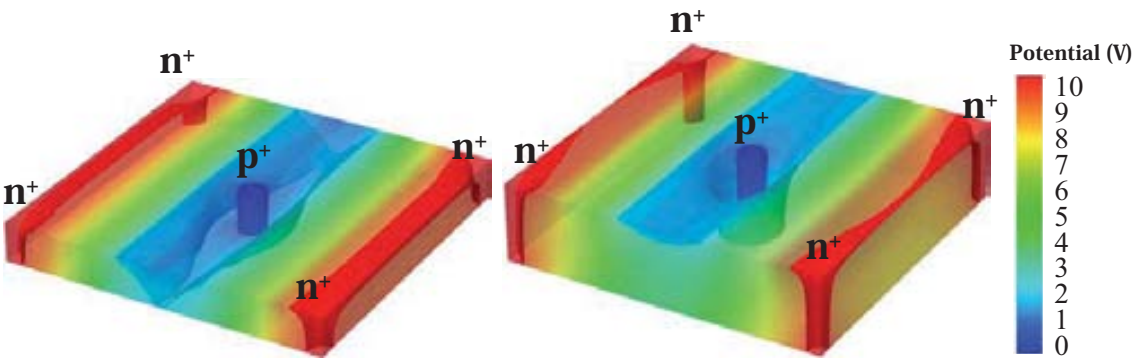

Figure 5.12: *Potential distributions within the volume of the 10 µm (left) and 20 µm (right) sensors for an applied voltage of 10 V in absence of charge at the Si/SiO₂ interface. The isopotential surfaces correspond to 0, 2 and 10 V.*

In the 20 µm detector, see figure 5.12b, the potential distribution at the top surface is also parallel to the metal strips, as occurred in the 10 µm detector. However, at the bottom surface the distribution is almost radial as it should correspond to columnar electrodes, so that there is a gradual fusion of both potential distribution shapes in the volume that depends on the distance from the top surface where are located the metal strips that promote this surface effect.

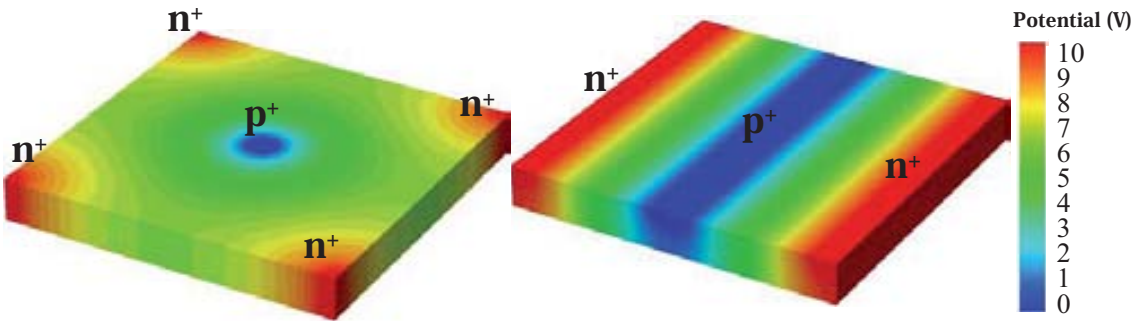

Figure 5.13: *Potential distributions within 10 µm of silicon for a configuration of columnar electrodes (left) and strip implantations (right).*

The field plate is not the only surface effect that must be taken into account in those detectors. In figure 5.14 are shown the potential distributions that correspond to the 10 µm and 20 µm detectors at full depletion when the charge in the Si/SiO_2 interface is 10^{10} cm^{-2}. The positive oxide charge attracts electrons from the bulk thus confining the substrate between two negatively charged layers. This negative charge extends the applied bias on the n^+ electrodes thus surrounding the top and bottom sides of the p^+ column. At the top surface, the metal strips create a field plate effect that enlarges the space charge region from the junction to the edge of the metallization. Applying a positive bias to the n^+ electrodes makes the space charge region to grow in two different ways: *1)* radial growth from the junction column at the bottom surface as corresponds to columnar electrodes, and *2)* parallel growth from the edge of the metal strips at the top surface. The main effect of the accumulated electrons below the oxide layers is to increase the required bias voltage to deplete the detector.

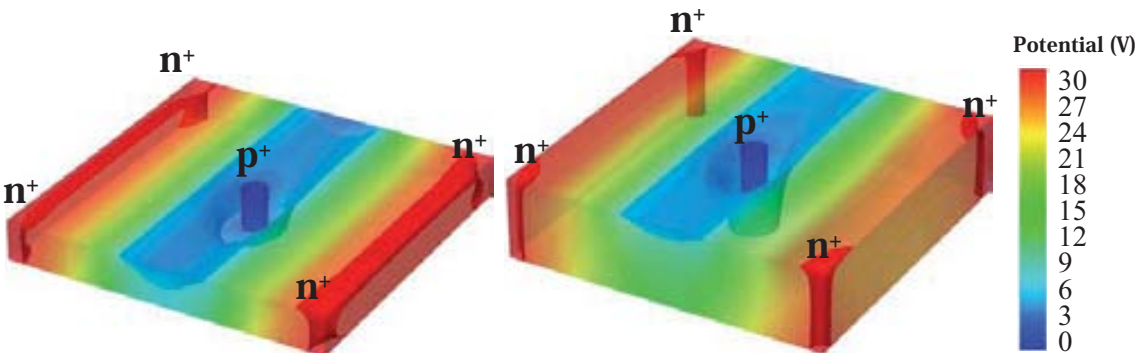

Figure 5.14: *Potential distributions within the volume of the 10 µm (left) and 20 µm (right) sensors for an applied voltage of 30 V when the charge at the Si/SiO_2 interface is set to 10^{10} cm^{-2}. The isopotential surfaces correspond to 0, 6 and 30 V.*

Electric field

The electric field distribution in ultra-thin 3D detectors is also dominated by the field plate effect as a consequence of the potential distribution described earlier. The potential drop between opposite electrodes at the top surface detector is carried out parallel to the metal strips what implies that the electric field profile is the same along the strips in that region. High field peaks are formed at the end of the metallization of each n^+ and p^+ electrodes due to the severe potential drop at the edge of the field plates, being higher at the end of the readout strip, p^+, as the substrate is n-type.

In coaxial detectors there is a severe potential drop from the junction column that leads to high field peaks around the cylindrical electrodes, as expressed in equation **77**. This effect is slightly observed in the 10 μm detector because the potential drop is disturbed by the field plate. However, in a thicker detector, as in the 20 μm, the high field peaks surrounding the bottom of the columnar electrodes are more appreciated as it can be seen in figure 5.15b.

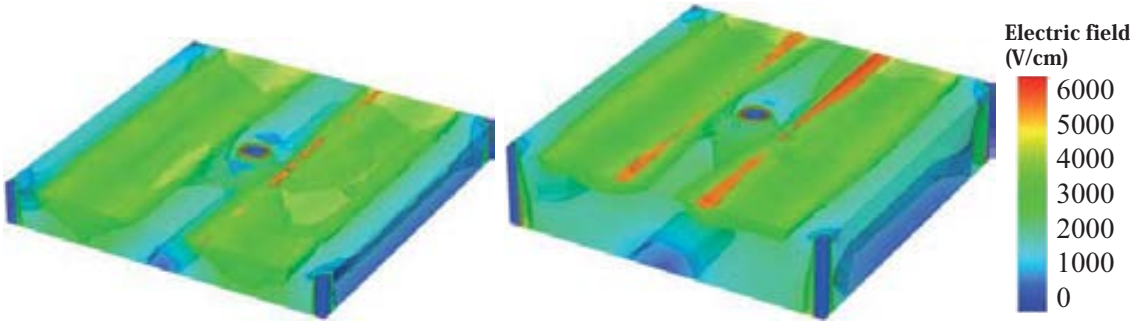

Figure 5.15: *Electric field distributions within the volume of the 10 μm (left) and 20 μm (right) sensors for an applied voltage of 10 V and without charge at the Si/SiO_2 interface. The isofield surfaces correspond to 1000, 3000 and 5000 V/cm.*

The introduction of oxide interface charge in the detector increases the inversion layer below the oxides causing an increment of the field peak at the end of the readout strips, shown in figure 5.16. This occurs because of a more severe potential drop that takes place at the end of the field plate and the beginning of the electron channel, due to attracted electrons from the bulk by the positive fixed charge of the oxide interface.

The same trend is obtained at the bottom surface, reaching higher values of field peaks where the electron channel meets the p^+ electrode. The contrary effect is therefore found at the ohmic columns, n^+, resulting in lower fields.

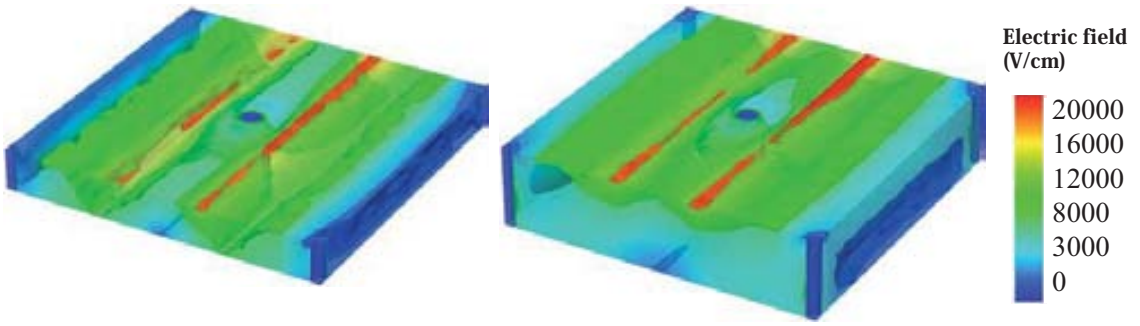

Figure 5.16: *Electric field distributions within the volume of the 10 μm (left) and 20 μm (right) sensors for an applied voltage of 30 V when the charge at the Si/SiO_2 interface is set to 10^{10} cm^{-2}. The isofield surfaces correspond to 2000, 9000 and 18000 V/cm.*

5.2.3 Fabrication process

Four n-type silicon SOI wafers were fabricated at the IMB-CNM (CSIC) Clean Room facilities. These wafers consisted of 10 µm high resistivity silicon (ρ > 1 k·Ωcm), then a layer of 1 µm of SiO_2 and finally 300 µm of low resistivity silicon as support wafer.

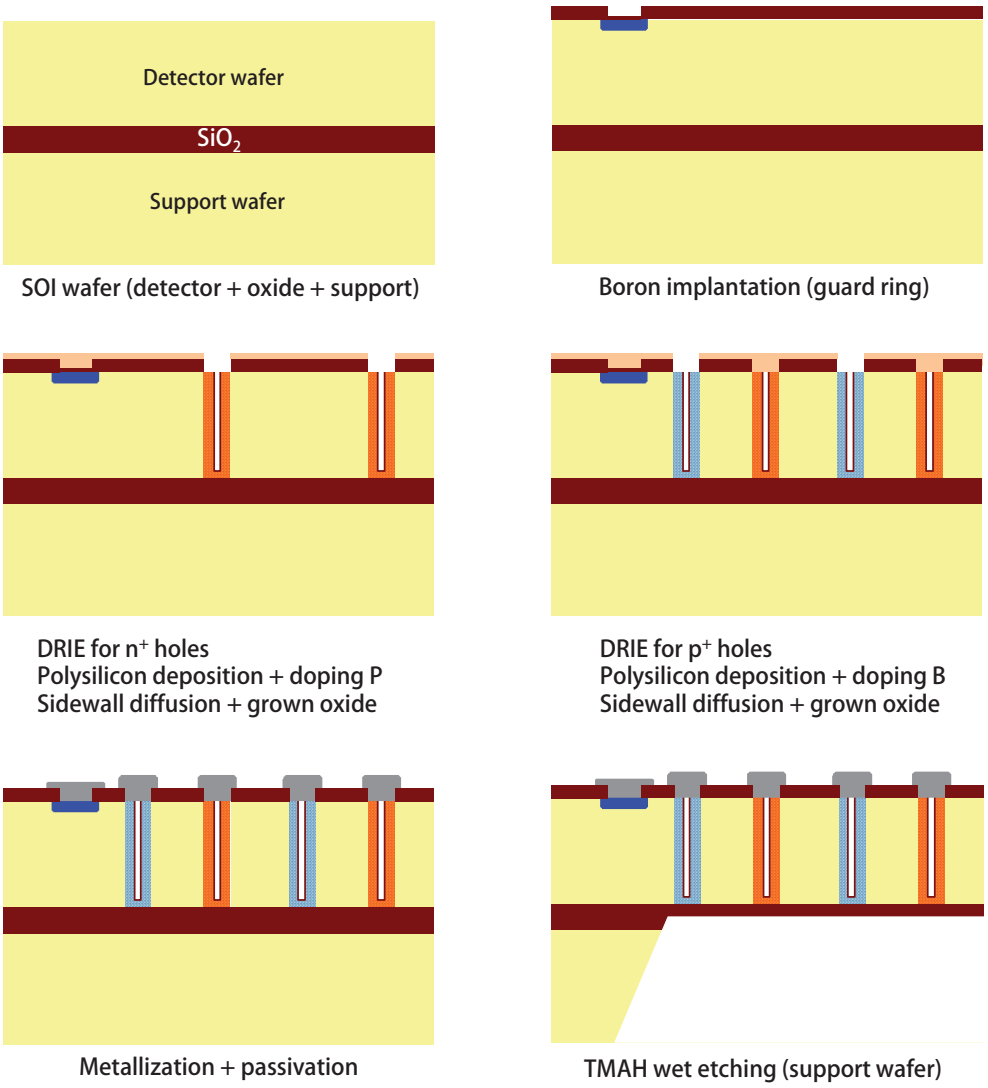

Figure 5.17: *Schematics of the fabrication process of U3DTHIN sensors [39][40].*

At first stage it is carried out the p^+ implantation of the guard ring used to collect any possible surface current from the cut edge. Then it is performed the photolithography for the creation of the n^+ holes by depositing a 2 µm layer of photoresist that is subsequently illuminated through the n^+ *holes mask* with UV light, and then annealed for hardening. Holes with diameter 5 µm are etched using inductively coupled plasma (ICP) as described in section 4.2.2, then they are partially filled with 1 µm of polysilicon. The phosphorous doping of polysilicon is made using $POCl_3$ at 1050ºC for 40 minutes. The same processes are repeated next for the creation of the p^+ columnar electrodes, in which the boron doping is made by annealing in front of a ceramic wafer of boron nitride (BN) at 1150ºC for 5 minutes. Both n^+ and p^+ electrodes are later metallized with 1 µm of aluminium/copper and passivated with 1 µm of silicon

oxide plus 0.5 µm of silicon nitride. The final step consisted on the wet etching of the support wafer for the entrance window of figure 5.5 using a TMAH solution which stops at the silicon/oxide interface of the SOI wafer. The entrance oxide of the SOI wafer is not etched off in this first batch of U3DTHIN detectors, however in upcoming batchs it is foreseen to be completely etched and then be deposited by using an atomic layer deposition (ALD) equipment available at IMB-CNM (CSIC) in order to create a thinner oxide entrance window (tens of nanometers) to passivate the backside surface.

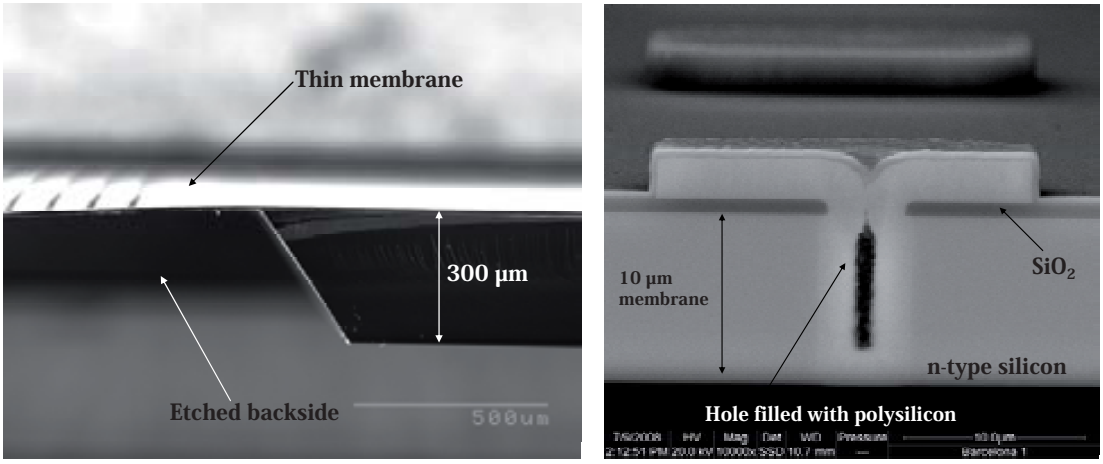

Figure 5.18: *SEM pictures of the thin membrane (left), and cross section of one U3DTHIN electrode filled with polysiclion (right) from test wafers.*

The resulting membrane of U3DTHIN detectors and a cross section of one hole filled with polysilicon from test wafers are shown in figure 5.18. The thickness of the deposited polysilicon was 2 µm instead of the 1 µm employed in working detectors, as it can be seen in figure 5.18b. Pictures of the resulting wafers are shown in figure 5.19, where the left-handed figure shown the front view of a wafer containing PAD and microstrip detectors not thinned, and the right-handed figure shows the back side of a wafer containing thinned microstrip detectors.

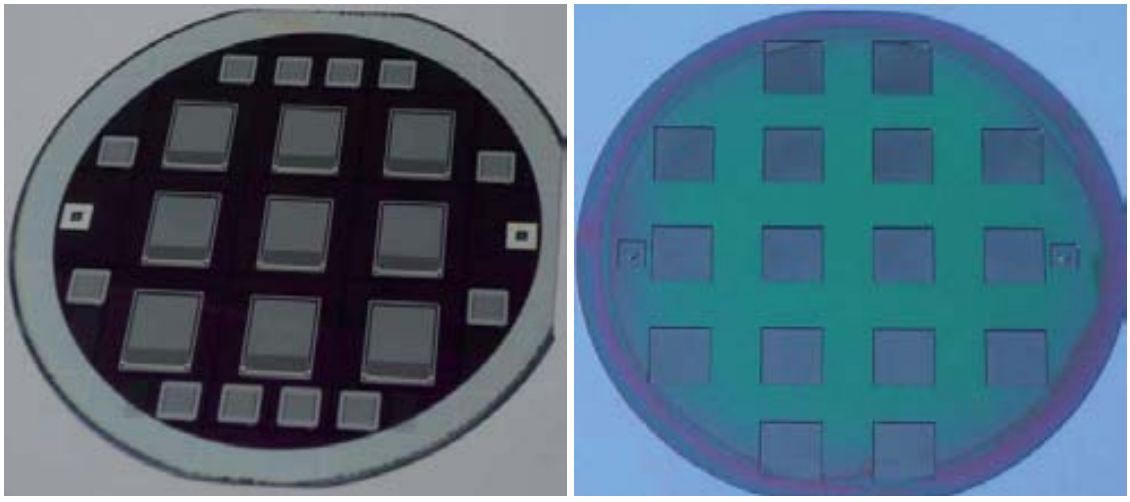

Figure 5.19: *Front view of a processed wafer containing 12 PAD and 9 microstrip detectors not thinned (left) and back side view of a wafer containing 16 thinned microstrip detectors (right).*

Figure 5.20 shows optical microscope images of U3DTHIN detectors. The left-handed figure corresponds to one microstrip detector showing the guard ring, the bias

pad and wire bonds pads, as in the detector layout of figure 5.6. The right-handed figure corresponds to one PAD detector where the guard ring structure and the bias pad electrode are clearly appreciated.

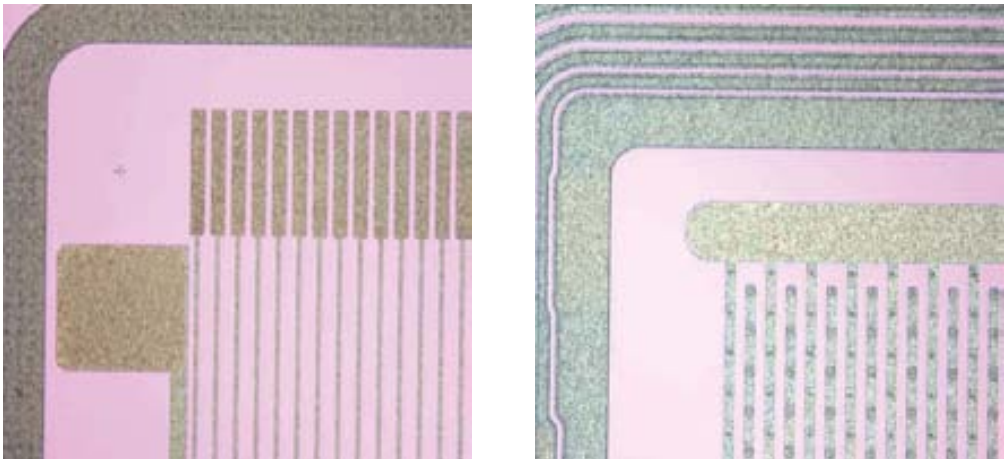

Figure 5.20: *Pictures corresponding to the U3DTHIN microstrip (left) and PAD (right) detectors using an optical microscope.*

5.2.4 Experimental results

Current-voltage and capacitance-voltage characteristics of U3DTHIN PAD and U3DTHIN microstrip detectors were performed at 20ºC at IMB-CNM (CSIC) facilities. The measured detectors belonged to the four processed wafers although there are specifications concerning those wafers that must be commented: only two of the four wafers (labelled #3 and #4) were treated with the TMAH solution on the support wafer needed to open the entrance. The other wafers #1 and #2 were not etched and were used to compare the effect of the membrane on the electrical characterization. Some examples of the measured leakage currents are shown in figure 5.21 compared with the simulation results that correspond to an oxide surface charge of 10^{10} cm^{-2} which has better agreement with both IV and CV experimental curves. Positive oxide charge is found in Si/SiO_2 interfaces when nearly all of the dangling bonds[2] of the silicon crystal boundary are saturated resulting in 10^{10} – 10^{12} cm^{-2} (depending on the quality of the grown oxide) on silicon with <1 0 0> orientation [24][122]. Increasing this surface charge in U3DTHIN detectors greatly affects their depletion voltage, as it can be seen in figure 5.10.

[2] Dangling bonds at the Si/SiO_2 interface are unsatisfied chemical bonds as a result of excess Si, excess O and impurities acting as interface trap states.

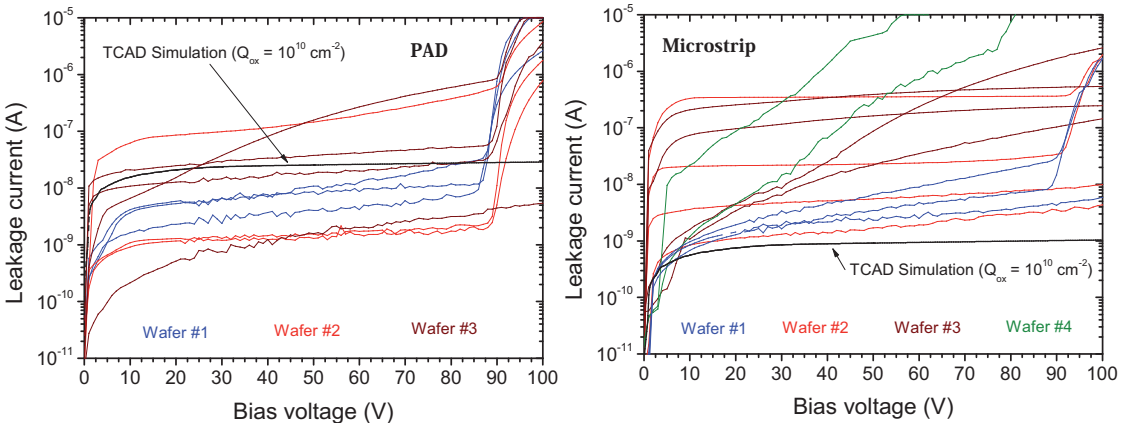

Figure 5.21: *Leakage current measurements of U3DTHIN PAD detectors (left) and from one single strips (right) performed at 20ºC.*

Experimental leakage currents on both detectors range from nanoamperes to tens of nanoampers in most of the cases, as it can be seen in both graphics in figure 5.21. Comparing the simulation result for the PAD detector, there is only agreement with the case of higher currents, while in the case of single strips better agreement is found for low currents. Measurements of wafer #3 and #4 show higher currents because of the mechanical stress of the thin membrane.

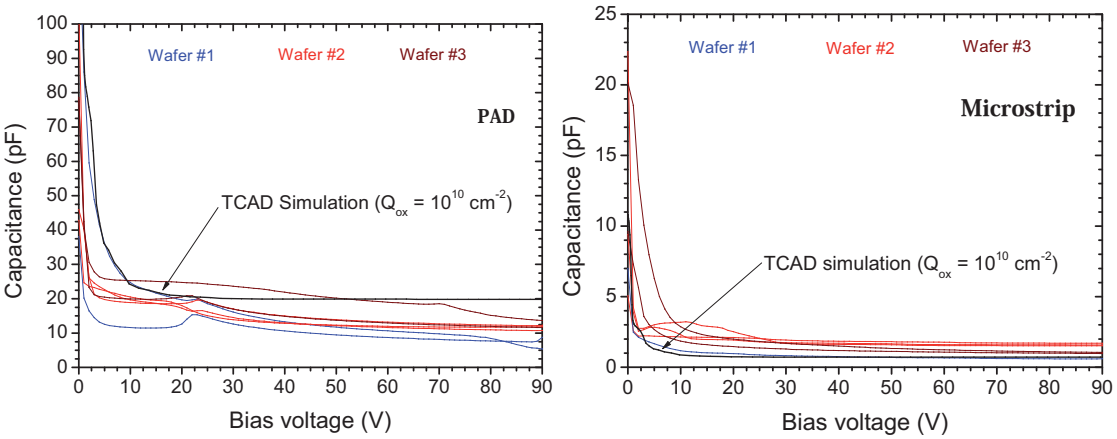

Figure 5.22: *Capacitance-voltage measurements of U3DTHIN PAD detectors (left) and from one single strip from the U3DTHIN microstrip detectors (right) performed at 20ºC.*

Measurements of the interstrip resistance were realized at 20ºC for several detectors from the four produced wafers obtaining values in the order of 10 GΩ, having an adequate interstrip insulation. Capacitances from PAD detectors and from single strips of microstrip detectors are shown in figure 5.22. The measurements were performed at 20ºC using an AC signal of 10 kHz. Both PAD and microstrip detectors evidenced a severe capacitance drop before 5-10 V, while this drop takes place around 10 V in the simulation. In PAD detectors, the value of the capacitance were 12 – 20 pF at 20 V, while for the single strip the values were 1 - 3 pF at 20 V, in agreement with expected value found in simulations.

Alpha source setup

An Americium-241 alpha source with an activity of 33 kBq was used to evaluate the U3DTHIN detectors for the detection of alpha particles of several MeV. First experimental measurements of alpha detection were carried out using not-thinned detectors from wafers #1 and #2 illuminated from the top surface, as it can be seen in the alpha setup of figure 5.23

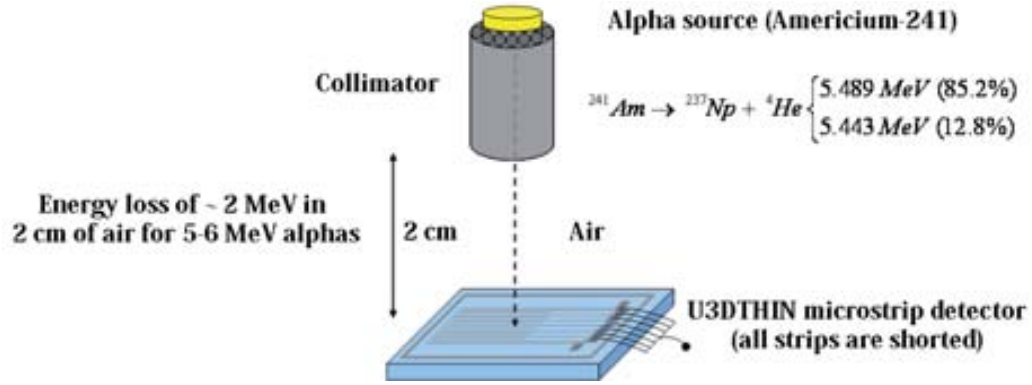

Figure 5.23: *Sketch of the alpha source setup using an U3DTHIN microstrip detector.*

According to the setup used to evaluate the microstrip detector, the energy loss in 2 cm of air for alpha particles with an energy of 5-6 MeV has been estimated using SRIM[3] resulting in ~ 2 MeV, so that the expected energy for alphas coming from ^{241}Am is around 3.5 MeV. The ranges for alphas of 3.5 MeV (source at 2 cm from the detector) and 5.5 MeV (alphas close to the detector) are estimated also using SRIM for the two possible cases: *1)* particle crossing the passivation oxide (0.8 µ,m) plus the silicon substrate, and *2)* particle crossing the aluminium strip (1 µm), the oxide (0.8 µm) and silicon. The resulting ranges and energy losses are shown in table 5.1.

Table 5.1: Energy losses and ranges of 5.5 MeV alpha particles in U3DTHIN detectors using SRIM.

	Alpha source at 2 cm	**Alpha source at 0 cm**
Energy loss in air	~ 2 MeV	0
Range crossing ***Al (1 µm) + SiO_2 (0.8 µm) + Si***	14.8 µm	27.9 µm
Range crossing ***SiO_2 (0.8 µm) + Si***	14.9 µm	28.3 µm
Energy loss in 10 µm Si	~ 2 MeV	~ 1.5 MeV

As the thickness of the silicon substrate of the detector is 10 µm, the energies deposited by alphas at two different distances from the source are also included in table 5.1. The measurements were performed at room temperature using a data acquisition system developed at IMB-CNM (CSIC) [123], obtaining the alpha spectrum of figure 5.24 after 25 minutes of sampling time. The different heights of voltage pulses are classified in 450 channels in the multi channel analyzer (MCA) with the threshold set in channel 40. As it is shown in table 5.1, the energy deposited by a 5.5 MeV alpha when

[3] Stopping and Range of Ions in Matter (SRIM) is a collection of software packages which calculate many features of the transport of ions in matter.

the ^{214}Am is placed at 2 cm from the detector (where it arrives with 3.5 MeV) is ~ 2 MeV, so alphas were not completely absorbed in 10 μm of silicon substrate.

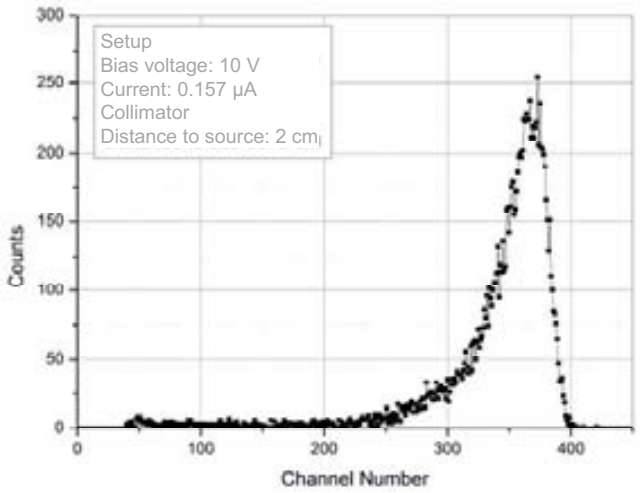

Figure 5.24: *Alpha spectrum from the radioactive source ^{241}Am [124].*

5.3 3D-DDTC detectors

The Large Hadron Collider (LCH) accelerator complex will undergo a series of upgrades to increase the integrated luminosity by a factor of 10 in the coming years. In order to cope with the higher luminosity, the ATLAS experiment of the LHC will need to be upgraded. The first upgrade consists of the introduction of a new inner pixel layer, called *Insertable B-Layer (IBL)*, initially proposed for the first long shutdown of LHC by 2013, while the second upgrade will replace the entire ATLAS tracking detector, expected by 2020.

Table 5.2: *Specifications for FE-I3 and FE-I4 pixel sensors [125, 126].*

	FE-I3	**FE-I4**
Pixel size	50 × 400 μm^2	50 × 250 μm^2
Pixel array	18 (col) × 160 (rows)	80 (col) × 336 (rows)
Chip size	7600 × 10800 μm^2	18860 × 20560 μm^2
Active fraction	74%	89%
Data rate	40 Mb/s	160 Mb/s

The pixel size of the current pixel sensors present in the inner detector of ATLAS, FE-I3 sensors, are unable to cope with the increasing hit rate due to the higher luminosity expected for the IBL and would cause pile up. Hence a smaller geometry is needed to reduce the pixel cross section, FE-I4 sensors, also obtaining an increasing in the total active fraction area of the sensor as the peripheral dead areas are also reduced using 3D guard rings and guard fences[4].

ATLAS is investigating radiation hard sensors able to withstand this high luminosity. Silicon 3D sensors are a suitable choice as their short collection distance and low full depletion voltages make them intrinsically radiation hard, significantly

[4] Guard fence: termination structure composed by ohmic columns.

reducing two of the main effects of radiation damage in silicon: increasing depletion voltages and reduction of the charge collected due to charge trapping.

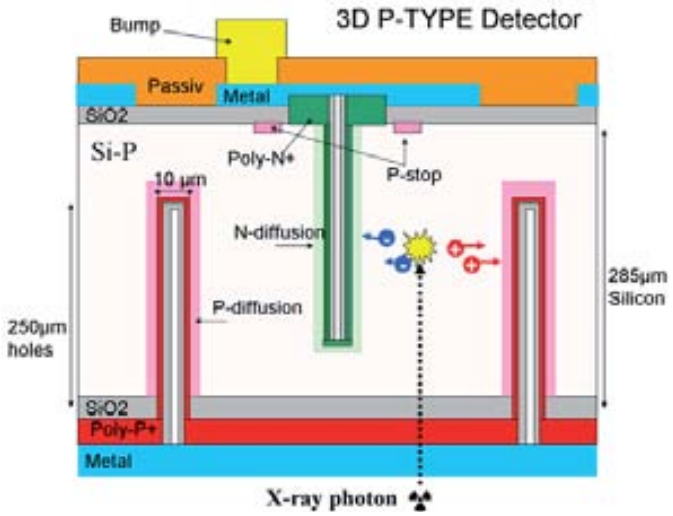

Figure 5.25: *Schematic of the 3D-DDTC design developed by IMB-CNM [37]. This model corresponds to a p-type silicon substrate.*

The future modules of the ATLAS Upgrade innermost detector and the Insertable B-Layer are composed by planar pixel sensors and 3D pixel sensors. The columnar electrodes of these 3D sensors are etched from both sides of the wafer without reaching the opposite surface of the substrate. This alternative 3D architecture, called *3D double-sided double type columns 3D-DDTC* [40], is simpler and cheaper to fabricate than the full 3D detectors as they do not need support wafer. The distribution of the pixels is adapted to the Front-End I-4 (FE-I4) read-out electronics [127], whose cell dimensions are 50 µm × 250 µm.

In order to study the radiation hardness of 3D detectors, 80 µm × 80 µm strip detectors in 3D architecture have been developed at IMB-CNM (CSIC). The irradiation of these strip detectors was performed at the Karlsruhe Institute of Technology with 25 MeV protons and their electrical characterization were carried out at the Universities of Freiburg [128, 129] and Glasgow [130], as well as at the IMB-CNM (CSIC) facilities [131, 132]. The results revealed that p-type detectors irradiated at 2×10^{15} n_{eq}/cm^2 presented charge multiplication effect for voltages above 150 V, while it was not found any significant difference between n and p-type after fluence of 2×10^{16} n_{eq}/cm^2. TCAD simulations on p-type substrates have been carried out as a part of the study of the behaviour of 3D sensors for the ATLAS 3D collaboration.

5.3.1 Detectors layouts

3D-DDTC detectors have been fabricated in both n and p-type silicon substrates, nevertheless this study is focused in the p-type ones for their higher radiation tolerance, faster collection times (electrons readout) and the charge multiplication effect reported in experimental measurements [128, 129].

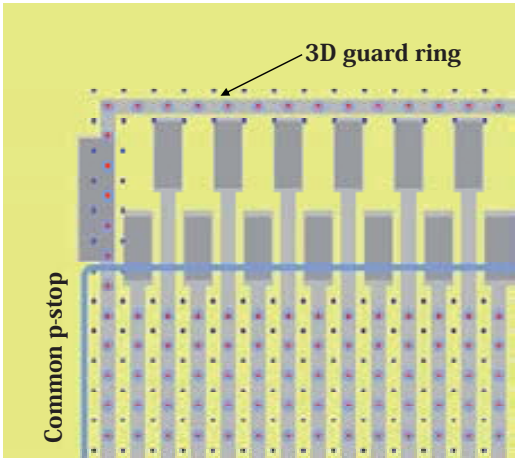

Features

- 3D guard ring
- 50 strips
- 50 electrodes/strip
- 4 mm long strips
- 80 µm pitch distance
- DC coupled
- Backplane contact for backside electrodes
- p-stop insulation for n^+ electrodes (p-type substrate)
- Common p-stop surrounding sensor area (p-type substrate)

Figure 5.26: *Layout of the p-type silicon strip detector (left), and design characteristics (right).*

Aluminium strips are used to collect the signal in the microstrip design, as it is shown in figure 5.26a, while the backplane is fully covered with aluminium for the contact of the backside electrodes. A common p-stop ring surrounding the sensor area has been added for insulation from possible surface currents from the cut edge, working as a channel stopper. The columns have a diameter of 10 µm and 250 µm depth.

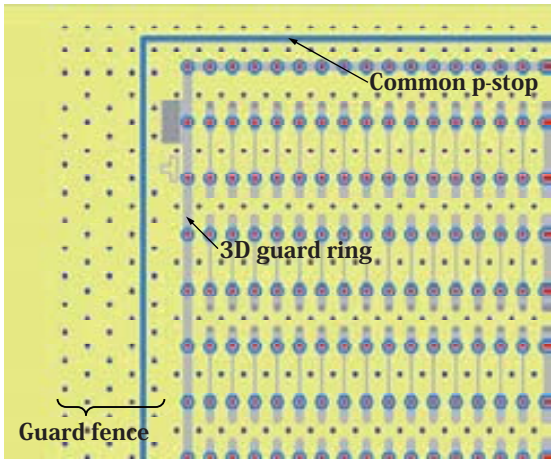

Features

- 3D guard ring
- Guard fence (ohmic columns)
- 80 × 336 pixels array
- Pixel size: 50 µm × 250 µm
- 200 µm dead region
- DC coupled
- Backplane contact for backside electrodes
- p-stop insulation for n^+ electrodes (p-type substrate)
- Common p-stop surrounding sensor area (p-type substrate)

Figure 5.27: *Layout of the p-type FE-I4 detector (left), and design characteristics (right).*

The layout of one pixel of the FE-I4 sensor is shown in figure 5.28. Each pixel is formed by two 3D cells where the n^+ electrodes are connected by an aluminium strip. The columns have a diameter of 10 µm and their depth is 210 µm. An array of 80 × 336 pixels forms the active area of the sensor reaching a total surface of 18860 × 20560 μm^2 (~ 2 cm^2), as it can be seen in table 5.2. The inactive region in these detectors is reduced to 200 µm at the edges where the guard fence is composed by 2 ohmic columns, and 400 µm when the guard fence has 5 ohmic columns.

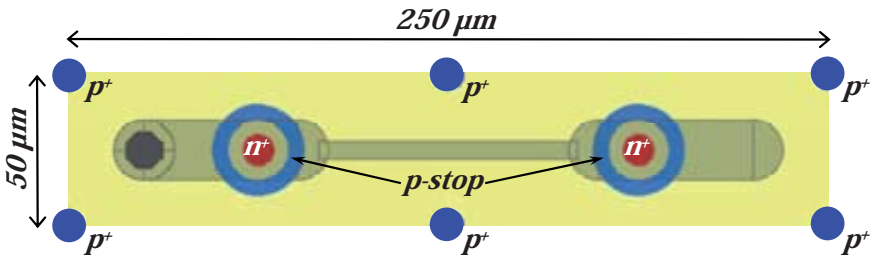

Figure 5.28: *Layout of one pixel of the FE-I4 sensor.*

5.3.2 TCAD simulations

The 3D cells used in the simulations of the microstrip detector are shown in figure 5.29a and figure 5.37a. They consist of tetrahedrons whose dimensions are 80µm × 80 µm × 285 µm, whose electrodes distribution depends on the nature of the information it is required to obtain. Thus the 5-columns 3D cell (4 ohmic columns in the corners plus 1 junction column in the center) is used to study the charge collected by the junction column n^+, and the 4-columns 3D cell (2 ohmic plus 2 junction columns) is used for obtaining information of induced charge on neighbouring electrodes. The cell used for the FE-I4 sensor is shown in figure 5.31a, whose dimensions are 50 µm × 125 µm × 230 µm. In all of the cases, the doping concentration of boron in the silicon substrate is 7×10^{11} cm^{-3}, corresponding to a resistivity of 19 kΩ·cm. The diameter of the columns is 10 µm and their depth is 250 µm in the case of the microstrip and 210 µm for the FE-I4 sensor. The doping concentration of the columns is 10^{19} cm^{-3} for both n^+ and p^+ electrodes. In p-type substrates an insulation method is required for prevention from shorts between n^+ electrodes. The insulation consists of a p-stop ring surrounding each of the n^+ electrodes, with a doping concentration of 8×10^{16} cm^{-3}. Both front and back surfaces of the cells are covered by an oxide layer of 0.8 µm. The oxides have opened windows for the metallization of the contacts for readout strips at the top, and for the backplane contact at the bottom, which is entirely covered by aluminium. Finally, the fixed positive charge in the Si/SiO_2 interface is taken into account by a surface charge density of 5×10^{11}cm^{-2}.

Before irradiation

Electrical properties of 3D cells before irradiation are simulated in this section. The first stage consisted of the bias ramping of the cell in order to get the current-voltage characteristics and thus obtaining information concerning the breakdown voltage and the electrostatic potential and electric field distributions along the volume. Figure 5.29a shows the 3D cell used in the simulations of the microstrip.

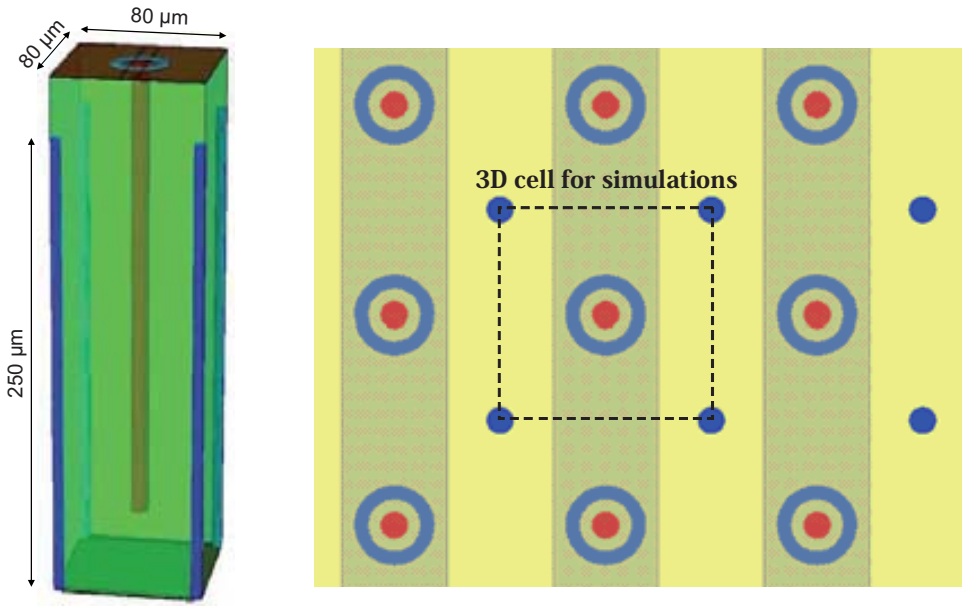

Figure 5.29: *3D cell used in the simulations of the microstrip detector.*

Given the low depletion voltage of the 3D geometry, the leakage current of the cell starts to saturate to 0.20 – 0.25 nA at low operation voltages. As the reverse bias is increased the current rise up rapidly around 250 V and reaches the electrical breakdown approximately at 290 V, as it is shown in the figure 5.30a.

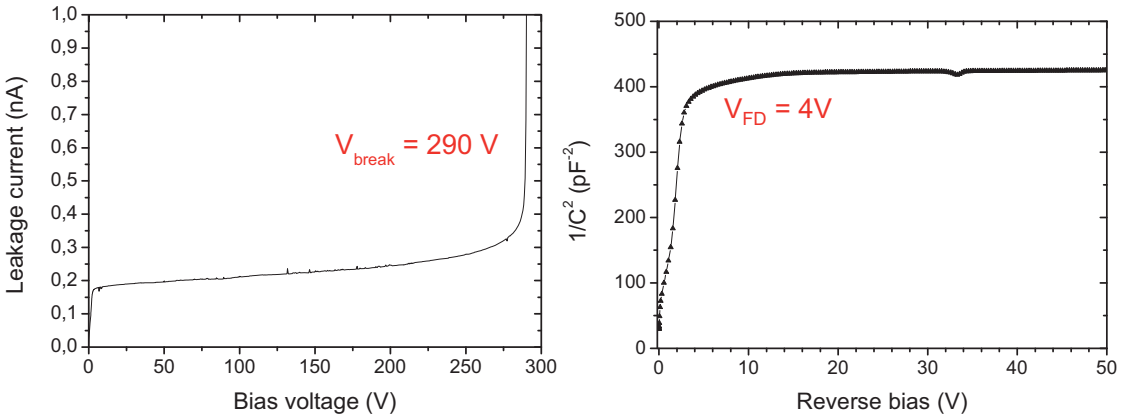

Figure 5.30: *Current-voltage (left) and capacitance-voltage (right) characteristics obtained from the 3D cell of the microstrip detector at a temperature of 20ºC.*

The capacitance of the 3D cell has been simulated also at room temperature, 20ºC, rising the bias up to 50 V with an AC signal at a frequency of 10kHz. Using the equation **86** for the approximation of this capacitance by the one of a cylindrical capacitor whose overlapping depth between columns is 215 µm, a value of 0.057 pF is obtained, according to the result of the simulations.

Substituting $r_{ext} = 40\mu m\sqrt{2} - r_{column}$ and $r_{\text{int}} = r_{column} = 5\mu m$ as the external and internal radii of the cylindrical capacitor in the equation **78**, the resulting nominal value for the lateral depletion is 2.6 V. From the $1/C^2$ plot of the figure 5.30b is deduced that the lateral depletion voltage is in the range 3 - 4 V while the full depletion voltage is

around 20 V, once the depletion region is extended from the tip of the n^+ column to the back surface. An unexpected tip is obtained for 34 V in the CV characteristic although it can be more appreciated in figure 5.30b. In experimental measurements of figure 5.56 a second drop in the CV is registered at the same bias (~ 35 V) corresponding to the depletion of both electron layers at the top and bottom Si/SiO_2 interfaces, however the simulator does not seem to reproduce such change in the capacitance, probably because the method used to define the oxide surface charge was using fixed positive charge at the interface and maybe the using of trapped positive charge could solve this problem. Another behaviour that support the second drop in the capacitance (and hence the real depletion voltage) is found in figure 5.47a, where the full collection of the charges introduced by the incident particle is obtained at 50 V.

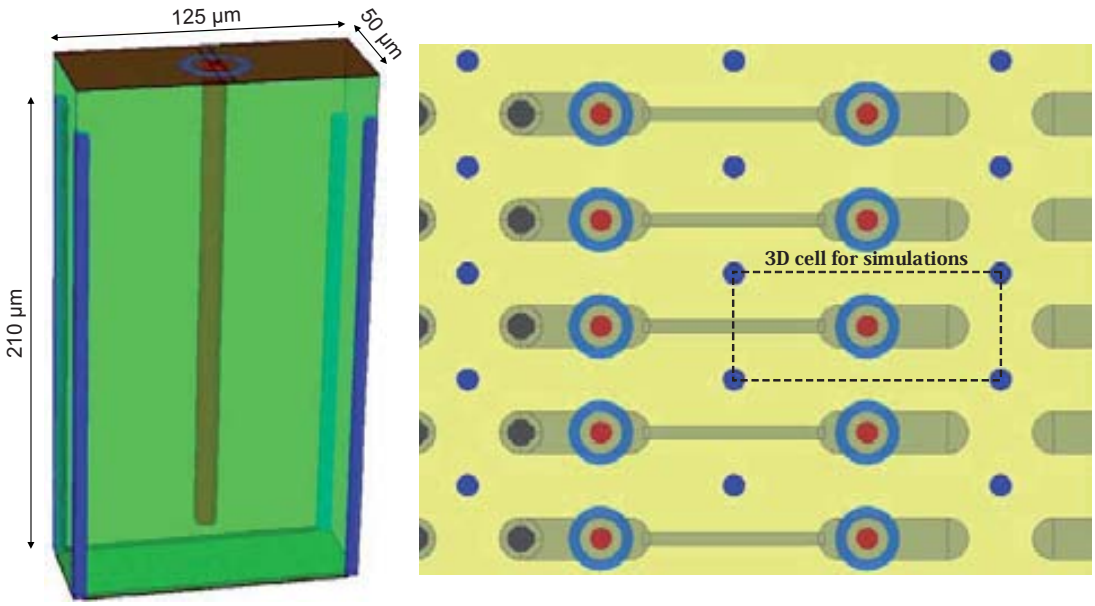

Figure 5.31: *3D cell used in the simulations of the FE-I4 detector, corresponding to half a pixel of figure 5.27.*

The 3D cell used for the simulations of half a pixel of the FE-I4 sensor is shown in figure 5.31a. The correspondent IV characteristic performed at room temperature is shown in figure 5.32a. In this design, the saturation of the leakage current is also reached after the depletion voltage with values from 0.14 nA to 0.20 nA. After 250 V the leakage current is increased rapidly and the breakdown is achieved for 270 V.

As the geometry of the 3D cell is quite different from a cylinder, this time is not used the equation that gives the capacitance of a cylinder capacitor for approximation. The CV characteristic of this cell was performed at room temperature, 20ºC, with an AC signal of 10 kHz, presenting a severe drop at around 4 – 5 V and obtaining a value for the capacitance of 0.035 pF. The same tip is also found in the CV simulation, also better appreciated in figure 5.32b. For this geometry it occurs at 20 V evidencing again that the real full depletion voltage is achieved after that value as it can be seen in the charge collection curve in figure 5.47b.

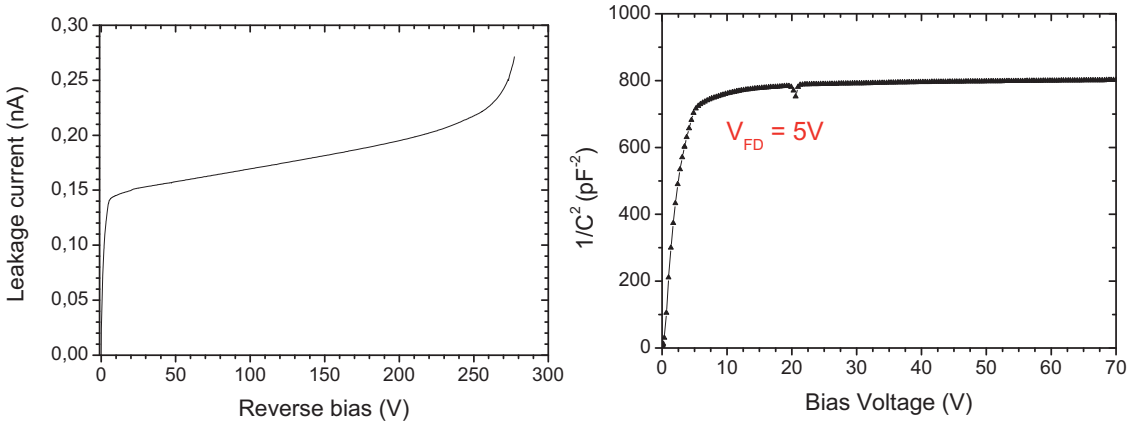

Figure 5.32: *Current-voltage (left) and capacitance-voltage (right) characteristics obtained from the 3D cell of the FE-I4 detector at a temperature of 20ºC.*

Potential and electric field distributions

The electrostatic potential and electric field distributions within the simulated 3D cells have been studied for different voltages, as shown in figures 5.33 and 5.34. In the case of the electrostatic potential, most of the substrate on both figures presents the same distribution due to the large overlapping depth between electrodes, however this distribution is different from the tips of the columns to their nearest surface (front or back). Below the front surface there is an accumulation of fixed positive charge in the oxide that attract electrons from the bulk thus creating an electron channel, that has no effect in the n^+ electrodes because of the p-stop insulation. This electron channel helps to extend the potential from the n^+ electrode to the rest of the surface, as it can be appreciated in figures 5.33a and 5.34a.

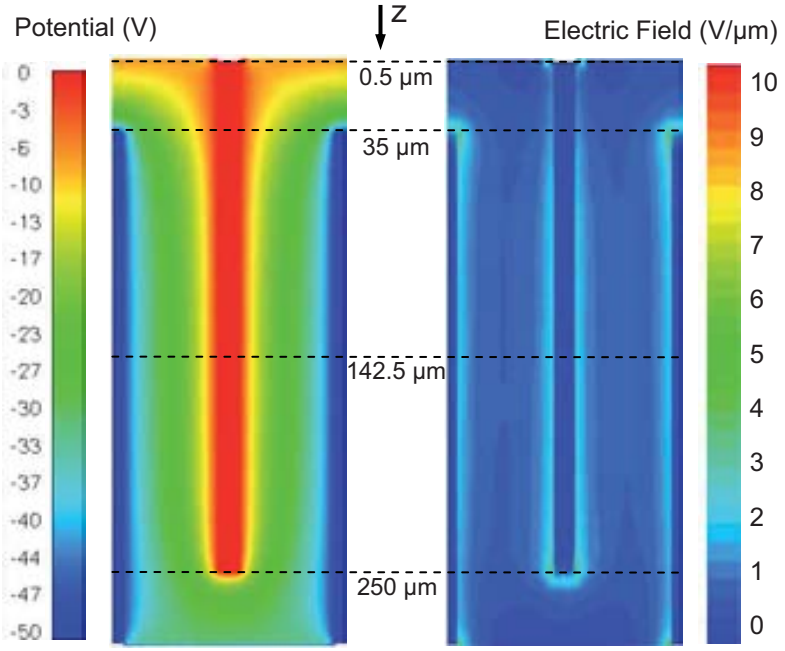

Figure 5.33: *Electrostatic potential and electric field distributions within the microstrip sensor volume across the straight line p^+-n^+-p^+. The temperature was set to 20ºC and the applied bias voltage to 50 V.*

At the back side, the oxide of the back surface is entirely covered by aluminum where is applied the negative bias (negative pole). That leads to a reduction of the fixed positive charge in the Si/SiO_2 interface and thus the electron channel is also reduced. Despite of this, the zone where the p^+ columns meet the electron channel still presents high electric field.

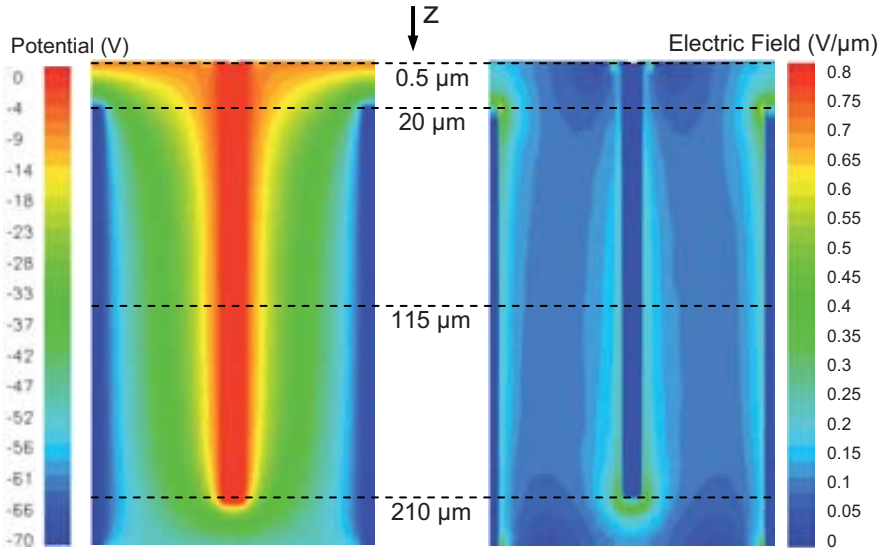

Figure 5.34: *Electrostatic potential and electric field distributions within the FE-I4 sensor volume across the straight line p^+-n^+-p^+. The temperature was set to 20ºC and the applied bias voltage to 70 V.*

High field regions are also located at the tips of both n^+ and p^+ columns and within the overlapped region, as it is shown in the figure 5.35, where the field decreases rapidly from the n^+ electrode towards the p-type bulk as a consequence of the distance dependence of the electric field, see equation **77**. At the bias columns there is an ohmic contact between two p-type silicon sides of different doping levels, p^+ diffusion of the ohmic column (10^{19} cm^{-3}) and the p-type substrate (7×10^{11} cm^{-3}). Solving the Poisson's equation in cylindrical coordinates for that region it is obtained an electric field distribution equal to the one for the n^+p junction but using the correspondent charge density distribution $\rho(x)$.

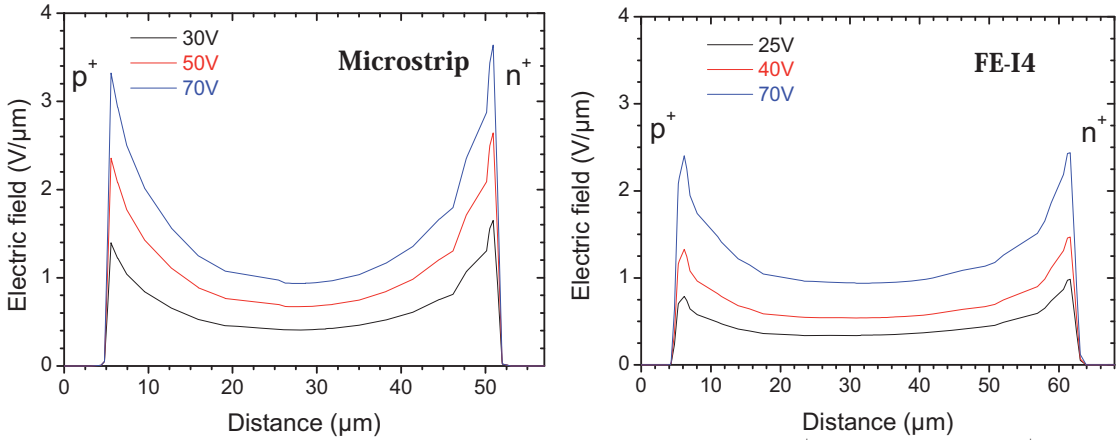

Figure 5.35: *Electric field profiles for several bias voltages between one p^+ electrode and the n^+ readout electrode. The slices correspond to the center of the overlapped region between columnar electrodes, at z = 142.5 μm for the microstrip detector (left) and at z = 115 μm for the FE-4 detector (right).*

Response to MIP particles

The response of the detectors to the pass of MIP particles which generate electron/hole paris across their path into the bulk is simulated for different bias voltages.

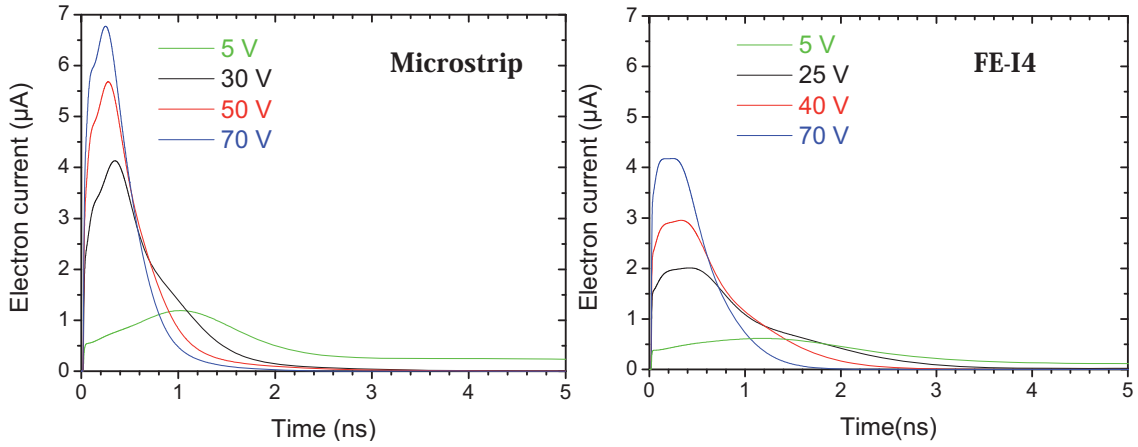

Figure 5.36: *Current pulses for several bias voltages for a MIP crossing at the intermediate position between opposite electrodes at (20, 20) for the microstrip detector (left) and at (31, 12.5) for the FE-I4 detector (right).*

These particles are crossing the detector in a perpendicular path to the front side, at an intermediate position between the n^+ and p^+ electrodes, creating 80 electron/hole pairs per micrometer. The thickness of the cell is 285 μm in the case of microstrip detector which makes that the total amount of generated electrons to be collected at the n^+ readout electrode is 22800 e^-. In the case of the FE-I4 detector the thickness is 230 μm, corresponding to 18000 e^-. As it can be seen in figure 5.36a, most of the charge is collected within the first 2 nanoseconds for bias voltages above the full depletion voltage in the microstrip detector, however in the FE-I4 sensor the collection distance is longer and thus the collection time for most of the charge is a bit higher as well although the difference is reduced as the voltage is increased, as it can be seen in figure 5.36b.

Weighting field – induced signals

The Shockley-Ramo Theorem [26] allows the calculation of the instantaneous electric current induced on electrodes due to the motion of charge carriers formed by the incident radiation. This movement of charge produces a local distortion of the electric field and therefore in the field lines that ends onto the electrode of interest. Thereby, the collection of induced current has no delay since the creation of the electron/hole pairs and ends after the last charge carrier arrives to its electrode. For studying the signal at the neighbouring strips, a new 3D cell for the microstrip detector has been designed to carry out the simulations, figure 5.37a. The weighting potential in the FE-I4 detector would be analogue to the one obtained for the microstrip detector, so only the simulations in the first model are performed.

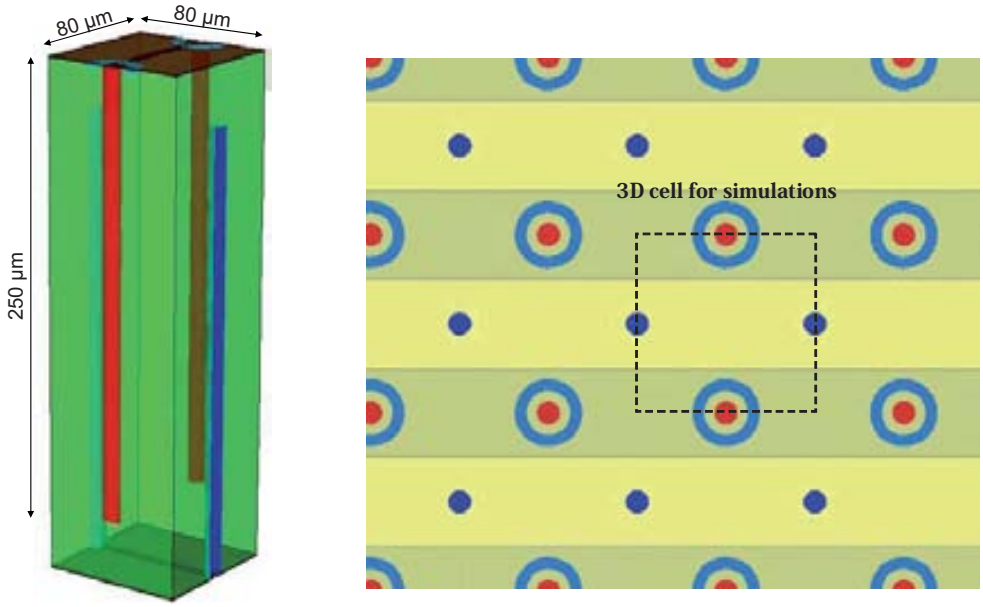

Figure 5.37: *3D cell used for the simulation of the weighting potential.*

The instantaneous current induced on an electrode is given by

$$i = q\vec{v} \cdot \vec{E}_w \qquad \textbf{[145]}$$

where v is the carrier velocity and E_w is the weighting field. The induced charge on an electrode by the movement of charge from one point x_A to another x_B is calculated through the weighting potential, $\Phi_w(x)$

$$Q = q\Delta\phi_w(x) = q\phi_w(x_B) - q\phi_w(x_A) \qquad \textbf{[146]}$$

The weighting potential provides the charge in the real potential distribution of the detector and is obtained by solving the Laplace equation for a given electrode with some artificial boundary conditions:

- The voltage on the electrode of interest is set to 1 V.
- The voltage in the rest of the electrodes is set to 0 V.
- Any charge is not taken into account in the Poisson equation even if there are lattice defects in the detector substrate which could trap charge carriers, thus the equation is reduced to the Laplace equation.

The path of the charge carriers is determined by the electric field lines present in the detector volume and can be used to determine the shape of the pulse profile by tracing out the profile of the induced current [26].

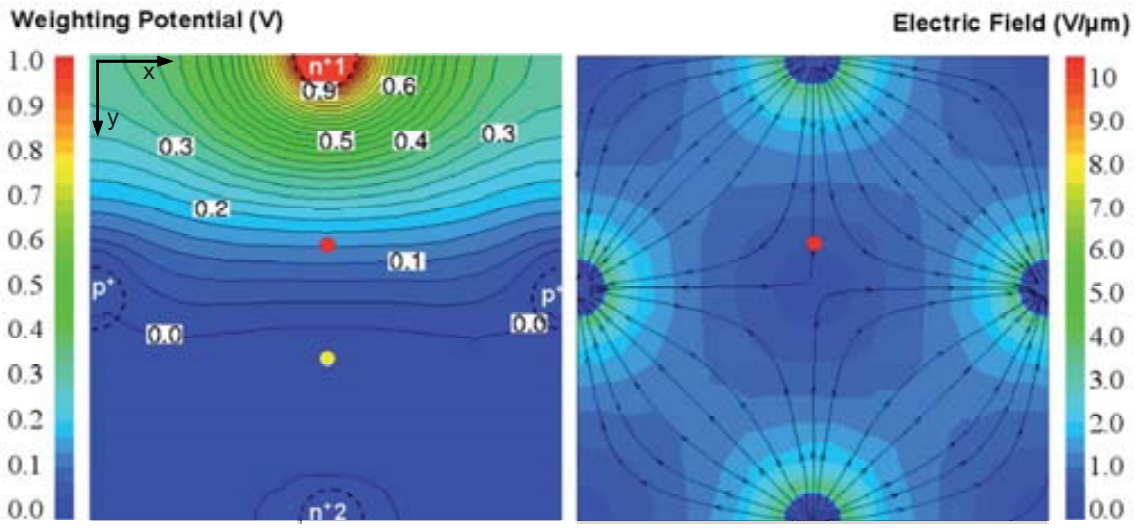

Figure 5.38: *Weighting potential for the n^+1 readout electrode (left), and electric field lines for an applied bias of 70 V (right). Both plots correspond to a slice at z = 142.5 μm.*

Let's consider an electron/hole pair created in the location (40, 30) denoted with a red circle in the figure 5.38a. The electron will flow to the n^+1 electrode driven by the electric field line at that position although in the opposite direction of the arrow due to its negative charge, as it can be seen in figure 5.37b. The weighting potential in the red position is 0.15, so the electron will induce a charge $Q = q\phi(x_B) - 0.15q$ as it is approaching to the electrode, according to the equation **146**. As the gradient of weighting field is increasing rapidly toward the n^+1 electrode, the induced charge in the next motion along the field line $Q' = q\phi(x_C) - q\phi(x_B)$ will be higher, corresponding to the first 0.2 ns on the figure 5.39a for 80 V. The induction of charge starts to end when the physical electrons are being collected, up to 0.6 ns in the same graph. The rest of the tail is due to those electrons outside the overlapped region between different type columns because the field there is less strong.

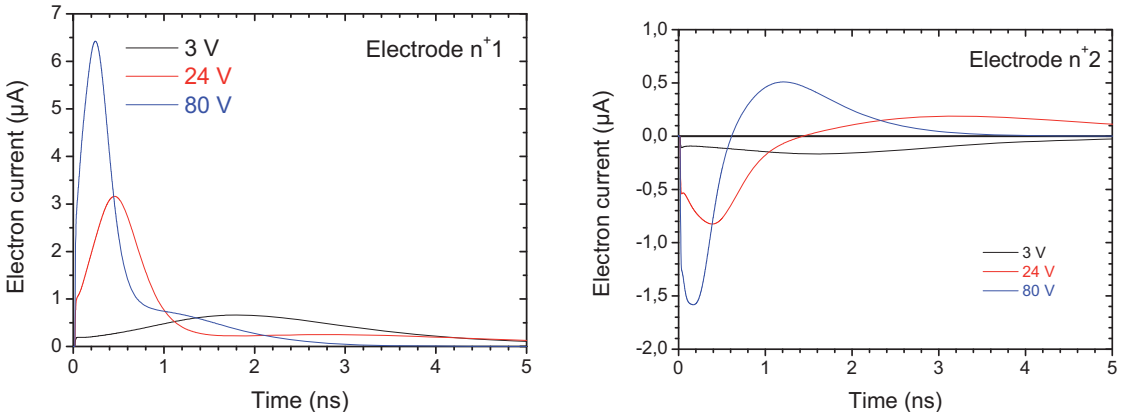

Figure 5.39: *Time pulse responses of the n^+1 and n^+2 electrodes for several bias voltages when an incident MIP is crossing at the location (40, 30), red circle in the previous figures.*

On the other hand, the induced charge on the n^+2 electrode due to the movement of an electron can be deduced from figure 5.38a inverting the roles of n^+1 and n^+2, but this time the point of interest is a further location marked as a yellow circle. The weighting

field in the yellow circle is null, what implies that electrons moving from that further point to an ever further location (neighbouring electrode), where the weighting field is also null, do not induce any charge in that electrode. Only a small fraction of the electrons generated outside the overlapped region are collected in the neighbouring electrode. The pulse of figure 5.39b is due to the displacement current inside a close circuit like in this case, involving also the n^+2 electrode. For a given bias voltage, if the collection time is lower than the one needed to let the displacement current back to the stationary state, a negative signal is obtained. The sum of both p^+ electrodes and the n^+2 electrode equals (changing the sign) the charge collected in the electrode n^+1. Table 5.3 shows the collected charge as explained in this section.

Table 5.3: *Charge collected at the electrodes for a collection time of 25 ns. The MIP incidence point is located at (40,30) creating 22800 electron/hole pairs.*

Bias voltage	Electrode n^+1	Electrode n^+2	Backplane
3 V	16659	–1384	–15275
24 V	20024	684	–20708
80 V	21810	589	–22399

After irradiation

The radiation induced defects and their consequences in the electrical behaviour were explained in Chapter 3. The main macroscopic effects are *i)* change in the effective doping concentration of the detector, that alters the potential and electric field distributions, the full depletion voltage, the capacitance, etc *ii)* increase in the reverse current as those defects act like generation/recombination centers, and *iii)* reduction of the charge collection efficiency, due to the charge carrier trapping that reduces the effective drift length for both electrons and holes.

The effects of the radiation have been simulated introducing physical parameters described in Section 3.3 and they are studied and described below. The temperatures for the microstrip detector correspond to those reported in the experimental measurements of Section 5.3.4, while for the FE-I4 detector the operational temperature is -15ºC, according to the sensor electrical specifications after irradiation [126].

Leakage current

The ramp voltage of the irradiated 3D cells has been performed up to 300 V for several temperatures. Resulting curves for the neutron equivalent fluence 2×10^{15} n_{eq}/cm^2 at -20ºC (microstrip) and at -15ºC (FE-I4) are plotted in black on figures 5.40a and 5.40b respectively.

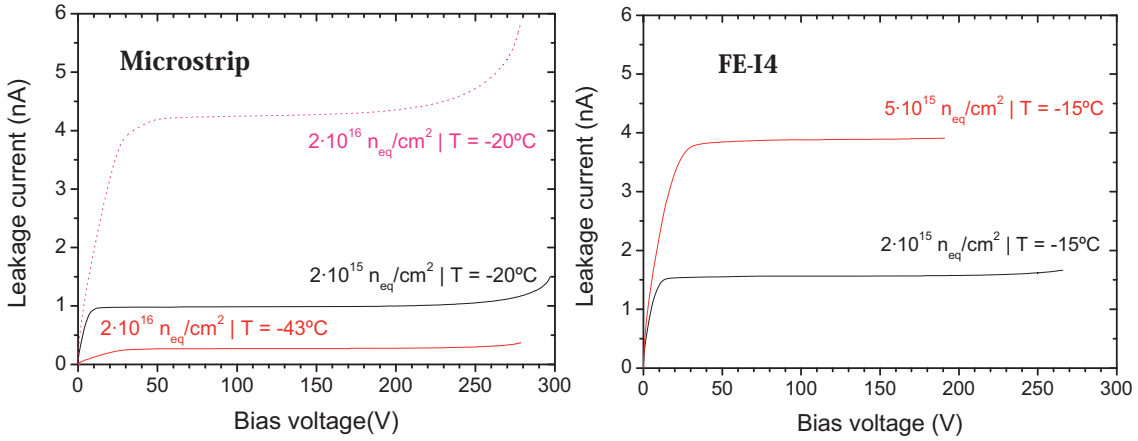

Figure 5.40: *Current voltage characteristics of the 3D cell for two different fluences, 2×10^{15} n_{eq}/cm^2 and 2×10^{16} n_{eq}/cm^2, at several temperatures. The dot line corresponds to rescaled current using the equation* ***83****.*

The current-voltage characteristic of the microstrip detector for the fluence 2×10^{16} n_{eq}/cm^2 has been simulated at -43ºC, red line in figure 5.39a, since the simulations of charge collection efficiency (CCE) have been carried out using the data files saved for this temperature in order to compare to the experimental measurements. To compare both fluences at the same temperature, -20ºC, a pink dotted line has been plotted also shown in figure 5.40a using the temperature-scaling equation **83**. As expected, the leakage current of the more irradiated cell is higher, as it was previously explained in Section 3.1.5., due to the higher concentration of defects in the traps model, but it also evidences the strong temperature dependence[5] of the leakage current whose consequence in the TCAD simulations is making the numerical solver to suffer from convergence problems for even lower voltages. This problem in the simulations is more accentuated as the irradiation is also increased, as it is shown in figure 5.40b for the fluence 5×10^{15} n_{eq}/cm^2 at -15ºC.

As the required voltage for the operation of the FE-I4 3D sensors at the IBL is ≤ 180 V [126, 133] the maximum voltage achieved in the simulations (190 V) for the radiation fluence 5×10^{15} n_{eq}/cm^2 is enough for this study.

Electric field

The electric field of the simulated cell is studied to understand the performance of these radiation detectors as well as for determining where the electrical breakdown of the sensors takes place.

Overlapped region

Given the fact that most part of the detectors volume is found between the overlapped columns of different type, the electric field has been studied in the middle of that region.

[5] The temperature dependence of the leakage current is expressed in equation **82**.

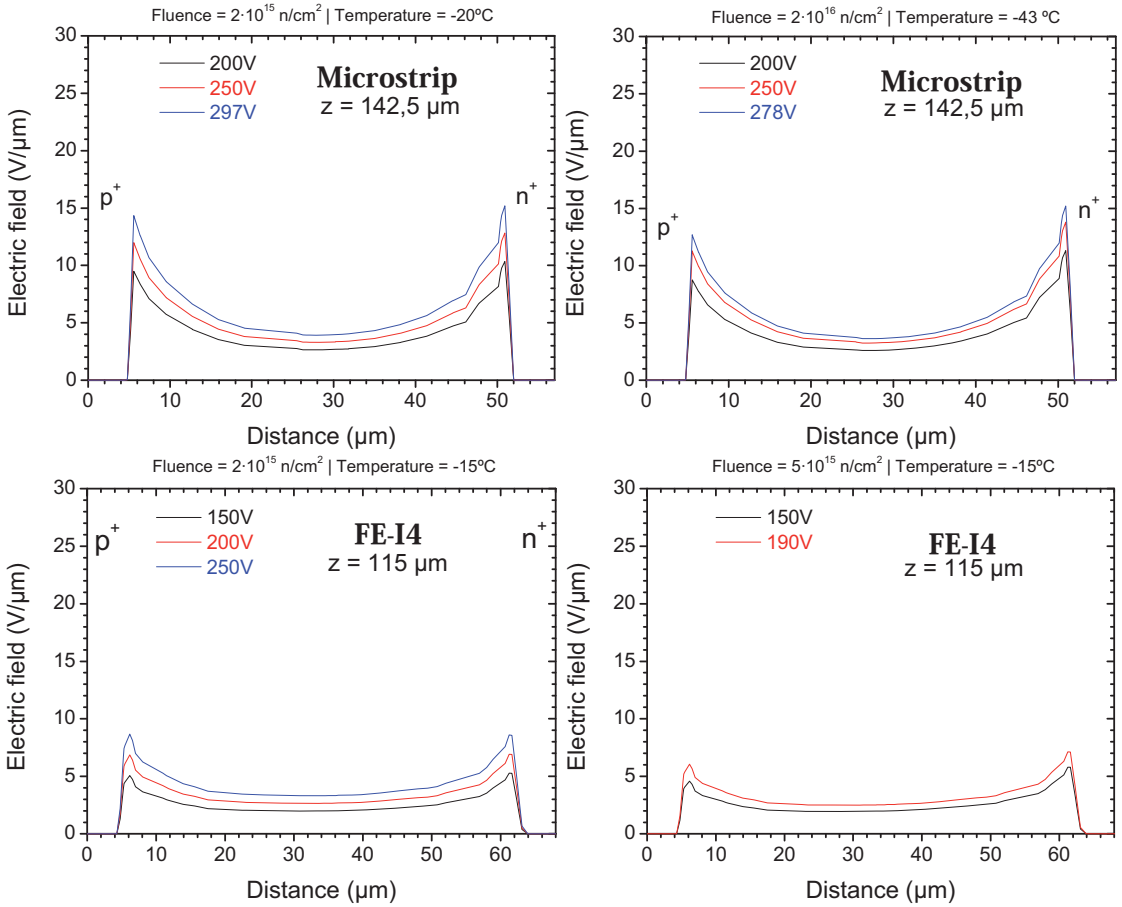

Figure 5.41: *Electric field profiles between one p^+ electrode and the n^+ readout electrode within the overlapped region of the microstrip detector (top) and FE-I4 detector (bottom) for several applied bias voltages and different radiation fluences.*

The electric field profiles between the central electrode n^+ and any of the p^+ electrodes located in the corners of the 3D cells are shown in figure 5.41 for several bias voltages and different radiation fluences. As in the unirradiated case, the fields present two peaks, one for each junction according to the equation 77. The effective doping concentration of the bulk, N_{eff}, that appears in that equation has changed from the original value due to the introduction of radiation induced defects, as explained in Section 3.1.5.

The electric field compatible with multiplication of electrons by impact ionization is estimated being above 13 V/µm. Such values of field are obtained in the microstrip detector for voltages around 240 V and 220 V, for fluences of 2×10^{15} n_{eq}/cm^2 and 2×10^{16} n_{eq}/cm^2, respectively. Field peaks near the columnar electrodes are lower in the FE-I4 detector as the potential drop is less severe due to the longer distance between opposite electrodes.

Electric field at the p-stop

The potential drop that takes place in such small distance between the p-stop and the n^+ electrode favours the formation of high fields in that region, as it can be seen in figure 5.42. The potential in the p-stop depends on the separation distance of opposite electrodes as the gradient of potential takes place between them, thus affecting the field peak in that region as it can be seen in figure 5.42 while comparing the microstrip and the FE-I4 detectors.

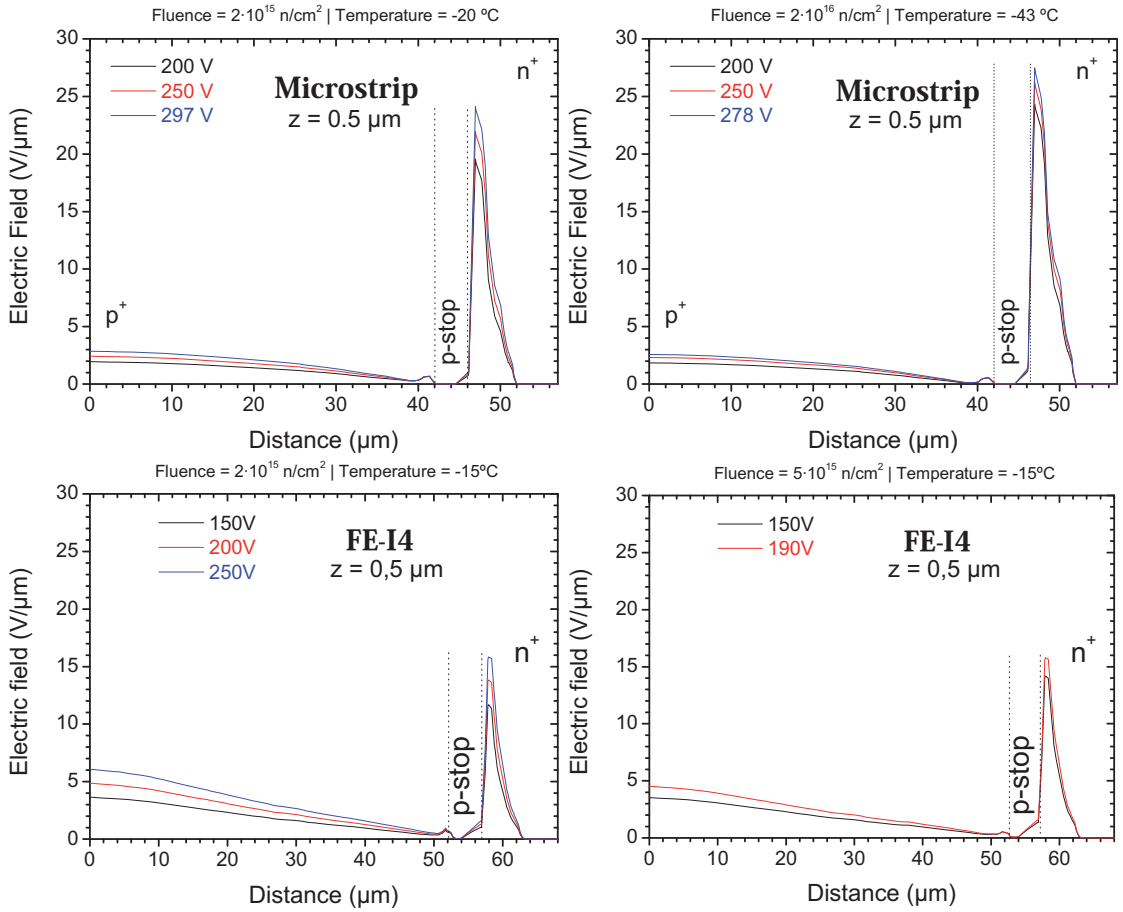

Figure 5.42: *Electric field profiles between one p^+ electrode and the n^+ readout electrode near the p-stop of the microstrip detector (top) and FE-I4 detector (bottom) for several applied bias voltages and different radiation fluences.*

The field peaks in this region increase with the fluence due to the increasing of the N_{eff} value according to equation **77**. This field acts accelerating holes in that small region towards the p-stop implantation and electrons towards the n^+ diffusion of the junction column. This region of high electric field is quite small (see figures 5.33b and 5.34b) compared with the regions of high field present near the tips of both ohmic and junction columns, however its contribution to the electrical breakdown increases as the radiation fluences are higher, reaching values of field peaks similar to those found at the columns tips.

Tip of the ohmic columns, p^+

Due to the shape of the tips of the columnar electrodes (hemispherical), the field in these regions also reaches very high values [134] and, for instance, they can be responsible and/or contribute to the electrical breakdown of the sensor.

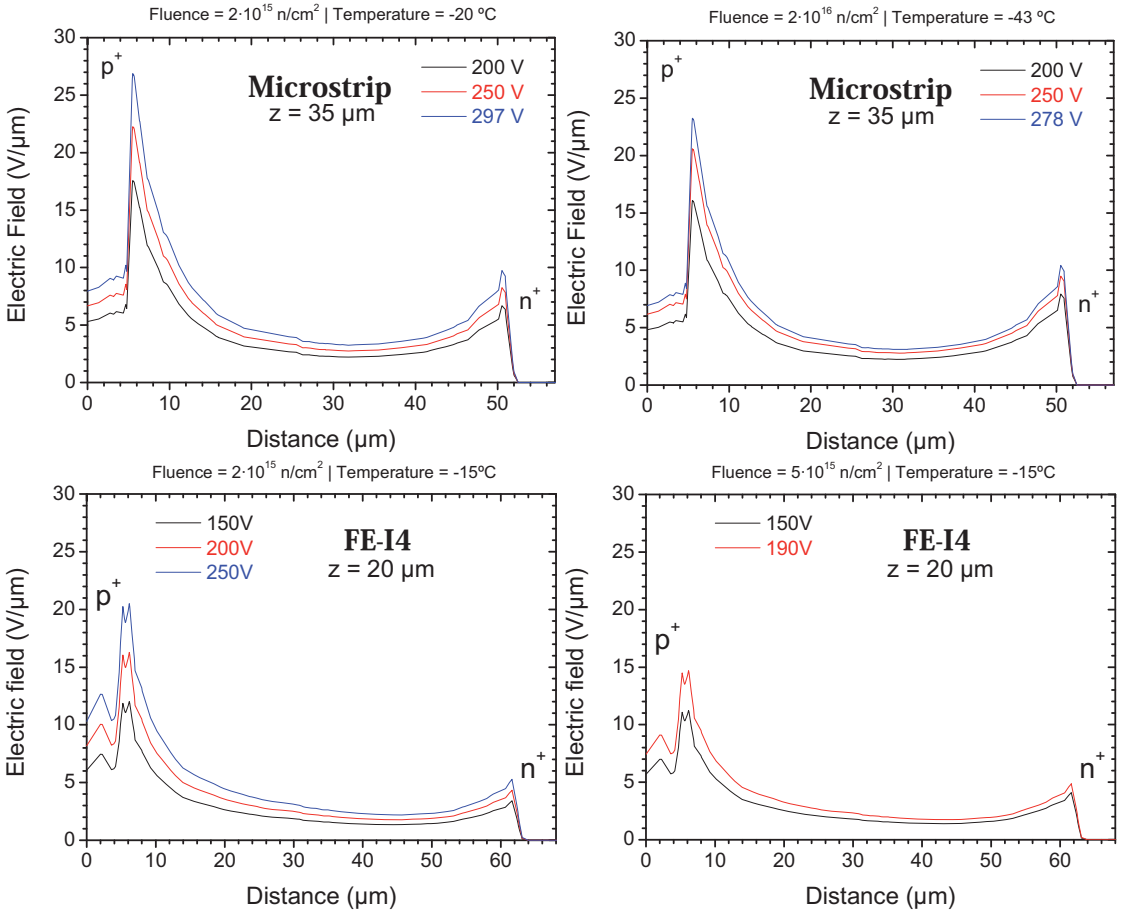

Figure 5.43: *Electric field profiles between one p^+ electrode and the n^+ readout electrode at the tip of the ohmic columns of the microstrip detector (top) and FE-I4 detector (bottom) for several applied bias voltages and different radiation fluences.*

Electric field profiles between an ohmic column and the junction column within the simulated cells irradiated at two fluences are shown in figure 5.43 for both detectors. Values of the field peaks in the p^+p contact are very high thus contributing to the electrical breakdown of the sensor. This contribution is reduced for higher fluences as most of the radiation induced defects act like acceptor states within the bulk and therefore the field in the p^+p contact is less strong. On the other side, the profile of the electric field at the pn^+ junction is similar to those found in the overlapped region, as it can be seen in figure 5.43.

Tip of the junction column, n^+

The case of the tip of the n^+ electrode is different. The increasing fluence affects turning the substrates more *p-type* and therefore the electric field at the pn^+ junction is also higher. The high electric fields achieved in this region are therefore the main contribution to the electrical breakdown of both sensors.

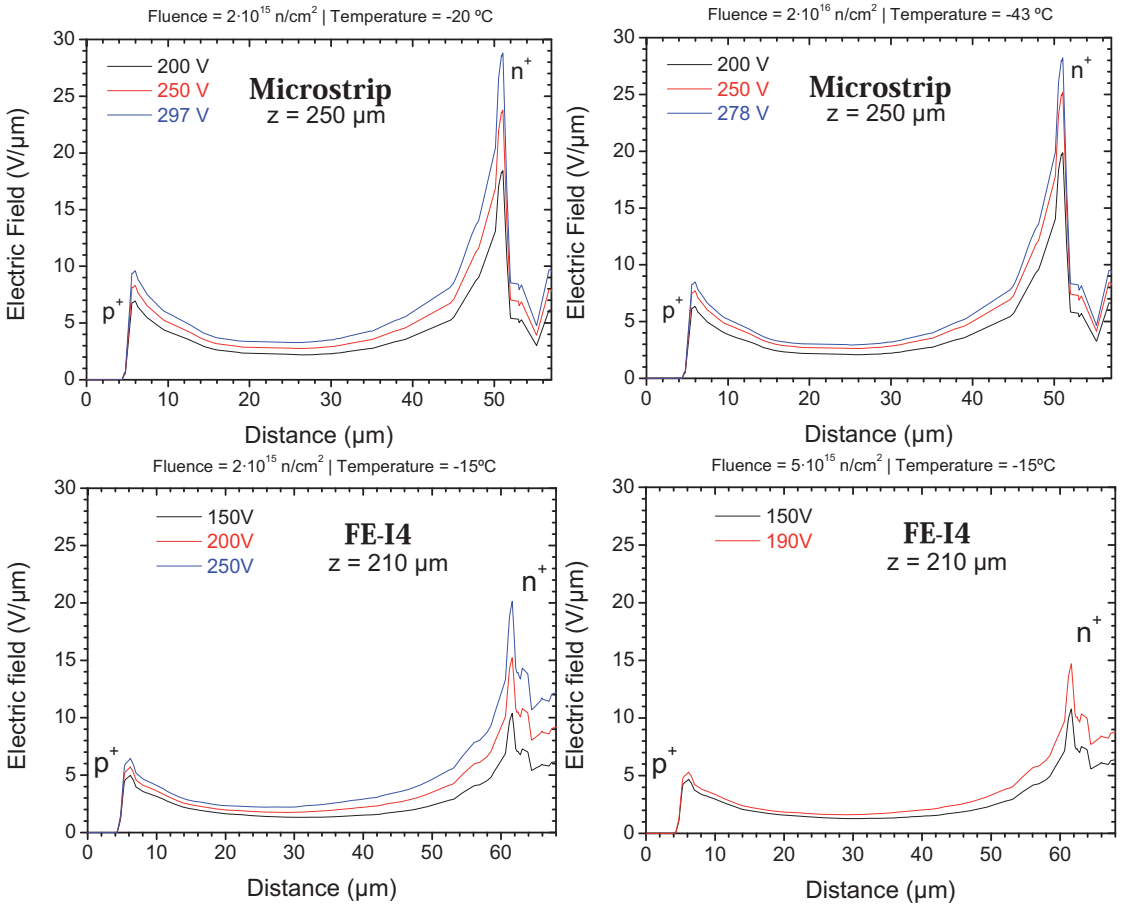

Figure 5.44: *Electric field profiles between one p^+ electrode and the n^+ readout electrode at the tip of the junction column of the microstrip detector (top) and FE-I4 detector (bottom) for several applied bias voltages and different radiation fluences.*

Maximum values of electric field achieved for each studied region at the breakdown voltage for both microstrip and FE-I4 detectors are gathered in tables 5.4 and 5.5 respectively. The higher contributions to the electrical breakdown in the microstrip detector before irradiation are obtained at the tip of both ohmic and junction columns, due to the hemispherical geometry [134]. After irradiation, the introduction of radiation induced defects, which are mostly acceptor traps, makes that the potential drop in the p-stop region leads to higher field peaks with increasing fluences. At the same time, this increase of *acceptor* traps within the bulk also increases the N_{eff} of the substrate and hence there will be less holes diffusion (majority carriers) at the ohmic contact p^+p that reduces the field peaks in those regions.

Table 5.4: Field peak values at the breakdown voltage at the p-stop ($z = 0.5\ \mu m$), at the tip of the ohmic columns ($z = 35\ \mu m$), in the middle of the overlapped region ($z = 142.5\ \mu m$) and at the tip of the junction column ($z = 250\ \mu m$) for the microstrip detector.

Fluence (n_{eq}/cm^2)	Unirradiated	2×10^{15}	2×10^{16}
Breakdown voltage V_{br} (V)	290	297	278
E_{max} @ z = 0.5 µm (V/µm)	13.7	24.1	**27.5**
E_{max} @ z = 35 µm (V/µm)	**28.3**	**26.9**	23.3
E_{max} @ z = 142.5 µm (V/µm)	15.3	15.2	15.2
E_{max} @ z = 250 µm (V/µm)	**30.4**	**28.8**	**28.2**

The same behaviour is obtained for the case of the FE-I4 detector, with the difference that the larger inter-electrode distances lengthen the potential drop reducing the field peaks.

Table 5.5: Field peak values at the breakdown voltage at the p-stop ($z = 0.5\ \mu m$), at the tip of the ohmic columns ($z = 20\ \mu m$), in the middle of the overlapped region ($z = 115\ \mu m$) and at the tip of the junction column ($z = 210\ \mu m$) for the FE-I4 detector.

Fluence (n_{eq}/cm^2)	Unirradiated	2×10^{15}	5×10^{15}
Breakdown voltage V_{br} (V)	277	265	190
E_{max} @ z = 0.5 µm (V/µm)	10.2	15.8	**15.8**
E_{max} @ z = 20 µm (V/µm)	**24.0**	**21.2**	**15.2**
E_{max} @ z = 115 µm (V/µm)	10.3	8.7	7.1
E_{max} @ z = 210 µm (V/µm)	**25.6**	**20.1**	**14.7**

Charge collection and efficiency

Simulation results concerning the response of the unirradiated 3D cell to the particle crossing have been previously studied. The pulses showed that most of the charge is collected within the first nanosecond for the unirradiated cell when the particle incident location is placed in the middle between two different type columns.

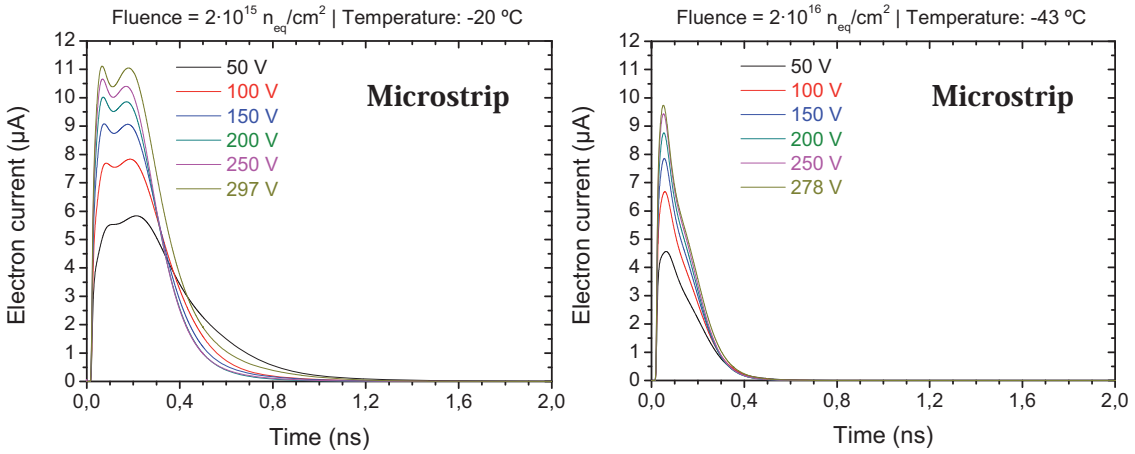

Figure 5.45: *Time pulse responses on the n^+ readout electrode for several applied bias in the irradiated microstrip detector. The radiation fluences are 2×10^{15} n_{eq}/cm^2 (left) and 2×10^{16} n_{eq}/cm^2 (right).*

After irradiation, the pulses have a slightly different behaviour due to the charge trapping. As it can be seen in figure 5.45a, in the first stage electrons start their movement towards the n^+ electrode inducing charge and being collected in that electrode, represented by the first peak in the curve. After that, it starts the contribution

of collected holes at 0.2 ns, and finally only remains the tail of collected holes. For higher voltages electrons are collected faster than holes and both contributions (peaks) are decoupled. Both peaks are also higher because of the faster collection that reduces the trapping. In FE-I4 sensors, the longer distance to reach the collection electrode makes more appreciable the difference between the contribution of electrons and holes collected, resulting in a first peak due to electrons and a second one less pronounced due to holes. Depending on their kinetic energy, carriers approaching to the electrode may produce impact ionization increasing the number of the collected electrons. For higher concentrations of defects, as in figures 5.45b and 5.46b, the charge trapping becomes much more important significantly reducing collection of both charge carriers, but especially on holes as they are more prone to the trapped (shorter trapping times as seen in equation **131**).

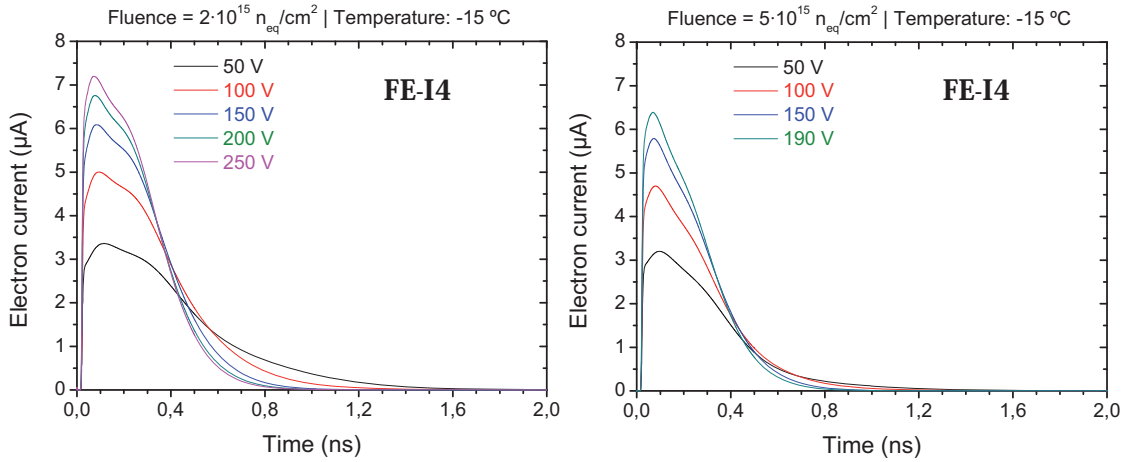

Figure 5.46: *Time pulse responses on the n^+ readout electrode for several applied bias in the irradiated FE-I4 detector. The radiation fluences are 2×10^{15} n_{eq}/cm^2 (left) and 5×10^{15} n_{eq}/cm^2 (right).*

Pulses of the previous figures have been integrated for 25 ns, as this is the time used in the experimental measurements carried out with the fabricated sensors according to the proton bunch frequency at LHC. Results of collected charge of both detectors are plotted in figures 5.47a and 5.47b, including the results of the unirradiated 3D cells to compare the charge loss due to the charge trapping and the charge multiplication effect for high voltages.

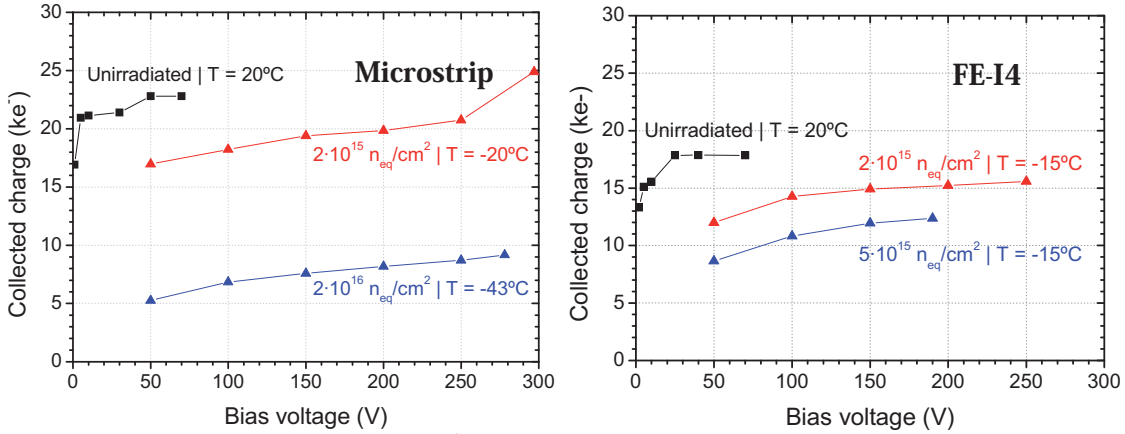

Figure 5.47: *Charge collected on the n^+ electrodes as a function of the applied voltage for a MIP crossing the intermediate location between opposite electrodes for different radiation fluences. The collection time is 25 ns.*

It is important to remark that the location of the incident particle plays a significant role in the charge collection as the electric field distribution in the 3D cells is not uniform. Radiation induced defects act as trapping centers which cause a reduction of the collectable charge. Short effective trapping times, and consequently short effective drift lengths[6], make electron/hole pairs generated in low electric field locations being more prone for being trapped.

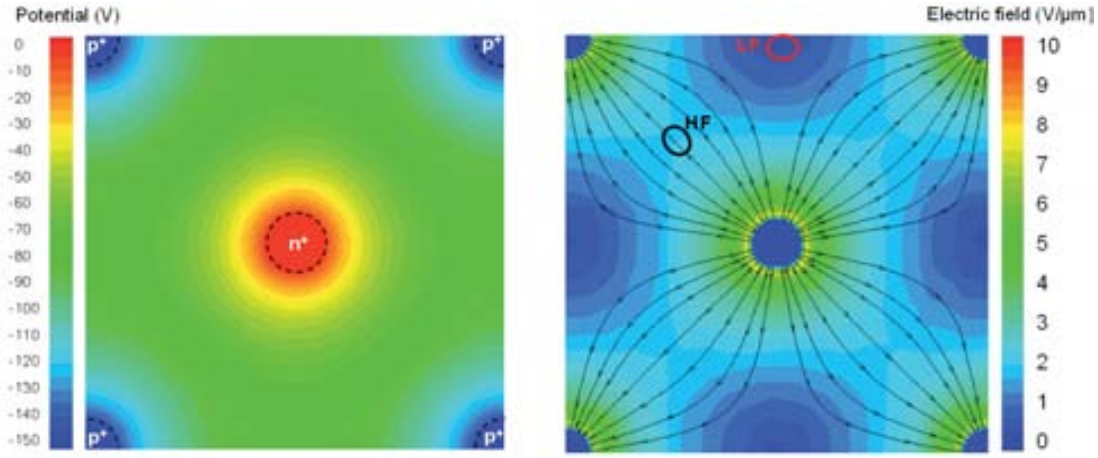

Figure 5.48: *Electrostatic potential (left) and electric field (right) distributions in the center of the overlapped region of the irradiated 3D cell of the microstrip design. The radiation fluence is 2×10^{15} n_{eq}/cm^2 and the applied bias 150 V.*

In figure 5.48b are represented two regions of the microstrip 3D cell at different distances from the central electrode whose electric field strengths are also different. As the region with higher field (HF) is closer to the electrode n^+, electrons generated in that region will be faster collected and will have less distance to cross than those generated in the lower field (LF) region. Collected electrons induced by MIP particles crossing those two regions, HF and LF, are plotted in figure 5.49 for two different fluences, 2×10^{15} n_{eq}/cm^2 and 2×10^{16} n_{eq}/cm^2.

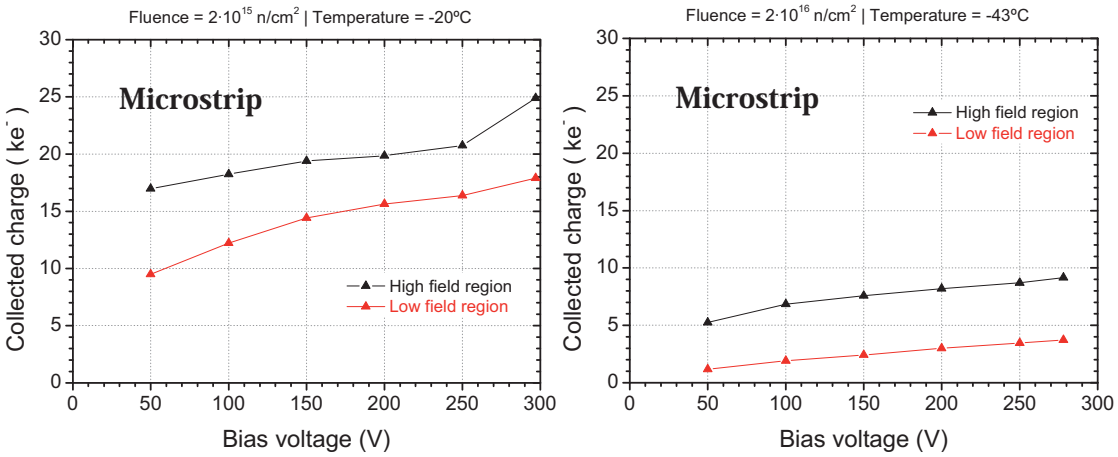

Figure 5.49: *Charge collected on the n^+ electrode as a function of the applied voltage for a MIP crossing two locations of different electric field strength, denoted HF and LF, and for two radiation fluences. The radiation fluences are 2×10^{15} n_{eq}/cm^2 (left) and 2×10^{16} n_{eq}/cm^2 (right) for a collection time of 25 ns.*

[6] As it can be appreciated in equation **135**.

There is a difference of around 5 k electrons between the two curves for the higher fluence. The charge multiplication effect is only observed for the microstrip design for the highest applied voltage, despite of having studied earlier than the electric field at the tip of the columnar electrodes is much higher than the required for impact ionization, ~ 13 V/µm. The explanation might be found in the fact that the three-level traps model of table 3.12 should include additional shallow-mid levels to allow the detrapping of electrons (holes) from deep level traps to the conduction (valence) band, thus increasing the charge collected.

Analogue potential and electric field distributions are obtained for the 3D cell of the FE-I4 detector. Two regions with different field strengths are marked in figure 5.50b for the charge collection study in which charge multiplication effect was not observed.

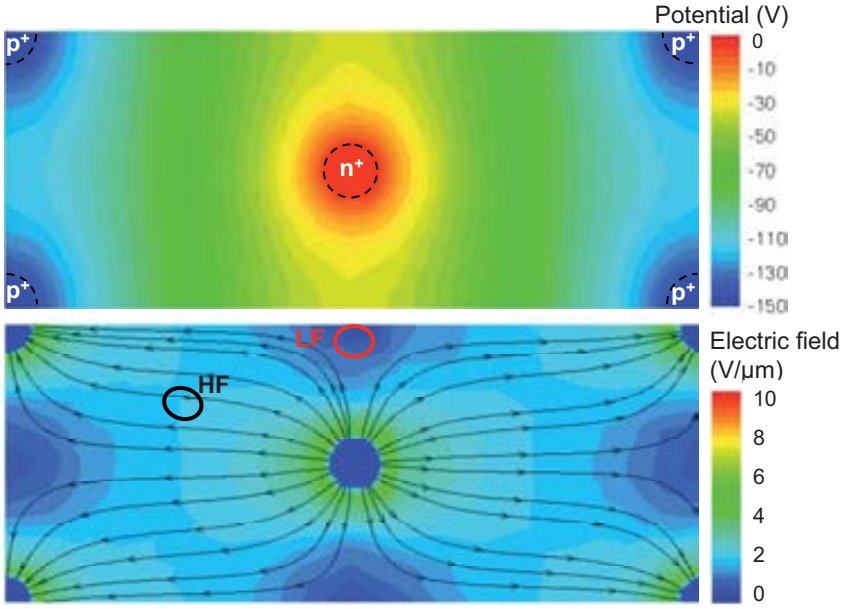

Figure 5.50: *Electrostatic potential (left) and electric field (right) distributions in the center of the overlapped region of the irradiated 3D cell of the FE-I4 design. The radiation fluence is 2×10^{15} n_{eq}/cm^2 and the applied bias 150 V.*

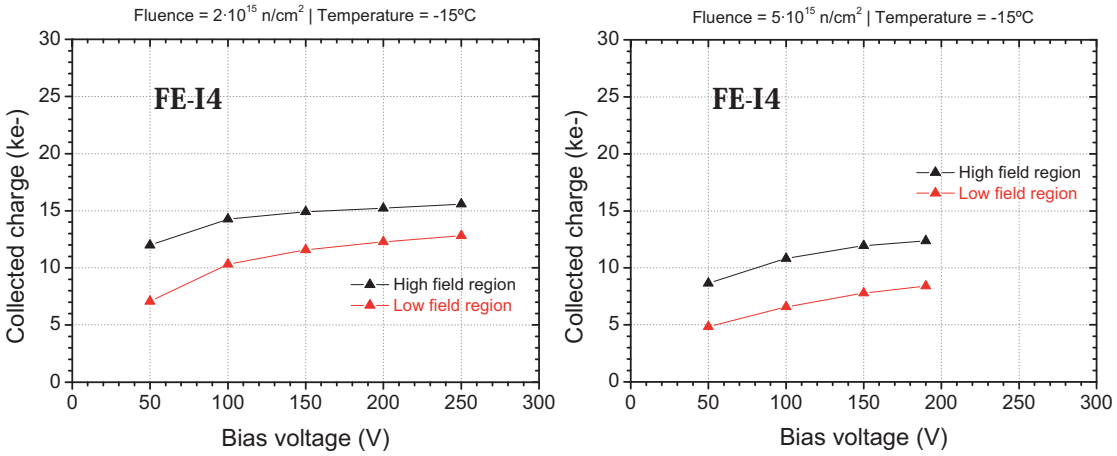

Figure 5.51: *Charge collected on the n^+ electrode as a function of the applied voltage for a MIP crossing two locations of different electric field strength, denoted HF and LF, for two radiation fluences. The radiation fluences are 2×10^{15} n_{eq}/cm^2 (left) and 5×10^{15} n_{eq}/cm^2 (right) for a collection time of 25 ns.*

5.3.3 Fabrication process

The fabrication process of full 3D detectors [38] involves the use of non-standard steps with respect to planar technology, such as DRIE-ICP and adhesive wafer bonding (supporting wafer). An alternative 3D architecture consists of 3D-DDTC (Double-sided, Double Type Columns) proposed by Giulio Pellegrini [40] in which the 3D electrodes are etched in both sides of the wafer without reaching the bottom surface of the substrate, partially overlapping n^+ and p^+ columns, as shown in figure 5.53b.

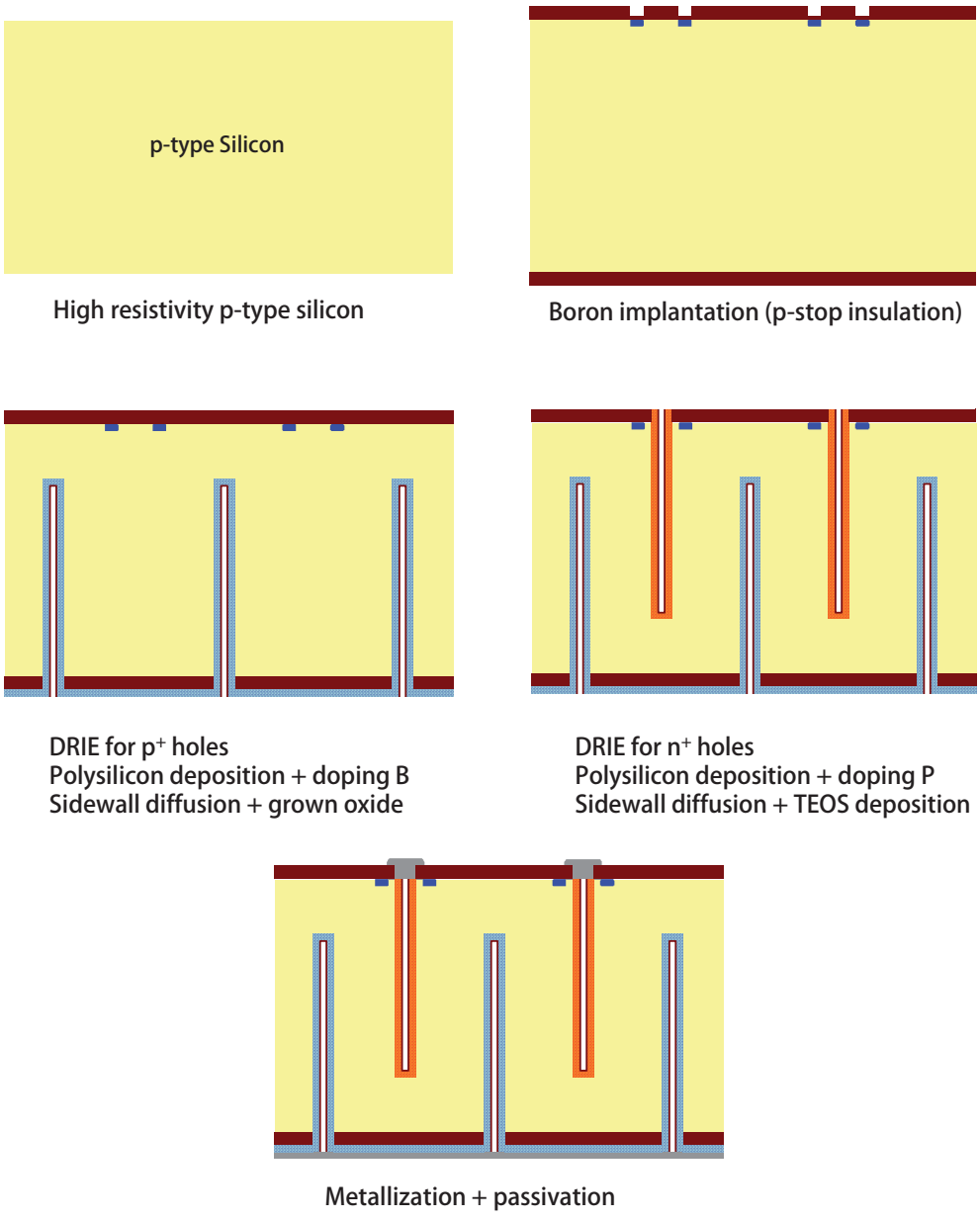

Figure 5.52: *Schematic of the fabrication process of double-sided 3D silicon detectors.*

3D-DDTC detectors have been fabricated in Float Zone <100> p-type silicon from Topsil manufacturer. Wafer thicknesses are 285 ± 15 µm with a resistivity ρ > 10 kΩ·cm (microstrip), and 230 ± 10 µm with the resitivity in the range 10 – 30 kΩ·cm (FE-I4). Boron implantation using an ion beam is made for the p-stop insulation of the

n^+ electrodes as well as for the common p-stop that surrounds the sensitive are of the detectors. The back side of the wafer was covered with 1 μm of aluminium (opened using the photolithography mask for p^+ holes) for protection during the etching of the 10 μm diameter n^+ holes, in an Alcatel 601E machine using the Bosch process described in Section 4.2.2, reaching depths of 250 μm in the case of microstrip and 210 μm for the FE-I4 detectors. Holes were partially filled depositing 2 μm of polysilicon that is subsequently doped with boron by the annealing in front of a ceramic wafer of boron nitride (BN) at 1150ºC for 0 minutes (ramp up to 1150ºC and ramp down). Then the aluminium mask was removed and a thin wet oxide is grown on the polysilicon inside the trench for passivation. Holes for n^+ electrodes were created on the front side in the same way than on the back side, however the phosphorous doping of polysilicon was made using $POCl_3$ at 1050ºC for 40 minutes and a 1 μm layer of TEOS is deposited for passivation of the doped polysilicon inside the trench. Next, it is performed the metallization depositing 1 μm of aluminium/copper on the front side and 1.5 μm on the back side. Finally, the front side is passivated with 0.4 μm of silicon oxide plus 0.4 μm of silicon nitride for protection. A schematic of the fabrication processes is shown in figure 5.52.

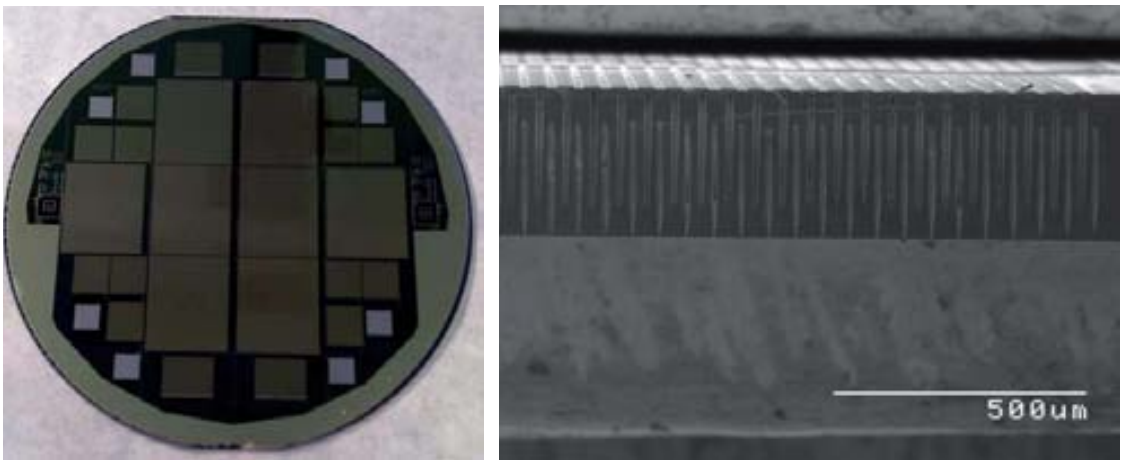

Figure 5.53: *Picture of one processed wafer containing 8 FE-I4 3D sensors (left) and a SEM picture of one double-sided silicon substrate 285 μm thick (right). The diameter of the columnar electrodes is 10 μm and 250 μm depth.*

Optical microscope images of final 3D-DDTC detectors are shown in figure 5.54. Picture on the left corresponds to the microstrip design (figure 5.26) where the 3D guard ring, the common p-stop and that wire bonds pads are appreciated, while picture on the right corresponds to the FE-I4 detector (figure 5.27), where it can be seen the common p-stop ring, the 3D guard ring and some pixels cells (see figure 5.28).

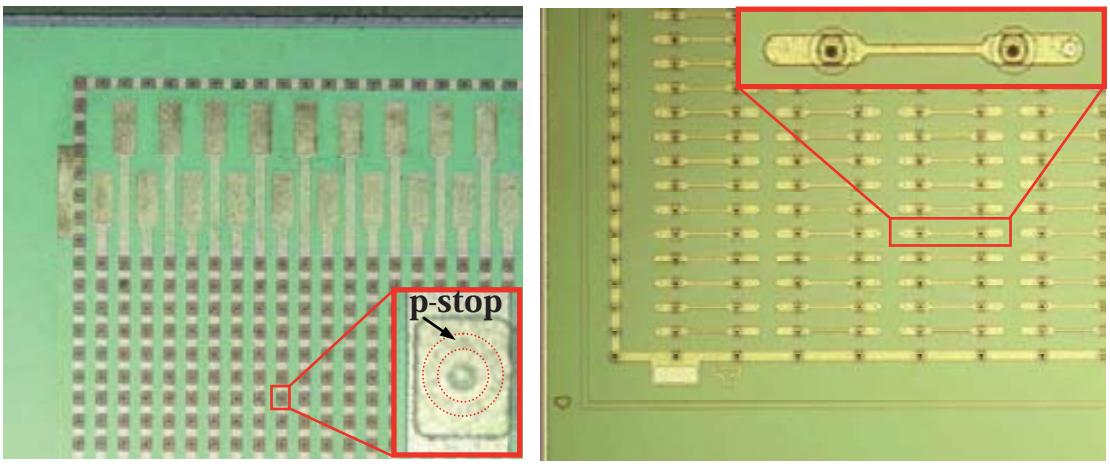

Figure 5.54: *Pictures of the microstrip (left) and FE-I4 (right) detectors.*

5.3.4 Experimental results

The performance of both 3D-DDTC microstrip and FE-I4 detectors fabricated on p-type substrates was measured before and after irradiation.

Microstrip detector

Current-voltage and capacitance-voltage measurements on the unirradiated sensors were done at room temperature. They revealed that only 2 of 19 presented early breakdown at less than 5 V, probably due to defects during the deep silicon etching of holes, while the rest showed two stages in the full depletion, firstly a lateral depletion between the junction and ohmic columns around 4 V, and secondly from the ends of the columns to the substrate surfaces, around 35 V [130, 132].

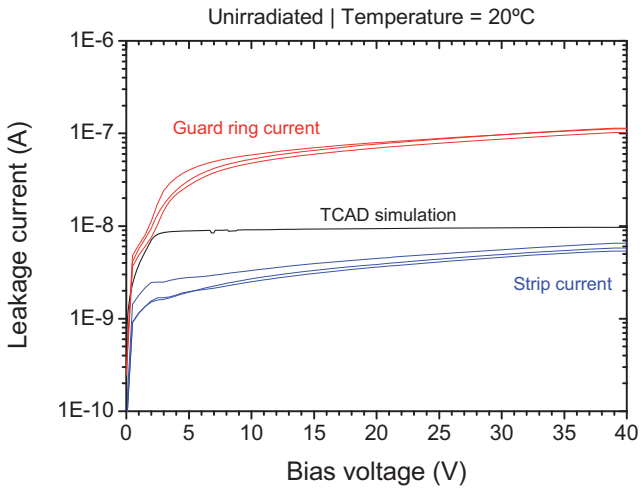

Figure 5.55: *Current voltage measurements of single strips and the guard ring from two different wafers (#1 and #8) performed at room temperature. The result from the TCAD simulation is included for comparison. The curve is only up to 40 V because of setup limitations.*

Figure 5.55 shows the comparison between the results of the experimental currents and the TCAD simulation. The guard ring currents are plotted in the same graph for additional information concerning the real devices. As the experimental measurement of the leakage current was performed for one strip, the leakage current of the simulated 3D cell of figure 5.28b has been multiplied for the number of single cells that are contained in one strip, 50 electrodes per strip. Due to setup limitations, the IV curves were measured only up to 40 V. Both simulated and measured currents rise up to the lateral depletion voltage following the same behaviour although reaching higher values for the real devices. Then, the simulated current remains with a slight positive slope while the slope of the real device is higher.

The capacitance between the junction columns n^+ and the ohmic columns p^+ of one strip was measured at 20ºC, using an AC signal of 10 kHz while biasing the two neighbouring strips at the same potential than the central strip, resulting about 5 pF/strip (12.5 pF/cm), while the interstrip capacitance measured at full depletion was 1.5 pF/strip (3.7 pF/cm). The interstrip capacitance is one of the major contributions to the load capacitance onto the amplifier and should be much smaller than the coupling capacitance[7], in the range of 32p F/cm. The inter-strip resistance, also measured at 20ºC, was in the order of 100 GΩ, showing an adequate interstrip insulation [130, 131].

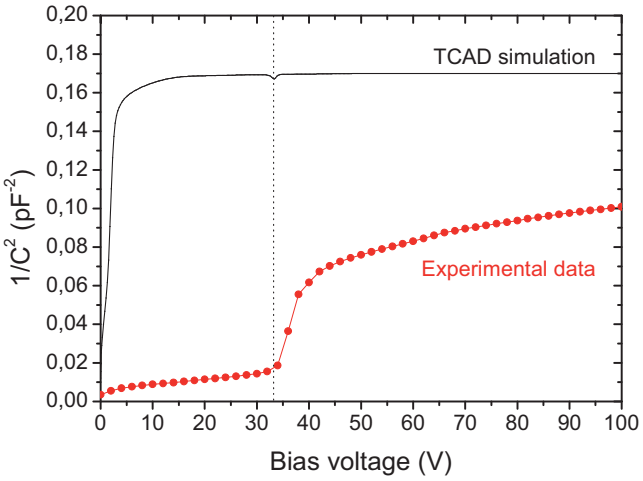

Figure 5.56: *Comparison between the capacitance voltage measurement and the result from the TCAD simlation. The measurement was performed at 20ºC.*

In the case of comparison of the capacitance-voltage characteristics high differences were found up to the full depletion voltage, estimated in ~35 V. The simulated capacitance decreases rapidly up to the lateral depletion value around 4 V, and then more slowly until it reaches the full depletion voltage, 15-20 V, and becomes stable, as seen in figure 5.56. The difference between these two stages in capacitance for the lateral depletion and full depletion voltages revealed being much more pronounced in the experimental measurements. Initially it was thought that the difference between CV measurements and simulations for the CNM sensors could be given as a consequence of the possible misalignment between the junction and ohmic columns that seems to be also the cause of the high induced negative signal collected by neighbouring strips in the laser measurements carried out by the University of Freiburg [135]. However, comparing the simulation of 5 µm of misalignment of the n^+ column from the nominal location led to almost the same CV curve. The source of this behaviour is therefore in

[7] See section 2.3.1.2

the interaction between the growth of the space charge region and the electron channel of the Si/SiO_2 interfaces for ~35 V, that are also depleted producing the second drop observed in the capacitance-voltage measurements.

The 3D-DDTC microstrip detectors were irradiated at the Karlsruhe Institute of Technology (Compact Cyclotron) with 25 MeV protons at room temperature reaching fluences up to 2×10^{16} n_{eq}/cm^2. A radiation hardness factor of 1.85 was applied to convert the measured fluences to 1 MeV neutron equivalent fluences [44]. After their irradiation the detectors were stored and -20ºC to prevent from unintentional annealing effects.

Current voltage characteristics after irradiation without annealing were carried out at the University of Freiburg (figure 5.57a) while the annealing study was performed at IMB-CNM (CSIC) (figure 5.55). The simulated reverse current has the same tendency than the unirradiated cell: strong increase up to the lateral depletion voltage, then a stable part and finally the electrical breakdown near 300 V. The experimental measurement has a different behaviour: it increases gradually until values compatible with charge multiplication are reached. Both TCAD and experimental measurements are in the same range of values, but the experimental ones reveal a greater concentration of deep level radiation-induced defects as its slope is higher due to charge multiplication.

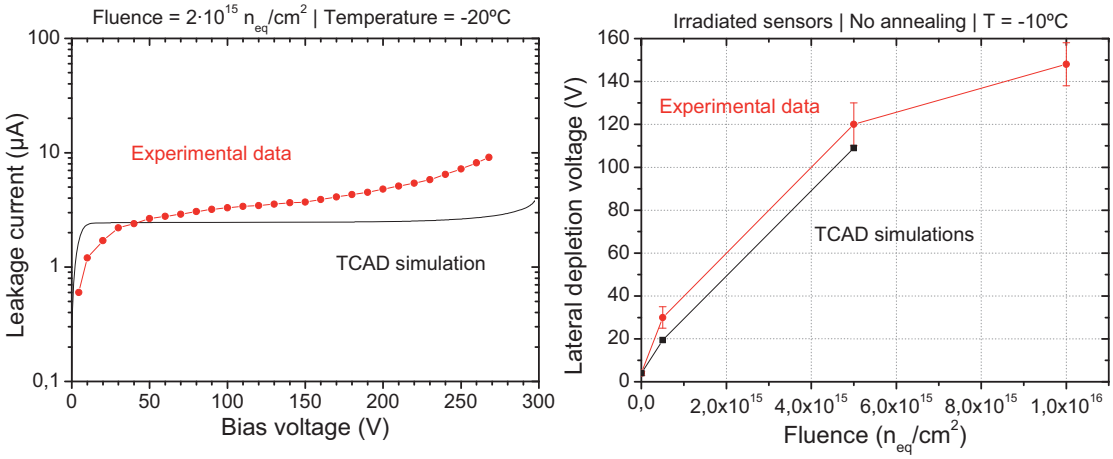

Figure 5.57: *Comparison between simulation and measurement of the leakage currents corresponding to the whole active area of the irradiated sensor, excluding the guard ring current, (left) [128]. The curves on the right show experimental and simulated values of the lateral depletion voltage for several radiation fluences obtained from CV curves [132].*

The p-stop isolation works well even for high fluences, 10^{16} n_{eq}/cm^2, obtaining a value of the inter-strip resistance of 100 MΩ. Depletion voltages were studied from the capacitance-current characteristics for the following fluences: 5×10^{14}, 5×10^{15} and 10^{16} n_{eq}/cm^2. The estimation of the full depletion voltages in the irradiated detectors could not be distinguished clearly from the CV measurements, thus figure 5.57b shows the values of the lateral depletion (more clearly appreciated) measured at -10ºC and compared to simulation results [132].

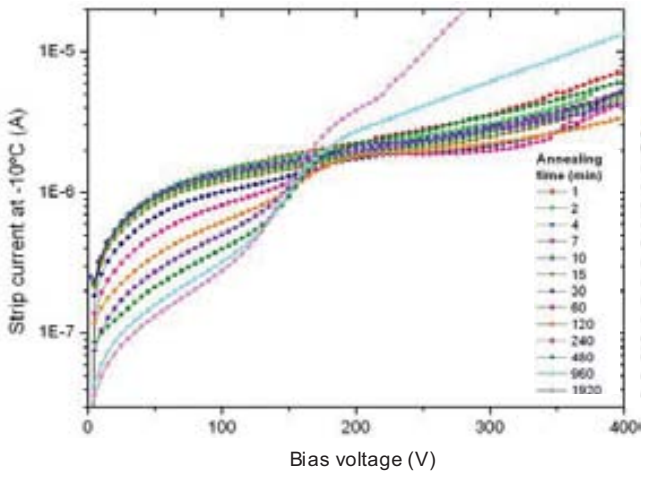

Figure 5.58: *Annealing of the leakage current measured for one strip of a microstrip sensor irradiated at 10^{16} n_{eq}/cm^2. Current measurements were performed at -10ºC after different time steps at 80ºC [132].*

The annealing study of the irradiated detector shown if figure 5.58 [132] was performed using a sensor irradiated at 10^{16} n_{eq}/cm^2. This process was carried out heating the detector in time steps at 80ºC and measuring the resulting current-voltage characteristic at a temperature of -10ºC. After annealing, two behaviours were observed: *1)* the first one is a decrease of the leakage current for low voltages, as it as previously mentioned in Section 3.1.5. However, *2)* for bias voltages above 200 V, this trend is changed because of the higher electric fields achieved at the tips of the columnar electrodes for the increasing of "p-type" defects after the annealing and charge multiplication is produced consequently increasing the leakage current. The second effect is more pronounced and earlier for longer annealing times, as more acceptor defects are introduced in long-term annealing stages leading to higher field peaks at the pn^+ junctions.

Beta source setup and pion test beam

Charge collection of 3D-DDTC microstrip detectors were measured by two different setups:

- *Laboratory conditions* at the University of Glasgow [130] and the University of Freiburg [128, 129], using a Sr-90 radioactive beta source, a scintillator located behind the device under test for triggering, and the ALIBAVA[8] data acquisition system, based on the Bettle front-end chip developed for the LHCb experiment[9]. The Bettle speed readout electronics is 40 MHz, sampling the shaper output every 25 ns because the bunch crossing at LHC occur in 25 ns intervals.

[8] ALIBAVA is a portable readout system for microstrip detectors developed within the collaboration of the University of Liverpool, the IMB-CNM (CSIC) of Barcelona and the IFIC (UV-CSIC) of Valencia.
[9] LHCb experiment: is one of the six experiments at LHC specialized in measuring parameters of CP violation in the interaction of hadrons which contain the bottom (*beauty*) quark.

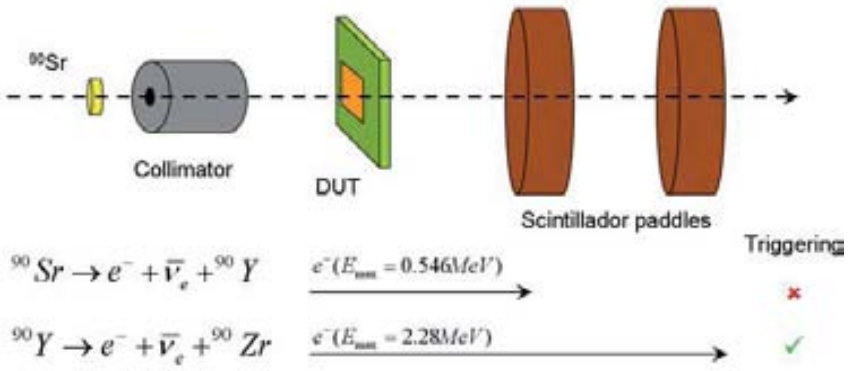

Figure 5.59: *Sketch of the detector under test (DUT) in the beta source setup.*

- *Realistic working conditions* at the CERN SPS H2 beam line, with 225 GeV pions that can be treated like minimum ionizing particle as their energy loss reaches a near-constant broad minimum value for relativistic energies [24]. Precision tracking was provided by the CMS Silicon Beam Telescope (SiBT) with a nominal resolution of 4 μm. The data acquisition system for this task was the CMS APV25 analogue front-end (40 MHz speed readout operation).

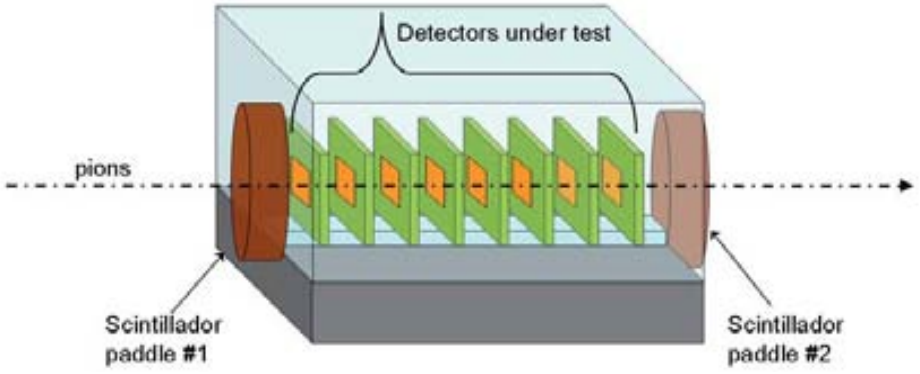

Figure 5.60: *Sketch of the pion test beam setup. The SiBT has 4 cm spacing between the 10 boards that hold the sensors under test.*

Beam test with high-energy pions and ^{90}Sr beta source measurements have been carried out on the unirradiated and irradiated sensors by the University of Freiburg [128, 129], whose results are corroborated in other ^{90}Sr beta source experiments by the University of Glasgow [130]. The charge collected curves with filled triangles of the figure 5.61 correspond to the measurements of the University of Freiburg using the beta source. The curve denoted with filled squares corresponds to the signal collected by the detector irradiated at fluence 2×10^{15} n_{eq}/cm^2 using high energy pions [128]. TCAD simulations previously analyzed in this work are denoted with empty symbols in the same figure for comparison.

Impact positions across the entire surface of the detector were considered in the measurements. The 100% of efficiency was obtained for the Landau most provable value from the unirradiated detector biased at 70 V, resulting approximately 22 ke^- [129], while in the TCAD simulations the impact position of the MIP is the intermediate

position of the straight line between the n^+ electrode and one p^+ electrode, and the 100% of efficiency corresponds to the charge introduced: 22.8 ke$^-$.

There is a great agreement for the experimental and simulated signals in the unirradiated case. Both signals are obtained for different temperatures but, as it will be treated in the next section, temperatures in the range of this study are not an important factor as the energy deposited by the particles does not depend on the temperature and the silicon bandgap does not change significantly. However, there are remarkable differences in the collected charge between the simulations and the experimental measurements of the irradiated detectors. The collected charge for low voltages in the experiments for the fluence 2×10^{15} n_{eq}/cm^2, up to 175 V, is lower than expected by the simulations, thus revealing more trapping due to the high values of carriers capture cross-sections and/or weaker electric fields. On the other hand, for voltages above 175 V there is a high increase of the collected charge revealing strong enough fields compatible with impact ionization. For the fluence 2×10^{16} n_{eq}/cm^2 a similar behaviour is obtained, with the difference that there is a higher reduction of the effective drift length that affects the trapping and therefore avoiding carriers to cover enough distance to earn enough kinetic energy for impact ionization.

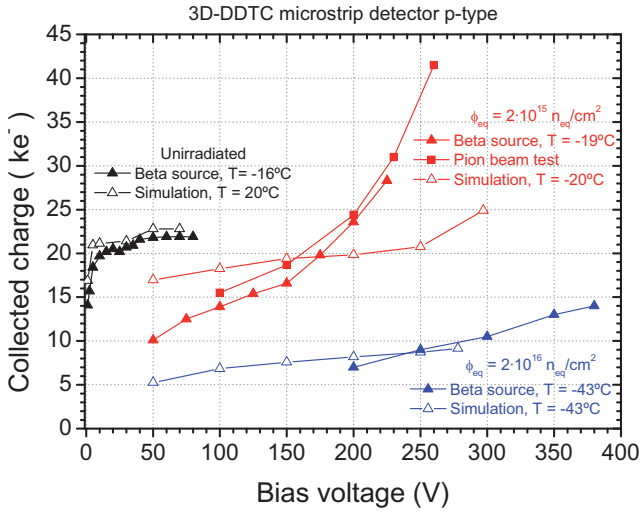

Figure 5.61: *Comparison graph showing the experimental measurements of the charge collected in the unirradiated/irradiated microstrip detectors for different bias voltages and the corresponding results from the TCAD simulations previously presented in this chapter.*

The slope of the collected charge for both fluences is higher in the experiments than in the simulations, so there is a greater importance of the applied voltage (electric field) in the real devices. It seems that defects with shallow levels within the bandgap are required; in the simulation model these additional defects would increase the trapped charge as occurs for low voltages, besides this introduction of intermediate levels between the energy levels implemented in the traps model also would favour the promotion of trapped electrons (holes) to the conduction (valence) band under high fields increasing the collected signals.

Temperature dependence

The temperature is a factor that affects the behaviour of the semiconductor devices through the microscopic parameters. Temperature is translated into kinetic energy for the charge carriers, independently if they are in the valence/conduction band or as free carriers. In the case of the electrons of the valence band, the increase of temperature can make them earn enough kinetic energy to eventually promote to the conduction band for statistical fluctuations, leaving a hole in the previous band that also participate in the conduction. From the point of view of that electron, it is as if the conduction band would be closer or as if the energy bandgap would be reduced; effect that is found in equation **8**. Free carriers are also favoured by higher temperatures increasing their kinetic energy and hence their drift velocity is also higher. Not all of the effects of higher temperatures are beneficial for the charge carriers. An increase of the lattice temperature involves a higher vibration of the silicon nuclei that form the silicon crystal, making them more prone to participate in coulomb collisions that reduce the mean free path of the free carriers. The beneficial and detrimental characteristics of the temperature in the carrier movement through the lattice are expressed in different parameters of the charge carriers, such as the temperature dependence in their mobility or mean free path/lifetime described in Chapter 2. As the temperature has influence on the kinetics of the carriers, impact ionization is also temperature-dependent following the equation **116**. As it was commented in the previous section, the introduction of charge by incident particles does not depend on the temperature and the temperature range of this study for the unirradiated detectors does not change significantly the properties of the carriers and silicon bandgap, as a consequence the collected signals in unirradiated detectors will hardly be altered.

In the case of irradiated substrates, there are other aspects that must be taken into account. The lattice defects induced by radiation, which act as traps for the charge carriers, are also affected by the lattice temperature as studied in Chapter 3. The temperature dependence of the effective trapping probability $\beta_{e,h}(T)$ is expressed in equation **134** revealing a reduction of the charge trapping when the temperature rises. In addition to this effect, the carrier mobilities and saturation drift velocities are also reduced making carriers more prone for being captured. The combination of these effects has as a result that there are no significant differences in the collected signals at low voltages for the range of temperatures of the experimental measurements performed on the irradiated detectors [135]. However, high enough voltages for impact ionization lead to higher differences due to a greater collected signal for the charge multiplication.

Laser setup

The importance of the incident MIP position has been exposed earlier with the TCAD simulation results. As it was explained, there are two factors that make the incident location alter the charge collection in the junction electrode. On one hand, the electric field distribution varies along the 3D cell volume, as it can be seen in figure 5.48b where the regions in the straight line between the junction and ohmic columns present medium and high fields, and whose highest values are obtained in the closest regions to the electrodes, while the field is almost null in the regions between ohmic columns. On the other hand, irradiated sensors have a uniform distribution of defects acting as charge traps and longer drift distances covered by the carriers make them more prone of being trapped. Distance is also an important factor for the impact ionization because charge carriers need space to earn enough kinetic energy to excite additional electron/hole pairs. The combination of these effects results in different collected signals for different incident locations for the ionizing/exciting particles. Taking into account these phenomena, the chosen positions for the incident particles are: *1)* intermediate region in the straight line between the junction and ohmic columns with medium-high electric field, *2)* a further location in the low field region between ohmic columns.

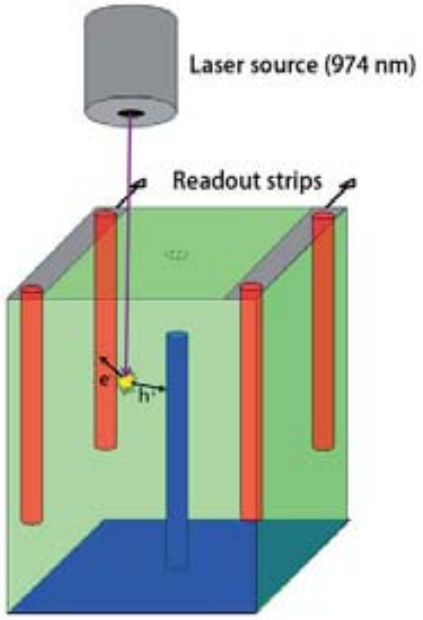

Figure 5.62: *Schematic of the laser setup used for the microstrip detectors.*

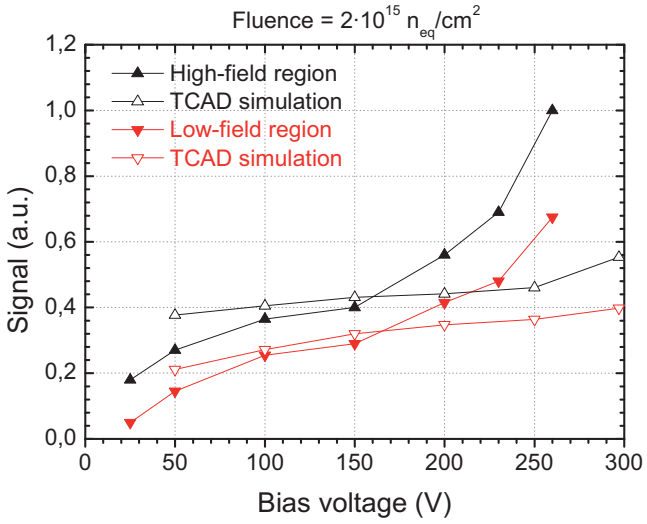

Figure 5.63: *Charge collected in the detector irradiated at 2×10^{15} n_{eq}/cm^2 for two locations of the incident MIP with different field strength, denoted HF and LF. Curves using filled symbols correspond to experimental laser measurements -30ºC, while empty symbols are obtained by TCAD simulations -20ºC for the irradiated case.*

The measurements have been carried out using a laser source whose wavelength is 974 nm. The absorption depth of this laser is ~100 μm in silicon at T = -30ºC. Each photon of this laser source has a kinetic energy of $E = \frac{hc}{\lambda} = 1.274\ eV$, higher than the silicon bandgap energy $E_g(-20^{\circ}C) = 1.136\ eV$, which is the required energy to promote a valence electron into the conduction band. The excited electrons are collected onto the n^+ readout electrode and give the signals which correspond to the two incident locations of the laser, high-field region *HF* and low-field region *LF*. The measured signals are plotted in arbitrary units (a.u.) scaled to their maximum signal for each fluence. In order to compare the measured signals and the charge collected due to the incident MIPs from the TCAD simulations, the simulated signals for 2×10^{15} n_{eq}/cm^2 are normalized using the 45 ke^- collected for *HF* at 260 V in the pion test, obtaining the plot of figure 5.63. The simulated signal of the *HF* is the same one that the simulated signal to compare with the ^{90}Sr beta source and beam test measurements as the position of the incident MIP is the same in both cases, thus the curve of figure 5.61 denoted in black with empty symbols are the same than in figure 5.63. The signals obtained from the low-filed region, *LF*, are denoted in red in figure 5.63. As occurred with the previous comparison between experimental measurements and simulations, there is a lack of intermediate traps to favour the detrapping from deep levels to reach the edges of the bands for higher voltages and the additional traps also would increase the trapped charge for lower voltages to match the experimental data. Concerning the qualitative differences between signals obtaining from the two incident locations, there is a great agreement between the signals from TCAD simulations and laser measurements for 2×10^{15} n_{eq}/cm^2.

In the study of Ref [135] it can be found another outstanding result obtained using laser scans with 2 μm step size using the IR laser of 974 nm wavelength and 4 μm step size using high energy pions on the unirradiated/irradiated 3D-DDTC microstrip detectors. Negative signals are measured in neighbouring readout strips to the hit strip. As it was commented in the section about *weighting potential – induction of current*, a negative pulse in the neighbouring electrode is obtained due to the displacement current because of the induced current on the electrode of interest. Then it is followed by a longer positive pulse as the physical electrons are being collected. The integrated signal on the neighbouring electrode depends on the applied voltage and the sampling time, as it can be seen in table 5.3. In 3D detectors it should be zero after the total charge collection but in the 3D-DDTC detectors it results in a small fraction of the electrons that are generated outside the overlapped region where the fields are very weak and charge sharing may take place. The negative signals are more pronounced for higher voltages, as it can be seen in figure 5.64, thus the hypothesis of applying low voltages causing losses of collected charge in the fixed sampling time (25 ns) is not sustainable. Besides, the negative signals also occur in 3D STC[10] [136] therefore the measured misalignment of the ohmic columns from their nominal position is neither the cause. It is still an open question to solve.

[10] 3D STC: Single Type Column detectors from FBK are fabricated following an alternative geometry for 3D sensors that consists of 3D columnar junction electrodes etched from the top surface of the sensor and a backplane contact of standard planar technology.

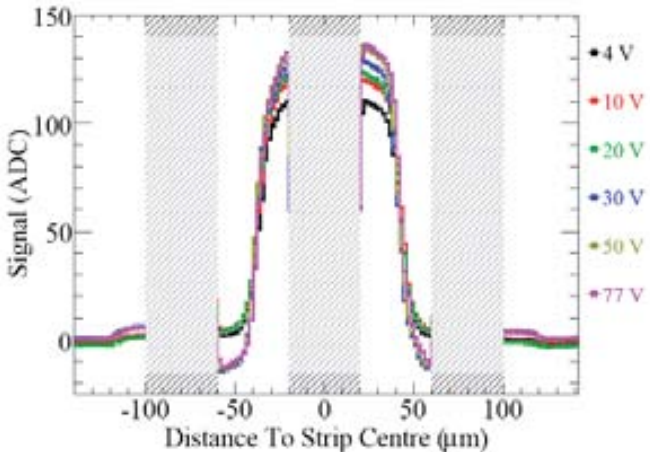

Figure 5.64: *Signals measured on the central strip as a function of the distance of the incident laser for an unirradiated n-in-p 3D microstrip detector measured at -20ºC [135]. Shaded regions correspond to metal strips.*

FE-I4 detector

Leakage current measurements of the 3D-DDTC FE-I4 detectors after the flip-chip[11] process to the electronics chip were performed before and after irradiation at IFAE[12] [137]. Because of the 3D architecture, measurements of the whole sensitive area in 3D pixel sensors could not be performed before the flip-chip as occurs with planar pixel detectors in which a high enough bias on one pixel would extend the bias to the rest of the pixels by punch-through. Thus experimental measurements of figures 5.66a and 5.66b using the daughterboard of figure 5.65 include also the current from the 3D guard ring.

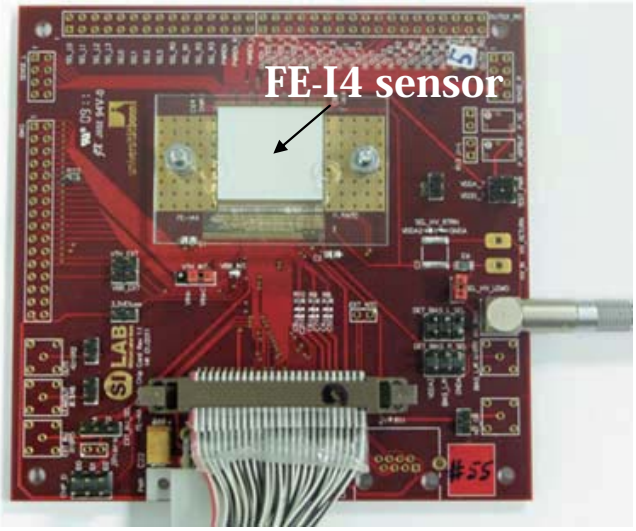

Figure 5.65: *Daughterboard used at IFAE to evaluate the performance of the FE-I4 sensors fabricated at the IMB-CNM (CSIC) Clean Room facilities.*

[11] Flip chip is the process in which pixels are bump-bonded to the readout electronic chip.
[12] IFAE: High Energy Physics Institute, belonging to the Autonomous University of Barcelona (UAB).

The same trend of microstrip detectors from figures 5.55 and 5.57a is found in the leakage current of the FE-I4 detectors. In the unirradiated case both experimental and simulation currents increase up to the depletion voltage. After the full depletion voltage, the current from the simulation increases slightly, contrary to the experimental currents from both unirradiated and irradiated whose increasing is higher maybe due to the contribution of the surface current flowing into the 3D guard ring. This increment in the currents after irradiation in the real devices is due to radiation induced defects that act as generation-recombination centers and due to impact ionization for higher voltages. In the simulations are required additional shallow-mid levels for increasing the trapping of free carriers at low voltages that also would enhance the detrapping for higher voltages.

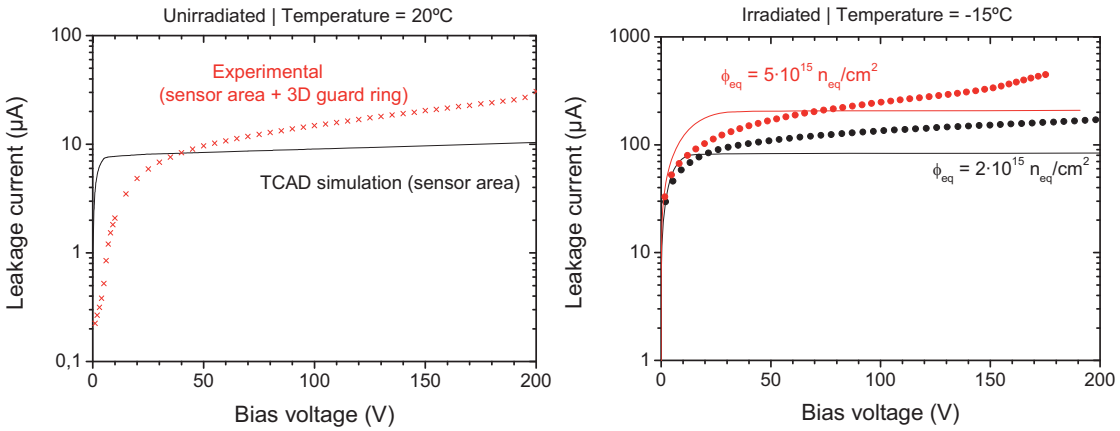

Figure 5.66: *Comparison between the simulated current of the sensor active area and the leakage current of the whole sensor (active area + 3D guard ring) for the FE-I4 detector before irradiation (left) and after irradiation (right). Straight lines correspond to simulations of the whole sensitive area while cross symbols correspond to experimental measurements of both sensitive area and 3D guard ring currents.*

Charge collection measurements of such detectors were carried out at IFAE using an analogue ^{90}Sr setup[137], as in figure 5.59, mounted inside a thermostatic case. The results are plotted in figure 5.67 and compared with the simulations, evidencing again a mismatch for the collected signals of irradiated sensors that might be improved as previously proposed including additional traps with shallow-mid levels within the bandgap.

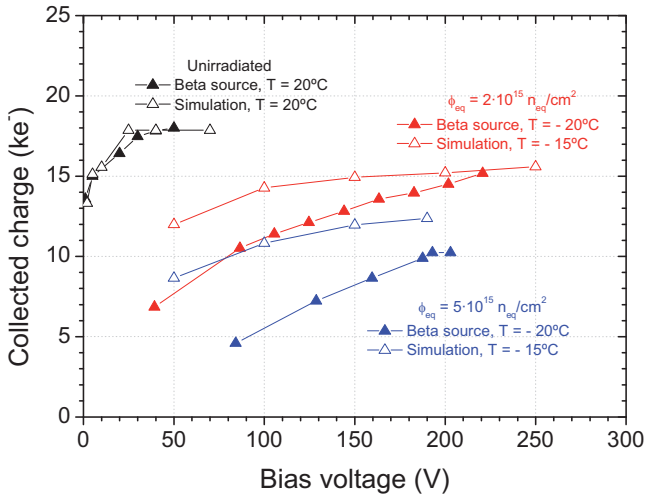

Figure 5.67: *Comparison graph showing the experimental measurements of the charge collected in the unirradiated/irradiated FE-I4 detectors for different bias voltages and the corresponding results from the TCAD simulations previously presented in this chapter.*

5.4 Low resistivity substrates

3D-DDTC (Double-side Double Type Column) microstrips detectors fabricated at IMB-CNM (CSIC) [37] and characterized in the University of Freiburg [128, 129, 135], present charge multiplication effect after irradiation due to the presence of high electric fields that exceed the field strength required for impact ionization. This effect increases the charge collected and offers the interesting possibility of developing thinner detectors with the same configuration that provide the same signal before irradiation. This task can be achieved combining properly lower resistivity substrates, with the drawback of increasing the depletion voltage, and low bias voltages but high enough to ensure electric fields suitable for charge multiplication. The main advantage of using detectors with low resistivity substrates relies on obtaining high field peaks in the absence of trapping, however higher bias voltages are required to avoid the losses of charge carriers by recombination in undepleted regions.

5.4.1 TCAD simulations

The simulated geometry is the same three-dimensional cell of figure 5.29a whose dimensions are 80 µm × 80 µm × 285 µm. Four ohmic columns are located in the corners while the junction column is placed in the centre. The junction column n^+ is surrounded by a p-stop ring for insulation from the electron channel. The columns have a 10µm diameter and 250 µm depth. Both sides, top and bottom, are covered by a 0.8µm SiO_2 layer and the surface charge density at the interface with silicon is set to 5×10^{11} cm^{-2}. The different values of the bulk resistivities are listed in table 5.6.

Leakage current

The leakage currents of the simulated cell for each resistivity are shown in figure 5.68. Reverse currents depend on the minority carrier densities so that increasing the effective doping concentration of the substrate will reduce the minority carriers densities according to the *mass action law*, equation **18**. This increasing of the doping concentration also leads to high fields near the pn^+ junction and therefore the electrical breakdown is reached for lower voltages. The values of breakdown voltages resulting from the TCAD simulations are listed in the table 5.6.

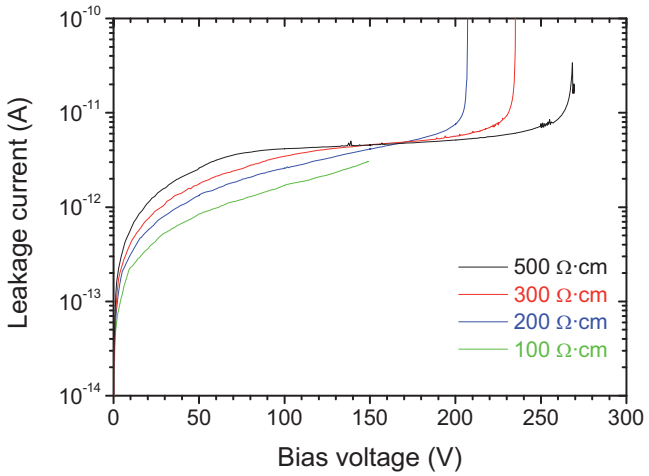

Figure 5.68: *Current voltage characteristics of the 3D cell for the different resistivities under study. The temperature in the simulations was set to -20ºC.*

Table 5.6: *Comparison of the different nominal values of full depletion from equation 78 and electrical breakdown voltages from the simulations for each resistivity.*

Resistivity (Ω•cm)	Nominal V_{FD} (V)	Breakdown voltage (V)
500	100	270
300	167	235
200	251	207
100	503	149

Electrostatic potential

The decreasing resistivity of the sensor substrate increases the effective doping concentration, N_{eff}, having effects on the depletion and breakdown voltages.

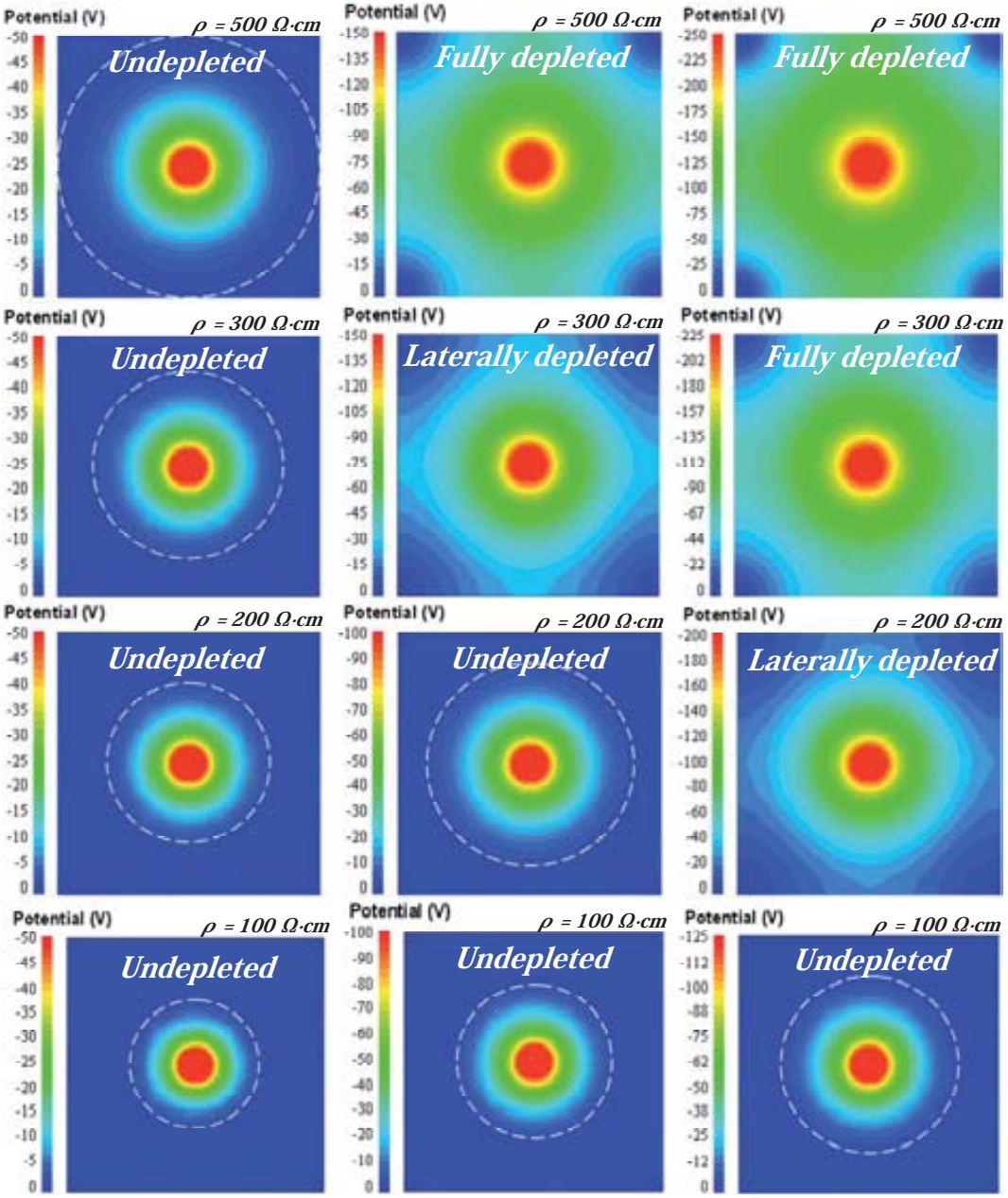

Figure 5.69: *Electrostatic potential distributions and space charge region (segmented circle) for a slice within the region of overlapped columns, z = 142.5 μm, for different resistivities.*

The increasing of the majority carriers diffusion at the *pn* junction leads to higher fields in that region; the equilibrium of the diffusion and drift currents has a result a higher build-in potential, V_{bi}, that increases the applied bias required to deplete the sensor. The depletion voltage is also increased due to the increase of the effective dopping concentration, obtaining the nominal values of table 5.6. On the other hand, increasing the applied bias to obtain a depleted sensor is not possible at the lowest resistivities of this study as the strong fields at the *pn* junction also increase producing electrical breakdown.

Electric field

The electric field of the simulated cell is studied to understand the performance of these radiation detectors as well as for determining where the electrical breakdown of the sensors takes place.

Overlapped region

Profiles of electric field between one p^+ electrode and the central electrode n^+ at the center of the overlapped region of the 3D cell for each resistivity under study are shown in figure 5.70 at different bias voltages. As it was previously commented, as the effective doping concentration is been increased, the electric field at the *pn* junction is also increased, while the field at the p^+p contact is reduced because of the lower gradient of doping concentrations.

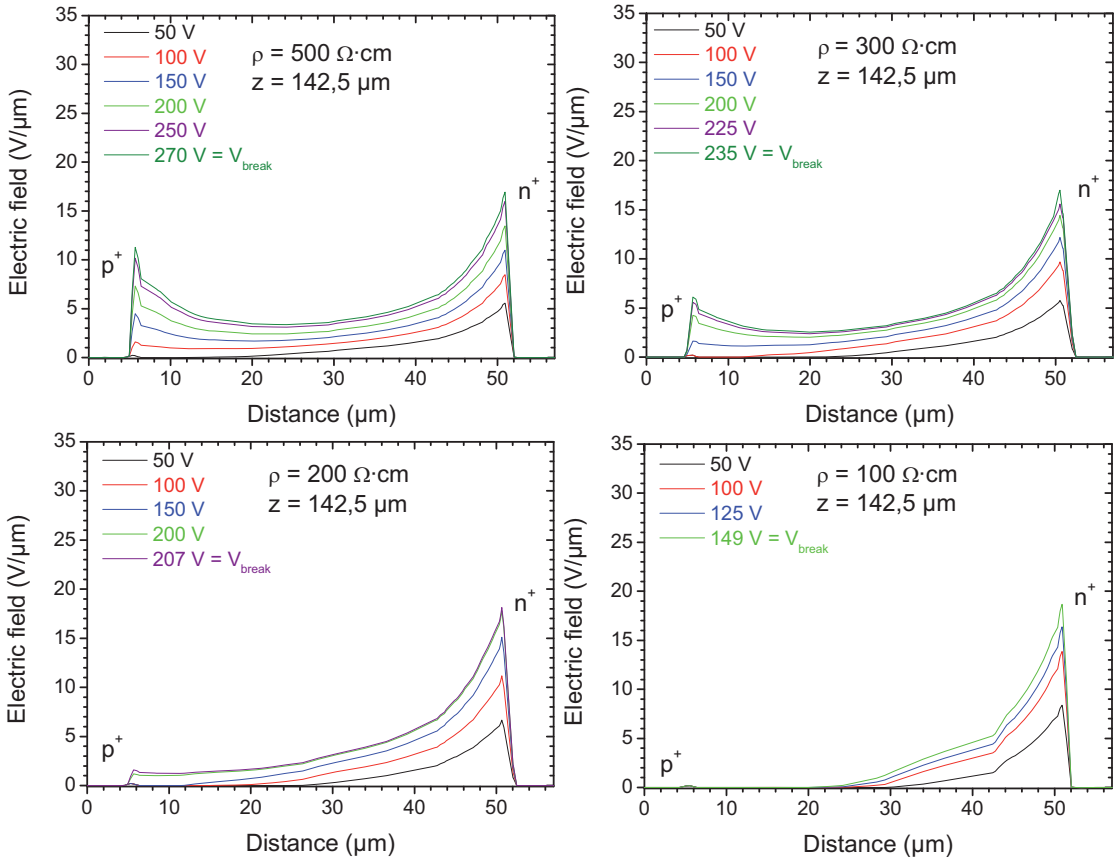

Figure 5.70: *Electric field profiles between one p^+ electrode and the n^+ readout electrode within the overlapped region for several applied bias voltages and different resistivities.*

Electric field at the p-stop

The short distance between the p-stop implantation and the junction columns is a region of special interest to study the electric field as it can be responsible or contribute to the electrical breakdown of the sensor. In figure 5.71 it can be observed that the lower the resistivity is, the higher the field peaks are. At the breakdown voltages, the field peaks reach values that in all of the cases exceed 20 V/µm. In the particular case of the lowest resitivity, 100 Ω·cm, the field peak at the p-stop reaches 35 V/µm resulting the main responsible of the electrical breakdown of the sensor.

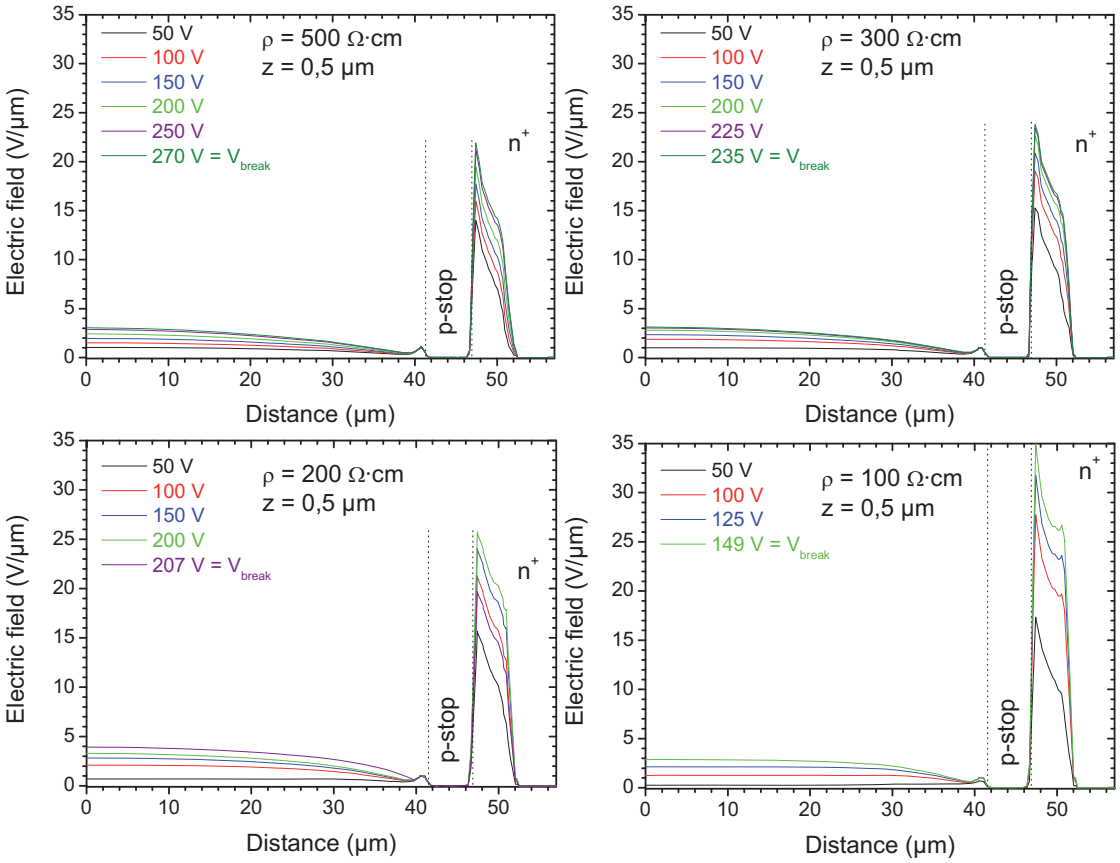

Figure 5.71: *Electric field profiles between one p^+ electrode and the n^+ readout electrode near the p-stop for several applied bias voltages and different resistivities.*

Tip of the ohmic columns, p^+

Due to the hemispherical geometry of the columnar tips, electric fields in those regions are higher than along the columnar electrodes [134]. As long as the resitivity of the substrate is reduced, the field peaks at the p^+p contacts are also reduced, although their spherical geometry makes this decrease less pronounced than at the contact of the columnar electrodes, as it can be appreciated comparing figures 5.70 and 5.72.

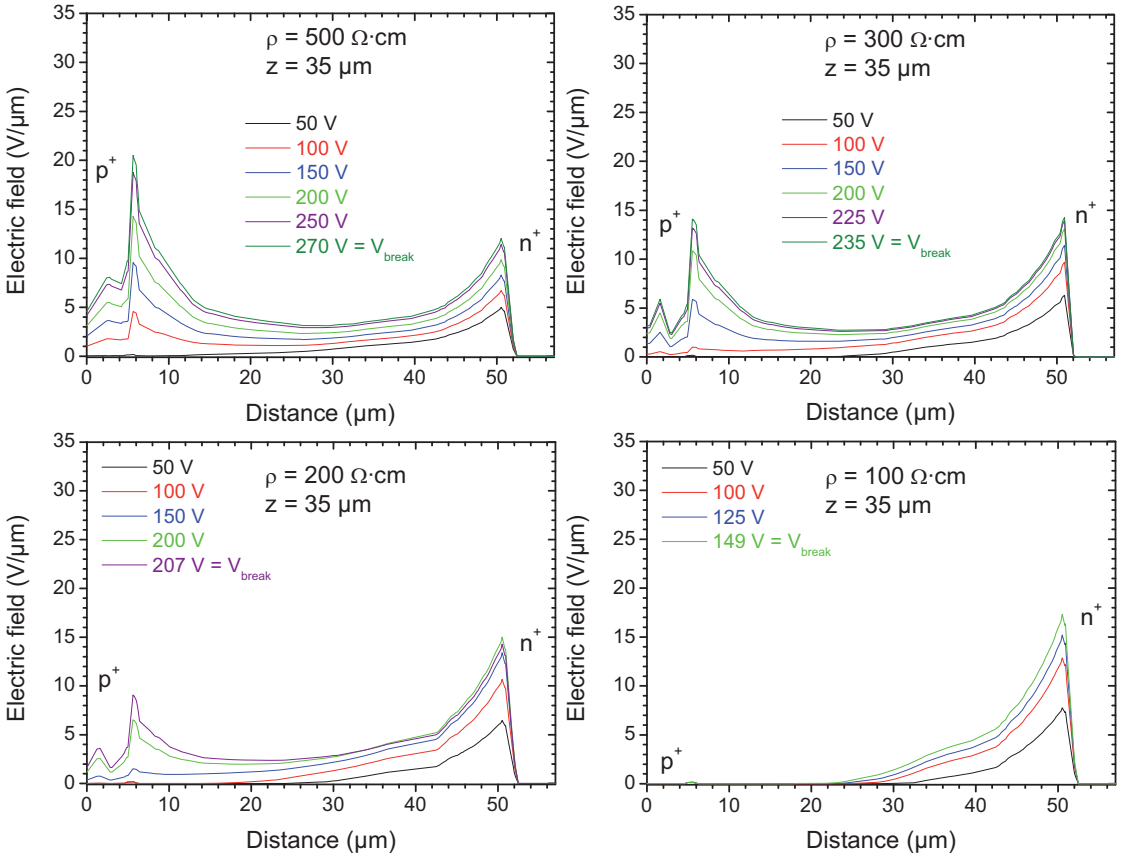

Figure 5.72: *Electric field profiles between one p^+ electrode and the n^+ readout electrode at the tip of the ohmic columns for several applied bias voltages and different resistivities.*

Tip of the junction column, n^+

The combination of the spherical geometry of the tip of the columnar electrodes and increasing gradient between doping concentrations at the junction columns favours the formation of very high electric field peaks in these regions, as it is shown in figure 5.73. These strong fields are the main responsible of the electrical breakdown of the sensor, with the exception of the substrate with resitivity 100 Ω·cm, in which the field peak at the p-stop region reaches higher values.

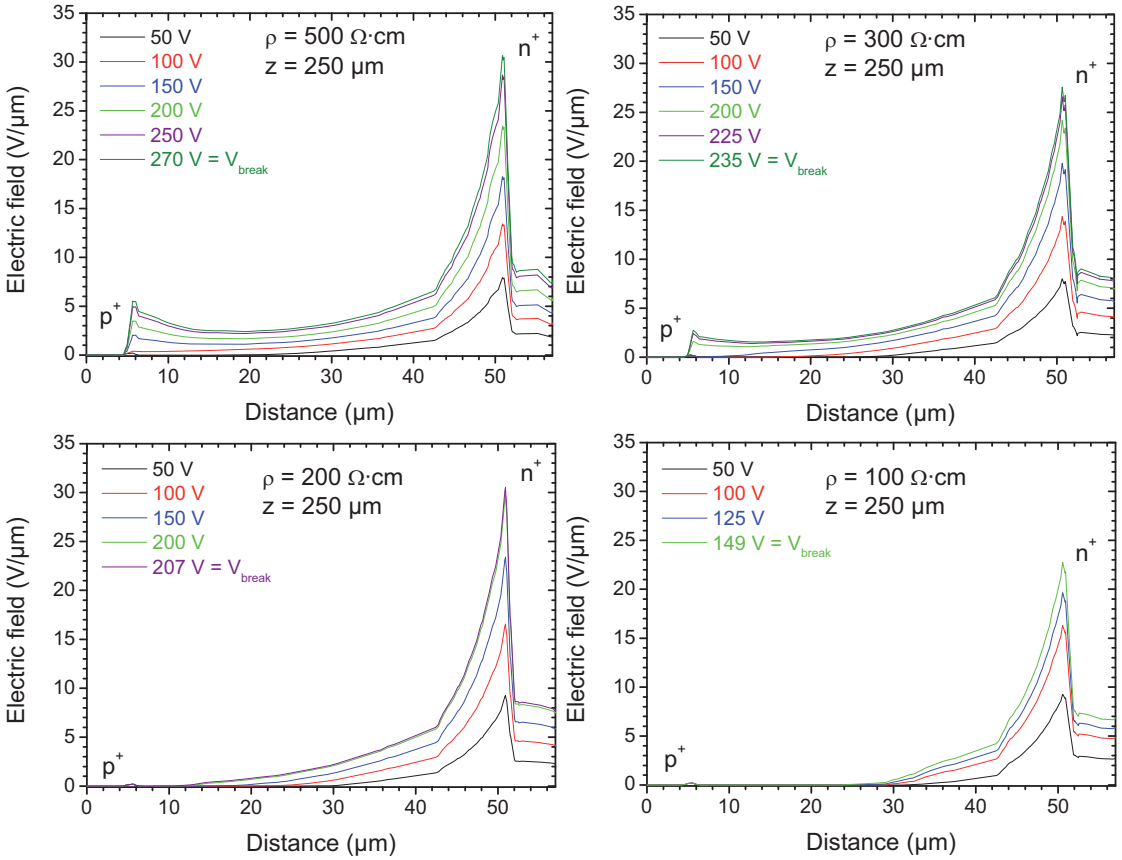

Figure 5.73: *Electric field profiles between one p^+ electrode and the n^+ readout electrode at the tip of the junction column for several applied bias voltages and different resistivities.*

Table 5.7 presents a summary of information concerning the electrical breakdown of the sensors. The maximum field peaks are gathered together for each resistivity to determine the relative contribution of each region of interest.

Table 5.7: Field peak values at the breakdown voltage at the p-stop ($z = 0.5\ \mu m$), at the tip of the ohmic columns ($z = 35\ \mu m$), in the middle of the overlapped region ($z = 142.5\ \mu m$) and at the tip of the junction column ($z = 250\ \mu m$) for different resistivities.

Resistivity (Ω•cm)	19000	500	300	200	100
N_{eff} (cm^{-3})	7.00×10^{11}	2.66×10^{13}	4.43×10^{13}	6.65×10^{13}	1.33×10^{14}
Nominal V_{FD} (V)	2.6	100	167	251	503
Breakdown voltage V_{br} (V)	290	270	235	207	149
E_{max} @ z = 0.5 μm (V/μm)	13.7	21.9	23.8	25.7	**35.0**
E_{max} @ z = 35 μm (V/μm)	**28.3**	20.5	14.3	14.3	17.3
E_{max} @ z = 142.5 μm (V/μm)	15.3	16.9	17.0	18.1	18.7
E_{max} @ z = 250 μm (V/μm)	**30.4**	**30.7**	**27.6**	**30.5**	22.8

Response to MIP particles

The response of the detector to the pass of particles has been simulated by the use of a MIP particle. The incident point of the particle is in the intermediate location between the central electrode and one of the bias electrodes, whose coordinates are (20, 20) at a distance from the collecting electrode of $d = 20\ \mu m \times \sqrt{2} = 28.3\ \mu m$. Transient simulations have been performed for different bias voltages below the breakdown voltage.

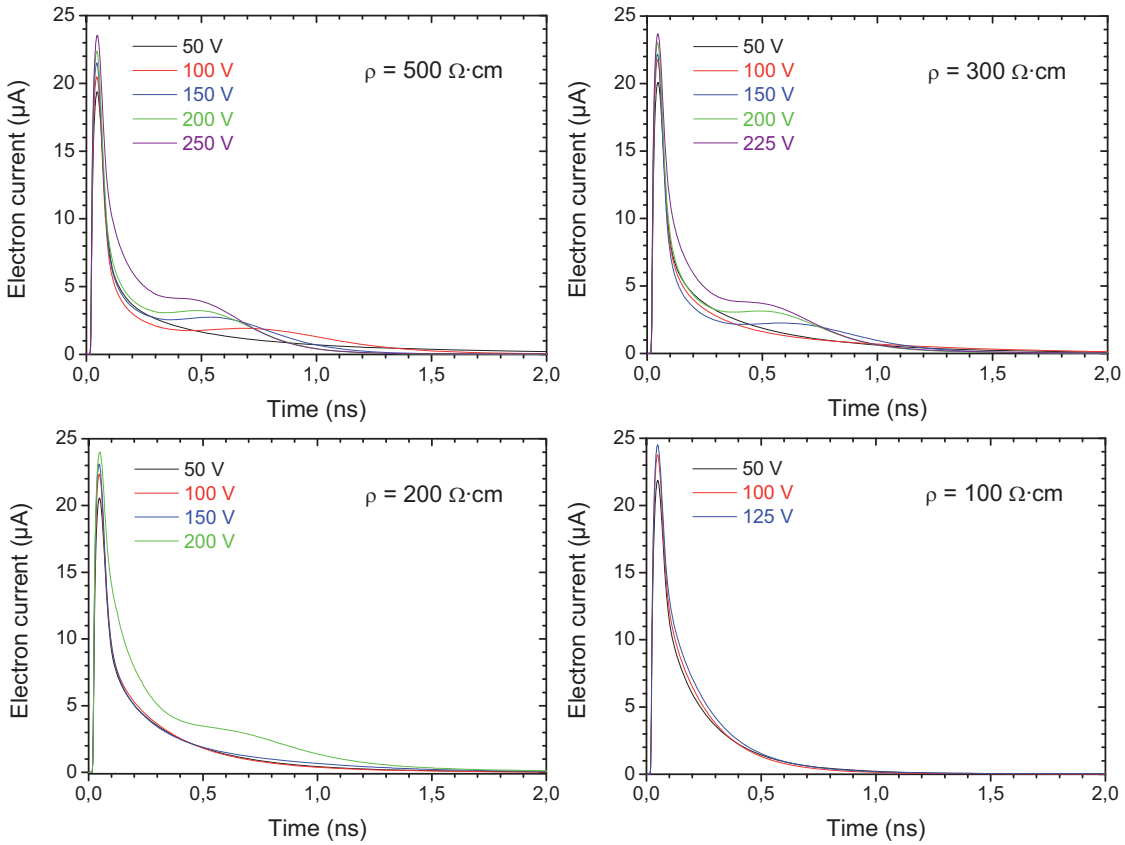

Figure 5.74: *Current pulses for several bias voltages for a MIP crossing at the intermediate position between opposite electrodes (20 μm, 20 μm).*

From figure 5.74 it can be appreciated that most of the charge is collected in the first nanosecond (faster than in high resistivity substrates of figure 5.36a) and the differences between each pulse lie on their increasing height with the higher applied bias, with more narrow peaks, and on the size of the secondary electronic hill (at around 0.5 ns – 1.0 ns) due to the contribution of collected holes. Pulses at higher voltages are also increased because of the contribution of electron/hole pairs produced by impact ionization.

It is also remarkable that when the applied bias is not high enough to depleted the detector, see figure 5.70, the contribution holes is negligible as those charge carriers are crossing an undepleted region and most of them (or all) are recombined.

Charge multiplication

Charge collection efficiency (CCE) for each applied bias and resistivity are shown in figure 5.75. They were obtained by integrating the different pulses of figure 5.76 for a collection time of 25 ns and dividing the result by the introduced charge, which is 80 e/h paris per µm × 285 µm = 22800 e/h pairs. For lower voltages than the depletion voltage the collected charge is around 96 % while for higher voltages all of the charge is collected and, if the applied bias is high enough, impact ionization occurs.

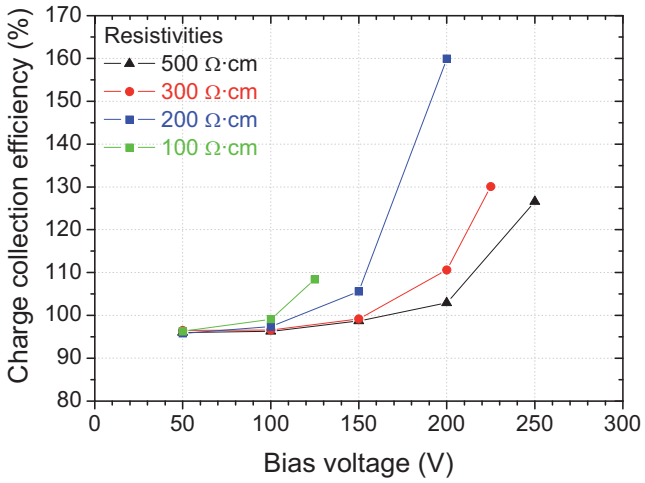

Figure 5.75: *Charge collection efficiency for different bias voltages in the substrates under study. The collection time of the pulses is 25 ns.*

In order to find the optimum configuration between low resitivity substrates that provide high multiplication of charge and a breakdown voltage below the bias for lateral depletion, the figure 5.76 summarizes all of the possible cases. The better choices are substrates whose resistivities are equal/higher than 200 Ω·cm operating at biases 5-10 % lower than breakdown voltages.

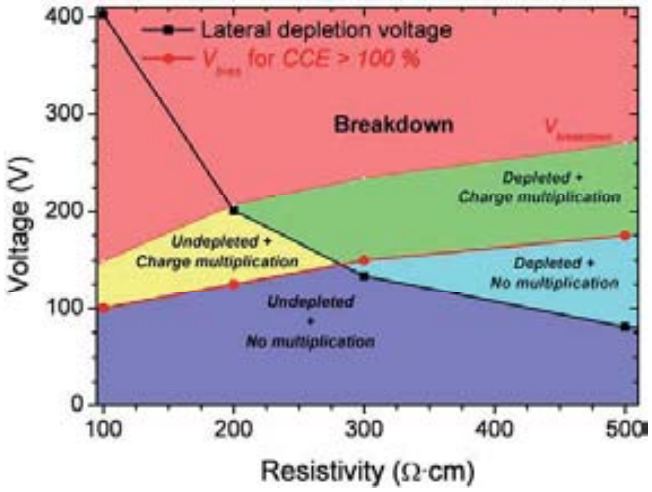

Figure 5.76: *Comparison of lateral depletion voltages and threshold bias for charge multiplication for different resistivity substrates. Values of depletion voltages in this curve are reduced by 20% from the nominal values according to the potential distributions in simulation results.*

5.5 Conclusions

U3DTHIN silicon detectors have been proposed as particle analyzers for plasma diagnosis of the future ITER fusion reactor. The low full depletion of the 3D electrodes geometry implemented in these detectors as well as their low capacitances make them suitable for the tasks of ion detection they are being proposed in this work. Their electrical properties have been simulated in different configurations to know their working behaviour.

Both aluminium strips and oxide surface charge play important roles in the electrical behaviour of these detectors. The field plate effect provided by the metallizations makes the potential and electric field to have distributions parallel to the aluminium strips, while the electron channels formed by electrons attracted by the positive charge located at the Si/SiO_2 interface makes the detectors require higher voltages to deplete those inversion layers to effectively fully deplete the sensors. This surface effect is more important if the sensor is thinner due to the proximity of both top and bottom electron layers.

U3DTHIN detectors are presently being used in neutron detection experiments at IMB-CNM (CSIC) after being covered by different boron converter layers: ^{10}B, H_3BO_3 (99% of ^{10}B) and o-carborane (natural B and 99% of ^{10}B), successfully measuring alphas [121] coming from the reaction

$$n + {}^{10}B \rightarrow {}^{7}Li + {}^{4}He$$

3D-DDTC silicon microstrip detectors on p-type substrates have been fabricated at IMB-CNM (CSIC) in order to evaluate the promising features that the 3D geometry offers on radiation hardness and low charge sharing [37] for the FE-I4 pixel sensors that will be mounted in the Insertable B-Layer at the ATLAS experiment. Electrical characterizations have been carried out at IMB-CNM [132] while charge collection studies before and after irradiation have been carried out by the University of Freiburg [128, 129, 135] and the University of Glasgow [130, 138]. In order to have a better knowledge of the behaviour of these detector such us electric field distributions or response of the sensor to MIP particles, TCAD simulations have been performed and compared with the experimental data. A 3D cell including a central junction columnar electrode n^+ and one quarter of ohmic p^+ electrode in each corner have been modelled. For the evaluation of the irradiated sensor a 3-level traps model from the University of Perugia and modified by the University of Glasgow have been implemented in the simulations. The results for the unirradiated sensor match the experimental measurements. The 3-level traps model have proved to work successfully in simulations of irradiated planar detectors [80] but in this 3D geometry is not working as good as the results from the simulations do not present enough agreement with the real measurements. Additional defects with shallow-mid levels within the silicon bandgap are needed to be implemented in the traps model to match the experimental leakage currents and charge collections for low and high voltages that present a more pronounced charge multiplication effect than in the simulations.

FE-I4 detectors were also fabricated and simulated at IMB-CNM (CSIC) and evaluated at IFAE [137] in the framework of the common project NEWATLASPLIXELS for the participation in the fabrication of 3D pixel detectors for the IBL. Simulation results were compared to experimental measurements which are suitable for the upcoming IBL scenario.

Radiation induced defects change the effective doping concentration of the substrate which becomes more p-type as long as the fluence/anneling-time is increased. This effect causes an increasing of the electric field around the n^+ electrodes as more majority carriers diffuse from both sides of the pn^+ junction. An increase of the collected signals has been observed in irradiated 3D-DDTC microstrip detectors due to the impact ionization that takes place in the presence of such high fields, as it can be seen in figure 5.61. In the same way, as long as the effective doping concentration of the substrate is increased (lower resistivities) the electric field in the pn^+ junctions is also higher, with the drawbacks of requiring higher voltage to deplete detectors of such resistivities, as well as presenting lower breakdown voltages, as it is shown in table 5.7. Unirradiated 3D-DDTC detectors fabricated using wafers with resistivities higher than 200 Ω·cm are a good choice to obtain signals affected by charge multiplication as they grant very high field peaks at the pn^+ junctions and their breakdown voltages are higher than the required voltages for lateral depletion.

Chapter 6

Conclusions

Two different traps models for n-type and p-type silicon detectors presented in Chapter 3 have been implemented in the simulations of irradiated detectors in this work. The modified n-type model used in p-in-n slim-edge detectors qualitative reproduces the radiation effects on the effective doping concentration, electrostatic potential and electric field distributions however the simulated collected charge is overestimated for high radiation fluences, revealing a lack of charge carriers trapping. In the case of the modified p-type model it has been proved that reproduces experimental results of planar detectors but it needs to be improved with additional radiation defects with mid-shallow energy levels within the bandgap to reproduce collected charge in irradiated 3D detectors as they presented charge multiplication that is only slightly observed in simulations. A possible solution: as most of the radiation induced defects are based on interstitials, vacancies, multi-vacancies and carbon and oxygen impurities of different substrates we have that the contribution of boron or phosphorus dopants on the radiation induced defects is negligible it is therefore more adequate to distinguish between neutron and fast charged hadron irradiations instead of n-type or p-type substrates to count on proper radiation damage models. These two new traps models for neutron and fast charged hadron irradiations should implement both shallow-mid levels and deep levels whose introduction rates should be proportional to the areas of the signals from TSC measurements after neutron/hadron irradiations, the correspondent electron/hole capture cross-sections should also match the effective trapping time constants of table 3.6. Each trap in the models do not need to present accurate values of a particular defect (energy level, capture cross-sections, introduction rate) as they will represent the whole spectrum of radiation induced detects in silicon and those trap parameters have to embrace similar defects in order to reduce the amount of traps of each model to a reasonable number. As the introduction rate of thermal donors after proton irradiation is much more important in oxygenated substrates due to oxygen dimmers O_{2i}, these two models can be reduced to one model in the case of Float Zone substrates for both n- and p-type silicon.

Slim-edge and active-edge termination techniques are introduced in Chapter 4 as two approaches in the reduction of the inactive area of silicon radiation detectors. The first method was developed at CERN [11] for the TOTEM experiment [5, 6] to detect particles emitted at low angles in the very forward cone, which is not covered by the large detectors present at CERN, and therefore they require detectors whose sensitive area approaches the envelope of the proton beam as close as possible. Slim-edge detectors are based on a current terminating structure with two grounded rings within

the first 50 μm from the edge: one at the edge of the detector (CTR) and another as clean-up ring (CUR). Both rings collect all the current generated by the lattice defects of the cut surface. Slim-edge p-in-n detectors have been successfully used in the TOTEM experiment at LHC [112]. The work done is this thesis in collaboration with CERN and other institutions includes slim-edge detectors fabricated on p-type silicon substrates as their higher radiation tolerance and faster readout (collection on electrons) make then suitable for TOTEM experiment at the HL-LHC.

The second termination technique studied in this work is called *active edge* [96] which is based on the sidewall doping thus extending the backplane electrode to the peripheral surfaces of the detector. This termination does not suffer from surface currents that are found after the diamond sawcut so the dead area of this sensor is limited to ~ 4 μm due to the thicknesses of the passivation oxide, the doped polysilicon and the diffusion length of the dopants within the silicon substrate. The main advantage of this termination is the possibility of tiling sensors to form arrays with negligible dead area, as it is required in small angle X-ray scattering (SAXS) and X-ray diffraction (XRD). Detectors implementing this termination technique are also suitable for close-to-beam experiments such as TOTEM experiment or X-ray beam monitoring in synchrotron facilities.

An innovative technique in the reduction of the insensitive area of radiation detectors that is now under investigation consists of the sidewall passivation of diced detectors with silicon oxide for n-type substrates and with alumina (Al_2O_3) for p-type substrates after scribing their peripheral sides using XeF_2 etch to obtain a cleavage plane without defects [139, 140]. This minimized damage surface has a reduced leakage current, while the passivation affects the potential distribution at the sidewall. The potential drop at the edge of the detectors depends strongly on the positive (negative) charge concentration at the interface with silicon oxide (alumina) used for passivating sidewalls of n-type (p-type) silicon substrates. Lower surface charge concentrations are preferred since the potential drop at the edge is more gradual, on the contrary a high surface charge concentration would extend the backplane potential (like in active-edge detectors) thus obtaining high field regions for short distances from the last electrode to the passivated sidewall.

Alumina can also be used for passivating top surfaces of 3D-DDTC detectors fabricated on p-type substrates studied in Chapter 5. The alumina deposition would suppress the need of p-stop/p-spray insulation and thus the contribution to the electrical breakdown of the high fields at those regions in heavily irradiated detectors would also disappear. In addition, a reduction of the doping concentration at the tip of the columnar electrodes would reduce the electric field due to the half-spherical geometry to prevent from avalanche breakdown. IMB-CNM (CSIC) is presently working in the development of n-in-p detectors passivated with alumina for research purposes as well as 3D-DDTC detectors with passivated slim edges.

Double-sided 3D silicon detectors for the ATLAS upgrades and the Insertable B-Layer include the last advances of the CERN RD50 collaboration in the development of radiation hard detectors, are studied in Chapter 5. The promising features of 3D-DDTC detectors were initially studied in microstrip detectors that were fabricated and electrically characterized at IMB-CNM (CSIC) while charge collection studies before and after irradiation were performed at the Universities of Freiburg and Glasgow. TCAD simulations have been also implemented to reproduce the experimental measurements for a better understanding of the performance of such detectors for

different radiation fluences and how could they be improved in terms of operation or efficiency. FE-I4 detectors were subsequently also fabricated and simulated at IMB-CNM (CSIC) and evaluated at IFAE obtaining successful results that make them suitable for the IBL scenario.

The architecture of columnar electrodes is also implemented in U3DTHIN detectors for alpha detection, as their sensitive substrate is in the order of tens of micrometers. This reduces the electrodes-to-backplane capacitance and the signal attenuation in comparison with detectors with the same thickness fabricated using standard planar technology. Both PAD and microstrip designs of these detectors were fabricated and simulated at IMB-CNM (CSIC), and were also tested successfully with alpha particles using ^{241}Am. They are also currently being used in neutron detection after the deposition of a converter layer of any material containing ^{10}B which has a high capture cross-section of thermal neutrons. Due to the short distance between top and bottom planes in U3DTHIN detectors, surface effects (field plate of strip metallizations, oxide surface charge) play important roles in their electrical behaviour.

As it was explained in this work, the positive surface charge of Si/SiO_2 interfaces attracts electrons from the bulk creating an electron channel that may shorten the n^+ electrodes on p-type substrates if they are not properly insulated with p-spray/p-stop rings, but it also plays an important role in the depletion of 3D detectors. Capacitance-voltage measurements in U3DTHIN detectors reveal that this surface charge increases the full depletion voltage as it was demonstrated with TCAD simulations. Also 3D-DDTC detectors are affected by the electron channels that are created at the top and bottom interfaces with the silicon oxide producing a second drop in the capacitance-voltage characteristic when those inversion layers are also depleted, although this behaviour is only envisaged in simulations through the charge collection curves. Implementing the oxide interface charge in the simulations as trapped positive charge instead of fixed positive charge could be a possible solution to obtain better accurate results on the capacitance measurements in both U3DTHIN and 3D-DDTC detectors.

References

1. Moll, M. *RD50 Collaboration. Radiation hard semiconductor devices for very high luminosity colliders.*; Available from: http://rd50.web.cern.ch/rd50.

2. Moll, M. *RD48 Collaboration. Research and development on silicon for future experiments.*; Available from: http://rd48.web.cern.ch/rd48.

3. *The Large Hadron Collider*. Available from: http://lhc.web.cern.ch/lhc.

4. *ATLAS Experiment*. Available from: http://atlas.ch.

5. Avati, V. and T. Collaboration, *The TOTEM Experiment at the LHC.* Progress of Theoretical Physics Supplement, 2011(187): p. 281-288.

6. Kienzle, W., *TOTEM. Total Cross Section, Elastic Scattering and Diffraction Dissociation at the LHC.*, 1997. p. 47.

7. *The ITER project*. Available from: http://www.iter.org.

8. *Diamond Light Source*. Available from: http://www.diamond.ac.uk.

9. *Proton beams.* . LHC Machine Outreach; Available from: http://lhc-machine-outreach.web.cern.ch/lhc-machine-outreach/beam.htm.

10. Oriunno, M., et al. *Roman pots for the LHC*. in *10th European Particle Accelerator Conference*. 2006. Edimburg, Scotland.

11. *TOtem STrip Edgeless Radiation detectors*. Available from: http://project-romanpot.web.cern.ch/project-romanpot/Intas_toster/Inatas_Toster.htm.

12. Klingenberg, R. and A.P. Collaboration, *The ATLAS pixel detector.* Nuclear Instruments & Methods in Physics Research Section a-Accelerators Spectrometers Detectors and Associated Equipment, 2007. **579**(2): p. 664-668.

13. Darbo, G., *The ATLAS IBL project*, 2010, CERN.

14. Marcisovsky, M., *ATLAS insertable B-layer.* Nuclear Instruments & Methods in Physics Research Section a-Accelerators Spectrometers Detectors and Associated Equipment, 2011. **633**: p. S224-S225.

15. Grenier, P., *Silicon sensor technologies for ATLAS IBL upgrade*, in *Technology and Instrumentation in Particle Physics*2011: Chicago.

16. Dietz, J., *The ITER fusion experiment.* Vacuum, 1996. **47**(6-8): p. 911-918.

17. *Summary of the ITER Final Design Report*, 2001.

18. *ITER Technical Basis*, 2001.

19. Afanasyev, V.I., et al., *Neutral particle analysis on ITER: present status and prospects.* Nuclear Instruments & Methods in Physics Research Section a-Accelerators Spectrometers Detectors and Associated Equipment, 2010. **621**(1-3): p. 456-467.

20. Garcia, F., et al., *A novel ultra-thin 3D detector-For plasma diagnostics at JET and ITER tokamaks.* Nuclear Instruments & Methods in Physics Research Section a-Accelerators Spectrometers Detectors and Associated Equipment, 2009. **607**(1): p. 57-60.

21. Jackson, J.D., *Classical Electrodynamics*. Third edition ed1999: Wiley.

22. Attwood, D., *Spatially filtered undulator radiation*: University of California, Berkeley.

23. Kenney, C.J., et al., *Use of active-edge silicon detectors as X-ray beam monitors.* Nuclear Instruments & Methods in Physics Research Section a-Accelerators Spectrometers Detectors and Associated Equipment, 2007. **582**(1): p. 178-181.

24. Lutz, G., *Semiconductor radiation detectors*, ed. Springer1999.

25. Sze, S.M., *Semiconductor devices: Physics and technology,*1985.

26. Goulding, F.S., *SEMICONDUCTOR DETECTORS FOR NUCLEAR SPECTROMETRY.* Nuclear Instruments & Methods, 1966. **43**(1): p. 1-&.

27. Knoll, G.F., *Radiation detection and measurement*. Third edition ed, ed. Wiley1999.

28. Marler, J.M. and P.V. Hewka, *COAXIAL DETECTORS FROM HIGH-PURITY GERMANIUM.* Ieee Transactions on Nuclear Science, 1974. **NS21**(1): p. 287-295.

29. Chilingarov, A., *Generation current temperature scaling*, 2011, CERN RD50 collaboration.

30. Synopsys, *DESSIS manual. ISE TCAD Release 10.0*.

31. Fleta, C., *Tecnología de detectores de partículas de silicon resistentes a la radiación*, in *Centro Nacional de Microelectrónica IMB-CNM (CSI)*2006, Universitat Autònoma de Barcelona.

32. Peisert, A., *Silicon microstrip detectors*, 1992, Instituto Nazionale di Fisica Nucleare: Padova.

33. Krammer, M., *Detector structures*, Talk, Editor 2010: XI ICFA School on Instrumentation, Argentina.

34. Barberis, E., et al., *CAPACITANCES IN SILICON MICROSTRIP DETECTORS.* Nuclear Instruments & Methods in Physics Research Section a-Accelerators Spectrometers Detectors and Associated Equipment, 1994. **342**(1): p. 90-95.

35. Hartmann, F., *Evolution of silicon sensor technology in particle physics*, ed. Springer2009.

36. Rossi, L., et al., *Pixel detectors, from fundamentas to applications.* Particle acceleration and detection., ed. Springer2006.

37. Mathieson, K., et al., *Charge sharing in silicon pixel detectors.* Nuclear Instruments & Methods in Physics Research Section a-Accelerators Spectrometers Detectors and Associated Equipment, 2002. **487**(1-2): p. 113-122.

38. Parker, S.I., C.J. Kenney, and J. Segal, *3D - A proposed new architecture for solid-state radiation detectors.* Nuclear Instruments & Methods in Physics Research Section a-Accelerators Spectrometers Detectors and Associated Equipment, 1997. **395**(3): p. 328-343.

39. Kenney, C., et al., *Silicon detectors with 3-D electrode arrays: Fabrication and initial test results.* Ieee Transactions on Nuclear Science, 1999. **46**(4): p. 1224-1236.

40. Pellegrini, G., et al., *First double-sided 3-D detectors fabricated at CNM-IMB.* Nuclear Instruments & Methods in Physics Research Section a-Accelerators Spectrometers Detectors and Associated Equipment, 2008. **592**(1-2): p. 38-43.

41. Affolder, A. and e. al., *Silicon detectors for the sLHC.* Nuclear Instruments & Methods in Physics Research Section A-Accelerators Spectrometers Detectors and Associated Equipment, 2011. **658**: p. 6.

42. Srour, J.R., C.J. Marshall, and P.W. Marshall, *Review of displacement damage effects in silicon devices.* Ieee Transactions on Nuclear Science, 2003. **50**(3): p. 653-670.

43. *ASTM E722-85, ASTM E722-93 (revised)*, 1993.

44. Moll, M., *Radiation damage in silicon particle detectors*, 1999, Hamburg: Faculty of physics.

45. Vasilescu, A. and G. Lindstroem, *RD48 (ROSE) Status Report 2000.* 2000.

46. Lindstrom, G., M. Moll, and E. Fretwurst, *Radiation hardness of silicon detectors - a challenge from high-energy physics.* Nuclear Instruments & Methods in Physics Research Section a-Accelerators Spectrometers Detectors and Associated Equipment, 1999. **426**(1): p. 1-15.

47. Watts, S.J., *Radiation induced defects in silicon.* High Purity Silicon V, 1998. **98**(13): p. 355-370.

48. Davies, G., et al., *A MODEL FOR RADIATION-DAMAGE EFFECTS IN CARBON-DOPED CRYSTALLINE SILICON.* Semiconductor Science and Technology, 1987. **2**(8): p. 524-532.

49. Oehrlein, G.S., *SILICON OXYGEN COMPLEXES CONTAINING 3 OXYGEN-ATOMS AS THE DOMINANT THERMAL DONOR SPECIES IN HEAT-TREATED OXYGEN-CONTAINING SILICON.* Journal of Applied Physics, 1983. **54**(9): p. 5453-5455.

50. Shi, Y., et al., *A NUMERICAL STUDY OF CLUSTER CENTER FORMATION IN NEUTRON-IRRADIATED SILICON.* Journal of Applied Physics, 1990. **67**(2): p. 1116-1118.

51. MacEvoy, B.C., G. Hall, and K. Gill, *Defect evolution in irradiated silicon detector material.* Nuclear Instruments & Methods in Physics Research Section a-Accelerators Spectrometers Detectors and Associated Equipment, 1996. **374**(1): p. 12-26.

52. Wolley, R.A., et al., *Defects in semiconductors*, in *Material science forum*1986: Paris. p. 6.

53. Lindstrom, G., *Radiation damage in silicon detectors.* Nuclear Instruments & Methods in Physics Research Section a-Accelerators Spectrometers Detectors and Associated Equipment, 2003. **512**(1-2): p. 30-43.

54. MacEvoy, B.C., *Defect evolution in silicon detector material.* Nuclear Instruments & Methods in Physics Research Section a-Accelerators Spectrometers Detectors and Associated Equipment, 1997. **388**(3): p. 365-369.

55. Huhtinen, M., *Simulation of non-ionising energy loss and defect formation in silicon.* Nuclear Instruments & Methods in Physics Research Section a-Accelerators Spectrometers Detectors and Associated Equipment, 2002. **491**(1-2): p. 194-215.

56. Hoenniger, F., et al., *DLTS measurements of radiation induced defects in epitaxial and MCz silicon detectors.* Nuclear Instruments & Methods in Physics Research Section a-Accelerators Spectrometers Detectors and Associated Equipment, 2007. **583**(1): p. 104-108.

57. Pintilie, I., et al., *Stable radiation-induced donor generation and its influence on the radiation tolerance of silicon diodes.* Nuclear Instruments & Methods in Physics Research Section a-Accelerators Spectrometers Detectors and Associated Equipment, 2006. **556**(1): p. 197-208.

58. Moll, M. and M. Bruzzi, *RD50 Status Report 2008*, in *Radiation hard semiconductor devices for vey high luminosity colliders.*2009.

59. Pintilie, I., et al., *Radiation-induced point- and cluster-related defects with strong impact on damage properties of silicon detectors.* Nuclear Instruments & Methods in Physics Research Section a-Accelerators Spectrometers Detectors and Associated Equipment, 2009. **611**(1): p. 52-68.

60. Fretwurst, E., et al. *Survey of recent radiation damage studies at hamburg.* in *3rd RD50 Workshop*. 2003. CERN.

61. Piemonte, C., *Device simulations of isolation techniques for silicon microstrip detectors made on p-type substrates.* Ieee Transactions on Nuclear Science, 2006. **53**(3): p. 1694-1705.

62. Lutz, G., *Radiation damage in structured silicon radiation detectors.*, 2002, IEEE Nuclear and space radiation effects conference.: Phoenix, Arizona.

63. Richter, R.H., et al., *Strip detector design for ATLAS and HERA-B using two-dimensional device simulation.* Nuclear Instruments & Methods in Physics Research Section a-Accelerators Spectrometers Detectors and Associated Equipment, 1996. **377**(2-3): p. 412-421.

64. Rohe, T., et al., *Position dependence of charge collection in prototype sensors for the CMS pixel detector.* Ieee Transactions on Nuclear Science, 2004. **51**(3): p. 1150-1157.

65. Casse, G., et al., *Performances of miniature microstrip detectors made on oxygen enriched p-type substrates after very high proton irradiation.* Nuclear Instruments & Methods in Physics Research Section a-Accelerators Spectrometers Detectors and Associated Equipment, 2004. **535**(1-2): p. 362-365.

66. Lozano, M., et al., *Ultimate limits for the radiation hardness of silicon strip detectors for sLHC.* Nuclear Instruments & Methods in Physics Research Section a-Accelerators Spectrometers Detectors and Associated Equipment, 2007. **581**(1-2): p. 365-367.

67. Eber, R. and F. Petry. *A comparative study of mixed irradiated silicon strip sensors*. in *19th RD50 Workshop*. 2011. CERN.

68. Hartke, J.L., *3-DIMENSIONAL POOLE-FRENKEL EFFECT.* Journal of Applied Physics, 1968. **39**(10): p. 4871-&.

69. Kuhnke, M., E. Fretwurst, and G. Lindstrom, *Defect generation in crystalline silicon irradiated with high energy particles.* Nuclear Instruments & Methods in Physics Research Section B-Beam Interactions with Materials and Atoms, 2002. **186**: p. 144-151.

70. Mikelsen, M., et al., *Kinetics of divacancy annealing and divacancy-oxygen formation in oxygen-enriched high-purity silicon.* Physical Review B, 2005. **72**(19).

71. Svensson, B.G., et al., *DIVACANCY ACCEPTOR LEVELS IN ION-IRRADIATED SILICON.* Physical Review B, 1991. **43**(3): p. 2292-2298.

72. Markevich, V.P., et al., *Trivacancy and trivacancy-oxygen complexes in silicon: Experiments and ab initio modeling.* Physical Review B, 2009. **80**(23).

73. Markevich, V.P., et al., *Structure and electronic properties of trivacancy and trivacancy-oxygen complexes in silicon.* Physica Status Solidi a-Applications and Materials Science, 2011. **208**(3): p. 568-571.

74. Lindstroem, G., et al., *Epitaxial silicon detectors for particle tracking - Radiation tolerance at extreme hadron fluences.* Nuclear Instruments & Methods in Physics Research Section a-Accelerators Spectrometers Detectors and Associated Equipment, 2006. **568**(1): p. 66-71.

75. Fretwurst, E. *Comparison of neutron damage in thin FZ, MCz and epitaxial silicon detectors.* in *10th RD50 Workshop*. 2007. Vilnius.

76. Casse, G. *Update on charge collection annealing.* in *19th RD50 Workshop*. 2011. CERN.

77. Kramberger, G., et al., *Determination of effective trapping times for electrons and holes in irradiated silicon.* Nuclear Instruments & Methods in Physics Research Section a-Accelerators Spectrometers Detectors and Associated Equipment, 2002. **476**(3): p. 645-651.

78. Seidel, S., J. Metcalfe, and M. Hoeferkamp. *Depletion Voltage and Effective Doping Concentration of Float Zone and Magnetic Czochralski Silicon Diodes Irradiated by Protons to Conditions Relevant to the High Luminosity HC*. in *19th RD50 Workshop*. 2011. CERN.

79. Eckstein, D. *Comparison of proton damage in thin FZ, MCz and epitaxial silicon detectors.* in *12th RD50 Workshop*. 2008. Ljubljana.

80. Kaska, L. *Annealing studies on MCz after 23 GeV proton irradiation and CCE of 150 µm epitaxial silicon devices.* in *12th RD50 Workshop*. 2008. Ljubljana.

81. Moll, M., et al., *Development of radiation tolerant semiconductor detectors for the Super-LHC.* Nuclear Instruments & Methods in Physics Research Section a-Accelerators Spectrometers Detectors and Associated Equipment, 2005. **546**(1-2): p. 99-107.

82. Pacifico, N. *Annealing study on 24 GeV/c proton irradiated p-type detectors*. in *19th RD50 Workshop*. 2011. CERN.

83. Krasel, O., et al. *Measurement of Trapping Time Constants in Proton-Irradiated Silicon Pad Detectors*. in *IEEE Nuclear Science Symposium and Medical Imaging Conference*. 2003. Portland, Oregon.

84. Metcalfe, J., *Silicon detectors for the sLHC.*, in *RD50 Report.*2010.

85. Affolder, A., P. Allport, and G. Casse, *Collected charge of planar silicon detectors after pion and proton irradiations Up to 2.2 x 10(16) n(eq) cm(-2).* Nuclear Instruments & Methods in Physics Research Section a-Accelerators Spectrometers Detectors and Associated Equipment, 2010. **623**(1): p. 177-179.

86. Affolder, A., P. Allport, and G. Casse, *Charge collection efficiencies of planar silicon detectors after reactor neutron and proton doses up to 1.6 x 10(16) n(eq) cm(-2).* Nuclear Instruments & Methods in Physics Research Section a-Accelerators Spectrometers Detectors and Associated Equipment, 2010. **612**(3): p. 470-473.

87. Cindro, V., et al. *Effects of long term annealing in p-type strip detectors irradiated with neutrons to Φeq=1E16cm-2, investigated by Edge-TCT*. in *19th RD50 Workshop*. 2011. CERN.

88. Kramberger, G., et al., *Effective trapping time of electrons and holes in different silicon materials irradiated with neutrons, protons and pions.* Nuclear Instruments & Methods in Physics Research Section a-Accelerators Spectrometers Detectors and Associated Equipment, 2002. **481**(1-3): p. 297-305.

89. Cindro, V., et al. *Trapping of Electrons and Holes in p-type Silicon Irradiated with Neutrons*. in *15th International Workshop on Room-Temperature*

Semiconductor X- and Gamma-Ray Detectors/ 2006 IEEE Nuclear Science Symposium. 2006. San Diego, CA.

90. Sadrozinski, H.F.W., et al., *Total dose dependence of oxide charge, interstrip capacitance and breakdown behavior of sLHC prototype silicon strip detectors and test structures of the SMART collaboration.* Nuclear Instruments & Methods in Physics Research Section a-Accelerators Spectrometers Detectors and Associated Equipment, 2007. **579**(2): p. 769-774.

91. Ma, T.P. and P.V. Dressendorfer, *Ionizing radiation effects in MOS devices and circuits.*1989: John Wiley & Sons.

92. Petasecca, M., et al., *Numerical simulation of radiation damage effects in p-type and n-type FZ silicon detectors.* Ieee Transactions on Nuclear Science, 2006. **53**(5): p. 2971-2976.

93. Pennicard, D., *3D Detectors for Synchrotron Applications.*, in *Physics and Astronomy Department.*2009, Glasgow.

94. Petasecca, M. *Modeling radiation damage effects in oxygenated silicon detectors.* in *9th RD50 Workshop*. 2006. CERN.

95. Lozano, M., et al., *Comparison of radiation hardness of P-in-N, N-in-N, and N-in-P silicon pad detectors.* Ieee Transactions on Nuclear Science, 2005. **52**(5): p. 1468-1473.

96. Kenney, C.J., et al., *Active-edge planar radiation sensors.* Nuclear Instruments & Methods in Physics Research Section a-Accelerators Spectrometers Detectors and Associated Equipment, 2006. **565**(1): p. 272-277.

97. Wu, B., A. Kumar, and S. Pamarthy, *High aspect ratio silicon etch: A review.* Journal of Applied Physics, 2010. **108**(5).

98. Doering, R. and Y. Nishi, *Handbook of Semiconductor manufacturing technology*. Second edition ed2008.

99. Verdonck, P., *Plasma etching*, 2006: Universidade Estadual de Campinas, Brasil. p. 11.

100. Ruggiero, G., et al., *Planar edgeless silicon detectors for the TOTEM experiment.* Ieee Transactions on Nuclear Science, 2005. **52**(5): p. 1899-1902.

101. Noschis, E., et al., *Final size planar edgeless silicon detectors for the TOTEM experiment.* Nuclear Instruments & Methods in Physics Research Section a-Accelerators Spectrometers Detectors and Associated Equipment, 2006. **563**(1): p. 41-44.

102. Verbitskaya, E., et al., *Electrical properties of the sensitive side in Si edgeless detectors.* Nuclear Instruments & Methods in Physics Research Section a-Accelerators Spectrometers Detectors and Associated Equipment, 2009. **604**(1-2): p. 246-249.

103. Balbuena, J.P., et al., *Simulation of Irradiated Edgeless Detectors*, in *2008 Ieee Nuclear Science Symposium and Medical Imaging Conference*2009. p. 1828-1831.

104. Noschis, E., V. Eremin, and G. Ruggiero, *Simulations of planar edgeless silicon detectors with a current terminating structure.* Nuclear Instruments & Methods in Physics Research Section a-Accelerators Spectrometers Detectors and Associated Equipment, 2007. **574**(3): p. 420-424.

105. Noschis, E.P., *Planar edgeless detectors for the TOTEM experiment ant the Large Hadron Collider*, in *Physical Sciences department*2006, University of Helsinky: Finland.

106. Verbitskaya, E., et al., *Concept of Double Peak electric field distribution in the development of radiation hard silicon detectors.* Nuclear Instruments & Methods in Physics Research Section a-Accelerators Spectrometers Detectors and Associated Equipment, 2007. **583**(1): p. 77-86.

107. Eremin, V., E. Verbitskaya, and Z. Li, *The origin of double peak electric field distribution in heavily irradiated silicon detectors.* Nuclear Instruments & Methods in Physics Research Section a-Accelerators Spectrometers Detectors and Associated Equipment, 2002. **476**(3): p. 556-564.

108. Eremin, V., et al., *Double peak electric field distortion in heavily irradiated silicon strip detectors.* Nuclear Instruments & Methods in Physics Research Section a-Accelerators Spectrometers Detectors and Associated Equipment, 2004. **535**(3): p. 622-631.

109. Verbitskaya, E., V. Eremin, and G. Ruggiero, *Status of silicon edgeless detector developments for close-to-beam experiments.* Nuclear Instruments & Methods in Physics Research Section a-Accelerators Spectrometers Detectors and Associated Equipment, 2010. **612**(3): p. 501-508.

110. Ruggiero, G., V. Eremin, and E. Noschis, *Planar edgeless silicon detectors for the TOTEM experiment.* Nuclear Instruments & Methods in Physics Research Section a-Accelerators Spectrometers Detectors and Associated Equipment, 2007. **582**(3): p. 854-857.

111. Bergamaschi, A., et al., *A detection system for clinical breast tomography with synchrotron radiation.* Nuclear Instruments & Methods in Physics Research Section a-Accelerators Spectrometers Detectors and Associated Equipment, 2004. **535**(1-2): p. 88-92.

112. Giani, S., *TOTEM. Preliminary physics results.*, O.b.o.t.T. Collaboration, Editor 2010, CERN: LHC Physics Center at CERN.

113. Ellis, P.J., A.E. Cohen, and S.M. Soltis, *Beamstop with integrated X-ray sensor.* Journal of Synchrotron Radiation, 2003. **10**: p. 287-288.

114. Owen, R.L., et al., *Determination of X-ray flux using silicon pin diodes.* Journal of Synchrotron Radiation, 2009. **16**: p. 143-151.

115. Hansen, T.-E., et al., *First fabrication of full 3D-detectors at SINTEF.* Journal of Instrumentation, 2009. **4**.

116. Pellegrini, G., et al., *Fabrication and simulation of novel ultra-thin 3D silicon detectors.* Nuclear Instruments & Methods in Physics Research Section a-Accelerators Spectrometers Detectors and Associated Equipment, 2009. **604**(1-2): p. 115-118.

117. Zoboli, A., et al., *Double-Sided, Double-Type-Column 3-D Detectors: Design, Fabrication, and Technology Evaluation.* Ieee Transactions on Nuclear Science, 2008. **55**(5): p. 2775-2784.

118. *A Joint European Torus (JET).* Available from: http://www.efda.org/JET/.

119. Orava, R., et al., *Back-thinned radiation detector with '3D' active region and corresponding methods for manufacturing and use*, 2008.

120. Pennicard, D., et al. *Simulation Results from Double-Sided 3D Detectors*. in *15th International Workshop on Room-Temperature Semiconductor X- and Gamma-Ray Detectors/ 2006 IEEE Nuclear Science Symposium*. 2006. San Diego, CA.

121. Guardiola, C., et al. *Active Neutron Detection with Ultra-Thin 3D Silicon Detectors in Radiotherapy Linacs,*. in *IEEE Nuclear Science Symposium and Medical Imaging Conference*. 2011. Valencia, Spain.

122. Brennan, K.F., *Introduction to semiconductor devices: for computing and telecommunication applications.*, ed. C.U. Press.2005.

123. Guardiola, C., et al. *Portable Silicon Neutron Detector System.* in *8th Spanish Conference on Electron Devices.* 2011.

124. Guardiola, C., et al., *Ultra-thin 3D silicon sensors for neutron detection.* Journal of Instrumentation, 2012.

125. Huegging, F. and A. Collaboration, *The ATLAS Pixel Insertable B-layer (IBL).* Nuclear Instruments & Methods in Physics Research Section a-Accelerators Spectrometers Detectors and Associated Equipment, 2011. **650**(1): p. 45-49.

126. Da Via, C., et al., *Technical Specifications and Acceptance Criteria for the 3D Sensors of the ATLAS IBL.*, in *3D IBL Sensor Technical Specifications.*2011: CERN.

127. Aad, G., et al., *ATLAS pixel detector electronics and sensors.* Journal of Instrumentation, 2008. **3**.

128. Koehler, M., et al. *Test beam and laser measurements with irradiated 3D silicon strip detectors.* in *16th RD50 Workshop*. 2010. Barcelona, Spain.

129. Koehler, M., et al. *Comparative studies of irradiated 3D silicon strip detectors on p-type and n-type substrate.* in *17th RD50 Workshop*. 2010. CERN.

130. Bates, R.L., et al. *Charge collection studies of heavily irradiated 3D Double-Sided sensors*. in *IEEE Nuclear Science Symposium Conference 2009*. 2009. Orlando, FL: Ieee.

131. Fleta, C., et al. *Laboratory and testbeam results on 3D detectors.* in *19th International Workshop on Vertex Detectors*. 2010. Loch Lomond, UK.

132. Fleta, C., M. Lozano, and G. Pellegrini. *Irradiation and annealing study of 3D p-type strip detectors.* in *16th RD50 Workshop*. 2010. Barcelona, Spain.

133. Grenier, P., *Silicon sensor technologies for ATLAS IBL upgrade*, in *Technology and Instrumentation in Particle Physics*2011: Chicago.

134. Sze, S.M. and G. Gibbons, *EFFECT OF JUNCTION CURVATURE ON BREAKDOWN VOLTAGE IN SEMICONDUCTORS.* Solid-State Electronics, 1966. **9**(9): p. 831-&.

135. Koehler, M., *Double-sided 3D silicon detectors for the High-Luminosity LHC.*, in *Faculty of Physics and Mathematics*2011, University of Freiburg.

136. Pahn, G., et al., *First Beam Test Characterisation of a 3D-stc Silicon Short Strip Detector.* Ieee Transactions on Nuclear Science, 2009. **56**(6): p. 3834-3839.

137. Grinstein, S., et al. *IBL activities at IFAE (ATLAS pixel upgrade).* in *VII Jornadas sobre la Participación Española en los Futuros Aceleradores Lineales (ILC).* 2011. Zaragoza, Spain.

138. Mac Raighne, A., et al., *Precision scans of the Pixel cell response of double sided 3D Pixel detectors to pion and X-ray beams.* Journal of Instrumentation, 2011. **6**: p. 25.

139. Christophersen, M., et al. *Laser-scribing and Al2O3 sidewall passivation of p-type sensors.* in *6th Trento Workshop on Advanced radiation detectors.* 2010. Trento, Italy.
140. Sadrozinski, H.F.W., et al. *Progress on Slim Edges. Cleaving and Sidewall Passivation.* in *19th RD50 Workshop*. 2011. CERN.